FIBRINOGEN-CONJUGATED GOLD-COATED MAGNETITE NANOPARTICLES FOR TARGETING ACTIVATED PLATELETS IN A WHOLE BLOOD SYSTEM

by

Cammy Truong

A Dissertation Submitted in

Partial Fulfilment of the

Requirements for the Degree of

Doctor of Philosophy

in Biological Sciences

at

The University of Wisconsin-Milwaukee

August 2020

ABSTRACT
FIBRINOGEN-CONJUGATED GOLD-COATED MAGNETITE NANOPARTICLES FOR TARGETING ACTIVATED PLATELETS IN A WHOLE BLOOD SYSTEM

by

Cammy Truong

The University of Wisconsin-Milwaukee, 2020
Under the Supervision of Professor Julie Oliver

Activated platelets are a key component of the arterial thrombi responsible for heart attack and stroke. Tissue plasminogen activator (tPA) is currently the only FDA-approved drug for ischemic stroke. It works by dissolving fibrin, thus breaking down the clot and restoring blood flow to the brain. However, it must be administered within 4.5 hours of the onset of stroke. This leaves a significant number of patients who are ineligible for intervention and who have poor clinical outcomes. Additionally, tPA is not injury site-specific; consequently, the side effects range from mild to severe. We are investigating targeting activated platelets in occlusive thrombi for magnetically-induced hyperthermia as an alternative therapy for ischemic stroke.

The binding of plasma fibrinogen to its platelet surface receptor is dependent on cell activation and could therefore function in selective targeting of activated platelets. When fibrinogen receptors are cross-linked by ligand, they engage the actin cytoskeleton and clear from the edges of platelets or groups of platelets, thereby exposing additional unoccupied receptors. We propose that fibrinogen-conjugated nanoparticles can be used to target activated platelets rather than fibrin within an existing occlusive clot as a means to restore blood flow in the vessel. In our model, selection for activated platelets over quiescent circulating platelets is critical in order to minimize bleeding complications that are especially dangerous in ischemic brain. We hypothesize that fibrinogen-conjugated, gold-coated magnetite nanoparticles can

specifically target activated platelets and disrupt occlusive thrombi when exposed to an oscillating magnetic field. We tested this using an *in vitro* model system of thrombosis that allows platelet activation and fibrin formation in platelet-rich plasma or whole blood. Exposing labeled samples to an oscillating magnetic field will cause hyperthermia and disrupt clots. Dense fibrin networks make nanoparticle penetration into the clots very difficult, so we have described clot structure and quantified nanoparticle access to the clot interior using the robust gold nanoparticle system. Our experiments found nanoparticles interact with both activated platelets, and fibrin, giving us multiple targets; clot structure influences how well the nanoparticles are incorporated; and multiple applications of nanoparticles may increase the power of clot busting. These results show our specific cell targeting with hyperthermia can be developed into a viable therapy for ischemic stroke.

© Copyright by Cammy Truong, 2020
All Rights Reserved

This dissertation is firstly dedicated to the memory of my beloved grandfather, who passed away three year ago. My grandfather received his Ph.D during the Vietnam war, and it helped him survive and afterward flourish in post-war Vietnam. I had promised to make my grandfather proud by achieving this monumental academic goal, and continue his legacy of obtaining a Ph.D. I hope that I have fulfilled this promise. I wish that he were still alive today to share with me the celebration and success of my graduation with a Doctor of Philosophy degree.

To my amazing mother, who has shared in all of my joys and sorrows; my trials, failures and achievements, and whose unconditional love and sacrificial care for me and my children have made the pursuit of this work possible.

To my loving husband, who kept me inspired through this, even though he may not read it… Also to his parents, who have accepted me graciously as their daughter, and give me endless support.

And to my dear children, Bao-Duy, Kimmy, Andy, Tammy, and May; each of whom has a special place in my heart. Always be the best you can be!

TABLE OF CONTENTS

CHAPTER 1 – Introduction....1
Figures and Figure Legends....30
References....36

CHAPTER 2 – Investigating Interaction of Nanoparticles with Clot Components
Abstract....56
Introduction....57
Materials and Methods....63
Results....71
Discussion....76
Figures and Figure Legends....83
References....107

CHAPTER 3 – Describing Clot Structure and Nanoparticle Penetration at a Physiologic Range of Thrombin Doses
Abstract....114
Introduction....115
Materials and Methods....120
Results....124
Discussion....134
Figures and Figure Legends....145
References....185

CHAPTER 4 – Optimizing the Penetration of Nanoparticles and Disrupting Labelled Clots
Abstract....190
Introduction....191
Materials and Methods....197
Results....202
Discussion....207
Figures and Figure Legends....212
References....226

CHAPTER 5 – Conclusions....233
References....241

Curriculum Vitae....244

LIST OF FIGURES

Figure 1: Schematic visualization of the molecular interactions regulating physiological fibrinolysis....30
Figure 2: A schematic representation of arterial blood clot formation *in vitro*....31
Figure 3: A schematic of mechanisms of platelet activation inhibitors....32
Figure 4: Structural features of a resting platelet and their functions....33
Figure 5: Platelet aggregation....34
Figure 6: Labeling of surface-activated and suspension-activated platelets using fibrinogen-conjugated gold nanoparticles (FGN-cAu_{18})....35
Figure 7: Schematic flow chart of isolation of human platelets....83
Figure 8: Schematic flow chart of isolation of human red blood cells....84
Figure 9: TEM micrographs of PRP clot cross sections....85
Figure 10: SEM micrographs of WB clot cross sections....86
Figure 11: SEM micrographs of the remaining supernatant from a fibrin clot labelled with FGN-cAu_{18} nanoparticles....87
Figure 12: SEM micrographs of the remaining supernatant from a fibrin clot labelled with FGN-cAu-Fe_3O_4 nanoparticles....88
Figure 13: Montage of medial fibrin clot section labelled with FGN-cAu_{18}....89
Figure 14: Montage of medial fibrin clot section labelled with FGN-cAu-Fe_3O_4 nanoparticles....90
Figure 15: Cross-section of fibrin clot and the remaining supernatant from a fibrin clot labelled with FGN-cAu_{18} nanoparticles....91
Figure 16: Cross-section of fibrin clot and the remaining supernatant from a fibrin clot labelled with FGN-cAu-Fe_3O_4 nanoparticles....92
Figure 17: SEM micrographs of suspended GFP labelled with FGN-cAu_{18}....93
Figure 18: SEM micrographs of platelet aggregate cross sections labelled with FGN-cAu_{18}....94
Figure 19: SEM micrographs of suspended GFP labelled with FGN-cAu-Fe_3O_4....95
Figure 20: SEM micrographs of platelet aggregate cross sections labelled with FGN-cAu-Fe_3O_4....96
Figure 21: Montage of medial platelet clot section labelled with FGN-cAu_{18} nanoparticles....97
Figure 22: Montage of medial platelet clot section labelled with FGN-cAu-Fe_3O_4 nanoparticles....98
Figure 23: Cross-section of platelet clot labelled with FGN-cAu_{18} nanoparticles....99
Figure 24: Cross-section of a platelet clot labelled with FGN-cAu-Fe_3O_4 nanoparticles....100
Figure 25: SEM micrographs of remaining supernatant from RBCs labelled with FGN-cAu_{18} nanoparticles....101
Figure 26: SEM micrographs of the remaining supernatant from RBCs labelled with FGN-cAu-Fe_3O_4 nanoparticles....102
Figure 27: Montage of medial RBC clot labelled with FGN-cAu_{18} nanoparticles....103
Figure 28: Montage of medial RBC clot section labelled with FGN-cAu-Fe_3O_4 nanoparticles....104
Figure 29: Cross-section of RBC clot and the remaining supernatant from RBC clot

formation labelled with FGN-cAu$_{18}$ nanoparticles 105
Figure 30: Cross-section of RBC clot and the remaining supernatant from RBC clot formation labelled with FGN-cAu-Fe_3O_4 nanoparticles 106
Figure 31: PRP clotting curve from different donors using various thrombin concentration 145
Figure 32: Time to V_{max} in response to different doses of thrombin 148
Figure 33: The volume of remaining supernatant after PRP clots formed at different thrombin concentrations, obtained from the platelet reader experiments 150
Figure 34: The volume of supernatant remaining after WB clots formed at different thrombin concentrations, obtained from the platelet reader experiments 152
Figure 35: PPP, PRP, and WB clotting time versus log thrombin concentration obtained from a fibrometer 155
Figure 36: PRP clot structures formed at low thrombin doses from three different donors 156
Figure 37: PRP clot structures formed at high thrombin doses from three different donors 157
Figure 38: WB clot structures formed at low thrombin doses from three different donors 158
Figure 39: WB clot structures formed at high thrombin doses from three different donors 159
Figure 40: Visualization of colloidal carbon penetration into PRP clot formed at low and high thrombin concentrations 160
Figure 41: Visualization of colloidal carbon penetration into WB clot formed at low and high thrombin concentrations 161
Figure 42: Comparison of area penetrated by ink of clots formed from PRP and WB 163
Figure 43: SEM montage medial cross-section of a PRP clot formed at low thrombin concentration of donor 1 with high magnification micrographs of FGN-cAu$_{18}$ at sites found inside clots 164
Figure 44: SEM montage of a medial cross-section of PRP clot formed at high thrombin concentration of donor 1 with high magnification micrographs of FGN-cAu$_{18}$ at the sites found inside clots 165
Figure 45: SEM montage of a medial cross-section of a WB clot formed at low thrombin concentration from donor 1 and high magnification micrographs of area where nanoparticles resided inside the clot 166
Figure 46: SEM montage of a medial cross-section of a WB clot formed at high thrombin concentration from donor 1 with high magnification micrographs of the area where nanoparticles were found 168
Figure 47: Penetration of FGN-cAu$_{18}$ into PRP clot formed at low thrombin concentration from three different donors 169
Figure 48: Penetration of FGN-cAu$_{18}$ into PRP clots formed at high thrombin concentration from three different donors 170
Figure 49: The penetration of nanoparticles into WB clots formed at low thrombin concentration from three different donors 172

Figure 50: The penetration of nanoparticles into WB clots formed at high thrombin concentration from three different donors 173
Figure 51: Light microscopy images of silver enhancement of FGN-cAu_{18} in labeled PRP and WB clots.....175
Figure 52: Reconstruction of the frozen sections of PRP clots formed at different thrombin concentrations labeled with FGN-cAu_{18} and treated with silver enhancement 177
Figure 53: Reconstruction of frozen cross-sections of WB clots formed at different thrombin concentrations with high magnification images of areas containing nanoparticles 179
Figure 54: Quantifying the nanoparticle penetration in PRP and WB clots using silver enhancement 183
Figure 55: TEM micrographs of magnetite nanoparticles produced by coprecipitation method after 3 days growing under argon 212
Figure 56: Effect of nanoparticle concentration and labeling time on nanoparticle penetration into PRP clots formed at 1nM thrombin.....213
Figure 57: Effect of nanoparticle concentration and labeling time on nanoparticle penetration into PRP clots formed at 10nM thrombin.....214
Figure 58: Effect of nanoparticle concentration and labeling time on nanoparticle penetration into WB clots formed at 1nM thrombin.....217
Figure 59: Effect of nanoparticle concentration and labeling time on nanoparticle penetration into WB clots formed at 10nM thrombin.....218
Figure 60: Light microscopy images analysis of magnetite nanoparticles and oscillating magnetic field (OMF) in RAW 264.7.....221
Figure 61: SEM micrographs showing the uptake of magnetite nanoparticles by RAW 264.7 222
Figure 62: SEM micrographs of magnetite nanoparticles and oscillating magnetic field (OMF) killed the RAW 264.7 cells.....223
Figure 63: SEM micrographs of surfaced-activated platelets labeled with fibrinogen-conjugated gold nanoparticles (FGN-cAu_{18}) and fibrinogen-conjugated gold-coated magnetite nanoparticles (FGN-cAu-Fe_3O_4) 224
Figure 64: SEM micrographs of magnetite nanoparticles and oscillating magnetic field (OMF) killed surfaced-activated platelet.....225

LIST OF TABLES

Table 1: Clotting time data obtained from PRP clotting curve from plate reader experiments 147
Table 2: Volume of remaining supernatant after PRP clot formation, obtained from plate reader experiment 149
Table 3: Volume of remaining supernatant after WB clots formed, obtained from plate reader from three different donors 151
Table 4: The clotting time data obtained from the fibrometer experiments 153
Table 5: The average clotting time of PPP, PRP, and WB calculated from Table 4 ... 154
Table 6: The percent area of the PRP and WB clots penetrated by colloidal carbon measured by the threshold function of the ImageJ program 162
Table 7: Measurements of clot diameters, deepest distance of nanoparticle migration, and percentages of nanoparticle penetration of PRP clots formed at various thrombin concentrations from 6 donors using the quick screening method (silver enhancement incorporated with light microscopy) 181
Table 8: Measurements of clot diameters, nanoparticle penetration, and percentage of nanoparticles collected from WB clots formed at various thrombin doses and from 6 different donors using silver enhancement 182
Table 9: Quantification of nanoparticle penetration in PRP clotted with 1nM thrombin, labeled with low or high concentration of FGN-cAu_{18} and incubated for either 15 or 60 minutes 215
Table 10: Quantification of nanoparticle penetration in PRP clotted with 10nM thrombin, labeled with low or high concentration of FGN-cAu_{18} and incubated for either 15 or 60 minutes 216
Table 11: Quantification of nanoparticle penetration in WB clotted with 1nM thrombin, labeled with low or high concentration of FGN-cAu_{18} and incubated for either 15 or 60 minutes 219
Table 12: Quantification of nanoparticle penetration in WB clotted with 10nM thrombin, labeled with low or high concentration of FGN-cAu_{18} and incubated for either 15 or 60 minutes 220

LIST OF ABBREVIATIONS

1. αIIbβ3: The integrin αIIbβ3 also known as glycoprotein IIb/IIIa
2. AA: arachidonic acid
3. BEI: Backscattered electron image
4. BSA: Bovine serum albumin
5. cAu_{18}: 18nm colloidal gold
6. cFe_3O_4: Colloidal magnetite
7. COX: Cyclooxygenase
8. ddH_2O: Double deionized water
9. FGN: Fibrinogen
10. FGN-cAu_{18}: Fibrinogen-conjugated gold nanoparticles
11. FGN-cAu-Fe_3O_4: Fibrinogen-conjugated, gold-coated magnetite nanoparticles
12. GFP: Gel-filtered platelet
13. GPCR: G-protein-coupled receptor
14. $HAuCl_4$: Gold Chloride Trihydrate
15. HEPES: 4-(2-hydroxyethyl)-1-piperazineethanesulfonic acid
16. MDDW: Millipore double deionized water
17. OMF: Oscillating magnetic field
18. PAR: Protease activator receptor
19. PEG: Polyethylene glycol
20. PPP: Platelet-poor plasma
21. PRP: Platelet-rich plasma
22. RBC: Red blood cell

23. RT: Room temperature
24. SE: Silver enhancement
25. SEI: Secondary electron image
26. SEM: Scanning electron microscopy
27. TEM: Transmission electron microscopy
28. TMAOH: Tetramethylammonium hydroxide
29. tPA: Tissue plasminogen activator
30. TXA-2: Thromboxane A2
31. WBC: White blood cell
32. WB: Whole blood

ACKNOWLEDGEMENTS

First and foremost, I would like to express my deep and sincere gratitude to my supervisor Dr. Julie Oliver for giving me the opportunity to do research and providing me invaluable guidance throughout this project. Your dynamism, vision, sincerity, and motivation have inspired me. Also, I greatly appreciate your friendship, empathy, and sense of humor. Last but not least, I thank you for favoring me, you are the best teacher and you have helped me achieve so much!

I am grateful to Dr. Heather Owen for her extraordinary mentoring in electron microscopy. You taught me much needed electron microscopy techniques, answered uncountable questions about electron microscopy, and never be tired of training me on how to use Photoshop. Without your guidance and persistent help this dissertation would not have been possible. Thank you from the bottom of my heart.

My appreciation also goes to my remaining committee members; Dr. Douglas Steeber, Dr. Ralph Albrecht, Dr. Charles Wimpee, and Dr. Marija Gajdardziska-Josifovska. Their meticulous scrutiny, scholarly advice, and scientific approach have helped in shaping my research and this dissertation.

Lastly, there is no way that I could have undertaken this Ph.D adventure without the help of many people from the biological sciences department here at the University of Wisconsin-Milwaukee and their support. I always place on my record, my sense of gratitude to one and all who directly or indirectly, have lent their helping hand in this endeavor.

Chapter 1- A Novel Treatment for Ischemic Stroke: Specific Cell Targeting with Nanoparticles for Hyperthermia

Impact of stroke worldwide and in the United States of America:

Worldwide, an estimated 11.6 million incident ischemic strokes and 5.3 million incident hemorrhagic strokes occur each year. Of the 16.9 million total, 6.1 million people died and about 5 million survivors were left disabled. In fact, strokes are the second leading cause of death and the third leading cause of disability in the world (1, 2).

In America, each year nearly 795,000 people experience a new or recurrent stroke. Of these, 610,000 of these are first attacks, and 185,000 are recurrent. Of the strokes in America, 87% are ischemic and 13% are hemorrhagic. Although less common, hemorrhage strokes have a higher mortality rate compared with ischemic strokes. Approximately 8% to 12% of ischemic strokes and 37% to 38% of hemorrhage strokes result in death within 30 days of stroke onset. Every 40 seconds, someone in America has a stroke. On average, every 3 minutes and 35 seconds someone dies of a stroke. Strokes account for 1 in every 19 deaths in America. When considered separate from other cardiovascular diseases, strokes rank fifth among all causes of death, behind diseases of the heart, cancer, chronic lower respiratory diseases and unintentional accidents (1). In addition, stroke is the leading cause of serious long-term disability in America (1, 3). In 2014 to 2015, the average annual cost of strokes in the US was $45.5 billion. $28 billion of which were direct medical costs, including outpatient or office-based provider visits, hospital inpatient stays, emergency department visits, prescribed medicines, and at home health care (1, 4).

Strokes appear to be a huge burden for not only our nation’s people and its economy, but also people and economies worldwide. Despite the enormous impact of strokes, there are still very few treatments currently available. Thus, new approaches to therapy are needed.

Pathology underlying stroke:

A stroke is defined simply as a “brain attack” or a “cerebrovascular accident”. Blood vessels that deliver blood to the brain or other parts of the body from the heart are called arteries. A stroke is a disease that affects the arteries leading to and within the brain. The brain needs a constant supply of blood carrying the oxygen and nutrients it needs to function. Specific arteries provide blood to specific areas of the brain. A stroke occurs when the blood vessels flowing to the brain either become blocked or ruptured. When the blood supply to the brain is cut off, the brain cells do not receive enough oxygen and nutrients. If the deprivation of oxygen and nutrients lasts long enough, these brain cells will start to die. When the cells begin to die, the functions controlled by that area of the brain, such as memory or muscle control, can be lost. The ultimate effect of the stroke on the patient primarily depends on several factors including the location of the obstruction or rupture, and how much the brain tissue is damaged (5-8). For example, if a stroke happens in the occipital lobe, it’s likely that a disability involving vision will result. Also, as sides of the brain have contralateral control of the body, a stroke on one side of the brain will cause neurological complications on the opposing side of the body.

Anyone can have a stroke at any age. Stroke risk factors include underlying medical conditions, lifestyle choices, genetics, age, sex, and ethnicity. Strokes are classified into two broad categories; ischemic (clots) and hemorrhagic (bleeds).

Hemorrhagic strokes account for 13% of all stroke cases (1). There are two main types of hemorrhagic stroke; intracranial hemorrhages happen when the bleeding occurs inside the brain and subarachnoid hemorrhages happen when the bleeding occurs between the brain and the meningeal membranes that cover it. Hemorrhagic stroke is usually the result of a weakened vessel, or aneurysm, that ruptures and bleeds into the surrounding brain. Thus, it allows blood to

leak and accumulate inside the brain. The sudden increase in pressure within the brain causes compression of the surrounding brain tissue and leads to neural damage. In addition, when neurons are exposed to high concentrations of the blood coagulation protease thrombin, it causes apoptosis via signaling through members of the protease activated receptor (PAR) family (9, 10). The available treatments for hemorrhagic stroke depend on what caused it, its location, and the size of the hemorrhage. Treatments include interventional radiology or neurosurgical procedures such as surgical clipping or coil embolization. Neurosurgical procedures are performed to stop the bleeding and reduce the pressure in the brain. Additionally, medications can be given to reduce swelling, pain, and prevent seizures. The best treatment for hemorrhagic stroke is detection of the aneurysm before it bursts and to undergo a surgical repair of the vessel. After rupture occurs, treatment becomes more difficult and outcomes can be poor (11).

The majority of strokes are ischemic. They account for 87% of all stroke incidences (1). Thus, it is implied that ischemic strokes are responsible for the majority of disabilities suffered by stroke victims. Ischemic strokes are caused by occlusive clots in arteries, where high shear rate contributes to platelet activation and fibrin formation. This results in rich-platelet thrombi that reduces blood supply to the brain and leads to a hypoxic condition and a lack of nutrients downstream of the blockage (12-14). Types of ischemic strokes can be further broken down by the cause of the occlusion. The most common type of ischemic stroke, known as a cerebral thrombosis, is a thrombus that develops at a fatty plaque build up within the blood vessel. Another type of ischemic stroke is called a cerebral embolism. It is a blood clot that forms at another location in the circulatory system, such as the heart or large artery of the upper chest and neck. Then, part of the blood clot breaks loose, enters the bloodstream, and travels through the brain's blood vessels until it reaches vessels too small to pass through. The embolism usually

originated in the heart in an unclosed foramen ovale or damaged heart valve, or in atherosclerotic arteries (15-17).

Both types of ischemic stroke have the same outcome of occluding the vessel and obstructing the flow of blood to the brain tissue supplied by the occluded artery. When blood stops flowing to brain tissues, it will develop two different areas of injury. The zone closest to the artery that has been blocked off is called the ischemic core. The zone on the periphery of the core is called the ischemic penumbra. During ischemic stroke, neurons and their supporting cells located within the ischemic core will die off quickly due to the deprivation of oxygen and nutrients, causing a metabolic drop in these cells because of the deregulation of cellular K^+ and Ca^{2+} ion gradients (18-20). Neurons and their supporting cells in the ischemic penumbra can live a little longer than those in the core because they get some blood supplied from surrounding arteries. However, these neurons still become silent due to reduced metabolism and are at risk of degradation as the ischemic stroke progresses. They eventually will die off if blood flow is not reestablished. The penumbra is the area where treatments are most likely to be effective compared to the ischemic core. Thus, if the blood flow can be restored safely into the ischemic area in a timely manner, neurons in the penumbra may regain normal function and damage to brain tissue can be minimized. As a result, a great interest lies in the quick reperfusion of the penumbra (21, 22).

Current treatment for ischemic stroke:

The only FDA-approved drug for ischemic stroke is recombinant tissue plasminogen activator (tPA), a clot-dissolving medication. The first-generation product on the market carries the generic name alteplase (Activase®, Genetech). This medication, administered intravenously

or directly to the site of the blockage, has to be provided within the first 4.5 hours of a stroke. tPA benefits patients through limiting the amount of brain tissue that dies by dissolving the blood clot in the brain and restoring blood flow to the affected brain territory before it sustains irreversible damage. Because the benefit of tPA is time dependent, it is critical to treat patients as quickly as possible. tPA is classified as a serine protease and is one of the essential components of the fibrinolysis pathway, which is an important first step in the wound healing process. tPA's primary function includes initiating fibrinolysis by catalyzing the conversion of plasminogen to a serine protease plasmin, the primary enzyme involved in dissolving blood clots (23, 24). Plasmin is the major protease responsible for local fibrinolysis and leads to the decrease in size of fibrin strands (Figure 1), causing fibrin to lose its function of trapping clot components such as platelets and red blood cells (RBCs). Thus, dissolution of the clot occurs, and blood flow is restored to the surrounding tissue and perfused ischemic neurons.

Since approval of tPA as a therapeutic for ischemic strokes in 1996, it has been found to be and is now considered a double-edged sword. tPA is not injury site-specific and can cause bleeding complications at sites outside of the occlusion. In some instance, administering tPA can be considered more dangerous than the stroke itself because it can cause brain hemorrhages. According to alteplase guidelines, the drug is only approved in patients suffering from an acute ischemic stroke. In order to receive tPA, patient criteria such as time restrictions, potential bleeding complications, medical history, and age issues have to align. If the potential benefit of tPA therapy is greater than the risk of side effects such as bleeding, the providers will administer tPA. In fact, the strict eligibility criteria for this medication lead to low rates of alteplase treatment (25, 26). Moreover, up to 2/3rds of stroke patients that received tPA treatment with large-vessel occlusions did not achieve recanalization. In addition, less than 50% of those treated

with tPA achieved a complete reperfusion by 24 hours and about 40% of the stroke patients remained severely disabled or died (27, 28). Thus, there is a need to develop a combinational therapy that could offset tPA side effects and improve efficacy in clinical practice or develop a new therapeutic as an alternative to tPA treatment for ischemic stroke.

Although tPA works well in dissolving smaller clots in narrower vessels, a safe dose of tPA administered by intravenous infusion often does not last long enough in the bloodstream to break down large clots. In fact, tPA has been shown to be ineffective against larger blood clots (29, 30). And since increasing the dose of tPA raises the risk of bleeding complications, raising tPA dosage is not a viable option. In addition to improving recanalization and reducing hemorrhage risk by limiting use of thrombolytics, there has been an explosion of interest into endovascular mechanical thrombectomy as a potential treatment for stroke (31-33). Mechanical thrombectomy is a minimally invasive procedure. During a mechanical thrombectomy procedure, neurovascular surgeons make a small incision either at the wrist or the abdomen to gain the access to an artery. Using fluoroscopy to observe real-time images of the blood vessels, the surgeon threads a catheter through the artery to the clot. Then, the clot can be removed from the body by suction or stent retriever. Studies have shown that patients that were treated with mechanical thrombectomy recover faster and with an improved quality of life compared to those patients using clot-busting tPA (31, 33-38). In 2004, the mechanical embolus removal in cerebral ischemia (MERCI) retriever became the first FDA approved device to be cleared for thrombectomy in acute ischemic stroke (31, 33). Since then, there have been multiple devices tested for this purpose including the Penumbra system, the Neuronet, the Catch device, the Phenox Clot Retriever system, and the Alligator Retriever device. Two newer devices that are robust and most successful at revascularization are the Trevo device and the Solotaire (39-45).

Despite advancements that have expanded the time window for ischemic stroke treatment to between 6 and 24 hours after onset and an ability to remove larger clots found in large artery occlusions, some issues that may limit the widespread clinical use of mechanical thrombectomy remain. First, time restrictions are still a problem with a majority of patients. It is estimated that only 10% of patients with acute ischemic stroke have a proximal large artery occlusion and present early enough to qualify for mechanical thrombectomy within 6 hours (46-49), and only 9% of patients presenting in the 6 to 24 hour time window qualify for mechanical clot removal (50). Second, it is worth mentioning that only health centers with advanced imaging facilities and well-experienced doctors can perform mechanical thrombectomies (51, 52). Third, like all surgical interventions, mechanical clot removal carries the risk of complications such as vascular injury, emboli, vasospasms and symptomatic hemorrhaging (28, 53).

So far, there are still very few FDA approved therapies for ischemic stroke. While tPA can be used to treat the majority of ischemic strokes occurring in smaller vessels, mechanical thrombectomy might be performed on thrombi occurring in relatively large vessels. However, both treatments still have strict limitations on which patients are eligible to receive them. In this regard, an alternative therapy for ischemic stroke may yet provide additional benefits to stroke patients that existing treatments do not.

Platelets as a potential target for ischemic stroke treatment:

There are very limited choices for treating ischemic stroke. However, evidence points to tPA as being the most effective and, at present, gold standard treatment for ischemic stroke (54). Despite approval more than 20 years ago, tPA administration does not help every patient who receives it.

Ischemic stroke caused by an arterial blood clot interrupts the delivery of oxygen and nutrients to tissue downstream of the blockage. This clot is mainly composed of fibrin and activated platelets. Since targeting fibrin using tPA seems not to be a universal treatment for all ischemic stroke patients, targeting platelets in an occlusive clot could be a viable option.

In mammals, platelets are small non-nucleated cells in circulation with a diameter of 1-2μm and are derived from megakaryocytes in the bone marrow. Platelets were first identified in 1874 by Osler (55) and their role in both physiological hemostasis and pathological thrombosis was established by Bizzozero in 1881 (56). In non-mammalian vertebrates, hemostasis is mediated by nucleated cells called thrombocytes (57). In fact, platelets are more effective than thrombocytes in forming occlusive clots under arterial shear stress (58). Platelets usually live between 7-10 days in humans and approximately 5 days in mice. The regulation of platelet production is exercised at the level of megakaryocytes.

Hemostasis is a critical physiological process to stop bleeding upon vascular injury. At the site of injury, endothelial cells are disrupted and expose subendothelial matrix proteins such as collagen, the most thrombogenic component of sub-endothelium (59-61). In physiological conditions, collagen initiates platelet adhesion, aggregation, degranulation, and subsequent recruitment of platelets to the injury site, producing an initial platelet plug that is the first wave of hemostasis. Soluble mediators released from activated platelets play a major role in platelet recruitment. Simultaneous activation of the coagulation system results in the generation of thrombin, the most potent agonist for platelet activation *in vivo* (62,63), and the protease that converts fibrinogen to fibrin. The second wave of hemostasis occurs as the fibrin polymers begin to form. They wrap around the platelet plug, stabilize it, and trap more platelets, red blood cells (RBCs) and white blood cells to form a whole blood clot (Figure 2). Thus, platelets play an

important role in hemostasis. However, the same normal processes that occur during hemostasis may also cause thrombosis and vessel occlusion if the platelet plug formation and blood coagulation processes are inappropriate. These circumstances lead to pathological conditions including strokes and heart attacks. Over the years, antiplatelet drugs have evolved to inhibit platelet adherence, aggregation, and activation. These are used to prevent further thrombotic events in patients who have already had an ischemic stroke or heart attack (Figure 3).

Upon platelet adherence and aggregation, platelets secrete thromboxane A2 (TXA-2) causing platelet recruitment and activation. TXA-2 is a product of arachidonic acid metabolism and synthesis within activated platelets. TXA-2 formation is catalyzed by the enzyme cyclooxygenase-1 (COX-1). Aspirin, also known as acetylsalicylic acid, is an irreversible COX-1 inhibitor that affects platelets for their entire lifespan, thereby completely abolishing platelet TXA-2 formation and causing reduced platelet function. Aspirin is commonly used to reduce the risk of death from heart attacks or the risk of strokes in people who are at high risk or who have cardiovascular disease (64-67).

After initial platelet activation, platelet dense granules release pro-aggregatory substances. One of these substances is adenosine diphosphate (ADP). ADP interacts with the family of purinergic G protein-coupled receptors on the platelet surface such as P2Y1, P2Y12 and P2X1 receptors, eventually leading to platelet aggregation. The activation of P2Y1 and P2X1 receptors initiate an influx of calcium into the platelet, causing shape change and weak reversible platelet aggregation. On the other hand, once ADP binds onto P2Y12 receptors, it activates a cascade of events leading to integrin $\alpha_{IIb}\beta_3$ receptor activation. This receptor is important for strong and irreversible platelet aggregation. Thienopyridines, including ticlopidine (Ticlid), clopidogrel (Plavix), and prasugrel (Effient), were generated to irreversibly block the

P2Y12 receptor. Thienopyridines in combination with aspirin is the standard of care in management of acute ischemic stroke (64, 68-70).

One of the most common pathways of platelet activation is the activation of the platelet glycoprotein IIb/IIIa receptor, also known as the platelet integrin $\alpha_{IIb}\beta_3$ receptor. The platelet integrin $\alpha_{IIb}\beta_3$ receptor serves as a platelet surface receptor for fibrinogen. Aggregating platelets stick together by the crosslinking of receptors by the bivalent fibrinogen molecule. Despite the dual antiplatelet treatment of aspirin and thienopyridine, platelets can still be activated through stimuli that are insensitive to these drugs such as thrombin, resulting in activation of integrin $\alpha_{IIb}\beta_3$ receptors. Thus, a class of drugs that block the integrin $\alpha_{IIb}\beta_3$ receptor was developed. Abciximab is a chimeric antibody that binds with high affinity to the integrin $\alpha_{IIb}\beta_3$ receptors and inactivates them. Tirofiban and eptifibatide are small molecules that competitively bind to the integrin $\alpha_{IIb}\beta_3$ receptors. These three agents for intravenous use have been shown to be effective in preventing heart attack and ischemic stroke (64, 71-73). The efficiency of aspirin, thienopyridines, and integrin $\alpha_{IIb}\beta_3$ receptor blockers in preventing strokes and heart attacks suggest that antiplatelet therapy could be a potential tool in precluding arterial blood clotting.

Normal platelet physiology:

In circulation, resting platelets have a discoid shape that is maintained by a ring-shaped bundle of microtubules at the platelet periphery, known as a circumferential microtubule band. The circumferential microtubule band is also important in encasing the cytoplasm of a platelet. In addition, platelets contain two types of granules named α-granules and dense granules. Upon platelet activation, α-granules and dense granules secrete contents that are required for creating a firm plug to seal the blood vessel damage. The α-granule is the most abundant organelle in

platelets and plays a crucial role in hemostasis, wound healing, and inflammation. They contain a plethora of proteins that comprise the bulk of the platelet secretome. For example, hemostatic factors (von Willerbrand factor (vWF), the adhesion molecule P-selectin, coagulation factor V, thrombospondin, fibrinogen), angiogenic factors (angiogenin, vascular endothelial growth factor), antiangiogenic factors (angiostatin, platelet factor-4), growth factors (platelet-derived growth factor, and tumor growth factor beta), proteases (matrix metalloproteinase-2, matrix metalloproteinase-9), necrotic factors (tumor necrosis factor alpha, tumor necrosis factor beta) and other cytokines are all found in α-granules (74-76). Dense granules are smaller than α-granules, fewer in number, and predominantly contain small molecules including magnesium, calcium, adenosine diphosphate (ADP), adenosine triphosphate (ATP), serotonin, and histamine. The true function of a dense granule is not clearly defined. However, the secretion of dense granules always occurs along with platelet activation. Studies have shown that dense granule deficiency causes prolonged bleeding time (77-79). The platelet interior also contains the open canalicular system, which is an internal membrane found inside platelets. The open canalicular system serves as a pathway for the transport of substances into the platelet and as a conduit for discharge of secretory products during platelet release reactions. Also, the open canalicular system helps increase the platelet surface area that is available for interaction with its outside environment and serves as a membrane reservoir of platelet plasma membrane that can be evaginated onto the platelet surface during interaction with surfaces (80-83). Additionally, mitochondria found in platelets have demonstrated an influence in a variety of purposes such as metabolism, activation, energy production, regulation of cell processes, and viability (84, 85). Platelet structures and their functions are shown in Figure 4.

Upon contact with the extracellular matrix through endothelial damage or exposure to soluble agonists, platelet activation stimulates the rapid reorganization of the cytoskeleton resulting in the transformation of platelets from discoid to fully spread cells. Generally, there are two steps in platelet shape change. In the first step, the discoid cells undergo extensive cytoskeletal rearrangement including the disassembly of the circumferential microtubule band, resulting in an intermediate spherical shape or a rounded ball. In the second step, actin polymerization causes the membranes of the cells to protrude, causing the creation of pseudopodia extensions (86-88). The extent of platelet shape change and the extension of the pseudopodia depend on the platelet activation pathway. When platelets are exposed to an activating surface, they will flatten and spread over that surface to greatly increase their contact area. In the body, this would allow for increased coverage of the site of vessel damage as well as providing more space for adhesion to occur (89, 90). Once platelets are activated, they release their granules to the extracellular environment, leading to several events. The granule contents play an important role in recruiting additional platelets to the site of injury where they bind to the adherent platelets and form aggregates, activating other platelets, promoting the blood coagulant cascade, and stimulating the wound healing process (91-93).

The common platelet activation pathways:

Mechanisms that control platelet activation require intracellular signal transduction initiated by platelet receptors for adhesion proteins and soluble agonists. These common adhesion proteins are collagen and vWF, and both are found in the vascular wall upon blood vessel injury. Other soluble agonists include thrombin, ADP and TXA-2. These are released from the sites of blood vessel injury, inflammation, or from other platelets during platelet

activation. These agonists and adhesive molecules activate platelets by binding to their respective receptors on platelet membranes, most of which are G-protein-coupled receptors (GPCR), leading to the activation of platelet adhesion receptors, mainly integrin $\alpha_{IIb}\beta_3$ receptor. The integrin $\alpha_{IIb}\beta_3$ receptor then mediates platelet aggregation.

Platelet activation via GPCRs involves three major G-protein mediated signaling pathways that are triggered by the activation of the G proteins $G_{\alpha i}$, $G_{\alpha q}$, and $G_{\alpha 12/13}$ (94, 95). $G_{\alpha i}$ functions by inhibiting adenylyl cyclase, preventing the accumulation of cAMP; thereby inducing platelet activation and aggregation (94, 96). $G_{\alpha q}$ activation stimulates the activity of phospholipase C-β, which catalyzes the release of diacylglycerol and inositol (1,4,5)-triphosphate from membrane phosphatidylinositol 4,5 bisphosphate. Diacylglycerol and inositol (1,4,5)-triphosphate in turn activate protein kinase C and stimulate the release of calcium from the dense granules into the cytoplasm. Elevation in cytosolic calcium concentration is essential for platelet activation (94, 97, 98). Activation of the $G_{\alpha 12/13}$ subunit in platelets initiates activation of the small GTPase RhoA. RhoA and Rho kinase activation trigger phosphorylation of myosin light chain kinases, which regulate the reorganization of the actin cytoskeleton associated with platelet shape change (94, 99).

Collagen is the most thrombotic component of the subendothelium. Upon vascular damage, collagen is exposed to circulating platelets where it can serve as a substrate for platelet adhesion and also can induce platelet activation. Two receptors involved in the platelet response to collagen are integrin $\alpha_2\beta_1$ and glycoprotein VI. Integrin $\alpha_2\beta_1$ functions to adhere platelets to collagen and allows platelets to interact with the lower affinity receptor glycoprotein VI, which is mainly responsible for platelet activation. Platelet activation in response to collagen is mediated by the binding of collagen to the platelet receptor glycoprotein VI. As a result of

ligation and clustering of glycoprotein VI, tyrosine phosphorylation occurs at the associated transmembrane protein and Fc receptor γ-chain within its immunoreceptor tyrosine-based activation motif. This promotes an association between the Fc receptor γ-chain and the tyrosine kinase Syk. Subsequent activation of Syk leads to the phosphorylation of phospholipase Cγ2, which leads to an increase in cytoplasmic calcium levels. An increase in intracellular calcium is associated with morphologic change, the presentation of procoagulant surfaces, and the secretion of platelet granule contents, resulting in platelet activation and aggregation (100-105). The interaction of collagen and platelets is crucial and may be considered to be the initial event in hemostasis and thrombosis (106).

Simultaneous activation of the coagulation system results in the generation of thrombin. Thrombin is a serine protease, the terminal enzyme of the hemostatic system, and the most potent agonist for platelet activation *in vivo*. During thrombus formation, thrombin converts fibrinogen to fibrin (Figure 2), activates factor XIII (cross links fibrin in the clot), and activates factors XI, VIII, and V (generates more thrombin). Also, thrombin serves as a major activator of platelets by binding and cleaving protease activator receptors (PARs). The PAR family is a subfamily of related G protein coupled receptors that are activated by proteolytic mechanisms. Specific cleavage of the amino terminal sequence that unmasks a new N-terminal sequence that functions as a tethered ligand, binding to a conserved region on the extracellular loop 2 domain of the PAR, and resulting in a series of cellular signaling events (107-111). In humans, PAR1 is the primary thrombin receptor on platelets. Since PAR1 contains a hirudin-like domain, which has a high affinity thrombin binding site, it recruits thrombin via its exosite I. This interaction enables thrombin to bind specifically and efficiently to activate PAR1 (107, 108). Thrombin also cleaves and activates PAR4, which is considered a secondary thrombin receptor. In contrast with

PAR1, PAR4 lacks a hirudin-like domain, and a higher concentration of thrombin is required to activate PAR4 and initiate intracellular signaling events (107, 108). Mice lack a PAR1 homologue; therefore, mouse PAR4 is utilized as their primary thrombin receptor. Thrombin-cleaved PAR1 or thrombin-cleaved PAR4 leads to the activation of $G_{\alpha 12/13}$ and $G_{\alpha q}$ and in turn induces Rho and Ca^{2+} signaling (108). Some studies have also shown PAR1 can bind to $G_{\alpha i}$ and cause the inhibition of adenylyl cyclase (112-113). When studying platelets, it is often desirable to activate PAR receptors to promote full platelet activation while avoiding surface proteolysis and fibrin formation caused by the proteolytic activities of thrombin. Thus, one can alternatively utilize synthetic peptides of the sequences corresponding to the tethered ligand portion of the receptor to activate PAR receptors. The human PAR1 peptide SFLLRN-NH_2 and the murine PAR4 peptide AYPGKF-NH_2 can be used as agonists to activate platelets (114-115). In our *in vitro* system, thrombin will be mainly used to stimulate clot formation.

Although ADP itself does not typically cause the initial platelet activation event as collagen or thrombin does, ADP is essential in promoting the secondary platelet response (91). Following platelet activation, platelet degranulation releases ADP into the platelets' surrounding environment. ADP activates platelets by interacting with the G protein-coupled receptors $P2Y_1$ and $P2Y_{12}$. The $P2Y_1$ receptor couples to $G_{\alpha q}$. It is now established that activation of the $P2Y_1$ receptor coupling with $G_{\alpha q}$ leads to the activation of phospholipase C-β, a subsequent increase in cytosolic calcium, and the activation of protein kinase C. However, the $P2Y_1$ receptor only causes a transient increase in the concentration of intracellular ionized calcium that is released from dense granules, which again initiates platelet aggregation and is responsible for platelet shape change. $P2Y_{12}$ receptors couple to $G_{\alpha i}$. The activation of the $P2Y_{12}$ receptor and subsequent coupling with $G_{\alpha i}$ leads to the inhibition of adenylyl cyclase and the activation of

phosphoinositide 3-kinase and causes the amplification of calcium levels. Thus, $P2Y_{12}$ activation results in amplification and stabilization of the aggregation response (116-120).

TXA-2 is not only produced and released by stimulated platelets; many studies have shown that TXA-2 is also released by a variety of other cells such as macrophages, neutrophils, and endothelial cells (121). TXA-2 is a chemically unstable lipid mediator involved in several pathophysiologic processes including primary hemostasis, atherothrombosis, inflammation, and cancer. In human platelets, the production of TXA-2 occurs via a sequential process that begins with arachidonic acid (AA). AA is incorporated in the phospholipid membrane of the body's cells. During coagulation, phospholipase A2 enzyme cleaves and frees AA from the phospholipid membrane. Then, the cyclooxygenase isoenzymes COX-1 and COX-2 catalyze AA into the formation of proinflammatory TXA-2, antithrombotic prostacyclin, and other prostaglandins. TXA-2 has prothrombotic properties, as it stimulates the activation of new platelets as well as platelet aggregation. This is achieved when it binds and activates its G protein-coupled receptor. As a result, $G_{\alpha q}$ and $G_{\alpha i}$ pathways are activated causing an increase in the free cytosolic calcium and drop in cAMP production. These events consequently induce platelet-shape change, degranulation and conformational change of integrin $\alpha_{IIb}\beta_3$ receptors on the platelet surface (122-125).

Each platelet activation pathway utilizes its own unique receptors and signal transduction mechanisms, which explains why various types of antiplatelet drugs were created to prevent platelet activation. For example, acetylsalicylic acid and non-steroidal anti-inflammatory drugs inhibit the COX-enzyme in the thromboxane pathway; vorapaxar is a competitive PAR-1 antagonist, and thienopyridines are selective ADP receptor inhibitors.

Calcium is an essential component of coagulation and platelet activation. Platelet activation can be inhibited *in vitro* by the use of calcium chelating agents such as ethylenediaminetetraacetic acid (EDTA) and sodium citrate. Both are commonly used as anticoagulants for the collection of blood samples. EDTA strongly and irreversibly chelates calcium and other divalent metal ions present in the blood, thus halting blood clotting. Sodium citrate acts similarly but not as strongly as EDTA. Sodium citrate anticoagulation can be readily reversed by the addition of calcium, which is required before platelets can become competent for activation again.

Fibrinogen and integrin $\alpha_{IIb}\beta_3$ receptor interaction - a potentially powerful strategy to specifically target activated platelets:

All of these platelet-signaling events converge on the final common pathway of platelet activation, which is the functional upregulation of integrin adhesion receptors. The activation of the integrin $\alpha_{IIb}\beta_3$ receptor or glycoprotein IIb/IIIa is most important. On the surface of platelets, the most abundant receptor is integrin $\alpha_{IIb}\beta_3$. There are about 80,000 copies per unstimulated platelet (126, 127). Integrin $\alpha_{IIb}\beta_3$ plays a particularly crucial role in thrombus formation by promoting platelet aggregation. Integrin $\alpha_{IIb}\beta_3$ function depends on two different signal transduction pathways: inside-out and outside-in signaling. The inside-out signaling pathway is initiated by the binding of one or more agonists to their platelet membrane receptors such as thrombin, collagen, ADP, or TXA-2. Receptor-mediated signaling events lead to the conversion of the integrin $\alpha_{IIb}\beta_3$ receptors from low affinity to high affinity conformation, thus making the $\alpha_{IIb}\beta_3$ receptors ready to bind to their ligand, which is fibrinogen. Once activated, the $\alpha_{IIb}\beta_3$ receptor is capable of binding fibrinogen at a single receptor binding site, leaving the second

binding site on the bivalent fibrinogen molecule free to bind onto an additional $\alpha_{IIb}\beta_3$ receptor either on the same platelet or on an adjacent activated platelet (128-130). This crosslinking of two receptors by bound fibrinogen allows platelet-platelet interaction and leads to platelet aggregation (Figure 5) (131). After $\alpha_{IIb}\beta_3$ binds fibrinogen and crosslinks adjacent receptors, integrin $\alpha_{IIb}\beta_3$ is then capable of reverse signal transmission inside the cell, called outside-in signaling (130, 132). Under integrin outside-in signaling, the ligand-occupied receptors interact with the actin cytoskeleton, causing the integrin with bound ligand to centralize on the plane of the platelet membrane moving along the underlying actin cytoskeleton. The final location of the migrated cross-linked receptors is dependent on the platelets' activation morphology (Figure 6). In surface-activated platelets, the integrin with bound ligand will centralize on the platelet surface from its periphery to the vicinity of the platelet granulomere; whereas, in suspension-activated platelets, ligand-occupied receptors will localize at the platelet-platelet junctions where platelets have become cross-linked together or will migrate into the open canalicular system of the platelet (133-136). Moreover, outside-in signaling through platelet integrin $\alpha_{IIb}\beta_3$ activation facilitates the clot retraction process that results in the fibrin clot gradually being pulled in on itself, shrinking to a smaller volume clot and extruding excess fluid. This draws the edges of damaged tissue together and forms a mechanically stable clot (137-139).

Fibrinogen is the primary ligand of the integrin $\alpha_{IIb}\beta_3$ receptor. Fibrinogen is a soluble glycoprotein complex that is synthesized by the liver and circulates in human blood at 3mg/mL. Fibrinogen is a dimer where each monomer consists of two chains of each α, β and γ held together by disulfide bonds. The N-terminal of all six chains come together to form the center of the molecule known as the E-domain, from which the monomers extend in opposite directions as coiled-coils followed by C-terminal globular D-domains (140-142). Respectively, the structure

of fibrinogen is presented as three linearly arranged domains, D-coil-E-coil-D. Fibrinogen plays important roles in both the blood coagulation cascade and platelet aggregate formation. During blood clot formation, the generation of thrombin triggers the conversion of soluble fibrinogen to insoluble fibrin. Thrombin cleaves the N-terminal fragments of the α and β chains within the E-domain of fibrinogen; this releases fibrinopeptides A and B, respectively, and produces fibrin. The release of fibrinopeptides A and B results in the exposure of four binding sites on the E-domain, each of which can interact with a D-domain from different fibrin molecules to form fibrin polymers that consist of lattice networks of fibrin that in turn form long, branching, and flexible fibers (142-144). Fibrin strands gather together to make a mesh that traps platelets, RBCs, and several different proteins and cells to form a clot. In addition, thrombin proteolytically converts the plasma protransglutaminase factor XIII (FXIII) to activated FXIII (FXIIIa) which cross-links fibrin molecules via the γ chain between D-domains to ensure stabilization and resistance to degradation of the fibrin clot (145, 146). Fibrinogen has a significant role in platelet response to injury. Fibrinogen binding to its platelet receptor requires platelet activation, which allows for platelet-platelet interaction and platelet aggregation. Platelet aggregation involves the binding of the platelet integrin $\alpha_{IIb}\beta_3$ receptor to the C-terminal D-domain of fibrinogen, a vital step in normal arterial bleeding response (147).

Since the binding of fibrinogen to its receptor is essential for platelet function, fibrinogen binding to its receptor on activated platelets has been extensively studied and characterized. The discovery that Glanzmann's thrombasthenia, an autosomal recessive bleeding disorder, is caused by deficient or dysfunctional integrin $\alpha_{IIb}\beta_3$, has led to a significant effort to develop antithrombotic agents that target and block the platelet fibrinogen receptors (148). Abciximab, (ReoPro®), is the Fab fragment of a human-murine chimeric monoclonal antibody that binds and

blocks the integrin $\alpha_{IIb}\beta_3$ on human platelets, and thus inhibits platelet aggregation. Abciximab has been shown to be effective in preventing restenosis during percutaneous coronary interventions and in myocardial infarctions (149). However, abciximab showed no significant benefit in the treatment of ischemic stroke (150). This is largely because abciximab has been associated with a significant increase in symptomatic intracranial hemorrhaging. Furthermore, patients treated with abciximab for myocardial infarction were at a higher risk of thrombocytopenia. The risk of thrombocytopenia was especially elevated in patients receiving abciximab re-administration (151, 152). The lack of specificity of abciximab for activated platelets limits its utility as a therapeutic for ischemic stroke. However, exploiting the interaction between fibrinogen and integrin $\alpha_{IIb}\beta_3$ remains a potential strategy if it were possible to specifically target activated platelets in occlusive thrombi.

Integrin $\alpha_{IIb}\beta_3$ receptors can bind fibrinogen via the recognition peptide sequence Arg-Gly-Asp (RGD) found on the α chain (153-156), although the primary interaction occurs through the C-terminal peptide of the γ chain. Thus, integrin $\alpha_{IIb}\beta_3$ on platelets has been targeted by using the binding of short synthetic RGD peptide sequences to inhibit aggregation of human platelets. However, using fibrinogen to target $\alpha_{IIb}\beta_3$ receptors on platelets may be superior to RGD peptides. Fibrinogen binding to its platelet integrin $\alpha_{IIb}\beta_3$ receptor requires agonist activation on platelets, which creates a method to distinguish between quiescent circulating platelets and activated platelets, whereas the binding of short synthetic RGD peptides does not (157). Additionally, fibrinogen targeting activated platelets would be superior to $\alpha_{IIb}\beta_3$-directed antibodies such as abciximab, which is only moderately selective for activated $\alpha_{IIb}\beta_3$ and has a systemic effect on all platelets. Many studies have successfully used fibrinogen conjugated-gold nanoparticles to demonstrate the interaction between fibrinogen and integrin $\alpha_{IIb}\beta_3$ receptors

using electron microscopy (80, 90, 158-164). These studies suggest that using fibrinogen-conjugated nanoparticles could be used to select activated platelets. Thus, we propose that we could use the full fibrinogen molecule to specifically target activated platelets in an occlusive clot and utilize this as a potential treatment for ischemic stroke.

Nanoparticle-based induced cell death:

While tPA based treatments of ischemic stroke target lysis of the fibrin within blood clots, we propose that specifically targeting activated platelets in an occlusive clot may provide a better treatment for ischemic stroke patients. Nanoparticles represent an active area of research and show great promise in biological applications (165). For example, in passive targeting, nanoparticles have been successfully developed for cancer therapy by taking advantage of unique tumor tissue biology. Tumors have high vascular density, increased vascular permeability, and impaired lymphatic drainage. These physiologic characteristics contribute to the formation of solid tumors and inflamed tissue. Together, these features of a tumor enhance nanoparticle accumulation in tumor tissue (166, 167). In fact, nanoparticles can be engineered to better target a particular tissue type cell by optimizing their physiochemical characteristics such as nanoparticle composition, size, shape, and surface properties (168). Active targeting involves the use of a targeting ligand for the enhanced delivery of nanoparticles to specific sites. Typical ligands include small molecules, peptides, antibodies and nucleic acids that have been conjugated to the nanoparticle surface via non-covalent or covalent methods (169). Ligand-conjugated nanoparticles facilitate active targeting of nanoparticles to receptors that are present on target cells, causing cell internalization, or specific uptake through receptor-mediated endocytosis (170, 171). Active targeting can allow for very specific targeting of a cell type, or

even selecting between activated and inactivated cells of the same type. Thus, active targeting using nanoparticles may have benefits in reducing systematic toxicities and other adverse effects.

These targeting methods have been focused mainly on the development of anticancer treatments; however, the concept can be applied to various cell types of interest if they express unique targetable features. Furthermore, the use of these therapies would require specific targeting of cells, but could also require nanoparticle properties that cause effects, such as damage to the cells of interest. Nanoparticle-based treatments could induce cell death either by cytotoxic agents or be capable of inducing cell death directly. If we can combine specific cell targeting with a method of causing cell death, then nanoparticle-induced side effects such as toxicity or disruption will be largely restricted to the targeted cells or a specific tissue site. For instance, doxorubicin is one of the best known and most widely used anticancer chemotherapy drug. The therapy-limiting factor for this drug is toxicity caused cardiomyopathy, which may produce congestive heart failure and death (172, 173). To avoid this complication, doxorubicin is encapsulated in a closed liposome as a carrier to reduce the systematic toxicity of the drug. Encompassing the drug in a liposome also allows a method for targeting cancer cells via ligand binding to functional folate receptors (174, 175). Other nanoparticle-based systems can lead to cellular destruction, such as death-induced gene therapy (apoptosis-induced gene therapy and toxin-induced gene therapy) (176, 177), or physical damage caused by hyperthermia (178).

Magnetically induced hyperthermia as alternative therapy for ischemic stroke:

Since nanoparticles can be engineered and modified with distinct compositions, size, shapes, functionalities, and surface chemistries, they can display unique physical and chemical properties and represent an increasing area of interest in the development of nanodevices. These

have the potential to be used in a wide range of applications that range from energy production to industrial production processes to biological applications. Considering the other properties including electric, optical, magnetic, and thermal attributes, nanoparticles could be used in variety of biological applications. Some of them are liposomes, albumin-bound, gold, and magnetic iron oxide.

Liposomes are the first nanoparticle platform. Liposomes are spherical vesicles that contain a phospholipid bilayer structure or membrane that spontaneously encloses an internal aqueous solution. The structure of the membrane can vary significantly, making it possible to create a vast number of different liposomes. In fact, liposomes can mimic biological cells; thereby, liposomes are highly biocompatible for drug delivery systems (165, 179-182). However, liposome drug development to larger-scale production and to the clinic are still restricted due to their instability, polydispersity, toxicity at repeated administration, and capability of inducing immune responses.

Albumin is a component of the human blood, so as an endogenous protein it shows no immunogenicity, ensuring that albumin-based nanoparticles have good biocompatibility. Albumin-bound nanoparticles use the endogenous albumin pathways to carry hydrophobic molecules in the bloodstream. As a result, albumin-based nanoparticles have been successfully adapted as drug delivery vehicles. Albumin-bound paclitaxel (Abraxane) is a highly successful treatment for metastatic breast cancer (165, 179, 183, 184).

Magnetic iron oxide nanoparticles have been studied extensively and are among the most widely used nanoparticles in many biomedical applications such as drug delivery, therapeutic treatment, contrast agents for MRI imaging, and *in vitro* diagnostics (185). Nanometer-sized particles are known to be superparamagnetic as a result of their small size. Superparamagnetic

nanoparticles only become magnetized when placed within a magnetic field and return to a non-magnetized state after an external magnetic field is removed. Therefore, the superparamagnetic property may be safe for use in biological system applications by giving the nanoparticles an on/off switch. Despite their great potential, using magnetic nanoparticles in biological systems poses challenges with respect to their electrical conductivity, optical properties, chemical stability, biocompatibility, and bioaffinity (186, 187). Gold nanoparticles have chemical inertness, surface properties, electronic structures, and optical properties that have made them appropriate for a number of clinical applications (188). Therefore, coating magnetic nanoparticles with gold could overcome some of the limitations of magnetic nanoparticles. Nanoparticles consisting of a gold coating with magnetic iron oxide (magnetite, Fe_3O_4) cores have been developed (186, 187, 189). The gold coating protects the magnetic iron oxide core from oxidation, ionization, and external pH. Additionally, the gold coating provides a surface that is capable of enhancing the conjugation with proteins (187, 189). Gold-coated magnetite nanoparticles have been used to target cultured human prostate and murine breast cancer cells through antibody-surface antigen interactions and then cause cell death after magnetic field exposure (189-192).

The synthesis of gold-coated magnetite nanoparticles involves two key processes: the iron core synthesis and the subsequent gold coating. Iron oxide magnetic nanoparticles can be synthesized by methods of thermal decomposition, aqueous alkaline, or microemulsion. Among these methodologies, magnetite synthesized by the aqueous alkaline method has been most frequently used due to its producing nanoparticles with strong magnetic behavior and because it allows for control nanoparticle size. In aqueous alkaline precipitation, dissolved iron salts are oxidized by a strong base which results in the precipitation of iron oxide from the solution to

form simple nanoparticles. The resultant nanoparticles are hydrophilic, and they tend to aggregate to reduce the surface energy caused by their large surface-area-to-volume ratio. Thus, using anionic surfactants, such as tetramethylammonium hydroxide (TMAOH), as dispersing agents impacts the negative charge on the nanoparticle surface and keeps them in a colloidal state (193-196). Since nanoparticles are synthesized in water, their surface is most compatible with an aqueous environment; therefore, their reaction by-products are relatively non-toxic. However, the presence of surfactant-stabilized iron oxide nanoparticles is toxic and unstable at physiologic salt and pH conditions (193,197-199). Stabilization can be further achieved by coating the surface with metal (197, 198, 200, 201) or proteins (197, 202-204) to protect the iron oxide nanoparticles from agglomerating under physiologic conditions and to provide a means to keep the nanoparticles stable within a biological system. The attachment of gold atoms onto magnetite cores can be achieved by using reducing agents such as hydrazine, sodium citrate, and sodium borohydride. In these procedures, the gold shell is prepared by mixing nanoparticles with a gold chloride aqueous solution, followed by the introduction of reducing agents. The addition of these agents reduces gold chloride to produce gold atoms that assemble on the magnetite core (205-207).

Hence, gold-coated magnetite nanoparticles are not simple molecules by themselves; they consist of a surface layer, shell layer, and a core. The surface layer can be functionalized with a variety of small molecules, proteins, metal ions, surfactants, and polymers. Also, the surface modifications do not impair the magnetic properties of the nanoparticles. In our study, the fibrinogen molecule is used as the surface layer to specifically target the integrin $\alpha_{IIb}\beta_3$ receptor on an activated platelet. The shell is chemically different material from the core. The gold shell improves stability of the iron oxide at physiological conditions and provides a surface for

conjugation with proteins, which in this case is fibrinogen. The core is magnetite and essentially the central portion of the nanoparticles and causes the heating effect when exposed to a magnetic field.

Hyperthermia refers to heat treatment that is delivered specifically to a lesion site to destroy unwanted tissues. As early as 1866, fever-like conditions were proposed as a significant therapeutic for cancer treatment. Tumors have increased susceptibility to elevated temperature compared to healthy tissue due to their increased rate of cell cycling, increased hypoxia, poor fluid exchange, and increased acidity (208). Therefore, hyperthermia has been commonly used in treating cancer. The biggest limitation of hyperthermia is the potential to damage normal surrounding tissue. Concentrating hyperthermia treatment more specifically at the target site by delivering small magnetic particles to the tumor would provide a therapeutic advantage. For example, as early as 1957 sub-micron sized magnetite particles were used to target metastases and induce hyperthermia by injection into the lymphatic system, followed by exposure to an oscillating magnetic field (OMF) (209). Treatment was refined by decreasing the diameter of particles to ~10 nm or smaller to minimize the damage to normal surrounding tissue (210-213). Although these treatments were successful in killing tumor cells such as prostate and mammary carcinoma, their application was limited to large solid tumors only. In these treatments, the nanoparticles were physically placed near the tumors rather than specifically targeted to the cancerous cells. When an external magnetic field was applied to heat the particles, the heat generated by the nanoparticles caused hyperthermic cell death. In this approach, creating the desired effect depends on bulk heating. Therefore, many surrounding normal cells were heated and killed along with cancerous cells. Methods to overcome the limitations of non-specific hyperthermia treatment have been pursued. For example, encasing magnetic particles in a

positively charged liposphere improves the particles' adsorption and accumulation properties. In fact, having a positive surface charge increases the affinity for rat glioma cells up to 10-fold as compared to neutral uncharged magnetoliposome (214). In other studies, conjugation of antibodies for cell-specific surface markers to the nanoparticles (215, 216) have been employed and primarily used for magnetic resonance imaging (MRI) studies. As mentioned above, antibody-conjugated gold-coated magnetite nanoparticles have successfully labeled prostate and breast cancer cells. When these labeled cancer cells were exposed to an oscillating magnetic field, they were successfully disrupted. Thus, gold-coated magnetite nanoparticles could be able to target and destroy specifically any type of cell that can be labeled using protein and antibodies as long as nanoparticles reach the cell surface or final target destination in sufficient amounts to convey hyperthermia damage. Therefore, it is possible to use magnetically induced hyperthermia as a treatment for ischemic stroke.

For our applications, fibrinogen-conjugated gold-coated magnetite nanoparticles can be injected into circulation and specifically target integrin $\alpha_{IIb}\beta_3$ receptors on activated platelets in an occlusive clot. When exposed to an external OMF, the resultant hyperthermia causes damages only at the area of interest. This treatment is preferred because it is non-invasive, and potentially highly localized with relatively minimal risk of adverse effects.

Applying the existing technology of hyperthermic anti-cancer techniques to anti-platelet therapy has the potential to benefit both fields. This novel approach to treating ischemic stroke by using fibrinogen-conjugated gold-coated magnetite nanoparticles to specifically target integrin $\alpha_{IIb}\beta_3$ on activated platelets followed by exposure to an OMF could be used as a replacement for, or in combination with, other ischemic stroke therapies including tPA. Additionally, the development of this novel anti-platelet therapy for ischemic stroke and

determining and optimizing the treatment conditions will be useful not only for targeting platelets, but also other pathologic cell types such as cancer.

Central hypothesis:

Our overall hypothesis is that fibrinogen-conjugated, gold-coated magnetite nanoparticles can specifically target activated platelets within occlusive thrombi, leading to disruption with an oscillating magnetic field. In the whole blood system, we propose that fibrinogen-conjugated nanoparticles will bind selectively onto activated platelets within a blood clot, potentially associate with the fibrin network, and not interact with RBCs. Since arterial clots consist mainly of activated platelets and fibrin, our targeting methods may give us multiple targets. We also propose that the complexity of fibrin clot structure, due to stimulation with varying doses of the agonist thrombin, can influence the efficiency of fibrinogen-conjugated, gold-coated nanoparticle penetration and incorporation into clots. Consequently, it leads to the realization that optimizing fibrinogen-conjugated, gold-coated magnetite nanoparticle penetration and concentration within arterial clots is essential in the success of disrupting clots. If we can improve nanoparticle penetration, concentration, and efficacy, then clots can be dislodged, and blood flow can be restored. The scope of these aims is to investigate and characterize fibrinogen-conjugated gold-coated magnetite nanoparticle targeting of activated platelets in a whole blood system *in vitro*. Even though all studies have only been performed *in vitro*, a strong emphasis was utilized to predict how the methodology is expected to perform *in vivo* in anticipation of future studies using a mouse model of arterial thrombosis and eventually, human therapeutic trials.

Figures and Figure Legends:

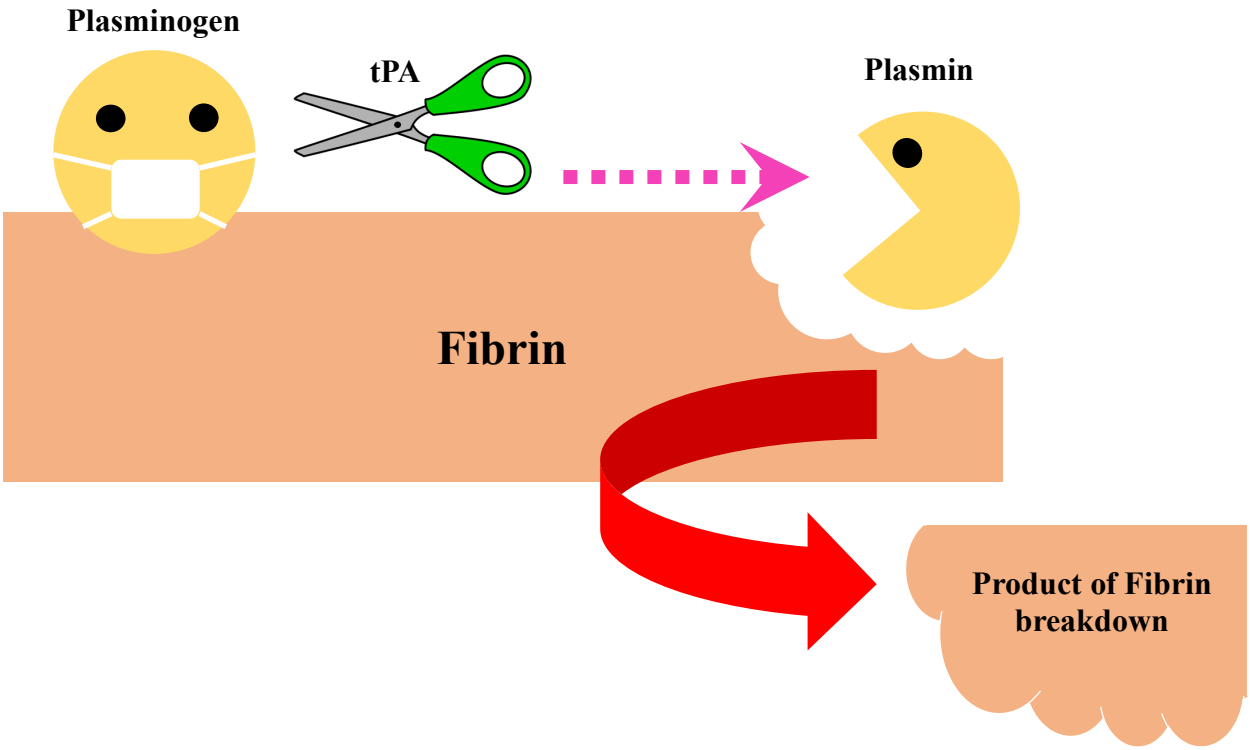

Figure 1. Schematic visualization of the molecular interactions regulating physiological fibrinolysis. On the fibrin surface, tissue plasminogen activator (tPA) converts plasminogen to the proteolytic enzyme plasmin. Plasmin then cleaves fibrin into smaller pieces.

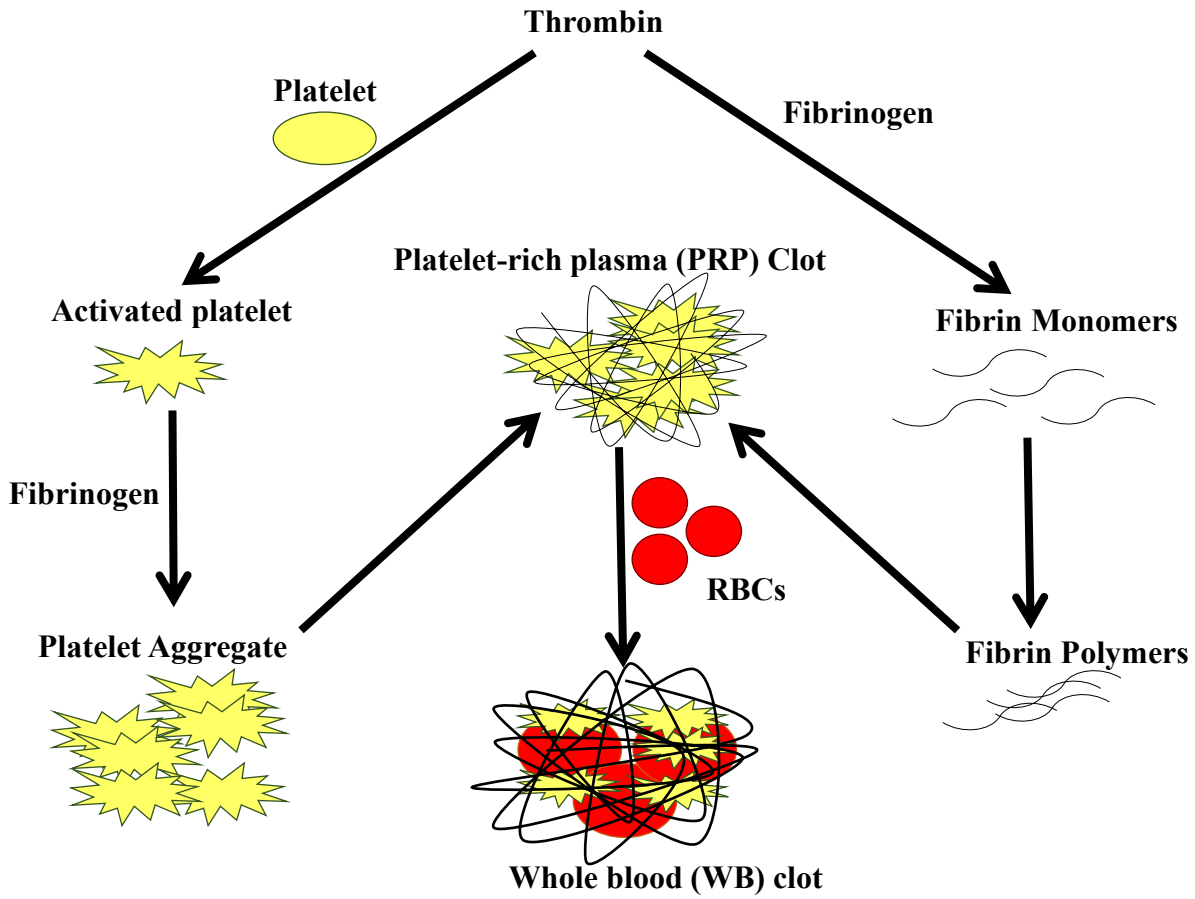

Figure 2. A schematic representation of arterial blood clot formation *in vitro*. Thrombin plays a central role in thrombus development. Thrombin generated at a site of injury activates resting platelets, and then activated platelets aggregate via fibrinogen mediated platelet-platelet interactions. Thrombin also converts fibrinogen into fibrin polymers, which together with platelet aggregates form fibrin clots. In the presence of red blood cells or other blood plasma components, whole blood clots are formed.

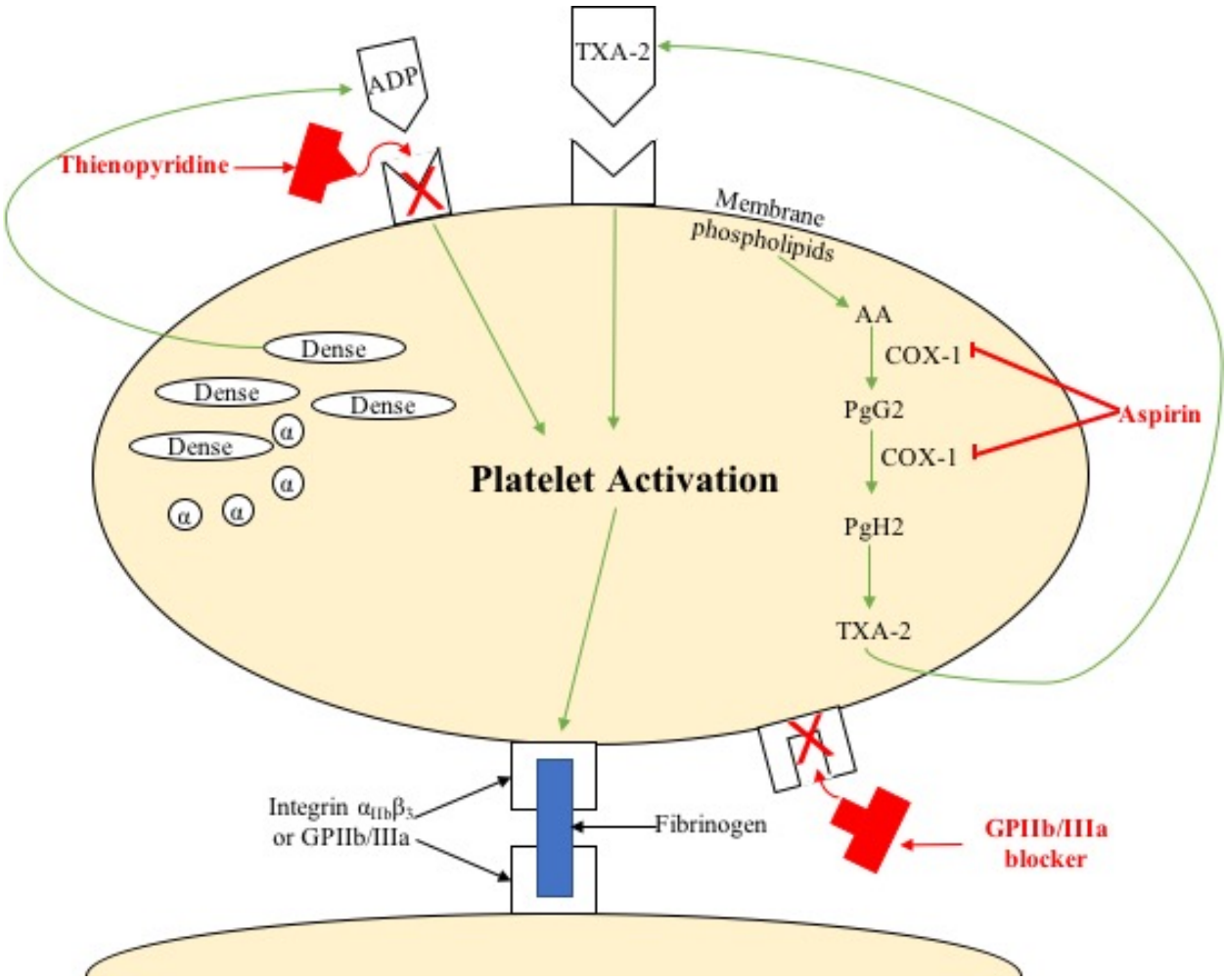

Figure 3. Schematic of mechanisms of platelet activation inhibitors- Aspirin, thienopyradine, and GPIIb/IIIa blockers modified from N. Clapper, 2007 (64). AA, arachidonic acid; ADP, adenosine diphosphate; COX-1, cyclooxygenase 1; Dense, dense granule; GPIIb/IIIa, glycoprotein IIb/IIIa; PgG2, prostagladin G2; PgH2, prostagladin H2; TXA-2, thromboxane A2; α, α granule.

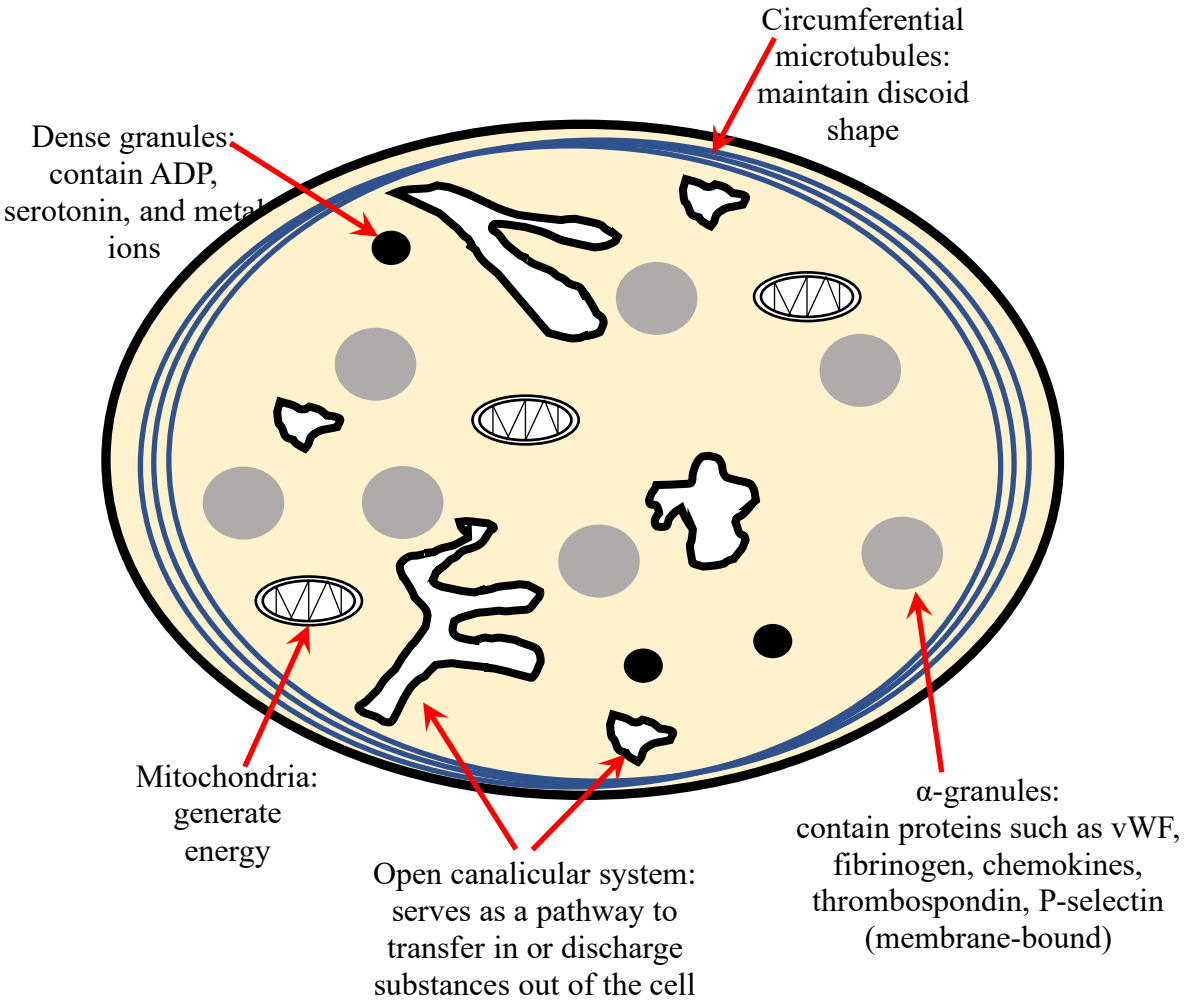

Figure 4. Structural features of a resting platelet and their functions.

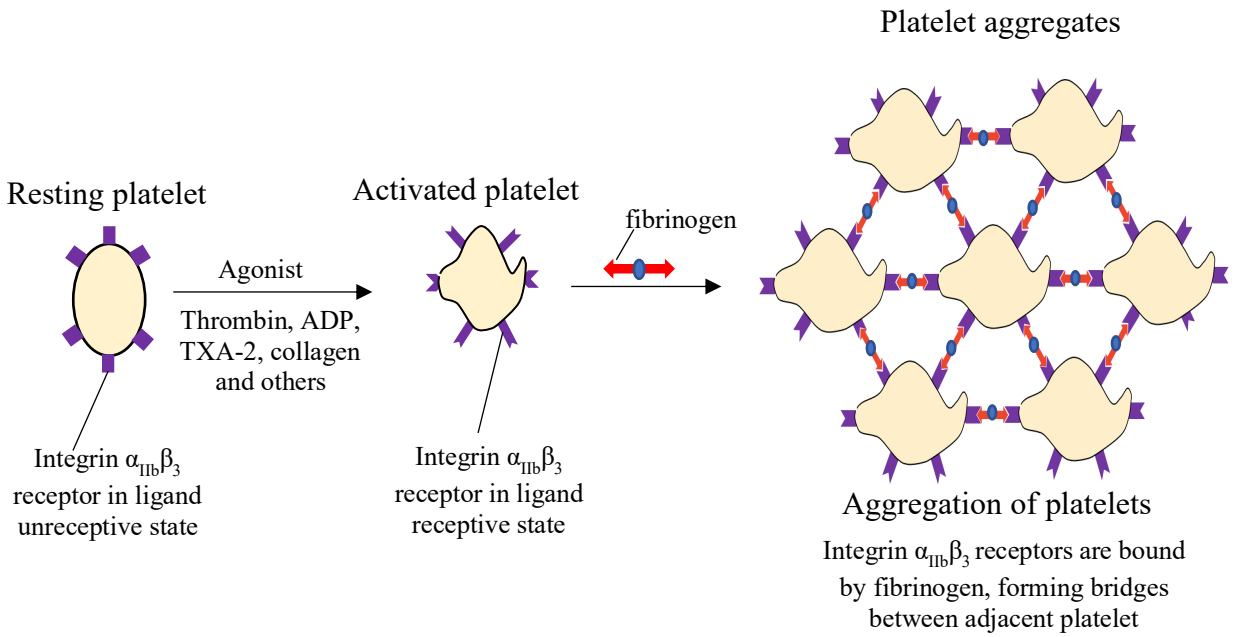

Figure 5. Platelet aggregation modified from Y. Yeghiazarians, 2000 (131). Upon platelet activation by agonists such as thrombin, ADP, TXA-2, and collagen, inside-out signaling triggers integrin $\alpha_{IIb}\beta_3$ receptors and they become competent to bind to their ligand - fibrinogen. Fibrinogen mediates platelet-platelet interactions; thereby, forming platelet aggregation.

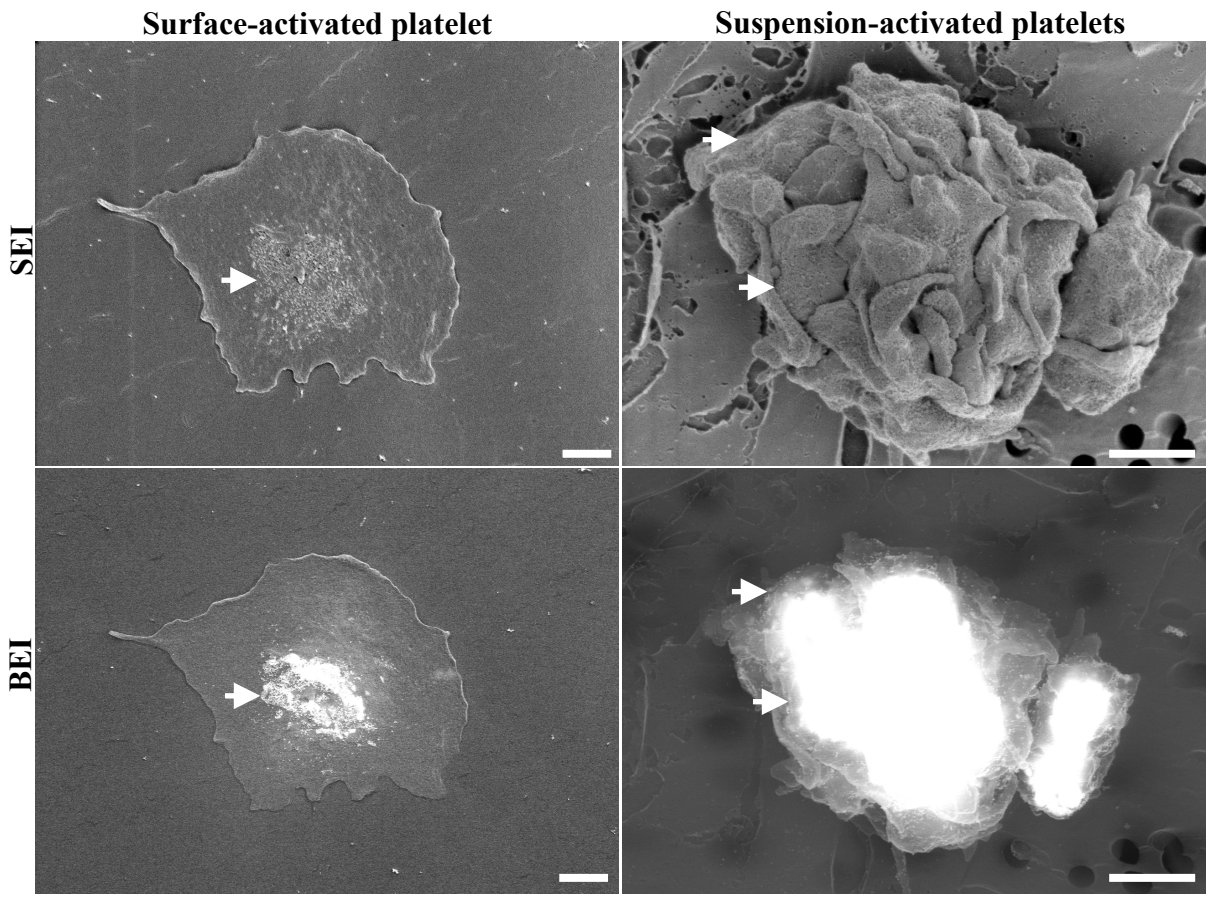

Figure 6. Labeling of surface-activated and suspension-activated platelets using fibrinogen-conjugated gold nanoparticles (FGN-cAu$_{18}$). In the surface-activated platelet, FGN-cAu$_{18}$ bind to the activated platelets tightly and displays the well characterized labeling pattern. The bound labels for the most part clear the periphery and are primarily centralized inside the platelet surface membrane, concentrating in the area around the granulomere. In suspension-activated platelets, some FGN-cAu$_{18}$ nanoparticles remain on the surface of aggregated platelets, but are primarily found at platelet-platelet junctions and internalized. White arrows indicate the presence of FGN-cAu$_{18}$. Secondary electron images (SEI) are on the top row and backscattered electron images (BEI) are on the bottom row. Size bars equal 1μm.

References:

1. Virani, S, S., A. Alonso, A. J. Benjamin, M. S. Bittencourt, C. W. Callaway, A. P. Carson, A. M. Chamberlain, A. R. Chang, S. Cheng, F. N. Delling, L. Djousse, M. S. V. Elkind, J. F. Ferguson, M. Fornage, S. S. Khan, B. M. Kissela, K. L. Knutson, T. W. Kwan, D. T. Lackland, T. T. Lewis, J. H. Lichtman, C. T. Longenecker, M. S. Loop, P. L. Lutsey, S. S. Martin, K. Matsushita, A. E. Moran, M. E. Mussolino, A. M. Perak, W. D. Rosamond, G. A. Roth, U. K. A. Sampson, G. M. Satou, E. B. Schroeder, S. H. Shah, C. M. Shay, N. L. Spartano, A. Stokes, D. L. Tirschwell, L. B. VanWagner, C. W. Tsao. 2020. Heart Disease and Stroke Statistics-2020 Update: A Report from the American Heart Association. Circulation. 141(9), e139-e596. https://doi.org/10.1161/cir.0000000000000757

2. Krishnamurthi, R. V., V. L. Feigin, M. H. Forouzanfar, G. A. Mensah, M. Connor, D. A. Bennett, A. E. Moran, R. L. Sacco, L. M. Anderson, T. Truelsen, M. O'Donnell, N. Venketasubramanian, S. Barker-Collo, C. M. M. Lawes, W. Wang, Y. Shinohara, E. Witt, M. Ezzati, M. Naghavi, C. Murray. 2013. Global and Regional Burden of First-ever Ischaemic and Haemorrhagic Stroke During 1990-2010: Findings from the Global Burden of Disease Study 2010. Lancet Global Health. 1: e259-e281. https://doi.org/10.1016/s2214-109x(13)70089-5

3. Center for Disease Control and Prevention (CDC). 2009. Prevelance and Most Common Causes of Disability Among Adults: United States, 2005. Morbidity and Mortality Weekly Report. 58: 421-426

4. Agency for Healthcare Research and Quality. Medical Expenditure Panel Survey: Household Component Summary Tables: Medical Conditions, United States, 1996-2015. Agency for Healthcare Research and Quality Website. https://www.meps.ahrq.gov/mepstrends/hc_cond/. Accessed March 29, 2020.

5. American Stroke Association. 2019. Explaining Stroke. Stroke. Accessed March 29, 2020. https://www.stroke.org/-/media/stroke-files/stroke-resourcecenter/explaining_stroke_brochure_6_25_19.pdf?la=en&hash=086743F6D5F1A1E3C462B2AFB0C8360F16631787

6. National Institutes of Health. What is a Stroke?. National Heart, Lung, and Blood Institute. Accessed March 29, 2020. http://www.nhlbi.nih.gov/health/health-topics/topics/stroke/

7. Donnan, G. A., M. Fisher, M. Macleod, S. M. Davis. 2008. Stroke. The Lancet. 371(9624): 1612-1623

8. Sims, N. R., H. Muyderman. 2010. Mitochondria, Oxidative Metabolism and Cell Death in Stroke. Biochimica Et Biophysica Acta Molecular Basis of Disease. 1802(1): 80-91

9. Smirnova, I. V., S. X. Zhang, B. A. Citron, P. M. Arnold, B. W. Festoff. 1998. Thrombin is an Extracellular Signal that Activates Intracellular Death Protease Pathways Inducing Apoptosis in Model Motor Neurons. Journal of Neurobiology. 36: 64-80

10. Vaughan, P. J., C. J. Pike, C. W. Cotman, D. D. Cunningham. 1995. Thrombin Receptor Activation Protects Neurons and Astrocytes from Cell Death Produced by Environmental Insult. Journal of Neuroscience. 15: 5389-5401

11. Hemphill III, J. C., S. M. Greenberg, C. S. Anderson, K. Becker, B. R. Bendok, M. Cushman, G. L. Fung, J. N. Goldstein, R. L. Macdonald, P. H. Mitchell, P. A. Scott, M. H. Selim, D. Woo. 2015. Guidelines for the Management of Spontaneous Intracerebral Hemorrhage. Stroke. 46(7): 2032-2060

12. Sato, Y., Ishibashi-Ueda, H., Iwakiri, T., Ikeda, Y., Matsuyama, T., Hatakeyama, K., and Asada, Y. 2012. Thrombus Components in Cardioembolic and Atherothrombotic Strokes. Thrombsis Research. 130 (2): 278-280

13. Turpie, A. G., G. Esmon, C. 2011. Venous and Arterial Thrombosis – Pathogenesis and the Rationale for Anticoagulation. Thrombosis and Haemostasis. 105 (4): 571-741

14. Nieswandt, B., Pleines, I., and Bender, M. 2011. Platelet Adhesion and Activation Mechanism in Arterial Thrombosis and Ischaemic Stroke. Journal of Thrombosis and Haemostasis. 9 (7): 92-104

15. Steiner, M. M., M. R. Di Tulio, T. Rundek, R. Gan, X. Chen, C. Liguori, M. Brainin, S. Homma, R. L. Sacco. 1998. Patent Foramen Ovale Size and Embolic Brain Imaging Findings Among Patients with Ischemic Stroke. Stroke. 29: 944-948

16. Adams, H. P., B. H. Bendixen, L. J. Kappelle, J. Biller, B. B. Love, D. L. Gordon, E. E. Marsh. 1993. Classification of Subtype of Acute Ischemic Stroke, Definitions for Use in a Multicenter Clinical Trial. TOAST. Trial of Org 10172 in Acute Stroke Treatment. Stroke. 24:35-41

17. Scharf, R. E., M. Hennerici, V. Bluschke, J. Lueck, R. G. Kladetzky. 1982. Cerebral Ischmia in Young Patients: It is Associated with Mitral Valve Prolapse and Abnormal Platelet Activity In Vivo? Stroke. 13: 454-458

18. Gido, G., T. Kristian, B. K. Siesjo. 1997. Extracellular Potassium in a Neocortical Core Area After Transient Focal Ischemia. Stroke. 28: 206-210

19. Kristian, T., B. K. Siesjo. 1998. Calcium in Ischemic Cell Death. Stroke. 29: 705-718

20. Astrup, J., B. K. Siesjo, L. Symon. 1981. Thresholds in Cerebral Ischemia-The Ischemic Penumbra. Stroke. 12: 723-725

21. Saver, J. L. 2005. Time Is Brain-Quantified. Stroke. 37: 263-266

22. Christou, I., A. V. Alexandrov, W. S. Burgin, R. A. Felberg, M. G. Malkoff, J. C. Grotta. 2000. Timing of Recanalization After Tissue Plasminogen Activator Therapy Determined by Transcriptional Doppler Correlates with Clinical Recovery from Ischemic Stroke. Stroke. 3: 1812-1816

23. Macfarlane, R. G., and Biggs, R. 1948. Fibrinolysis. Its Mechanism and Significance. Blood. 3 (10): 1167-1187

24. Collen, D. 1996. Fibrin-Selective Thrombolytic Therapy for Acute Myocardial Infarction. Circulation. 93 (5): 857-865

25. Demaerschalk, B. M., Demaerschalk, D, O., Adeoye, O, M., Demchuk, A, M., Fugate, J, E., Grotta, J, C., Khalessi, A, A., Levy, E, I., Palesch, Y, Y., Prabhakaran, S., Saposnik, G., Smith, E, E. 2016. Scientific Rationale for the Inclusion and Exclusion Criteria for Intravenous Alteplase in Acute Ischemic Stroke A Statement for Healthcare Professionals From the American Heart Association/American Stroke Association. Stroke. 47: 00-00

26. Jilani, T. N., A. H. Siddiqui. 2020. Tissue Plasminogen Activator. Treasure Island (FL): StatPearls Publishing. https://www.ncbi.nlm.nih.gov/books/NBK507917/

27. National Institute of Neurological Disorders and Stroke rt-PA Stroke Study Group. 1995. Tissue Plasminogen Activator for Acute Ischemic Stroke. The New England Journal of Medicine. 333(24): 1581-1587

28. Leng, T., Z. G. Xiong. 2019. Treatment for Ischemic Stroke: From Thrombolysis to Thrombectomy and Remaining Challenges. Brain Circulation. 5(1): 8-11

29. Fischer, U., J. Kaesmacher, V. M. Pereira, R. Chapot, A. H. Siddiqui, M. T. Froehler, C. Cognard, A. J. Furian, F. L. Saver, J. Gralla. 2017. Direct Mechanical Thrombectomy Versus Combined Intravenous and Mechanical Thrombectomy in Large-Artery Anterior Circulation Stroke. Stroke. 48(10): 2912-2918

30. Riedel, C. H., P. Zimmermann, U. Jensen-Kondering, R. Stingele, G. Deuschl, O. Jansen. 2011. The Importance of Size: Successful Recanalization by Intravenous Thrombolysis in Acute Anterior Stroke Depends on Thrombus Length. Stroke. 42(6): 1775-1777

31. Beadell, N. C., H. Lutsep. 2013. New Stent Retriever Devices. Current Atherosclerosis Report. 15(6): 333. https://doi.org/10.1007/s11883-013-0333-9

32. Smith, W. S., A. J. Furlan. 2016. Brief History of Endovascular Acute Ischemic Stroke Treatment. Stroke. 47: e23-e26. https://doi.org/10.1161/STROKEAHA.115.010863

33. Smith, W. S. 2006. Safety of Mechanical Thrombectomy and Intravenous Tissue Plasminogen Activator in Acute Ischemic Stroke. Results of the Multi Mechanical Embolus

Removal in Cerebral Ischemia (MERCI) Trial, Part I. American Journal of Neuroradiology. 27(6): 1177-1182

34. Bracard, S., X. Ducrocq, J. L. Mas, M. Soudant, C. Oppenheim, T. Moulin, F. Guillemin. 2016. Mechanical Thrombectomy After Intravenous Alteplase Versus Alteplase Alone After Stroke (THRACE): a Randomised Controlled Trial. The Lancet Neurology. 15(11): 1105-1107

35. Dorn, F., H. Lockau, H. Stetefeld, C. Kabbasch, B. Kraus, C. Dohmen, T. Henning, A. Mpotsaris, T. Liebig. 2015. Mechanical Thrombectomy of M2-Occlusion. Journal of Stroke and Cerebrovascular Diseases. 24(7): 1465-1470

36. Furlan A, R. Higashida, L. Wechsler, M. Gent, H. Rowley, C. Kase, M. Pessin. A. Ahuija, F. Callahan, W. M. Clark, F. Silver, F. Rivera. 1999. Intra-arterial Prourokinase for Acute Ischemic Stroke. The PROACT II Study: A Randomized Controlled Trial. Prolyse in Acute Cerebral Thromboembolism. Journal of American Medical Association. 282(21):2003–2011

37. Ribo, M, J. Alvarez-Sabin, J. Montaner, J. F. Romero, P. Delgado, M. Rubiera, R. Delgado-Mederos, C. A. Molina. 2006. Temporal Profile of Recanalization After Intravenous Tissue Plasminogen Activator: Selecting Patients for Rescue Reperfusion Techniques. Stroke. 37(4):1000–1004

38. Alexandrov, A. V., C. A. Molina, J. C. Grotta, Z. Garami, S. R. Ford, J. Alvarez-Sabin, J. Montaner, M. Saqqur, A. M. Demchuk, L. A. Moye, M. D. Hill, A. W. Wojner. 2004. Ultrasound-Enhanced Systemic Thrombolysis for Acute Ischemic Stroke. The New England Journal of Medicine. 351(21): 2170–2178

39. Penumbra Pivotal Stroke Trial Investigators. 2009. The Penumbra Pivotal Stroke Trial: Safety and Effectiveness of a New Generation of Mechanical Devices for Clot Removal in Intracranial Large Vessel Occlusive Disease. Stroke. 40(8): 2761–2768

40. Fussell D., H. C. Schumacher, P. M. Meyers, R. T. Higashida. 2007. Mechanical Interventions to Treat Acute Stroke. Current Neurology and Neuroscience Reports. 7(1): 21–27

41. Brekenfeld C., G. Schroth, M. El-Koussy, K. Nedeltchev, M. Reinert, J. Slotboom, J. Gralla. 2008. Mechanical Thromboembolectomy for Acute Ischemic Stroke: Comparison of the Catch Thrombectomy Device and The Merci Retriever *In Vivo*. Stroke. 39(4): 1213–1219

42. Mordasini P., M. Hiller, C. Brekenfeld, G. Schroth, U. Fischer, J. Slotboom, M. Arnold, J. Gralla. 2010. *In Vivo* Evaluation of the Phenox CRC Mechanical Thrombectomy Device in a Swine Model of Acute Vessel Occlusion. American Journal of Neuroradiology. 31(5): 972–978

43. Kerber, C. W., I. Wanke, J. Jr. Bernard, H. H. Woo, M. W. Liu, P. K. Nelson. 2007. Rapid Intracranial Clot Removal with a New Device: The Alligator Retriever. American Journal of Neuroradiology. 28(5): 860–863

44. Nogueira, R. G., H. L. Lutsep, R. Gupta, T. G. Jovin, G. W. Alber, G. A. Walker, D. S. Liebeskid, W. S. Smith, TREVO 2 Trialists. 2012. Trevo Versus Merci Retrievers for Thrombectomy Revascularisation of Large Vessel Occlusions in Acute Ischaemic Stroke (TREVO 2): A Randomised Trial. Lancet. 380(9849): 1231–1240. Primary publication from the TREVO 2 Investigators Evaluating the Efficacy of the TREVO 2 Device in Comparison to the MERCI Device.

45. Saver, J. L., R. Jahan, E. I. Levy, T. G. Jovin, B. Baxter, Nogueira, W. Clark, R. Budzik, O. O. Zaidat, SWIFT Trialists. 2012. Solitaire Flow Restoration Device Versus the Merci Retriever in Patients with Acute Ischaemic Stroke (SWIFT): A Randomised, Parallel-Group, Non-Inferiority Trial. Lancet. 380(9849): 1241–9. Primary publication from the SWIFT investigators evaluating the efficacy of the Solitaire device versus the Merci retriever.

46. Campbell, B. C. V., G. A. Donna, K. R. Lees, W. Hacke, P. Khatri, M. D. Hill, M. Goyal, P. J. Milchell, J. L. Saver, H. Diener, S. M. Davis. 2015. Endovascular Stent Thrombectomy: The New Standard of Care for Large Vessel Ischemic Stroke. The Lancet Neurology. 14(8): 846-854

47. Furlan, A. J. 2015. Endovascular Therapy for Stroke- It's About Time. The New England Journal of Medicine. 372: 2347-2349

48. Cohen, D. L., R. Kearney, M. Griffiths, V. Nadesalingam, R. Bathula. 2015. Around 9% of Patients with Ischaemic Stroke Are Suitable for Thrombectomy. The British Medical Journal. 351: h3969. Doi: 10.1136/bmj.h3969.

49. Chia, N. H., J. M. Leyden, J. Newbury, J. Jannes, T. J. Kleinig. 2016. Determining the Number of Ischemic Strokes Potentially Eligible for Endovascular Thrombectomy: A Population-Based Study. Stroke. 47(5): 1377-1380

50. Jadhav, A. P., S. M. Desai, C. L. Kenmuir, M. Rocha, M. T. Starr, B. J. Molyneaux, B. A. Gross, B. T. Jankowitz, T. G. Jovin. 2018. Eligibility for Endovascular Trial Enrollment in the 6- To 24-Hour Time Window: Analysis of A Single Comprehensive Stroke Center. Stroke. 49(4): 1015-1017

51. Josephson, S. A., H. Kamel. 2018. The Acute Stroke Care Revolution Enhancing Access to Therapeutic Advances. The Journal of the American Medical Association. 320(12): 1239-1240

52. Deguchi, I., S. Mizuno, S. Kohyama, N. Tanahashi, M. Takao. 2018. Drip-and-Ship Thrombolytic Therapy for Acute Ischemic Stroke. Journal of Stroke and Cerebrovascular Diseases. 27(1): 61-67

53. Zoppo, G. J., J. L. Saver, E. C. Jauch, H. P. Adams. 2009. Expansion of the Time Window for Treatment of Acute Ischemic Stroke with Intravenous Tissue Plasminogen Activator. Stroke. 40(8): 2945-2948

54. Jivan, K., K. Ranchod, G. Modi. 2013. Management of Ischemic Stroke in the Acute Setting: Review of the Current Status. Cardiovascular Journal of Africa. 24(3): 86-92

55. Osler, W., 1874. An Account of Certain Organism Occurring in the Liquor Sanguinis. The Monthly Microscopical Journal, 12: 141-148. https://doi.org/10.1111/j.1365-2818.1874.tb01798.x

56. Hou, Y., N. Carrim, Y. Wang, R. C. Gallant, A. Marshall, H. Ni. 2015. Platelets in Hemostasis and Thrombosis: Novel Mechanisms of Fibrinogen-Independent Platelet Aggregation and Fibronectin-Mediated Protein Wave of Hemostasis. The Journal of Biomedical Research. 29(6): 437-444

57. Levin, J. 1997. The Evolution of Mammalian Platelets. Thrombopoiesis and Thrombopoietins. Human Press. 63-78

58. Schmaier, A. A., T. J. Stalker, J. J. Runge, D. Lee, C. Nagaswami, P. Mericko, M. Chen, S. Cliché, C. Gariepy, L.F. Brass, D. A. Hammer, J. W. Weisel, K. Rosenthal, M. L. Kahn. 2011. Occlusive Thrombi Arise in Mammals But Not Birds in Response to Arterial Injury: Evolutionary Insight Into Human Cardiovascular Disease. Blood. 118(13): 3661-3669

59. Qiu, Y., J, Ciciliano, D. R. Myers, R. Tran, W. A. Lam. 2015. Platelets and Physics: How Platelet "Feel" and Respond to Their Mechanical Microenvironment. Blood Review. (29) 377-386

60. Nieswandt, B., S. P. Watson. 2003. Platelet-Collagen Interaction: Is GPVI the Central Receptor?. Blood. 102: 449:461

61. Gibbins, J, M., M. Okuma, R. Farndale, M. Barnes, S. P. Watson. 1997. Glycoprotein VI is the Collagen Receptor in Platelets Which Underlies Tyrosine Phosphorylation of the Fc Receptor γ-Chain. FEBS Letter. 413 (2): 255- 259

62. Smith, G., L. K. Jennings. 2015. Spectrum of Thrombin in Acute Coronary Syndromes. Thrombosis Research 135: 782-787.

63. Kahn M. L., M. Nakanishi-Matsui, M. J. Shapiro, H. Ishihara, S. R. Coughlin. 1999. Protease-Activated Receptors 1 and 4 Mediate Activation of Human Platelets by Thrombin. Journal of Clinical Investigation. 103(6): 879-887

64. Clappers, N., M. A. Brouwer, F. W. A. Verheugt. 2007. Antiplatelet Treatment for Coronary Heart Disease. Heart. 93: 258-265

65. Aspirin for Reducing Your Rick of Heart Attack and Stroke: Know the Facts. U.S. Food and Drug Administration (FDA). Retrieved 2 April 2020. https://www.fda.gov/drugs/safe-daily-use-aspirin/aspirin-reducing-your-risk-heart-attack-and-stroke-know-facts

66. Seshasai, S. R. K., S. Wijesuriya, R. Sivakumaran, S. Nethercott, S. Erqou, N. Sattar, K. K. Ray. 2012. Effect of Aspirin on Vascular and Nonvascular Outcomes: Meta-Analysis of Randomized Controlled Trials. Archives of Internal Medicine. 172(3): 209-216

67. Hirsh, J. 1985. Progress Review: The Relationship Between Dose of Aspirin, Side-Effects and Antithrombotic Effectiveness. Stroke. 16: 1-4

68. Mills, D. C., R. Puri, C. J. Hu, C. Minniti, G. Grana, M. D. Freedman, R. F. Colman, R. W. Colman. 1992. Clopidogrel Inhibits the Binding of ADP Analogues to the Receptor Mediating Inhibition of Platelet Adenylate Cyclase. Arteriosclerosis, Thrombosis, and Vascular Biology. 12: 430-436

69. Norgard, N. B., M. Abu-Fadel. 2009. Comparison of Prasugrel and Clopidogrel in Patients with Acute Coronary Syndrome Undergoing Percutaneous Coronary Intervention. Vascular Health and Risk Management. 5: 873-882

70. Wijeyeratne, Y. D., S. Heptinstall. 2011. Anti-Platelet Therapy: ADP Receptor Antagonists. British Journal of Clinical Pharmacology. 72(4): 647-657

71. Antoniucci, D. 2007. Differences Among GP IIb/IIIa Inhibitors: Different Clinical Benefits in Non-ST-Segment Elevation Acute Coronary Syndrome Percutaneous Coronary Intervention Patients. European Heart Journal Supplements. 9(Supplements A): A32-A36

72. De Luca, G., E. Navarese, P. Marino. 2009. Risk Profile and Benefits from GP IIb-IIIa Inhibitors Among Patients with ST-Segment Elevation Myocardial Infarction Treated with Primary Angioplasty: A Meta-Regression Analysis of Randomized Trials. European Heart Journal. 30: 2705-2713

73. Tcheng, J. E., D. E. Kandzari, C. L. Grines, D. A. Cox, M. B. Effron, E. Garcia, J. J. Griffin, G. Guagliumi, T. Stuckey, M. Turco, M. Fahy, A. J. Lansky, R. Mehran, G. W. Stone. 2003. Benefits and Risks of Abciximab Use in Primary Angioplasty for Acute Myocardial Infarction: The Controlled Abciximab and Device Investigation to Lower Late Angioplasty Complications (CADILLAC) Trial. Circulation. 108: 1316-1323

74. Blair, P., R. Flaumenhaft. 2009. Platelet α-Granule: Basic Biology and Clinical Correlates. Blood Review. 23: 177-189

75. Whiteheart, S.W. 2011. Platelet Granules: Surprise Packages. Blood. 118(5): 1190-1191

76. Harrison, P., E. M. Cramer. 1993. Platelet Alpha-Granules. Blood Review. 7(1): 52-62

77. McNicol, A., S. J. Israels. 1999. Platelet Dense Granules: Structure, Function and Implications for Haemostasis. Thrombosis Research. 95: 1-18

78. Ambrosio, A. L., J. A. Boyle, S. M. Di Pietro. 2012. Mechanism of Platelet Dense Granule Biogenesis: Study of Cargo Transport and Function of Rab32 and Rab38 in a Model System. Blood. 120(19): 4072-4081

79. Israels, S. J., A. McNicol, C. Robertson, G. M. Gerrard. 1990. Platelet Storage Pool Deficiency: Diagnosis in Patients with Prolonged Bleeding Times and Normal Platelet Aggregation. Journal of Hematology. 75: 118-121

80. Escolar, G., E. Leistikow, J. G. White. 1989. The Fate of The Open Canalicular System in Surface and Suspension-Activated Platelets. Blood. 74(6): 1983-1988

81. Escolar, G., J. G. White. 1991. The Platelet Open Canalicular System: A Final Common Pathway. Blood Cells. 17(3): 467-485

82. White, J. G., G. Escolar. 1991. The Blood Platelet Open Canalicular System: A Two-Way Street. European Journal of Cell Biology. 56(2): 233-242

83. White, J. G., C. C. Clawson. 1980. The Surface-Connected Canalicular System of Blood Platelets- A Fenestrated Membrane System. The American Journal of Pathology. 101: 353-364

84. Melchinger, H., K. Jain, T. Tyagi, J. Hwa. 2019. Role of Platelet Mitochondria: Life in a Nucleus-Free Zone. Frontiers in Cardiovascular Medicine. 6:153. https://doi.org/10.3389/fcvm.2019.00153

85. Hayashi, T., S. Tanaka, Y. Hori, F. Hirayama, E. F. Sata, M. Inoue. 2011. Role of Mitochondria in the Maintenance of Platelet Function During *In Vitro* Storage. Transfusion Medicine. 21(3): 166-174

86. Aslan, J. E., A. Itakura, J. M. Gertz, O. J. T. McCarty. 2012. Platelet Shape Change and Spreading. Methods in Molecular Biology. 788: 91-100

87. Lee, D., K. P. Fong, M. R. King, L. F. Brass, D. A. Hammer. 2012. Differential Dynamics of Platelet Contact and Spreading. Biophysical Journal. 102: 472-482

88. Shin, E. K., H. Park, J. H. Noh, K. M. Lim, J. H. Chung. 2017. Platelet Shape Changes and Cytoskeleton Dynamics as Novel Therapeutic Targets for Anti-Thrombotic Drugs. Biomolecules and Therapeutics. 25(3): 223-230

89. Ghoshal, K., M. Bhattacharyya. 2014. Overview of Platelet Physiology: Its Hemostatic and Nonhemostatic Role in Disease Pathogenesis. The Scientific World Journal. https://doi.org/10.1155/2014/781857

90. Loftus, J. C., R. M. Albrecht. 1984. Redistribution of the Fibrinogen Receptor of Human Platelets After Surface Activation. Journal of Cell Biology. 99: 822-829

91. Dorsam, R. T., S. P. Kunapuli. 2004. Central Role of The P2Y12 Receptor in Platelet Activation. Journal of Clinical Investigation. 113: 340-345

92. Monroe, D. M., M. Hoffman, H. R. Roberts. 2002. Platelet and Thrombin Generation. Arteriosclerosis. Thrombosis Vascular Biology. 22: 1381-1389

93. Lynch, S. E., J. C. Nixon, R. B. Colvin, R. B. Colvin, H. N. Antoniades. 1987. Role of Platelet-Derived Growth Factors in Wound Healing: Synergistic Effects with Other Growth Factors. Proceeding of the National Academy of Sciences of the United States of America. 84: 7696-7700

94. Woulfe, D. S. 2005. Platelet G Protein-Coupled Receptors in Hemostasis and Thrombosis. Journal of Thrombosis and Haemostasis. 3(10): 2193-2200

95. Offermanns, S. 2006. Activation of Platelet Function Through G Protein-Counpled Receptors. Circulation Research. 99(12): 1293-1304

96. Fuentes, E., I. Palomo. 2013. Relationship Between Platelet PPARs, cAMP Levels, and P-Selectin Expression: Antiplatelet Activity of Natural Products. Evidence-Based Complementary and Alternative Medicine. 2013. https://doi.org/10.1155/2013/861786

97. Nesbitt, W. S., S. Giuliano, S. Kulkarni, S. M. Dopheide, I. S. Harper, S. P. Jackson. 2003. Intercellular Calcium Communication Regulates Platelet Aggregation and Thrombus Growth. Journal of Cell Biology. 160(7): 1151-1161

98. Varga-Szabo, D., A. Braun, B. Nieswandt. 2009. Calcium Signaling in Platelets. Journal Thrombosis and Haemostasis. 7(7): 1057-1066

99. Klages, B., U. Brandt, M. I. Simon, G. Schultz, S. Offermanns. 1999. Activation of G_{12}/G_{13} Results in Shape Change and Rho/Rho-Kinase-Mediated Myosin Light Chain Phosphorylation in Mouse Platelets. Journal of Cell Biology. 144: 745–54.

100. Hubbard, G. P., S. Wolffram, J. A. Lovegrove, J. M. Gibbins. 2004. Ingestion of Quercetin Inhibits Platelet Aggregation and Essential Components of the Collagen- Stimulated Activation Pathway in Humans. Journal of Thrombosis and Haemostasis. 2: 2138-2145

101. Roberts, D. E., A. McNicol, R. Bose. 2004. Mechanism of Collagen Activation in Human Platelets. The Journal of Biological Chemistry. 279(19): 19421-19430

102. Gibbins, J., J. Assenlin, R. Farndale, M. Barnes, C. L. Lay, S. P. Watson. 1996. Tyrosine Phosphorylation of the Fc Receptor γ-Chain in Collagen-Stimulated Platelets. The Journal of Biological Chemistry. 27(30): 18095-18099

103. Munnix, I. C. A., A. Strehl, M. J. E. Kuijpers, J. M. Auger, P. E. van der Meijden, M. A. M. van Zandvoort, M. G. A. oude Egbrink, B. Nieswandt, J. W. M. Heemskerk. 2005. The Glycoprotein VI-Phospholipase Cγ2 Signaling Pathway Controls Thrombus Formation Induced by Collagen and Tissue Factor In Vitro and In Vivo. Arteriosclerosis Thrombosis and Vascular Biology. 25(12): 2673-2678

104. Inoue, O., K. Suzuki-Inoue, W. L. Dean, J. Frampton, S. P. Watson. 2003. Integrin $\alpha_2\beta_1$ Mediates Outside-in Regulation of Platelet Spreading on Collagen Through Activation of Src Kinases and PLCγ2. Journal of Cell Biology. 160: 769-780

105. Pasquet, J. M., B. Gross, L. Quek, N. Asazuma, W. Zhang, C. L. Sommers, E. Schweighoffer, V. Tybulewicz, B. Judd, J. R. Lee, G. Koretzky, P. E. Love, L. E. Samelson, S. P. Watson. 1999. LAT Is Required for Tyrosine Phosphorylation of Phospholipase Cγ2 and Platelet Activation by the Collagen Receptor GPVI. Molecular and Cellular Biology. 19: 8326-8334

106. Sangkukl, K., A. R. Shuldiner, T. E. Klein, R. B. Altman. 2011. Platelet Aggregation Pathway. Pharmacogenetics and Genomics. 21(8): 516-521

107. Andersen, H., D. L. Greenberg, K. Fujikawa, W. Xu, D. W. Chung, E. W. Davie. 1999. Protease-Activated Receptor 1 Is the Primary Mediator of Thrombin-Stimulated Platelet Procoagulant Activity. Proceedings of the National Academy of Sciences of the United States of America. 96: 11189-11193

108. Heuberger, D. M., R. A. Schuepbach. 2019. Protease-Activated Receptors (PARs): Mechanisms of Action and Potential Therapeutic Modulators in PAR-Driven Inflammatory Diseases. Thrombosis Journal. 17(4). https://doi.org/10.1186/s12959-019-0194-8

109. Nieman, M, T., Schmaier, A, H. 2007. Interaction of Thrombin with PAR1 and PAR4 at the Thrombin Cleavage Site. Biochemistry. 46(29): 8603-8610

110. Gurbel, P. A., A. Kuliopulos, U. S. Tantry. 2015. G-Protein-Coupled Receptors Signaling Pathways in New Antiplatelet Drug Development. Arteriosclerosis, Thrombosis and Vascular Biology. 35(3): 500-512

111. Kahn, M. L., Y. W. Zheng, W. Huang, V. Bigornia, D. Zeng, S. Moff, R. V. Farese, Jr. C. Tam, S. R. Coughlin. 1998. A Dual Thrombin Receptor System for Platelet Activation. Nature. 394:690-694

112. Hung, D. T., Y. H. Wong, T. K. Vu, S. R. Coughlin. 1992. The Clone Platelet Thrombin Receptor Couples to at Least Two Distinct Effectors to Stimulate Phosphoinositide Hydrolysis and Inhibit Adenylyl Cyclase. Journal of Biological Chemistry. 267: 20831-20834

113. Offermanns, S., K. L. Laugwitz, K. Spicher, G. Schultz. 1994. G Protein of the G12 Family Are Activated Via Thromboxane A2 and Thrombin Receptors in Human Platelets.

Proceeding of the National Academy of Sciences of the United States of America. 91: 504-508

114. Hollenberg, M. D., M. Saifeddine, S. Sandhu, S. Houle, N. Vergnolle. 2004. Proteinase-Activated Receptor-4: Evaluation of Tethered Ligand-Derived Peptides as Probes for Receptor Function and as Inflammatory Agonists in Vivo. British Journal of Pharmacology. 143: 443-454

115. Faruqi, T. R., E. J. Weiss, M. J. Shapiro, W. Huang, S. R. Coughlin. 2000. Structure Function Analysis of Protease-Activated Receptor 4 Tethered Ligand Peptides: Determinants of Specificity and Utility in Assays of Receptor Function. Journal of Biological Chemistry. 275: 19782-19734

116. Bodor, E. T., G. L. Waldo, S. B. Hooks, J. Corbitt, J. L. Boyer, T. K. Harden. 2003. Purification and Functional Reconstitution of the Human $P2Y_{12}$ Receptor. Molecule Pharmacology. 64: 1210-1216

117. Hollopeter, G., H. M. Jantzen, D. Vincent, G. Li, L. England, V. Ramakrishnan, R. B. Yang, P. Nurden, A. Nurden, D. Julius, P. B. Conley. 2001. Identification of the Platelet ADP Receptor Targeted by Antithrombotic Drugs. Nature. 409: 202-207

118. Puri, R. N., R. W. Colman. 1997. ADP-Induced Platelet Activation. Critical Review Biochemistry and Molecular Biology. 32(6): 437-502

119. Packhan, M. A., M. L. Rand. 2011. Historical Perspective on ADP-Induced Platelet Activation. Purinergic Signalling. 7(3): 283-292

120. Hardy, A. R., P. B. Conley, J. Luo, J. L. Benovic, A. W. Poole, S. J. Mundell. 2005. $P2Y_1$ and $P2Y_{12}$ Receptors for ADP Desensitize by Distinct Kinase-Dependent Mechanisms. Blood. 105(9): 3552-3560

121. Nakahata, N. 2008. Thromboxane A2: Physiology/Pathophysiology Cellular Signal Transduction and Pharmacology. Pharmacology and Therapeutics. 118(1): 18-35

122. Patrono, C., B. Rocca. 2019. Measurement of Thromboxane Biosynthesis in Health and Disease. Frontiers in Pharmacology. 10:1244. https://doi.org/10.3389/fphar.2019.01244

123. Tallima, H., R. E. Ridi. 2018. Arachidonic Acid: Physiological Roles and Potential Health Benefit- A Review. Journal of Advanced Research. 11: 33-41

124. Burke, J. E., E. A. Dennis. 2009. Phospholipase A2 Structure/Function, Mechanism, and Signaling. Journal of Lipid Research. 50 Supplement. S237-S242

125. Fitzpatrick, F. A. 2004. Cyclooxygenase Enzymes: Regulation and Function. Current Pharmaceutical Design. 10(6): 577-588

126. Bennett, J. S. 2005. Structure and Function of the Platelet Integrin $\alpha_{IIb}\beta_3$. The Journal of Clinical Investigation. 115(12): 3363-3369

127. Madan, M., S. D. Berkowitz, J. E. Tcheng. 1998. Glycoprotein IIb/IIIa Integrin Blockade. Circulation. 98(23): 2629-2635

128. Shattil, S. J., J. A. Hoxie, M. Cunningham, L. F. Brass. 1985. Change in the Platelet Membrane Glycoprotein IIb/IIIa Complex During Platelet Activation, Journal of Biological Chemistry. 260:11107-11114

129. Ma, Y. Q., E. P. Plow. 2007. Platelet Integrin $\alpha_{IIb}\beta_3$: Activation Mechanisms. Journal of Thrombosis and Haemostasis. 5: 1345-1352

130. Shattil, S. J., H. Kashiwagi, N. Pampori. 1998. Integrin Signaling: The Platelet Paradigm. Blood. 91: 2645-2657

131. Yeghiazarians, Y., J. B. Braunstein, A. Askari, P. H. Stone. 2000. Unstable Angina Pectoris. The New England Journal of Medicine. 342: 101-114

132. Naik, U. P., M. U. Naik. 2003. Association of CIB with GPIIb/IIIa During Outside-in Signaling is Required for Platelet Spreading on Fibrinogen. Blood. 102: 1355-1362

133. Wencel-Drake, J. D., C. Boudignon-Proudhon, M. G. Dieter, A. B. Criss, L. V. Parise. 1996. Internalization of Bound Fibrinogen Modulate Platelet Aggregation. Blood. 87(2): 602-612

134. Belitser, N., M. Anischuk, T. Pozdnjakova, O. Gorkun. 1993. Fibrinogen Internalization by ADP-Stimulated Blood Platelets. Ultrastructure Studies with Fibrinogen-Colloid Gold Probes. Thrombosis Research. 69(5): 413-424

135. Leistikow, E. A., M. I. Barnhart, G. Escolar, J. G. White. 1990. Receptor-Ligand Complexes Are Cleared to the Open Canalicular System of Surface-Activated Platelets. British Journal of Haematology. 74: 93-100

136. Escolar, G., E. Leistikow, J. G. White. 1989. The Fate of the Open Canalicular System in Surface and Suspension Activated Platelets. Blood. 74(6): 1983-1988

137. Tucker, K. L., T. Sage, J. M. Gibbins. 2012. Clot Retraction. Methods in Molecular Biology. 788: 101-107

138. Tutwiler, V., H. Wang, R. I. Litvinov, J. W. Weisel, V. B. Shenoy. 2017. Interplay of Platelet Contractility and Elasticity of Fibrin/Erythrocytes in Blood Clot Retraction. Biophysical Journal. 112(4): 714-723

139. Osdoit, S., J. P. Rosa. 2001. Fibrin Clot Retraction by Human Platelets Correlates with $\alpha_{IIb}\beta_3$ Integrin-dependent Protein Tyrosine Dephosphorylation. The Journal of Biological Chemistry. 276(9): 6703-6710

140. Doolittle, R. F. 1983. The Structure and Evolution of Vertebrate Fibrinogen. Annals of the New York Academy of Sciences. 408:13-27

141. Mosesson, M. W., K. R. Siebenlist, D. A. Meh. 2001. The Structure and Biological Features of Fibrinogen and Fibrin. Annals of the New York Academy of Sciences. 936: 11-30

142. Mosesson, M. W. 2005. Fibrinogen and Fibrin Structure and Functions. Journal of Thrombosis and Haemostasis. 3: 1894-1904

143. Scheraga, H. A. 2004. The Thrombin-Fibrinogen Interaction. Biophysical Chemistry. 112: 117-130

144. Medved, L., J. W. Weisel. 2009. Recommendations for Nomenclature on Fibrinogen and Fibrin. Journal of Thrombosis and Haemostasis. 7(2): 355-359

145. Wolberg, A. S. 2018. Fibrinogen and Factor XIII: Newly Recognized Roles in Venous Thrombosis Formation and Composition. Current Opinion in Hematology. 25(5): 358-364

146. Bereczky, Z., E. Katona, L. Muszbek. 2004. Fibrin Stabilization (Factor XIII), Fibrin Structure and Thrombosis. Pathophysiology of Haemostasis and Thrombosis. 33: 430-437

147. Podolnikova, N. P., V. P. Yakubenko, G. L. Volkov, E. F. Plow, T. P. Ugarova. 2003. Identification of a Novel Binding Site for Platelet Intergins $\alpha_{IIb}\beta_3$ (GPIIbIIIa) and $\alpha_5\beta_1$ in the γ-C Domain of Fibrinogen. Journal of Biological Chemistry. 27(34): 32251-32258

148. Seligsohn, U. 2002. Glanzmann Thrombasthenia: A Model Disease Which Paved the Way to Powerful Therapeutic Agents. Pathophysiology of Haemostasis and Thrombosis. 32(5-6): 216-217

149. Mehilli J., A. Kastrati, S. Schulz, S. Frungel, S. G. Nekolla, W. Moshage, F. Dotzer, K. Huber, J. Pache, J. Dirchinger, M. Seyfarth, S. Martinoff, M. Schwaiger, A. Schomig. 2009. Abciximab in Patients with Acute ST-Segment-Elevation Myocardial Infarction Undergoing Primary Percutaneous Coronary Intervention After Clopidogrel Loading. Circulation. 119(14): 1933-1940

150. Ciccone, A., C. Motto, I. Abraha, F. Cozzolino, I. Santilli. 2014. Glycoprotein IIb-IIIa Inhibitors for Acute Ischaemic Stroke. Cochrane Database of Systematic Review. 3: CD005208. Doi: 10.1002/14651858.CD005208.pub3

151. Luca, G. D., H. Suryapranata, G. W. Stone. 2005. Abciximab as Adjunctive Therapy to Reperfusion in Acute ST-Segment Elevation Myocaridial Infarction A Meta-Analysis of Randomized Trials. Journal of the American Medical Association. 293(14): 1759-1765

152. Tcheng, J. E., D. J. Kereiahes, M. Lincoff, B. George, N. S. Kleiman, D. C. Sane, D. B. Cines, R. E. Jordan, A. Mascelli, M. A. Langrall, L. Damaraju, A. Schanntz, M. B. Effron,

G. A. Braden. 2001. Abciximab Readministration: Results of the ReoPro Readministration Registry. Circulation. 104(8): 870-875

153. Yamada, T., Y. Shimada, M. Kikuchi. 1996. Integrin-Specific Tissue-Type Plasminogen Activator Engineered by Introduction of the Arg-Gly-Asp Sequence. Biochemical and Biophysical Research Communications. 228: 306-311

154. Absar, S., S. Choi, F. Ahsan, E. Cobos, V. C. Yang, Y. M. Kwon. 2013. Preparation and Characterization of Anionic Oligopeptide-Modified Tissue Plasminogen Activator for Trigger Delivery: An Approach for Localized Thrombolysis. Thrombosis Research. 131: e91-e99

155. Cheresh, D. A., S. A. Berliner, V. Vicente, Z. M. Ruggeri. 1989. Recognition of Distinct Adhesive Sites on Fibrinogen by Related Integrins on Platelets and Endothelial Cells. Cell. 58(5): 945-953

156. Huang, T. F., J. R Sheu, C. M. Teng, S. W. Chen. C. S. Liu. 1990. Triflavin, An Antiplatelet Arg-Gly-Asp-Containing Peptide, Is a Specific Antagonist of Platelet Membrane Glycoprotein IIb-IIIa Complex. Journal of Biochemistry. 109: 328-334

157. Du, X. P., E. F. Plow, A. L. Frelinger III, T. E. O'Toole, J. C. Loftus, M. H. Ginsberg. 1991. Ligands "Activate" Integrin $\alpha_{IIb}\beta_3$ (Platelet GPIIb-IIIa). Cell. 65(3): 409-416

158. Oliver, J. A., R. M. Albrecht. 1987. Colloidal Gold Labelling of Fibrinogen Receptors in Epinephrine-and ADP-Activated Platelet Suspensions. Scanning Microscopy. 1: 745-756

159. Grouse, L. H., J. G. White. 1989. Gold-Labeled Bovine Fibrinogen for Study of Human Platelets. Thrombosis and Haemostasis. 62: 1112-1115

160. Beliser, N., M. Anischuk, Y. Veklich, T. Pozdjakova, O. Gorkun. 1993. Fibrinogen Internalization by ADP-Stimulated Blood Platelets. Ultrastructure Studies with Fibrinogen-Colloidal Gold Probes. Thrombosis Research. 69: 413-424

161. Albrecht, R. M., J. A. Oliver, J. C. Loftus. 1986. Observation of Colloidal Gold Labelled Platelet Surface Receptors and the Underlying Cytoskeleton Using High Voltage Electron Microscopy and Scanning Electron Microscopy. The Science of Biological Specimen Preparation: 185-193

162. Loftus, J. C., J. Choate, R. M. Albrecht. 1984. Platelet Activation and Cytoskeletal Reorganization: High Voltage Electron Microscopic Examination of Intact and Triton-Extracted Whole Mounts. Journal of Cell Biology. 98: 2019-2025

163. Olorundare, O. E., S. R. Simmons, R. M. Albrecht. 1992. Cytochalasin D and E: Effects on Fibrinogen Receptor Movement and Cytoskeletal Reorganization in Fully Spread, Surface-Activated Platelets: A Correlative Light and Electron Microscopic Investigation. Blood. 79: 99-109

164. Simmons, S. R., P. A. Sims, R. M. Albrecht. 1997. Alpha IIb Beta 3 Redistribution Triggered by Receptor Cross-Linking. Arteriosclerosis, Thrombosis, and Vascular Biology. 17: 3311-3320

165. Wang, E. C., A. Z. Wang. 2014. Nanoparticles and Their Applications in Cell and Molecular Biology. Integrative Biology: Quantitative Biosciences from Nano to Macro. 6(1): 9-26

166. Jain, R. K., T. Stylianopoulos. 2010. Delivering Nanomedicine to Solid Tumors. Nature Reviews Clinical Oncology. 7: 653-664

167. Maeda, H., J. Wu, T. Sawa, Y. Matsumura, K. Hori. 2000. Tumor Vascular Permeability and The EPR Effect in Macromolecular Therapeutics: A Review. Journal of Controlled Release. 65: 271-284

168. Verna, A., O. Uzun, Y. Hu, H. S. Hu, Y. Han, N. Watson, S. Chen, D. J. Irvine, F. Stellacci. 2008. Surface-Structure-Regulated Cell-Membrane Penetration by Monolayer-Protected Nanoparticles. Nature Materials. 7: 588-595

169. Wang, A. Z., F. Gu, L. Zhang, J. M. Chan, A. Radovic-Moreno, M. R. Shaikh, O. C. Farokhzad. 2008. Biofunctionalized Targeted Nanoparticles for Therapeutic Applications. Expert Opinion on Biological Therapy. 8: 1063-1070

170. Farokhzad, O. C., J. Cheng, B. A. Teply, I. Sherifi, S. Jon, P. W. Kantoff, J. P. Richie, R. Langer. 2006. Targeted Nanoparticle-Aptamer Bioconjugates for Cancer Chemotherapy in Vivo. Proceedings of the National Academy of Sciences of the United States of America. 103: 6315-6320

171. Werner, M. E., J. A. Copp, S. Karve, N. D. Cummings, R. Sukumar, C. Li, M. E. Napier, R. C. Chen, A. D. Cox, A. Z. Wang. 2011. Folate-Targeted Polymeric Nanoparticle Formulation of Docetaxel Is an Effective Molecularly Targeted Radiosensitizer with Efficacy Dependent on the Timing of Radiotherapy. ACS Nano. 5: 8990-8998

172. Lee, R. J., P. S. Low. 1994. Folate-Mediated Tumor Cell Targeting of Liposome-Entrapped Doxorubicin in Vitro. Biochimica Et Biophysica Acta. 1233: 134-144

173. Octavia, Y., C. G. Tocchetti, K. L. Gabrielson, S. Janssens, H. J. Crijns, A. L. Moens. 2012. Doxorubicin-Induced Cardiomyopathy: From Molecular Mechanisms to Therapeutic Strategies. Journal of Molecular and Cellular Cardiology. 52(6): 1213-1225

174. Lohade, A. A., R. R. Jain, K. Iyer, S. K. Roy, H. H. Shimpi, Y. Pawar, M. G. R. Rajan, M. D. Menon. 2015. A Novel Folate-Targeted Nanoliposomal System of Doxorubicin for Cancer Targeting. AAPS PharmSciTech. 17: 1298-1311

175. Yang, X., J. J. Grailer, I. J. Rowland, A. Javadi, S. A. Hurley, V. Z. Matson, D. A. Steeber, S. Gong. 2010. Multifunctional Stable and pH-Responsive Polymer Vesicles Formed by Heterofunctional Triblock Copolymer for Targeted Anticancer Drug Delivery and Ultrasensitivity MR Imaging. ACS Nano. 4: 6805-6817

176. Luo, C., L. Miao, Y. Zhao, S. Musetti, Y. Wang, K. Shi, L. Huang. 2016. A Novel Cationic Lipid with Intrinsic Antitumor Activity to Facilitate Gene Therapy of TRAIL DNA. Biomaterials. 102: 239-248

177. Glinka, E. M. 2012. Eukaryotic Expression Vectors Bearing Genes Encoding Cytotoxic Proteins for Cancer Gene Therapy. Plasmid. 68(2): 69-85

178. Chatterjee, D. K., P. Diagaradjane, S. Krishnan. 2011. Nanoparticle-Mediated Hyperthermia in Cancer Therapy. Therapeutic Delivery. 2(8): 1001-1014

179. Khan, I., K. Saeed, I. Khan. 2019. Nanoaprticles: Properties, Applications and Toxicities. Arabian Journal of Chemistry. 12(7): 908-931

180. Akbarzadeh, A., R. Rezaei-Sadabady, S. Davaran, S. W. Joo, N. Zarghami, Y. Hanifehpour, M. Samiel, M. Kouhi, K. Nejati-Koshki. 2013. Liposome: Classification, Preparation, and Applications. Nanoscale Research Letters. 8:102. http://www.nanoscalereslett.com/content/8/1/102

181. Lasic, D. D. 1998. Novel Applications of Liposomes. Trends in Biotechnology. 16(7): 307-321

182. Daraee, H., A. Etemadi, M. Kouhi, S. Alimirzalu, A. Akbarzadeh. 2014. Application of Liposomes in Medicine and Drug Delivery. Artificial Cells, Nanomedicine, and Biotechnology. 44: 381-391

183. Cucinotto, I., L. Fiorillo, S. Gualtieri, M. Arbitrio, D. Ciliberto, N. Staropoli, A. Grimaldi, A. Luce, P. Tassone, M. Caraglia, P. Tagliaferri. 2013. Nanoparticle Albumin Bound Paclitaxel in the Treatment of Human Cancer: Nanodelivery Reaches Prime-Time? Journal of Drug Delivery. 2013. https://doi.org/10.1155/2013/905091

184. An, F., X. H. Zhang. 2017. Strategies for Preparing Albumin-Based Nanoparticles for Multifunctional Bioimaging and Drug Delivery. Theranostics. 7(15): 3667-3689

185. Akbarzadeh, A., M. Samiei, S. Davaran. 2012. Magnetic Nanoparticles: Preparation, Physical Properties, and Applications in Biomedicine. Nanoscale Research Letters. 7(1):144

186. Silva, S. M., R. Tavallaie., L. Sandiford, R. D. Tiley, J. J. Gooding. 2016. Gold Coated Magnetic Nanoparticles: From Preparation to Surface Modification for Analytical and Biomedical Application. Chemical Communications. 52: 7528-7540

187. Zhang X. 2015. Gold Nanoparticles: Recent Advances in Biomedical Application. Cell Biochemistry and Biophysics. 72(3): 771-775

188. Krystofiak, E. S., E. C. Mattson, P. M. Voyles, C. J. Hirschmug, R. M. Albrecht, M. Gajdardziska-Josifovska, J. A. Oliver. 2013. Multiple Morphologies of Gold-Magnetite Heterostructure Nanoparticles are Effectively Functionalized with Protein for Cell Targeting. Microscopy and Microanalysis. 19: 821-834

189. Krystofiak, E. S., V. Z. Matson, D. A. Steeber, J. A. Oliver. 2012. Elimination of Tumor Cells Using Folate Receptor Targeting by Antibody-Conjugated, Gold-Coated Magnetite Nanoparticles in a Murine Breast Cancer Model. Journal of Nanomaterials. 2012. Article ID 431012

190. Kaiser, M., J. Heintz, I. Kandela, R. M. Albrecht. 2007. Tumor Cell Death Induced by Membrane Melting via Immunotargeted, Inductively Heated Core/Shell Nanoparticles. Microscopy and Microanalysis. 13(SupplementS02): 18-19

191. Hildebrandt, B., P. Wust, O. Ahlers, A. Dieing, G. Sreeenivasa, T. Kerner, R. Flelix, H. Riess. 2002. The Cellular and Molecular Basis of Hyperthermia. Critical Reviews in Oncology/Hematology. 43(1): 33-56

192. Johannsen, M., B. Thiesen, A. Jordan, K. Taymoorian, U. Gneveckow, N. Waldofner, R. Scholz, M. Koch, M. Lein, K. Jung, S. A. Loening. 2005. Magnetic Fluid Hyperthermia (MFH) Reduces Prostate Cancer Growth in the Orthotopic Dunning R3327 Rat Model. The Prostate. 64(3): 283-292

193. Ali, A., H. Zafar, M. Zia, I. U. Haq, A. R. Phull, J. S. Ali, A. Hussain. 2016. Synthesis, Characterization, Applications and Challenges of Iron Oxide Nanoparticles. Nanotechnology, Science and Applications. 9: 49-67

194. Kudr, J., Y. Haddad, L. Richtera, Z. Heger, M. Cernak, V. Adam, O. Zitka. 2017. Magnetic Nanoparticles: From Design and Synthesis to Real World Applications. Nanomaterials. 7: 243. http://dx.doi.org/10.3390/nano7090243

195. Kim, D., Y. Zhang, W. Voit, K. V. Rao, M. Muhammed. 2001. Synthesis and Characterization of Surfactant-Coated Superparamagnetic Monodispersed Iron Oxide Nanoparticles. Journal of Magnetism and Magnetic Materials. 225(1): 30–36

196. Kim, D. K., M. Mikhaylova, Y. Zhang, M. Muhammed. 2003. Protective Coating of Superparamagnetic Iron Oxide Nanoparticles. Chemistry of Materials. 15(8): 1617–1627

197. Lyon, J. L., D. A. Fleming, M. B. Stone, P. Schiffer, M. E. Williams. 2004. Synthesis of Fe Oxide Core/Au Shell Nanoparticles by Iterative Hydroxylamine Seeding. Nano Letters. 4: 719-723

198. Cho, S. J., J. C. Idrobo, J. Olamit, K. Liu, N. D. Browning, S. M. Kauzlarich. 2005. Growth Mechanisms and Oxidation Resistance of Gold-Coated Iron Nanoparticles. Chemistry of Materials. 17: 3181-3186

199. Hu, J. D., Y. Zevi, X. M. Kou, J. Xiao, X. J. Wang, Y. Jin. 2010. Effect of Dissolved Organic Matter on the Stability of Magnetite Nanoparticles Under Different pH and Ionic Strength Conditions. Science of the Total Environment. 408: 3477-3489

200. Cui, Y. R., C. Hong, Y. L. Zhou, Y. Li, X. M. Gao, X. X. Zhang. 2011. Synthesis of Orientedly Bioconjugated Core/Shell Fe3O4@Au Magnetic Nanoparticles for Cell Separation. Talanta. 85: 1246-1252

201. Mandal, M., S. Kundu, S. K. Ghosh, S. Panigrahi, T. K. Sau, S. M. Yusuf, T. Pal. 2005. Magnetic Nanoparticles with Tunable Gold or Silver Shell. Journal of Colloid Interface Science. 286: 187-194

202. Mornet, S., J. Portier, E. Duguet. 2005. A Method for Synthesis and Functionalization of Ultrasmall Superparamagnetic Covalent Carriers Based in Maghemite and Dextran. Journal of Magnetism and Magnetic Materials. 293: 127-134

203. Lattuada, M., T. A. Hatton. 2006. Functionalization of Monodisperse Magnetic Nanoparticles. Langmuir. 23: 2158-2168

204. Hu, F. Q., L. Wei, Z. Zhou, Y. L. Ran, Z. Li, M. Y. Gao. 2006. Preparation of Biocompatible Magnetite Nanocrystals for In Vivo Magnetic Resonance Detection of Cancer. Advanced Materials. 18: 2553-2556

205. Silva, S. M., R. Tavallaie, L. Sandiford, R. D. Tilley, J. J. Gooding. 2016. Gold Coated Magnetic Nanoparticles: From Preparation to Surface Modification for Analytical and Biomedical Applications. Chemical Communications. 52: 7528-7540

206. Ahmad, T., H. Bae, I. Rhee, Y. Chang, S. U. Jin, S. Hong. 2012. Gold-Coated Iron Oxide Nanoparticles as a T2 Contrast Agent in Magnetic Resonance Imaging. Journal of Nanoscience and Nanotechnology. 12(7): 5132-5137

207. Ghorbani, M., H. Hamisherhkar, N. Arasalani, A. A. Entezami. 2015. Preparation of Thermo and pH-Responsive Polymer @Au/Fe_3O_4 Core/Shell Nanoparticles as a Carrier for Delivery of Anticancer Agent. Journal of Nanoparticle Research. 17:305. https://doi.org/10.1007/s11051-015-3097-z

208. Jordan, A., R. Scholz, P. Wust, H. Fähling, F. Roland. 1999. Magnetic Fluid Hyperthermia (MFH): Cancer Treatment with AC Magnetic Field Induced Excitation of Biocompatible Superparamagnetic Nanoparticles. Journal of Magnetism and Magnetic Materials. 201(1-3): 413-419

209. Gilchrist, R. K., R. Medal, W. D. Shorey, R. C. Hanselman, J. C. Parrott, B. Taylor. 1957. Selective Inductive Heating of Lymph Nodes. Annals of Surgery. 146(4): 596-606

210. Ma, M., Y. Wu, J. Zhou, Y. Sun, Y. Zhang, N. Gu. 2004. Size Dependence of Specific Power Absorption of Fe_3O_4 Particles in AC Magnetic Field. Journal of Magnetism and Magnetic Material. 268(1-2): 33-39

211. Sonvico, F., C. Dubernet, P. Colombo, P. Couvreur. 2005. Metallic Colloid Nanotechnology, Applications in Diagnosis and Therapeutics. Curr Pharm Design. 11(16): 2095-2105

212. Luderer, A. A., N. F. Borrelli, J. N. Panzarino, G. R. Mansfield, D. M. Hess, J. L. Brown, E. H. Barnett, E. W. Hahn. 1983. Glass-Ceramic-Mediated, Magnetic-Field-Induced Localized Hyperthermia: Response of a Murine Mammary Carcinoma. Radiation Research. 94 (1): 190-198

213. Ito, A., K. Tanaka, H. Honda, S. Abe, H. Yamaguchi, T. Kobayashi. 2003. Complete Regression of Mouse Mammary Carcinoma with a Size Greater Than 15 mm by Frequent Repeated Hyperthermia Using Magnetite Nanoparticles. Journal of Bioscience and Bioengineering. 96(4): 364-369

214. Suzuki, S., K. Arai, T. Koike, K. Oguchi. 1990. Studies on Liposomal Ferromagnetic Particles and a Technique of High Frequency Inductive Heating-in vivo Studies of Rabbits. Nippon Gan Chiryo Gakkai Shi. 25(11): 2649-2658

215. Pankhurst, Q. A., J. Connolly, S. K. Jones, J. Dobson. 2003. Applications of Magnetic Nanoparticles in Biomedicine. Journal of Physics D: Applied Physics. 36(13): R167

216. Mornet, S., S. Vasseur, F. Grasset, E. Duguet. 2004. Magnetic Nanoparticle Design for Medical Diagnosis and Therapy. Journal of Materials Chemistry. 14(14): 2161-2175

Chapter 2 - Investigating Interaction of Nanoparticles with Clot Components

Abstract:

Ischemic stroke patients have limited treatment options available. The only FDA-approved drug, tissue plasminogen activator, comes with a significant risk of bleeding complications. We are investigating an alternative treatment that specifically targets activated platelets in occlusive clots using fibrinogen-conjugated, gold-coated magnetic nanoparticles (FGN-cAu-Fe_3O_4) for hyperthermia. Previous work showed that FGN-cAu-Fe_3O_4 could specifically target activated platelets in a purified platelet system (1). *In vivo*, however, there are more factors that might potentially impact the binding of nanoparticles such as fibrin, red blood cells (RBCs), and other cells and proteins present in whole blood to consider. Thus, it is important to examine the interaction of nanoparticles with plasma components such as platelets, RBCs, and fibrin to determine the extent of off-target nanoparticle association with clot components.

We hypothesize that fibrinogen-conjugated nanoparticles specifically interact with activated platelets, potentially bind onto fibrin, and do not associate with RBCs. To test the interaction of nanoparticles with clot components, each of fibrinogen, platelet-rich plasma (PRP), or platelet-poor plasma spiked with RBCs were allowed to form clots using thrombin. Then, samples were labelled with fibrinogen-conjugated nanoparticles, followed by either scanning electron microscopy or transmission electron microscopy preparation. Supernatants, sections, and medial cross-sections were analyzed by scanning electron microscopy to observe both the topography and interior of the samples. As expected, no interaction between fibrinogen-conjugated nanoparticles and RBCs was observed. This suggested that our method is specific and could be safe enough to be used *in vivo* for treatment of ischemic stroke. While we proposed targeting activated platelets, the potential for fibrinogen-

conjugated nanoparticles to associate with the fibrin network was significant. Interestingly, many labels found were associated with fibrin more often than with activated platelets. These results suggested that along with activated platelets, fibrinogen-conjugated nanoparticles can interact strongly at high concentration with fibrin. Fibrin might be a competitor of activated platelets in binding with nanoparticles; on the other hand, it can also be another potential site-specific target to treat ischemic stroke. These experiments helped to better understanding these nanoparticle interactions and educated us about the feasibility of using fibrinogen-conjugated nanoparticles *in vivo* to treat ischemic stroke.

Introduction:

Previous studies have shown that fibrinogen-conjugated gold coated-magnetite nanoparticles could specifically target activated platelets in a purified platelet system. When labeled aggregates were exposed to an oscillating magnetic field (OMF), the aggregates were successfully disrupted (1). This suggested that the method could be a means to restore the flow of blood through an occluded vessel. We have proposed that our method specifically targets the activated platelets in occlusive clots and leaves quiescent platelets unaffected, which is critical in developing a stroke therapy with minimal risk of bleeding complications. However, the arterial clots that cause ischemic stroke not only contain activated platelets but also fibrin, red blood cells (RBCs), white blood cells (WBCs), and other proteins including coagulation factors. These components might contribute to potential extensive off-target binding and affect the specificity of fibrinogen-conjugated nanoparticles in targeting the clots. Therefore, a better understanding of these nanoparticle interactions will educate us about the feasibility of using fibrinogen-conjugated nanoparticles *in vivo* to treat ischemic stroke.

Arterial thrombosis results from clot formation within atherosclerotic arteries. This happens when fatty or calcium deposits cause artery walls to thicken, leading to a buildup of plaque in the artery walls. As a result, this plaque can suddenly rupture. This is followed by platelet aggregation, thrombus formation and vessel occlusion, and potentially heart attack or ischemic stroke occurs (2, 3). In addition, arterial thrombosis often occurs at places of high shear flow. Typically, arterial clots are rich in platelets and form at the sides of or around ruptured atherosclerotic plaques, giving them the appearance of a white clot. In addition to platelets, arterial thrombi contain fibrin. In fact, many reports have showed that in the coronary and other large arteries, most of the thrombi detected at atherosclerotic plaque rupture sites consisted of a mixture of fibrin and platelets, with fibrin being more abundant (4-7). In addition to fibrin and platelets, arterial thrombi consist of RBCs, cellular microvesicles, and leukocytes. It has been reported that arterial thrombi contained by volume 43% fibrin, 31% platelets, 17% RBCs, 5% cellular microvesicles, and 2% leukocytes (7).

The interactions of fibrinogen with platelets via platelet integrin $\alpha_{IIb}\beta_3$ (GPIIb/IIIa) receptors is well-studied. Platelet integrin $\alpha_{IIb}\beta_3$ is the most abundant receptor on the platelet surface. There are about 80,000 receptors per unstimulated platelet (8). Fibrinogen binding to its platelet receptor requires platelet activation. Upon platelet activation of the integrin by an inside-out signal, the integrin changes its conformation from bent to extended, allowing it to bind to its ligand, fibrinogen. Once fibrinogen has been bound, its ability to crosslink receptors on different platelets results in aggregation (9-11). Additionally, ligand-occupied receptors undergo integrin outside-in signaling, allowing the receptor to interact with the actin cytoskeleton, causing the integrin with its bound ligand to centralize in the plane of the platelet membrane. Clearing occupied receptors from the peripheral regions of the platelet in an actin-myosin dependent

manner removes steric hindrance and makes additional unoccupied receptors available for fibrinogen binding (12-15). Importantly, outside-in signaling by platelet integrin $\alpha_{IIb}\beta_3$ plays an important role in clot retraction, in which a fibrin clot gradually pulls in upon itself, shrinking to a smaller volume after platelet activation and fibrin deposition are well underway (16, 17).

Previous studies have shown that fibrinogen-conjugated nanoparticles specifically bind onto surface-activated platelets around the granulomere (18-22). In suspension, most fibrinogen labels will bind to their platelet receptors, and move along the surface of the platelet to a final destination in the open canalicular system (15, 23-25). The migration of fibrinogen-conjugated nanoparticles to the interior of platelet aggregates is desirable for targeting in that it will allow the treatment to disrupt the entire volume of platelet aggregates or clot rather than only those platelets exposed on the surface of the clot. Also, the location of fibrinogen-conjugated nanoparticles at the center of clots is crucial for how nanoparticle-induced hyperthermia will affect both platelet structure and clot integrity. In our particular experiment, normal platelets in plasma were allowed to form clots before being exposed to fibrinogen-conjugated nanoparticles. We were interested in how specifically fibrinogen-conjugated nanoparticles interact with activated platelets in an existing platelet-rich clot such as would be found in arterial thrombi. The feasibility of using fibrinogen-conjugated nanoparticles needs to be evaluated under this simplified condition before we can apply this cell-targeting method *in vivo*.

Fibrin is the most abundant component of the arterial clot. It accounts for 43% of the total volume of the arterial clot. Fibrin is fibrous, non-globular protein and it is formed by the cleavage of fibrinogen by the protease thrombin, which causes it to polymerize. As a result, the polymerized fibrin traps platelets and RBCs and forms a clot (11, 26-29). In our experiment, thrombin enzymatic activity is sustained until samples are fixed, so it may convert both plasma

fibrinogen and fibrinogen-conjugated nanoparticles into fibrin. Because of the ability of fibrin to polymerize, it is possible for both plasma fibrin and fibrin-conjugated nanoparticles to become incorporated into the fibrin meshwork of the growing clot. The potential of highly localized targeting of fibrin could strengthen our power in disrupting a clot.

It has been assumed that RBCs play a largely passive role in thrombosis and hemostasis. However, now it has become apparent that RBCs have a variety of important functions and exert substantial impacts on hemostasis and thrombosis (7, 30, 31). Even though RBCs only account for 17% of arterial clot volume, RBCs still contribute to the bulk, structure, and potential occlusive behavior of the clot. Therefore, when using fibrinogen-conjugated nanoparticles to target arterial clots *in vivo*, we cannot neglect the possibility that RBCs might associate with fibrinogen-conjugated nanoparticles.

In fact, studies have shown that fibrinogen played an important role in RBC aggregation. In the 1960s, fibrinogen was identified as a cause of RBC aggregation (32, 33). In addition, elevating fibrinogen concentration resulted in an increase in RBC sedimentation rate and the clustering of red blood cells caused thrombosis and similar agglomerates (34-36). Fibrinogen-induced erythrocyte aggregation is considered to be caused by a combination of a nonspecific binding mechanism of fibrinogen to the erythrocyte membrane and a specific binding between fibrinogen and the erythrocyte membrane via an erythrocyte's integrin $\alpha_{IIb}\beta_3$ like-receptor and CD47 (integrin-associated protein) (30, 35, 37- 41).

Although studies showed the fibrinogen-erythrocyte interaction exists, they failed on further characterizing it. A study using atomic force microscopy reported that the fibrinogen-erythrocyte interaction is transient, and this transient interaction cannot lead to stable clot formation but is only able to increase erythrocyte aggregation (30). Under physiological

conditions *in vivo*, the applied shear forces can break clusters into single cells (42). This suggests that in high shear conditions in an artery, existing fibrinogen-erythrocyte interactions would be weak. Indeed, duration of the fibrinogen-erythrocyte bond is very short at only 0.04% of the duration of fibrinogen-platelet binding. Not only that, fibrinogen has low affinity for binding onto RBCs in comparison to platelets (30). Furthermore, it is possible that the fibrinogen-erythrocyte interaction can be lost and masked by the presence of abundant serum albumin. Albumin is known to have a capacity to bind to lipids, so it may bind to the erythrocyte phospholipid membrane, coating part of the erythrocyte surface and making the fibrinogen receptors on erythrocyte membrane less accessible for fibrinogen binding (43, 44). Also, there is variation in fibrinogen-erythrocyte interactions during cell aging. The fibrinogen-erythrocyte receptors progressively become non-functional as RBCs age due to the depletion of sialic acids, which is the principal source of negative charges on RBC membranes (39). In brief, even though fibrinogen-erythrocyte interactions exist, the strength and amount of the fibrinogen-erythrocyte interaction is still questionable.

Here, we will examine the interaction of fibrinogen-conjugated nanoparticles and RBCs that are already entangled by fibrin mesh and incorporated into RBC clots. We anticipated that fibrinogen-conjugated nanoparticles and RBC interactions would be rare events. Therefore, we expected to detect minimal number of nanoparticles found inside RBCs or bound onto the RBC membrane surface. Since our experiment occurred *in vitro* without any of the flow or shear found in physiological conditions such as arteries, any interactions between fibrinogen-conjugated nanoparticles and RBCs observed might be impossible *in vivo*.

Gold nanoparticles have a robust synthesis due to their ease of performance, high production yield, and stability (45, 46). Conjugation of proteins to gold nanoparticles is often

done by non-ionic adsorption, which is rapid, economical, and results in a protein-conjugated gold nanoparticle with high avidity. Also, most proteins can be conjugated onto gold nanoparticles by non-ionic adsorption and not lose their functionality (47-49). Additionally, it has been expected that coating magnetite nanoparticles with gold will still provide a surface for non-ionic protein adsorption similar to that of colloidal gold. Thus, gold nanoparticles have been not only commonly used for biological labeling but also are considered a standard model that can predict the functionalization of magnetic nanoparticles in targeting specific cell types, shown through their use with fibrinogen, and with antibodies targeting activated platelet and tumor cells, respectively (50, 51). Since synthesizing fibrinogen-conjugated, gold-coated magnetite nanoparticles (FGN-cAu-Fe_3O_4) is not a robust procedure, previous studies and we ourselves (1, 15, 19, 22, 52, 53) have routinely used the more robust fibrinogen-conjugated gold nanoparticle (FGN-cAu_{18}) model in light and electron microscopy to examine labeling and platelet physiology.

In this chapter, we will be comparing the interaction of FGN-cAu_{18} and FGN-cAu-Fe_3O_4 with clot components to confirm whether or not FGN-cAu_{18} and FGN-cAu-Fe_3O_4 share a common characteristics and functionalization in terms of targeting clots. Then, FGN-cAu_{18} will be used as representative model or the control to examine nanoparticle penetration, concentration, and disruption of clots in the next chapters.

We hypothesize that fibrinogen-conjugated nanoparticles will specifically bind onto activated platelets, may associate with the fibrin network, and will not interact significantly with RBCs. The results from these experiments will provide insight into whether using fibrinogen-conjugated nanoparticles can be developed into a safe *in vivo* treatment for ischemic stroke or not.

Materials and Methods:

Synthesis of colloidal gold nanoparticles (cAu_{18}):

Glassware used for gold synthesis was washed with 7X detergent (MP Biomedicals, Solon, OH) and rinsed extensively with distilled water (ddH_2O) and Millipore distilled deionized water (MDDW). 18nm gold (cAu_{18}) preparation was synthesized as described previously (20,54). Briefly, 4% gold (III) chloride [$HAuCl_4 \bullet 3H_2O$] (Sigma-Aldrich) was added to 0.2µm filtered MDDW in a round-bottom flask to a final concentration of 0.01%. Under the fume hood, a heating mantle was used to boil the reaction flask for 5 minutes. Then, fresh 0.2µm filtered 1% trisodium citrate dihydrate (Fisher Scientific, Pittsburgh, PA) was added directly into the boiling reaction mixture to a final concentration of 0.02%. The flask was swirled vigorously and continuously until the distinct red color was developed. The color changed from yellow to colorless, then black, blue, purple, and finally red in approximately 5 minutes. The reaction was then refluxed for 30 minutes. The mixture flask was allowed to cool to room temperature (RT), and stored at 4ºC. The average size of the cAu_{18} was read with a UV–visible spectrophotometry (DU800®, Beckman Coulter Inc) at 522nm.

Conjugation of fibrinogen to 18nm colloidal gold nanoparticles (FGN-cAu_{18}):

Fibrinogen was conjugated to cAu_{18} by non-ionic protein adsorption (15,19). An adsorption isotherm was performed to determine the optimal protein concentration to stabilize the colloidal gold. The minimum amount of fibrinogen required to prevent flocculation was 8µg/ml of the gold solution. Also, previous work showed that the optimum adsorption of fibrinogen onto gold nanoparticles occurs at or slightly basic to the isoelectric point of the protein, which was pH 6.5. First, the cAu_{18} was warmed to RT before the gold solution was

adjusted to pH 6.5 with 0.2N K_2CO_3 as measured by using a gel-filled electrode (Accumet®, Fisher Scientific). If the desired pH went too high, more 18nm colloidal gold solution was added. Next, human fibrinogen (plasminogen, von Willebrand factor and fibronectin depleted, Enzyme Research Laboratories, South Bend, IN) at twice the stabilizing concentration (16μg/ml) was incubated with the cAu_{18} for 5 minutes. Then, fresh 1% polyethylene glycol (PEG) (average MW 20,000, Sigma-Aldrich) was added to the reaction mixture at a final concentration of 0.004% as a stabilizing agent. The fibrinogen-conjugated cAu_{18} (FGN-cAu_{18}) nanoparticles were concentrated and excess protein was removed by centrifugation at 16,000 x g for 10 minutes. The supernatant was aspirated and the soft pellet was resuspended in Tyrode's buffer containing 0.1% bovine serum albumin (BSA) (15mM HEPES, pH 7.4, 3.3mM Na_2HPO_4, 138mM NaCl, 2.7mM KCl, 5.5mM glucose, 1mM $MgCl_2$, 1mg/mL BSA) at one-tenth the original nanoparticle volume. To roughly assess the cAu_{18} concentration of the preparation, the optical density was read at 522nm (OD_{522}) by using a UV–visible spectrophotometry. OD_{522} was adjusted between 0.2 and 1.0 for use in labeling experiments.

Synthesis of colloidal magnetite nanoparticles (cFe_3O_4):

Magnetite nanoparticles (cFe_3O_4) were synthesized by an aqueous alkaline coprecipitation method (55) with some modifications. Briefly, to remove all oxygen from the water, MDDW was heated to near boiling with a microwave before degassing the water under vacuum for a minimum of 1 hour with stirring at 60rpm and applied heat at 215°C. Degassed water was transferred into a 3-angle neck flask in the fume hood, with a stirring apparatus run by a variable-speed power drill in one port and an oxygen-free argon source introduced through another. Under argon, 5mL of a solution of 0.64M anhydrous $FeCl_3$ and 0.32M anhydrous

$FeCl_2$ (Sigma-Aldrich, St Louis, MO) in 0.4M HCl was added dropwise through the third port to 50mL of 1.5M NaOH in degassed water at 32°C-38°C with stirring. The colloid was allowed to precipitate, then was washed three times by centrifugation at 5000 x g for one minute and resuspended in degassed water. A last wash in 0.1M tetramethylammonium hydroxide (TMAOH) (Alfa Aesar, Ward Hill, MA) was processed in the same manner. Magnetite nanoparticles were size fractionated by centrifuging at 7000 x g for 5 minutes in 0.1M TMAOH. The suspended cFe_3O_4 particles were aged for exactly three days at 4°C before use in the gold coating procedure.

Preparation of gold-coated magnetite nanoparticles (cAu-Fe_3O_4):

After the cFe_3O_4 were aged for three days at 4°C in 0.1M TMAOH under argon atmosphere, gold growth on cFe_3O_4 was performed as previously reported (56). Under argon, cFe_3O_4 sol was diluted 100-fold in 0.00275% hydrazine hydrate (Sigma-Aldrich) in a total volume of 100mL using degassed water. Then, the total of 120µL of 4% aqueous $HAuCl_4 \cdot 3H_2O$ was added dropwise in 4 aliquots while mixing vigorously, resulting in a final concentration of 0.12mM Au^{3+}. The cAu-Fe_3O_4 were assessed by a UV–visible spectrophotometry and visually by the color of the resultant colloid. Blue sols were discarded, and successful products were red in color and stored under argon at RT. Successful colloid preparations were used within one week for labelling experiments.

Conjugation of fibrinogen to gold-coated magnetite nanoparticles (FGN-cAu-Fe_3O_4):

Fibrinogen was conjugated to cAu-Fe_3O_4 by non-ionic protein adsorption as described previously (15), with some modification. First, pH of the cAu-Fe_3O_4 was adjusted by adding 1M

4-(2-hydroxyethyl)-1-piperazineethanesulfonic acid (HEPES) (Acros, Fisher Scientific), pH 6.5, to a final concentration of 10mM. Then, cAu-Fe_3O_4 was incubated with fibrinogen at a final concentration of 16μg/mL for 5 minutes at RT. Next, 1% PEG was added to a final concentration of 0.004% to stabilize the nanoparticles. FGN-cAu-Fe_3O_4 nanoparticles were centrifuged to separate them from excess protein at 16,000 x g for 10 minutes. The supernatant was discarded, and the pellet was resuspended in Tyrode's buffer with 0.1% BSA. To roughly assess the concentration of FGN-cAu-Fe_3O_4 in the sol, the optical density was read at 522nm (OD_{522}) using a UV–visible spectrophotometry. OD_{522} was adjusted between 0.2 and 1.0 for use in labeling experiments.

Isolation of human platelets:

Whole blood (WB) was withdrawn from healthy donors in accordance with the University of Wisconsin-Milwaukee Institutional Review Board. WB was drawn by venipuncture of healthy donors currently not taking anticoagulant or antiplatelet drugs. Venous blood was anticoagulated with 3.8% sodium citrate. Then, the anticoagulated blood was centrifuged at 100 x g for 15 minutes at RT. The platelet-rich plasma (PRP) layer, was carefully transferred to polypropylene tubes. Relatively small amounts of PRP were left in the collection tubes to ensure no contamination by any WBCs and RBCs occurred. Then, the remainder was spun at 300 x g for 15 minutes to obtain platelet-poor plasma (PPP). During centrifugation, the PRP was applied to a 25mm x 90mm column of Sepharose CL-2B (Sigma-Aldrich, St. Louis, MO) that was equilibrated with Tyrode's buffer with 0.1% BSA to obtain gel-filtered platelets (GFPs). GFP count was adjusted to 150,000 cells per μL by diluting in autologous PPP (Figure

7). The isolated platelets were used within 2 hours of blood draw to ensure normal platelet functions were preserved.

Isolation of human red blood cells (RBCs):

The same procedure found above in the isolation of human platelets, through the obtaining of PPP step, was used. Briefly, WB was obtained from a healthy donor, citrated, and centrifuged at 100 x g for 15 minutes at RT. The supernatant was fully removed, including a small volume of RBCs to ensure complete removal of the buffy coat containing WBCs and a few platelets. The supernatant was centrifuged again at 300 x g for 15 minutes at RT to produce PPP. The packed RBCs were diluted with autologous PPP to bring the suspension back to its original volume of citrated WB (Figure 8).

Fibrin(ogen) and fibrinogen-conjugated nanoparticle interaction:

Human fibrinogen stock was diluted to 3mg/mL in 5mM NaCl. It was then supplemented with 2mM $CaCl_2$ and clotted with 1nM of human thrombin (Haematologic Technologies Inc., Essex Junction, VT) for 10 minutes at 37°C in a microcentrifuge tube. Then, FGN-cAu_{18} or FGN-cAu-Fe_3O_4 was added to a final nanoparticle-associated fibrinogen concentration of 96μg/mL. The clots were soaked in the labels for 15 minutes. Clot and supernatant were collected and prepared by scanning electron microscopy (SEM) and transmission electron microscopy (TEM) procedures.

Platelet and fibrinogen-conjugated nanoparticle interaction:

The procedure of examining the interaction of plasma proteins, platelets, and fibrinogen-conjugated nanoparticles was followed as for fibrin(ogen). First, 150,000 platelets per μL were supplemented with 2mM $CaCl_2$. Then, thrombin was added a final concentration of 1nM to stimulate the formation of the clot. After 10 minutes at 37°C, the sample was incubated with either FGN-cAu_{18} or FGN-cAu-Fe_3O_4 at a final nanoparticle-associated fibrinogen concentration of 96μg/mL for 15 minutes at 37°C. Again, supernatant and clots were obtained and processed by SEM and TEM procedures.

Red blood cell and fibrinogen-conjugated nanoparticle interaction:

The RBCs were processed as for fibrin and platelets. Briefly, $CaCl_2$ and thrombin were added into RBCs in PPP at the final concentrations of 2mM and 1nM, respectively, to stimulate RBC clot formation for 10 minutes at 37°C. The sample was labeled with FGN-cAu_{18} or FGN-cAu-Fe_3O_4, to a final nanoparticle-associated fibrinogen concentration of 96μg/mL, for 15 minutes at 37°C. Then, both supernatant and clot were collected, followed by SEM and TEM preparation.

Scanning electron microscopy (SEM) standard preparation for supernatant samples:

SEM preparation was followed as described previously (1) with some modifications. Supernatants were diluted 1:20 in 1% glutaraldehyde (Ted Pella, Inc.) in 0.1M HEPES, pH 7.4 and fixed for 30 minutes at RT. After 30 minutes primary fixation, samples were collected on Whatman® Nuclepore™ Track-Etched Membranes with 13mm diameter and 0.4μm pore size using 5cc syringes attached to 13mm MilliporeSigma™ Swinnex™ filter holders. Then, the

membranes were washed 3 times with 0.1M HEPES, pH 7.4, for 10-15 minutes and followed by post-fixation with 0.05% OsO_4 (Ted Pella, Inc.) in HEPES for 30 minutes at RT. The membranes were washed with distilled deionized water before transfer into a critical point dry holder and processed by dehydration in a graded ethanol series for 10-15 minutes incrementally beginning with 25%, then 50%, 70%, 80%, 85%, 90%, 95%, twice with 100%, and once with 100% ethanol over type 3A molecular sieves (Grace Davison, Columbia, MD). The samples were dried in a Balzer CPD 020 unit, using sieve-dried 100% ethanol as the intermediate fluid and liquid carbon dioxide (CO_2) as the transitional fluid. After critical point drying, samples were affixed to 13mm Cambridge stubs by carbon conductive double-sided adhesive tabs (Lift-N-Press ™, Ted Pella, Inc.). Conductive isopropanol-based graphite paint (Pelco®, Ted Pella, Inc.) was applied around the edges of the stubs and allowed fully to dry before the samples were coated with carbon in an Edwards E306A thermal evaporation coating system. Analysis was performed on a Hitachi S-4800 FE-SEM scanning electron microscope using 2-3kV accelerating voltage for secondary electron (SE) imaging and 15kV accelerating voltage for backscattered electron (BE) imaging.

Scanning electron microscopy (SEM) standard preparation for clots:

SEM preparation of clots was similar to supernatant SEM preparation with a few modifications. The clots were fixed in 1% glutaraldehyde in 0.1M HEPES for 2 hours at RT, followed by fresh 1% glutaraldehyde with 1% tannic acid in 0.1M HEPES, pH of 7.4, overnight at 4°C. Clots were washed 3 times with 0.1M HEPES, pH 7.4, for 10-15 minutes followed by post-fixation with 0.05% OsO_4 for 2 hours at RT. The clots were then washed with distilled deionized water before being transferred into the critical point drier holder and dehydrated in a graded ethanol series for an hour at each increment (25%, 50%, 70%, 80%, 85%, 90%, 95%,

twice with 100%, and once with 100% EtOH stored over type 3A molecular sieves). The clots were dried by the above procedure in a Balzer CPD 020 unit. The clots were mounted onto 13mm Cambridge stubs with 2 Ton® clear medium cure water-resistant adhesive epoxy (Devcon®). The epoxy was cured overnight, and the clots were secured onto the stubs. Clots were then fractured in half using new stainless-steel GEM® razor blades. The samples were coated using the Edwards E306A thermal evaporation coating system, with carbon fiber as the source. The samples were examined with a Hitachi S-4800 FESEM. The backscattered images were taken at 15kV accelerating voltage between 200X and 2000X magnification. The 200X magnification images were montaged using Adobe® Photoshop® CC version 14.1.2 x 32 to generate 2D images of entire clot sections.

Transmission electron microscopy standard preparation for clots or supernatants:

After primary fixation in 1% glutaraldehyde with 1% tannic acid in 0.1M HEPES pH 7.4, supernatants were centrifuged at 16,000 x g to pellet fibrin strands, platelets, or the RBCs that were not incorporated into clots. Then, the supernatants were discarded. A drop of molten 2% agar (Difco®, Bacto® Agar, Detroit, Michigan, USA) in 0.1M HEPES pH 7.4 was added into each pellet, mixed well, and allowed to solidify. These pellets were prepared for TEM in parallel with the fixed clots. Pellets and clots were washed 3 times with 0.1M HEPES, pH 7.4, for 10-15 minutes, followed by post-fixation with 0.05% OsO_4 in 0.1M HEPES, pH 7.4, at RT for 2 hours. The samples were then washed using distilled deionized water 3 times for 10-15 minutes each before staining with 1% uranyl acetate for 2 hours. Samples were dehydrated in a graded ethanol series for at least 1 hour at each increment (25%, 50%, 70%, 80%, 85%, 90%, 95%, and two times 100%), followed by two changes of propylene oxide (Electron Microscopy Sciences®) for

one hour each. The samples were infiltrated and embedded in low viscosity Quetol-Spurr's resin (Electron Microscopy Sciences®) (57). The samples were cured for 72 hours at 60°C. Semi-thin (~30-50μm) sections were cut using an RMC MT-7000 ultramicrotome. The sections were picked up on 12mm diameter round glass coverslips (Fisherbrand®, Fisher Scientific) and affixed onto 13mm Cambridge stubs using conductive carbon tapes (Ted Pella, Inc.). Conductive isopropanol-based graphite paint was applied around the edges of the stubs and allowed to fully dry before the samples were coated with carbon using an Edwards E306A compact thermal evaporation coating system. Sections were examined between 5kV and 7kV accelerating voltage in ExB backscattered mode using a Hitachi S-4800 FE-SEM.

Results:

Previous work has shown fibrinogen conjugated-gold nanoparticles, including both FGN-cAu_{18} and FGN-cAu-Fe_3O_4, associating specifically with activated platelets in a purified platelet system. However, PRP and WB systems appear more complex not only in structural organization but also in cell components. Besides activated platelets, PRP and WB clots contain an additional large amount of fibrin(ogen) and fibrin(ogen) plus RBCs, respectively (Figure 9,10). This might affect the specificity of fibrinogen-conjugated nanoparticle targeting, and the ability of the nanoparticles to interact with activated platelets. Thus, examining the interaction of fibrinogen-conjugated nanoparticles with other clot components, such as fibrin(ogen) and RBCs, allowed us to characterize the specificity of their binding to clot components and determine the extent of their off-target nanoparticle associations.

To examine the potential interactions between fibrinogen-conjugated nanoparticles and fibrin, plasma platelets, or RBCs, these experiments were done three times with three different donors of platelets and RBCs. Commercial purified human fibrinogen was used.

Fibrin(ogen) and fibrinogen-conjugated nanoparticle interaction:

Fibrin clots were formed by stimulating 3mg/mL fibrinogen with 1nM thrombin, followed by labelling with FGN-cAu_{18} or FGN-cAu-Fe_3O_4. The clots formed were relatively small in size and pink colored after the labeling step. Many small pink fibrin strands remained suspended in the supernatant. Pink color indicated that FGN-cAu_{18} or FGN-cAu-Fe_3O_4 interacted strongly with the fibrin(ogen). Since both fibrin clots and supernatant visually looked pink, we concluded that FGN-cAu_{18} or FGN-cAu-Fe_3O_4 was present in the fibrin clots and associated with suspended fibrin(ogen) strands. As expected, secondary electron images (SEI) of the suspended fibrin strands remaining after clot formation were observed as long fibers. Also, many FGN-cAu_{18} nanoparticles were bound onto fibrin strands. Under backscattered electron imaging (BEI), the signal from FGN-cAu_{18} was strongly detected and appeared brightly throughout the samples (Figure 11). In findings consistent with the observations of remaining supernatant from FGN-cAu_{18} labeled fibrin clots, samples of remaining supernatant from fibrin clots labeled with FGN-cAu-Fe_3O_4 nanoparticles also showed a strong interaction between fibrin and FGN-cAu-Fe_3O_4 nanoparticles. Again, FGN-cAu-Fe_3O_4 nanoparticles were found throughout the fibrin network (Figure 12). The only minor difference between FGN-cAu_{18} nanoparticles and FGN-cAu-Fe_3O_4 nanoparticles was that FGN-cAu-Fe_3O_4 nanoparticles appeared less bright in comparison to FGN-cAu_{18} nanoparticles when using BEI images. This is due to the lower atomic number of magnetite as compared to gold-79.

Observation of fixed medial sections of fibrin clots labeled with either FGN-cAu_{18} or FGN-cAu-Fe_3O_4 nanoparticles showed that both types of nanoparticles were able to penetrate successfully from the outside of the clot to its interior. Furthermore, high nanoparticle concentrations were found both inside and outside the fibrin clots (Figure 13, 14).

Observation from cross-sections of FGN-cAu_{18} and FGN-cAu-Fe_3O_4 labeled fibrin clots and the remaining supernatant allowed us to clearly visualize the association between the nanoparticles and fibrin strands (Figure 15, 16). Many fibrinogen-conjugated nanoparticles were found clustered together and bound to fibrin strands. They were also found between fibrin strands, and at the junctions between fibrin strands. Moreover, significantly high concentrations of fibrinogen-conjugated nanoparticles were found not only in the fibrin clot but also throughout the supernatant remaining over the clot.

These experiments showed that FGN-cAu_{18} and FGN-cAu-Fe_3O_4 share similar characteristics when they interact with fibrin. First, both types of fibrinogen-conjugated nanoparticles interacted strongly with fibrin strands. Secondly, it appeared that fibrinogen-conjugated nanoparticles had the ability to penetrate deep into the interior of fibrin clots. Lastly, significantly high concentrations of fibrinogen-conjugated nanoparticles were found at the periphery and interior of fibrin clots.

Platelet, plasma fibrinogen, and fibrinogen-conjugated nanoparticle interaction:

When GFPs in autologous PPP were stimulated with 1nM thrombin, the activated platelets and fibrin interacted with each other to form GFP clots. Also, some small platelet aggregates formed that did not associate with GFP clots, instead remaining suspended in the plasma. After thrombin treatment, samples were labelled with FGN-cAu_{18} or FGN-cAu-Fe_3O_4.

Platelet aggregates looked pink when collected on the Nuclepore membrane, whereas GFP clots appeared wrapped around by pink webbing. Upon SEM analysis, the platelet aggregates, even though they were not included into the clot, were still heavily labeled with FGN-cAu_{18} or FGN-cAu-Fe_3O_4 (Figure 17, 19). This accounted for the pink color observed on the Nuclepore filter membrane when the platelet aggregates were collected. Likewise, SEM analysis of GFP clots showed the fibrinogen-conjugated nanoparticles bound to the clot periphery (Figure 21, 22), accounting for the pink webbing observed wrapped around the clot.

As we expected, we observed similar results with platelet aggregates labeled with FGN-cAu_{18} or FGN-cAu-Fe_3O_4. From SEI images, labels were observed at the surface of the activated platelets, and at platelet-platelet junctions. Additionally, bright signals were detected from nanoparticles inside the activated platelets, as seen in the BEI images (Figure 17, 19). Notably, cross-section images showed that FGN-cAu_{18} and FGN-cAu-Fe_3O_4 localized in the center of activated platelets at remarkably high concentrations compared to the nanoparticle concentration found at the periphery of platelet aggregates (Figure 18, 20).

The montage assembled of medial GFP clot sections labelled with FGN-cAu_{18} and FGN-cAu-Fe_3O_4 nanoparticles showed similar results. It appeared that nanoparticles were able to penetrate deep inside of the GFP clots, although a higher concentration of nanoparticles was found near the periphery. While lower nanoparticle concentration was observed at the interior of the clots, the labels were scattered throughout the entirety of clot and many small nanoparticle clutters were observed (Figure 21, 22). In comparison with the fibrin clot labeled with fibrinogen-conjugated nanoparticles, higher amounts of nanoparticles were incorporated into the fibrin clot than into the GFP clot.

Cross-section images of GFP clots showed that both FGN-cAu_{18} and FGN-cAu-Fe_3O_4 were able to penetrate deep into the interior of GFP clots. Nanoparticles slightly interacted with activated platelets within the GFP clots, as cross-section images of the clots reveal (Figure 23, 24). However, nanoparticle concentration within GFP clots was relatively low compared to nanoparticle concentration found within fibrin clots.

In brief, these results provided several important insights relating to platelet and nanoparticle interaction. First, FGN-cAu_{18} and FGN-cAu-Fe_3O_4 interacted with platelets similarly. Second, nanoparticles specifically interacted with activated platelets. Third, nanoparticles had an ability to penetrate both platelet clots and platelet aggregates. Fourth, there were higher concentrations of nanoparticles interacting with platelets in aggregates not associated with clots (in the supernatant over the clot) than with activated platelets found inside of platelet clots.

RBCs and fibrinogen-conjugated nanoparticles interaction:

When RBCs suspended in PPP were stimulated with 1nM thrombin, clots and supernatants formed and were labelled with either FGN-cAu_{18} or FGN-cAu-Fe_3O_4. Results from the samples collected did not differ between FGN-cAu_{18} and FGN-cAu-Fe_3O_4 labels.

From the supernatant, we found either a very minimal number of or no nanoparticles associated with RBCs. Some nanoparticles were found on the surface of the RBCs, but they did not specifically bind to RBCs. Instead, FGN-cAu_{18} strongly interacted with the fibrin strands present (Figure 25, 26).

RBC clots visually appeared to be the largest clots among RBC, GFP, and fibrin clots. RBC clots mainly contained RBCs wrapped around with fibrin strands (Figure 27, 28). Low

nanoparticle concentration was found both at the periphery and interior of the RBC clots. It appeared that nanoparticles were limited to the outside edge of RBC clots and were unable to penetrate deep into the interior of the clot. Therefore, minimal amounts of the label were found at the center of RBC clots. Even though a few nanoparticles were present in RBC clots, those nanoparticles interacted with fibrin strands rather than RBCs.

Cross-sections of RBC clots labeled with FGN-cAu_{18} and FGN-Fe_3O_4 showed that labels specifically associated with fibrin strands and not RBCs. Also, nanoparticles were able to penetrate into RBC clots. Moreover, nanoparticles were scattered throughout the RBC clots at low concentrations and only incorporated with the fibrin network. Again, no nanoparticles were found at the site of RBCs (Figure 29, 30).

Cross-sections of RBCs remaining in the supernatant labeled with either FGN-cAu_{18} or FGN-Fe_3O_4 showed no nanoparticles in supernatant samples. There was absolutely no interaction between nanoparticles and RBCs in the supernatant since no nanoparticles bound onto RBCs and no nanoparticles localized inside RBCs (Figure 29,30).

Overall, FGN-cAu_{18} and FGN-cAu-Fe_3O_4 bound specifically to fibrin and not RBCs. FGN-cAu_{18} and FGN-cAu-Fe_3O_4 had the ability to penetrate into RBC clots via their interaction with fibrin strands. Although FGN-cAu_{18} and FGN-cAu-Fe_3O_4 were found within RBC clots, there were very limited amounts of label occurring in both the periphery and interior of RBC clots.

Discussion:

Previous studies have shown fibrinogen-conjugated nanoparticles specifically target the activated platelets in a purified platelet system (1). However, PRP and WB systems are more

complex in terms of both protein and cell components, and are more representative of the physiological system. Thus, examining the specificity and the potential extent of off-target fibrinogen-conjugated nanoparticle association with clot components such as fibrin, platelets and RBCs in plasma provided meaningful information about the feasibility of using fibrinogen-conjugated nanoparticles to treat ischemic stroke *in vivo*. First, the interaction between fibrinogen-conjugated nanoparticles and activated platelets in plasma, even after clotting occurred, was confirmed. Fibrinogen-conjugated nanoparticles were able to penetrate the platelet-rich GFP clots, where they specifically bound onto activated platelets, were found at platelet-platelet junctions, and were primarily localized in the interior of the activated platelets. Second, fibrinogen-conjugated nanoparticles strongly interacted with fibrin. A significantly high FGN-cAu_{18} or FGN-cAu-Fe_3O_4 concentration was observed both in fibrin clots and fibrin strands taken from the supernatant over clots. Additionally, the association of FGN-cAu_{18} or FGN-cAu-Fe_3O_4 with fibrin strands outweighed their association with activated platelets and RBCs. Thus, *in vivo* fibrin can compete with activated platelets as label targets. However, if binding were highly localized, fibrin could serve as a very attractive additional target of fibrinogen-conjugated nanoparticles. Since arterial clots contain both fibrin and activated platelets as their main components, having an extra target could be an advantage of this method over tPA in treating ischemic stroke. Third, RBCs displayed no interaction with fibrinogen-conjugated nanoparticles. When RBC clots or their supernatants were labeled with either FGN-cAu_{18} or FGN-cAu-Fe_3O_4, there was no binding or penetrating of the labels into RBC samples. This suggests that using FGN-conjugated nanoparticles for cell targeting is specific enough that it may be safe enough for *in vivo* use. Fourth, FGN-cAu_{18} and FGN-cAu-Fe_3O_4 behaved similarly in terms of interacting with clot components. FGN-cAu_{18} is a robust synthesis; whereas, FGN-cAu-Fe_3O_4 is a more

variable procedure. Thus, these results confirm that FGN-cAu$_{18}$ can be a representative model for FGN-cAu-Fe$_3$O$_4$ in term of studying the penetration of nanoparticles into clots.

Fibrinogen-conjugated nanoparticles target activated platelets:

When platelets were activated by thrombin and then labeled with fibrinogen-conjugated nanoparticles, the nanoparticles bound to the activated platelets tightly and display a well characterized labeling pattern. In the supernatant samples, labeling occurred on the surface of aggregated platelets, at platelet-platelet junctions, and inside platelets. High amounts of label accumulated especially at the center of activated platelets within the open canalicular system. These events can be explained by the regulation of integrin $\alpha_{IIb}\beta_3$ in platelets (8,58). Upon platelet activation due to the stimulation of soluble agonist-thrombin, the inside-out signal results in the activation of integrin $\alpha_{IIb}\beta_3$ with high affinity, allowing it to bind to its ligand fibrinogen. Once fibrinogen has bound, its ability to crosslink receptors on different platelets results in aggregation (8-11,59). Additionally, ligand-occupied receptors undergo integrin outside-in signaling for the receptor to interact with the actin cytoskeleton, causing integrin with bound ligand to centralize on the platelet membrane plane and move along the underlying actin cytoskeleton (12-15). As a result, fibrinogen-conjugated nanoparticles were observed most significantly at the center of platelet aggregates rather than at the periphery. Furthermore, we expected that fibrinogen-conjugated nanoparticles would have the ability to penetrate and effectively incorporate into existing platelet clots. However, as we observed, labeling was somewhat scattered throughout the cross-section of the clot. This result could be due to a few reasons. First, labeling time with FGN-cAu$_{18}$ or FGN-cAu-Fe$_3$O$_4$ for both clots and supernatant were only 15 minutes. Second, platelet-rich clots were relatively bigger in size and volume in

comparison to platelet aggregates. Thus, 15 minutes of labeling might only be sufficient for nanoparticles to migrate into moderately sized platelet aggregates, but not large platelet-rich clots. Therefore, in order to experience a higher concentration of nanoparticles inside of platelet-rich GFP clots, longer labeling time might be required. In the present study, we focused on examining the interaction between fibrinogen-conjugated nanoparticles and various components of clots, not optimizing label conditions. We feel that using 15 minutes of incubation with the label was sufficient to address these interactions between platelets. Here, we confirmed that fibrinogen-conjugated nanoparticles specifically interacted with platelet aggregates and had the ability to penetrate into platelet-rich clots.

Fibrinogen-conjugated nanoparticles do not associate with RBCs:

Throughout all RBC samples labeled with either FGN-cAu_{18} or FGN-cAu-Fe_3O_4, the presence of nanoparticles either inside of RBC clots or in supernatants appeared insignificant and virtually undetectable. Also, no nanoparticles were found in the interior of the RBCs. Although a few labels were found, the labels tended to associate with fibrin strands rather than RBCs.

The lack of fibrinogen-conjugated nanoparticle interaction with RBCs could be due to several factors. First, the fibrinogen-conjugated nanoparticles might have a low affinity for binding onto the RBC membrane via an integrin $\alpha_{IIb}\beta_3$ like receptor. In fact, it has been reported that the interaction between fibrinogen and an unknown receptor on the RBC membrane has a lower affinity for binding compared to the platelet receptor (30). This could have influenced how well the fibrinogen-conjugated nanoparticles bound to RBCs. Second, the fibrinogen-erythrocyte interaction is transient. As a result, disruption of the interaction between fibrinogen and RBCs could be expected. It has shown that even though there is a specific fibrinogen-erythrocyte

interaction, the fibrinogen-erythrocyte bond is only 0.04% the lifetime of fibrinogen-platelet binding (30,39). That may explain why the binding of fibrinogen-conjugated nanoparticles onto RBCs seemed a rare event. Third, fewer receptors for fibrinogen exist on the RBCs surface (31), together with interference from the fibrin network that wrapped around the outside of clotted RBCs, could mask fibrinogen from binding to its erythrocyte receptor. As a result, the chance of fibrinogen-conjugated nanoparticles associating with RBCs trapped inside of the clot was limited. Therefore, we observed the label associating mostly with fibrin instead of RBCs. Fourth, a previous study showed that a decrease in fibrinogen-erythrocyte interaction occurred because of RBC aging (39). Knowing that, newer RBCs might bind more to fibrinogen. This is likely to be only a minor factor in explaining low fibrinogen-conjugated nanoparticle-erythrocyte interaction occurring in our experiments, as we used fresh blood samples that are expected to have a normal distribution of ages of RBCs. If we combine all the factors listed above, we can reasonably conclude that fibrinogen-conjugated nanoparticles do not interact, or have only very minimal interaction, with RBCs.

Fibrinogen-conjugated nanoparticles strongly associate with fibrin(ogen):

We observed a significant association of fibrinogen-conjugated nanoparticles with both fibrin clots and fibrin strands in the clot supernatants. The results matched our expectations. The mechanism of fibrin(ogen)-fibrin interaction is well defined. Thrombin cleaves fibrinopeptides from the fibrinogen molecule to create fibrin monomers. The cleavage of fibrinopeptides allows "knob-hole" interaction between fibrin monomers, causing the fibrin monomers to polymerize and form protofibrils which aggregate laterally to make fibers. Branching, both longitudinal and lateral growth of fibers, leads to a three-dimensional gel network or formation of a fibrin clot

(10,28,60,61). Using that knowledge could help to explain our experiments' results. When thrombin was introduced to stimulate the formation of the fibrin clot, plasma fibrinogen was converted into fibrin. Similarly, fibrinogen-conjugated nanoparticles might be converted to fibrin-conjugated nanoparticles. Because of the ability of the interaction to form fibrin networks via polymerization of monomers and fibers, the interaction of plasma fibrin and fibrin-conjugated nanoparticles might also occur. Therefore, we observed the presence of labels throughout fibrin clots and supernatant at significant concentrations. Additionally, since in this experiment we formed the clot with one component, plasma fibrin, the fibrin clot was smaller in volume and less complex in structural components and organization. Thus, it could have allowed for maximal interaction of fibrinogen-conjugated nanoparticles and fibrin, causing nanoparticles to penetrate into fibrin clots or associate with fibrin strands in the supernatant. The results of fibrinogen-conjugated nanoparticles and fibrin interactions suggested when using fibrinogen-conjugated nanoparticles to target clots *in vivo*, the association of fibrinogen-conjugated nanoparticles with fibrin is unavoidable.

Expected *in vivo* application:

These results suggest that fibrinogen-conjugated nanoparticles can interact strongly with activated platelets in an existing clot. Thus, targeting platelets for magnetically-induced hyperthermia as a treatment for ischemic stroke could be a viable option. However, these results also revealed that fibrinogen-conjugated nanoparticles strongly interact with fibrin strands. Thus, fibrin seems to be a competitor of activated platelets for binding with fibrinogen-conjugated nanoparticles. While we originally proposed specifically targeting activated platelets in occlusive thrombi, having an additional target in fibrin might strengthen our power to disrupt clots. If

binding of the fibrinogen-conjugated nanoparticles was limited to the area of the occlusion, fibrin could be another potential site-specific target to treat ischemic stroke. Because arterial clots are mainly composed of fibrin and activated platelets (4-7, 62, 63), fibrinogen-conjugated nanoparticles could bind to both protein and cellular components, strengthening our targeting strategy. Since nanoparticle binding to fibrin is dependent on clot formation, this could work synergistically with activated platelet binding as a treatment for ischemic stroke. Additionally, these results demonstrated that there was no interaction between fibrinogen-conjugated nanoparticles and RBCs. RBCs contribute to the bulk and the occlusive potential of a clot. Hence, our method could have a minimal amount of extended off-targeting and provide a safe treatment for ischemic stroke when performed *in vivo*.

Figures and Figure Legends:

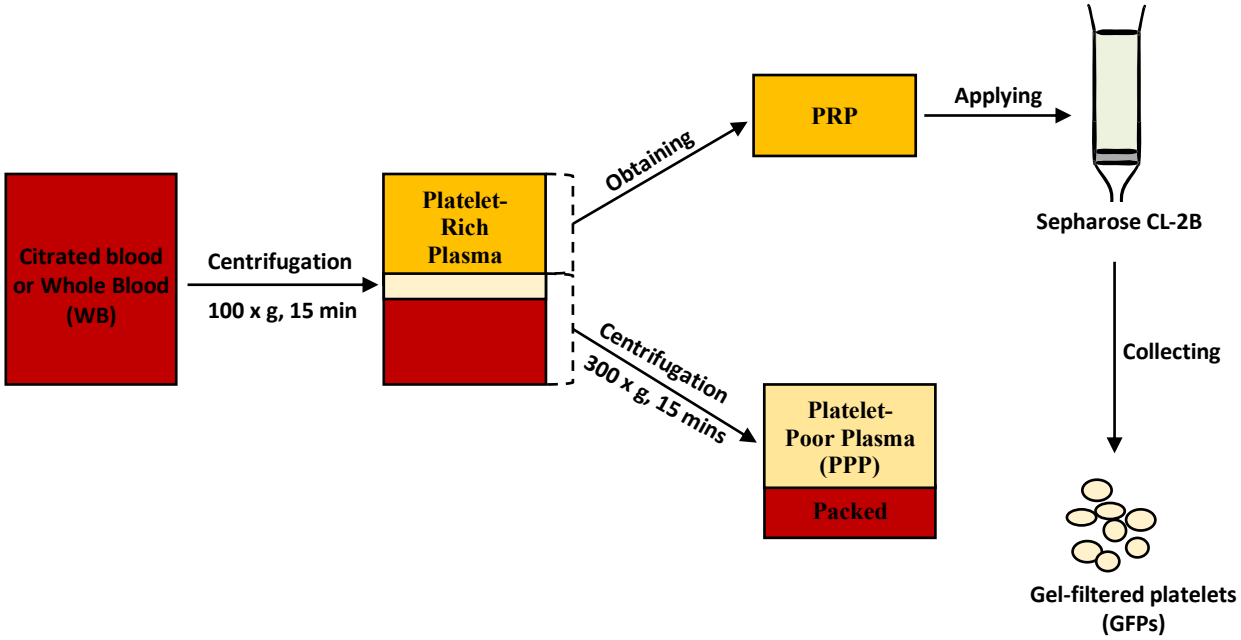

Figure 7. Schematic flow chart of isolation of human platelets. Whole blood (WB) was drawn from a healthy donor and anticoagulated with 3.8% sodium citrate. Citrated blood was centrifuged at 100 x g for 15 minutes to obtain platelet-rich plasma (PRP). To isolate purified platelets (gel-filtered platelets, GFPs), PRP was applied to a Sepharose CL-2B column. GFPs were adjusted to 150,000 platelets per µL by dilution in platelet-poor plasma (PPP), which was collected by centrifuging the sample remaining after PRP was collected at 300 x g for 15 minutes.

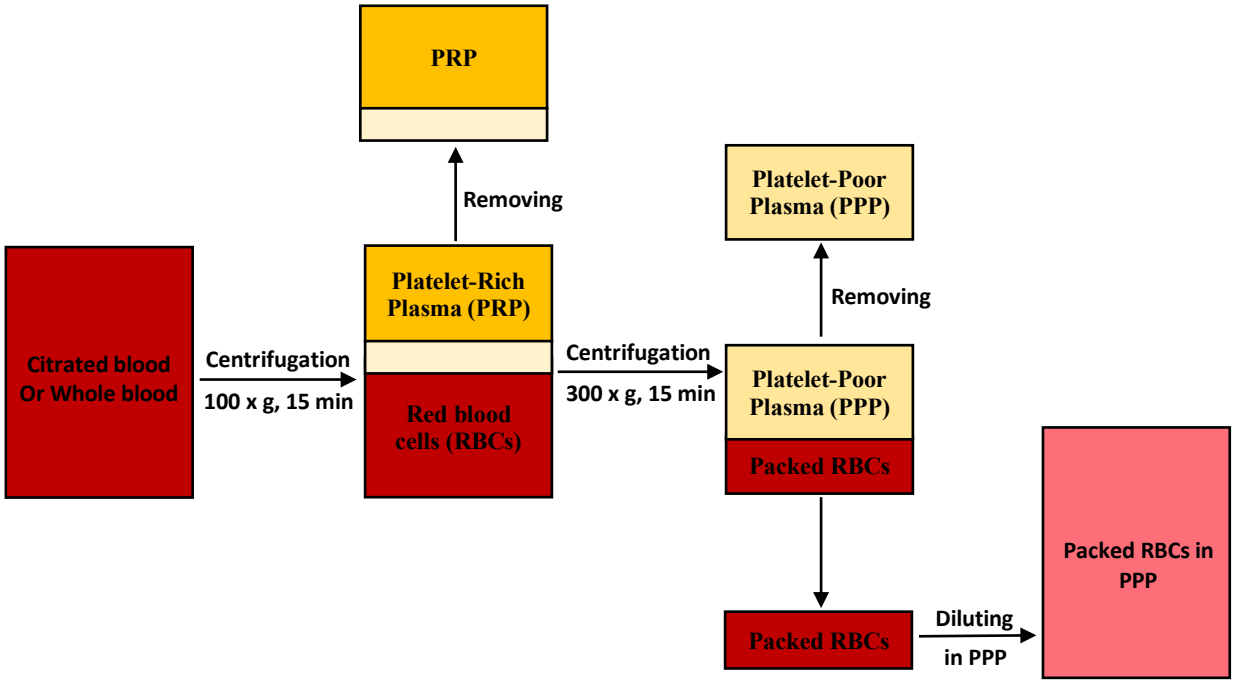

Figure 8. Schematic flow chart of isolation of human red blood cells. Citrated blood was centrifuged twice: first at 100 x g for 15 minutes, then at 300 x g for 15 minutes to remove all PRP, WBCs, and PPP from packed RBCs. Then, packed RBCs were resuspended in PPP back to the original volume of citrated blood in the first step.

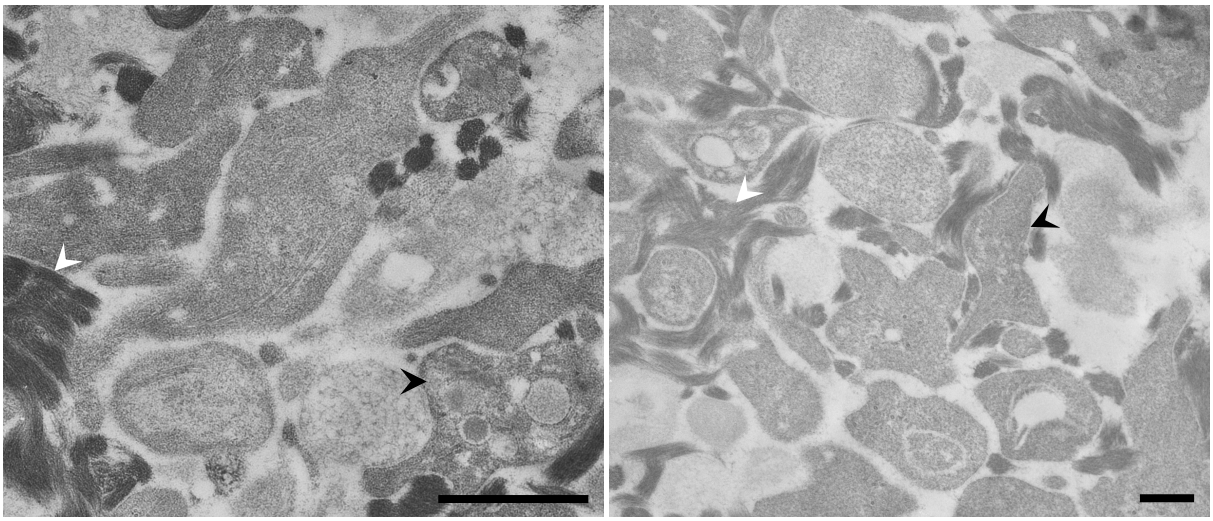

Figure 9. TEM micrographs of PRP clot cross sections. Many fibrin strands and activated platelets were present throughout PRP clots. White and black arrows indicate fibrin and platelets, respectively. Scale bars equal 1μm.

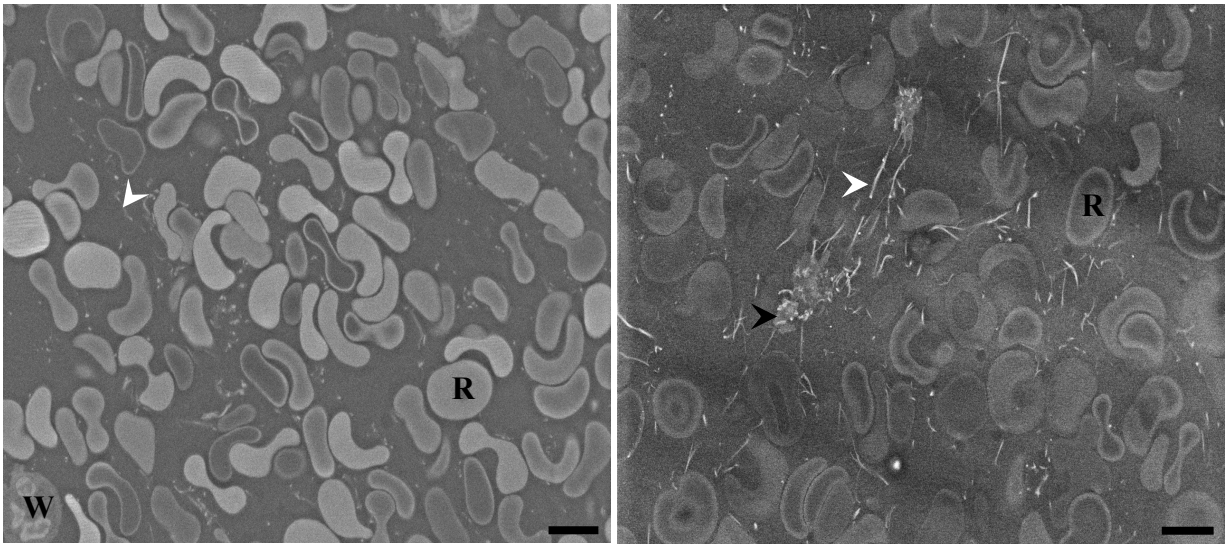

Figure 10. SEM micrographs of WB clot cross sections. Few WBCs and activated platelets were observed in the WB clots. Many RBCs were trapped by fibrin strands. White and black arrows indicate fibrin and platelets respectively. R and W indicate RBCs and WBCs, respectively. Size bars equal 5μm.

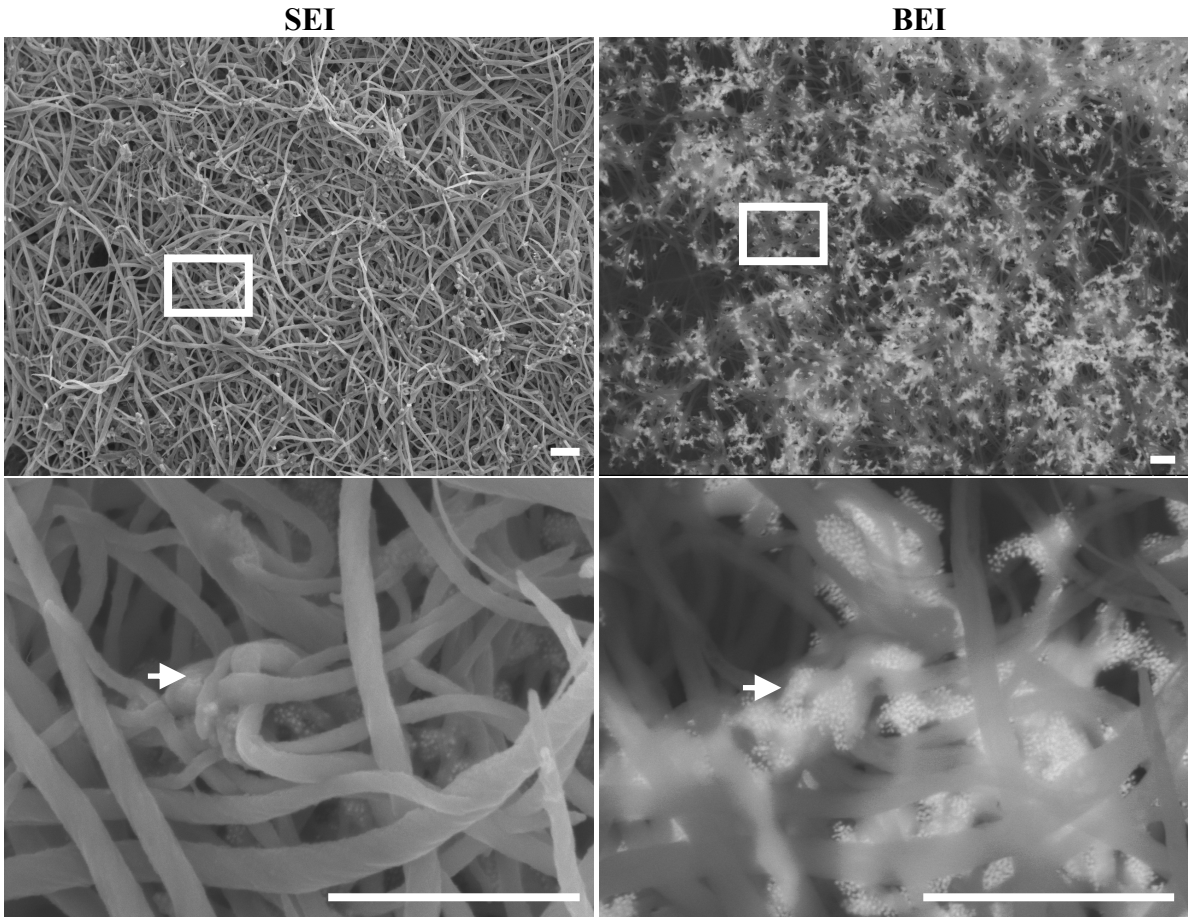

Figure 11. SEM micrographs of the supernatant remaining over a fibrin clot labelled with FGN-cAu_{18} nanoparticles. FGN-cAu_{18} nanoparticles strongly interacted with fibrin(ogen) strands. Low magnification images appear on the top row and high magnification of the areas indicated in the boxes are shown in the bottom row. Secondary electron images (SEI) are the left column and backscattered electron images (BEI) form the right column. White arrows indicate the presence of FGN-cAu_{18}. Size bars equal 1μm.

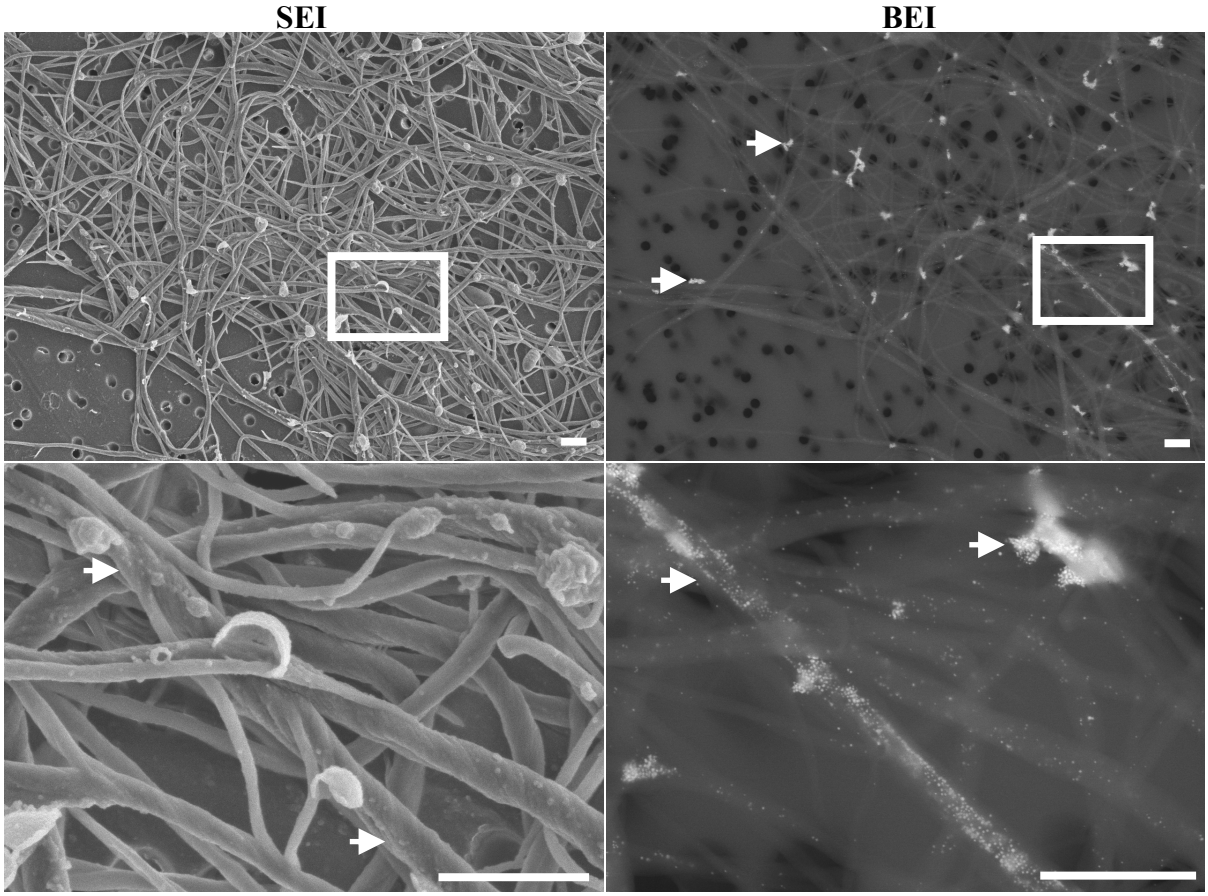

Figure 12. SEM micrographs of the supernatant remaining over a fibrin clot labelled with FGN-cAu-Fe_3O_4 nanoparticles. In SEI, long fibrin strands connected together to form a fibrin network, and many FGN-cAu-Fe_3O_4 nanoparticles bound to fibrin strands, giving a bumpy appearance. Under BEI, FGN-cAu-Fe_3O_4 nanoparticles resolved as small bright spots found throughout the sample. High numbers of FGN-cAu-Fe_3O_4 nanoparticles associated with fibrin strands. Low magnification images are on the top row and high magnification of the areas indicated in the boxes are in bottom row. White arrows indicate the presence of FGN-cAu_{18}-Fe_3O_4. Size bars equal 1μm.

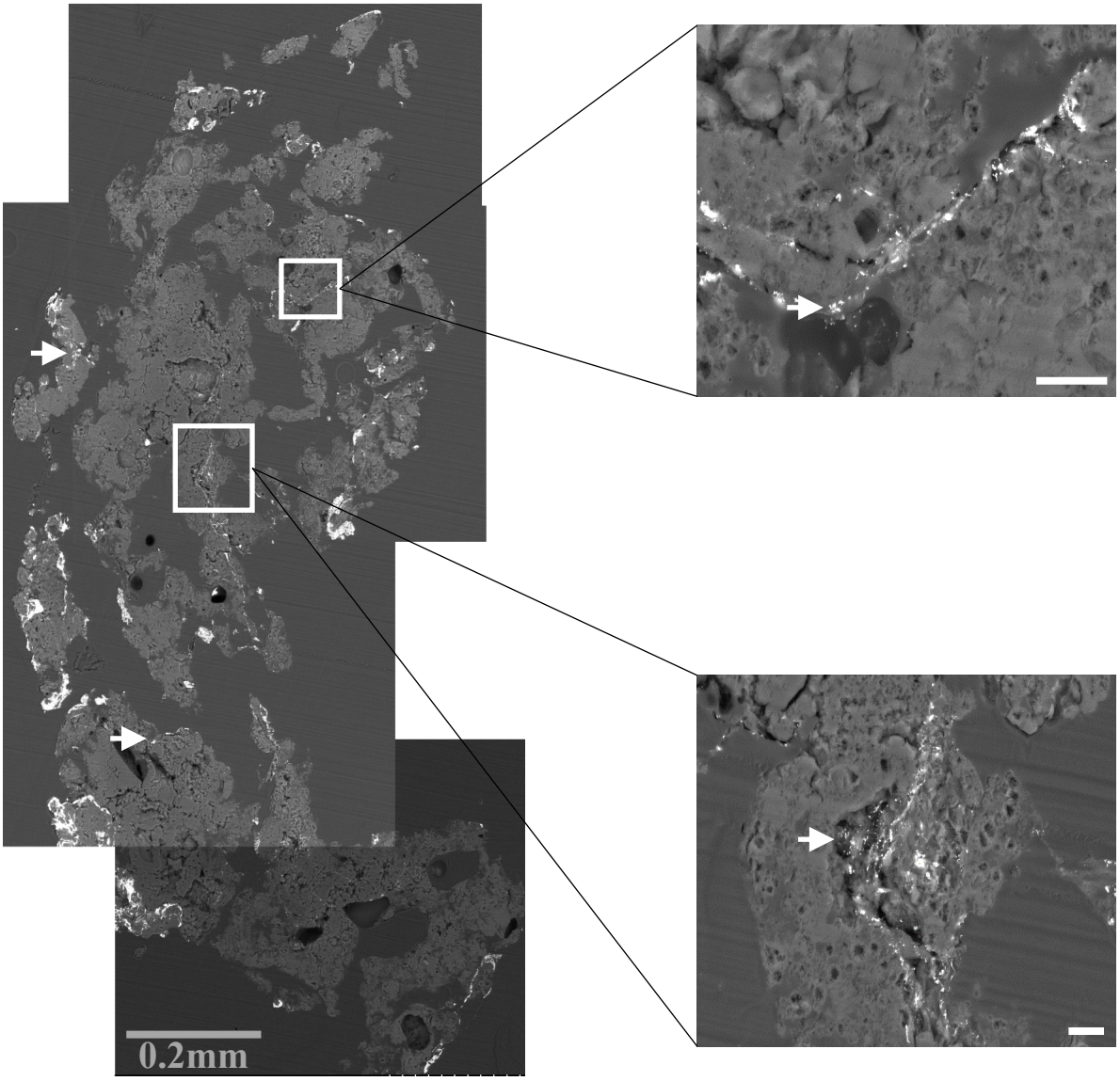

Figure 13. Montage of medial fibrin clot section labeled with FGN-cAu$_{18}$. FGN-cAu$_{18}$ nanoparticles penetrated throughout the fibrin clot from the periphery to the interior. White boxes indicate the areas shown at higher magnification. White arrows indicated representative FGN-cAu$_{18}$ nanoparticles. White size bars equal 10μm.

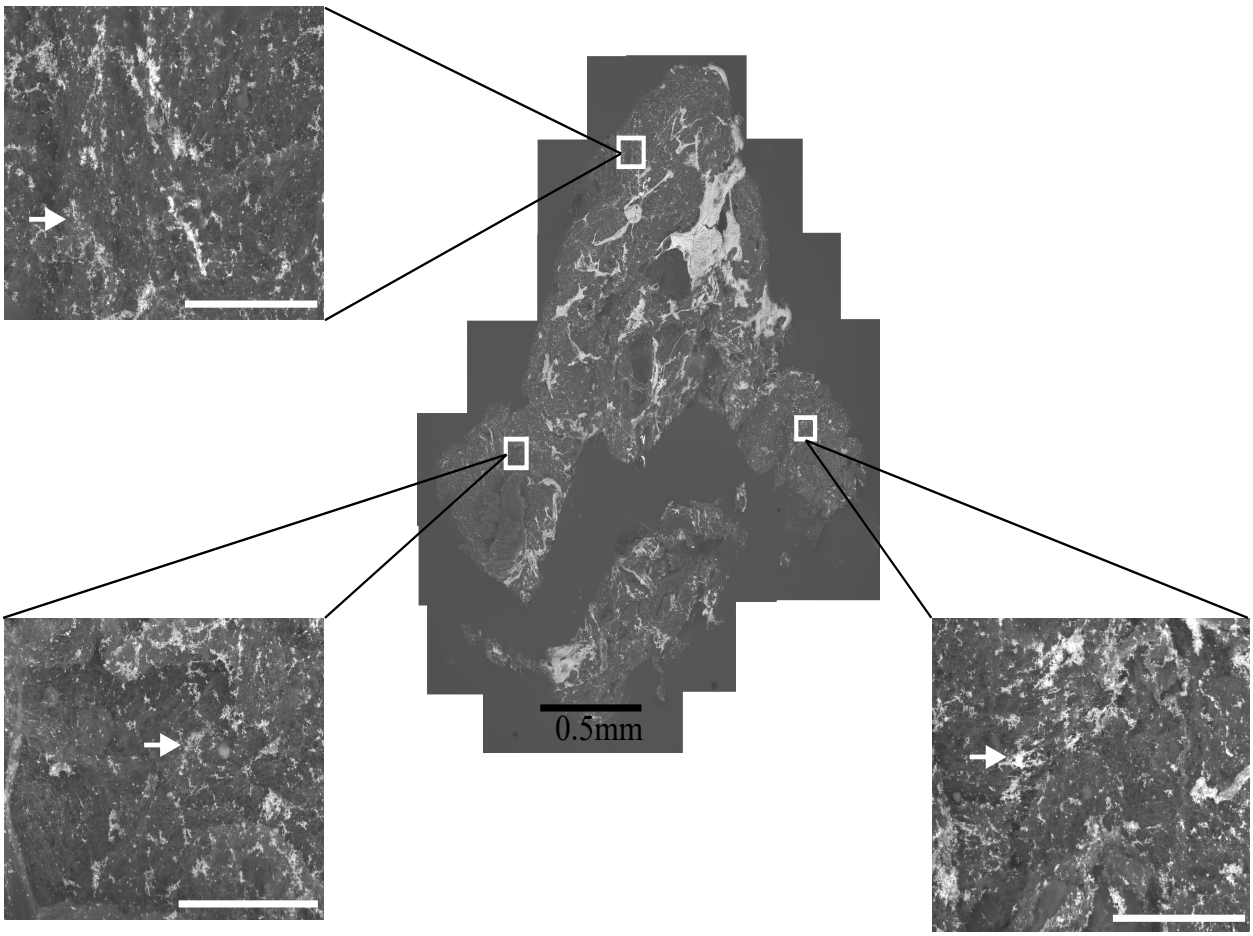

Figure 14. Montage of medial fibrin clot section labeled with FGN-cAu-Fe_3O_4 nanoparticles. FGN-cAu-Fe_3O_4 nanoparticles appear as very bright spots in SEM images. FGN-cAu-Fe_3O_4 nanoparticles were found not only at the periphery but also at the interior of the fibrin clot. Also, high concentrations of FGN-cAu-Fe_3O_4 nanoparticles accumulated throughout the fibrin clot. White boxes indicate the areas shown at higher magnification. White arrows indicate representative FGN-cAu-Fe_3O_4 nanoparticles. White size bars equal 50μm.

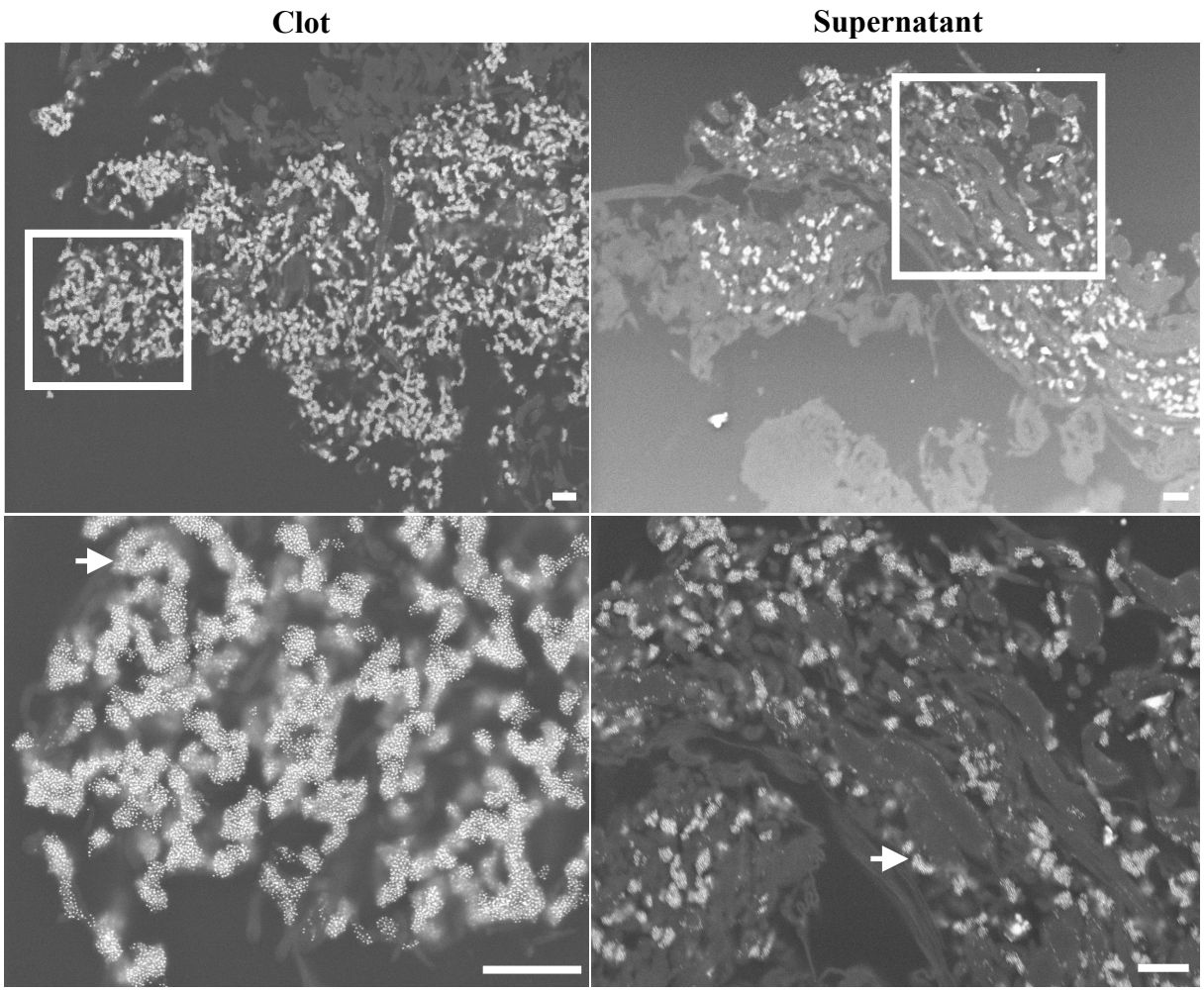

Figure 15. Cross-section of fibrin clot and the supernatant remaining over a fibrin clot labelled with FGN-cAu$_{18}$ nanoparticles. FGN-cAu$_{18}$ nanoparticles interacted with fibrin at the junctions between fibrin strands. FGN-cAu$_{18}$ nanoparticles penetrated into the fibrin network. High concentrations of FGN-cAu$_{18}$ nanoparticles localized both in the fibrin clot and remaining supernatant samples. White arrows indicate the FGN-cAu$_{18}$ nanoparticles. White boxes indicate the area of higher magnification found on the bottom row. Scale bars equal 1μm.

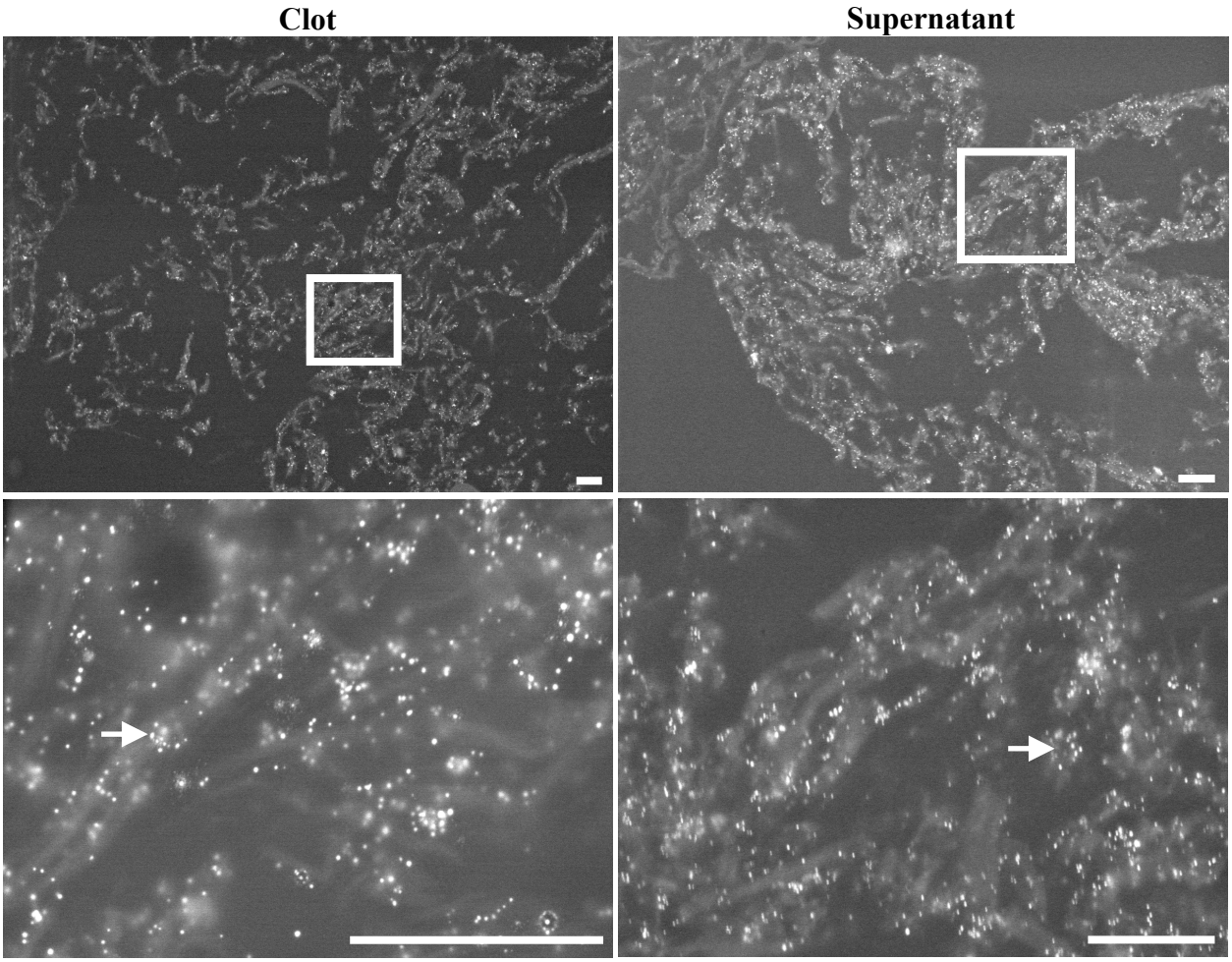

Figure 16. Cross-section of fibrin clot and the supernatant remaining over a fibrin clot labeled with FGN-cAu-Fe_3O_4 nanoparticles. FGN-cAu-Fe_3O_4 nanoparticles bound onto fibrin strands and were present throughout the supernatant and clot. Additionally, FGN-cAu-Fe_3O_4 nanoparticles were found at high concentrations in both the supernatant and deep inside the fibrin clot. White arrows indicate FGN-cAu-Fe_3O_4 nanoparticles. White boxes indicate the area of higher magnification found on the bottom row. Scale bars equal 1μm.

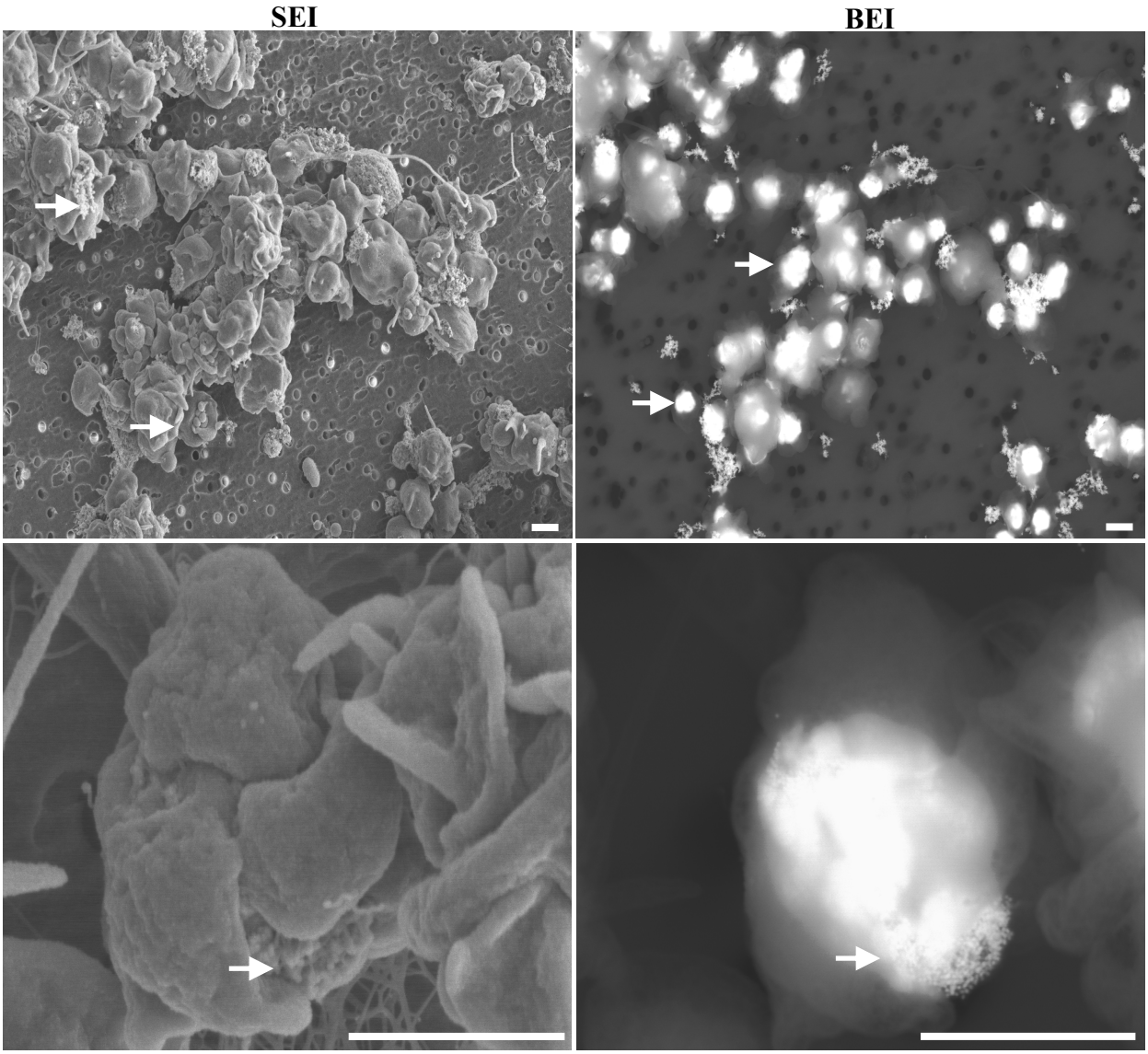

Figure 17. SEM micrographs of suspended GFP labeled with FGN-cAu$_{18}$. Labels were found at the surface, at area of platelet-platelet interaction, and inside activated platelets. White arrows indicate FGN-cAu$_{18}$. SEI on the left displayed topography of the platelet aggregates and BEI on the right shows the localization of the FGN-cAu$_{18}$. Size bars equal 1μm.

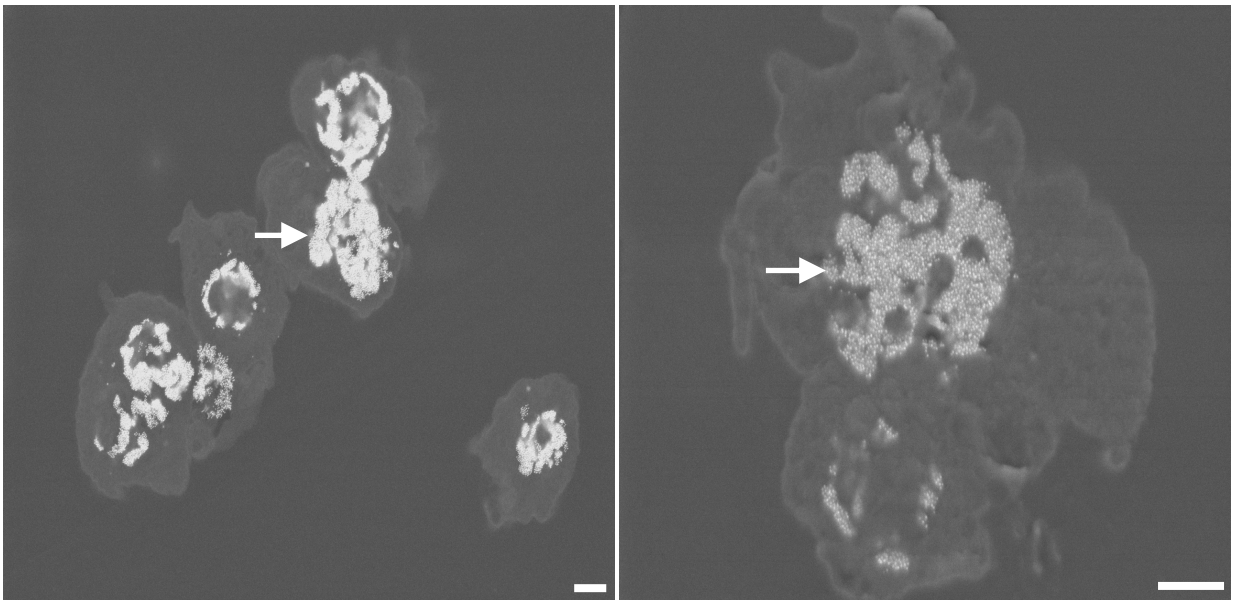

Figure 18. SEM micrographs of cross sections of platelet aggregate labeled with FGN-cAu$_{18}$. FGN-cAu$_{18}$ accumulated mostly in the center of the activated platelets. Comparatively few nanoparticles were found at the periphery of platelets or at platelet-platelet junctions. White arrows indicate FGN-cAu$_{18}$. Scale bars equal 1μm.

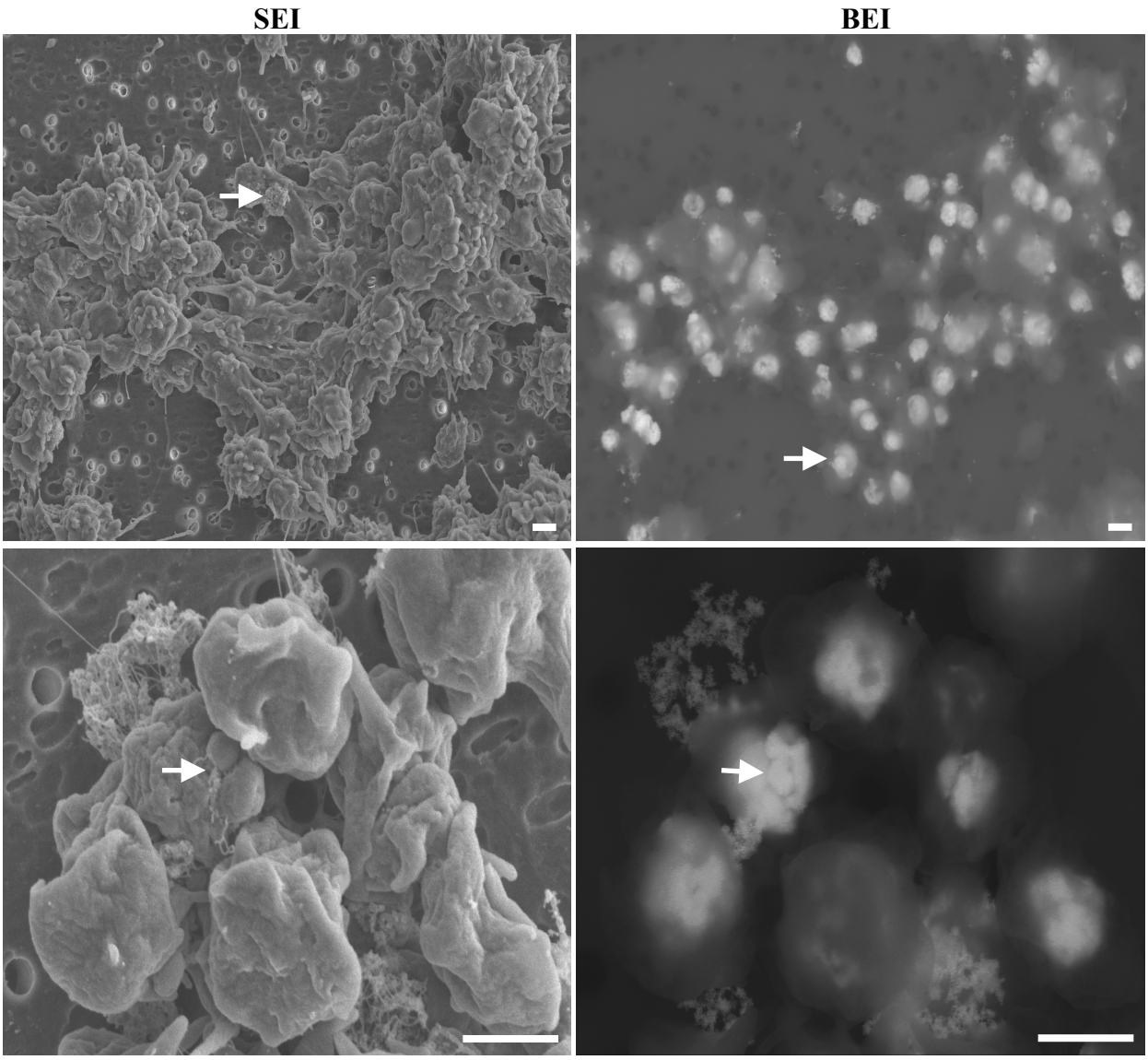

Figure 19. SEM micrographs of suspended GFP labeled with FGN-cAu-Fe_3O_4. Labels were found at the surface, at area of platelet-platelet interaction, and inside activated platelets. White arrows indicate FGN-cAu-Fe_3O_4. SEI on the left shows the topography of platelet aggregates and BEI on the right shows the localization of the FGN-cAu_{18}-Fe_3O_4. Size bars equal 1μm.

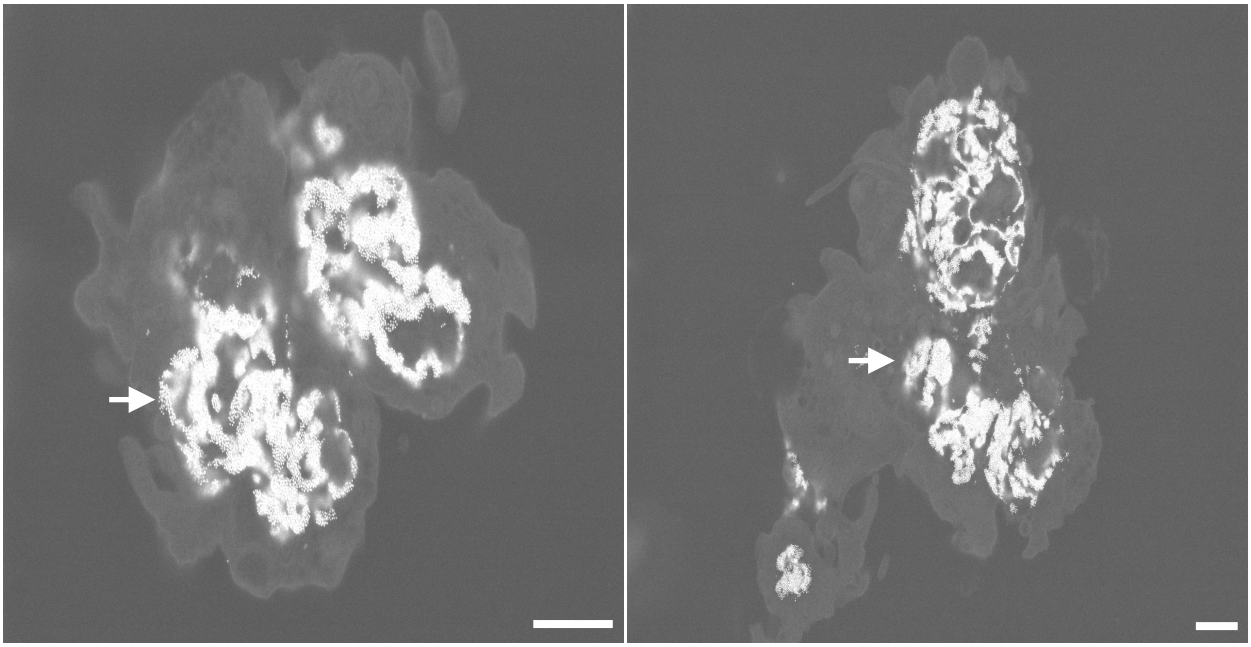

Figure 20. SEM micrographs of cross sections of platelet aggregates labeled with FGN-cAu-Fe_3O_4. FGN-cAu-Fe_3O_4 accumulated most in the center of activated platelets. Comparatively few nanoparticles were found on the periphery of platelets or at platelet-platelet junctions. White arrows indicate FGN-cAu-Fe_3O_4. Scale bars equal 1μm.

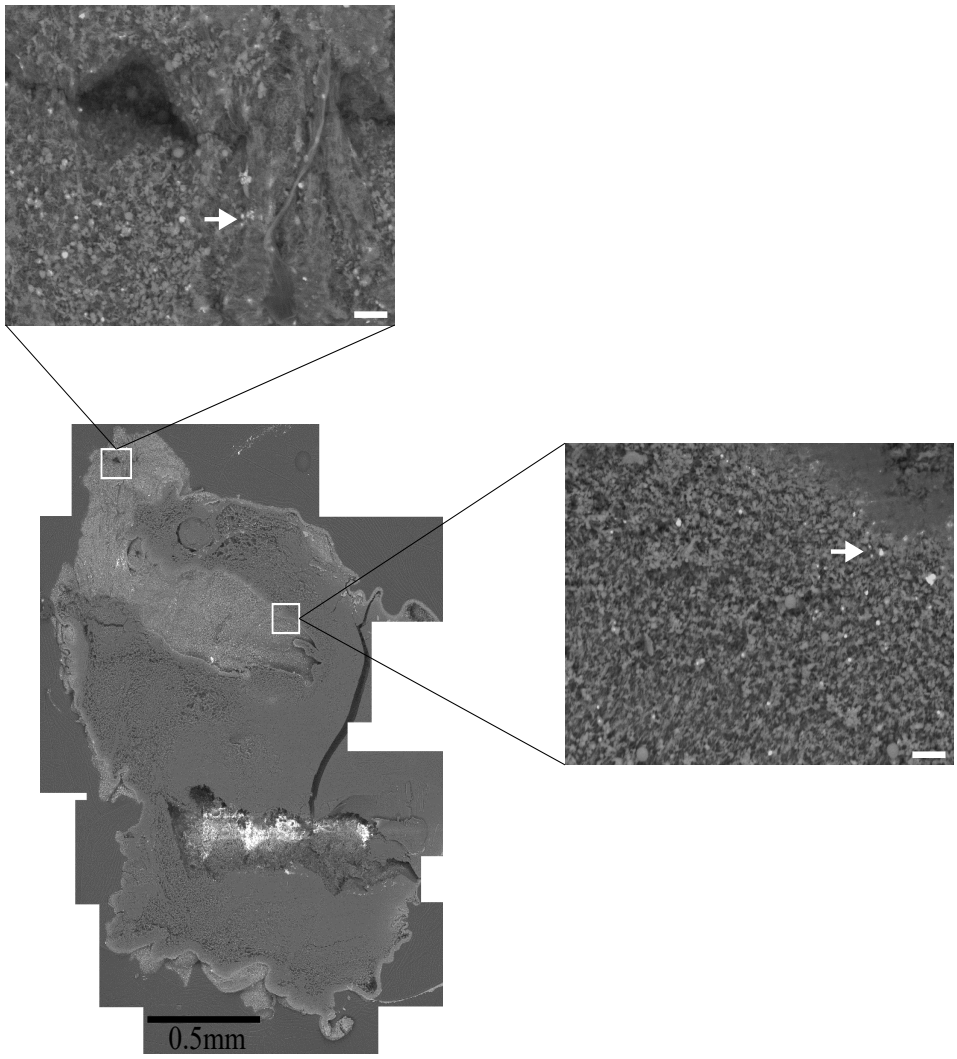

Figure 21. Montage of medial platelet clot section labeled with FGN-cAu$_{18}$ nanoparticles. FGN-cAu$_{18}$ nanoparticles appear as bright spots in the SEM images. FGN-cAu$_{18}$ nanoparticles were found not only at the periphery but also inside of platelet clots. However, as observed by moving from the outside to the inside of the platelet clot, nanoparticles concentration became reduced. White boxes indicate the areas shown at higher magnification. White arrows indicate representative FGN-cAu$_{18}$ nanoparticles. White size bars equal 10μm.

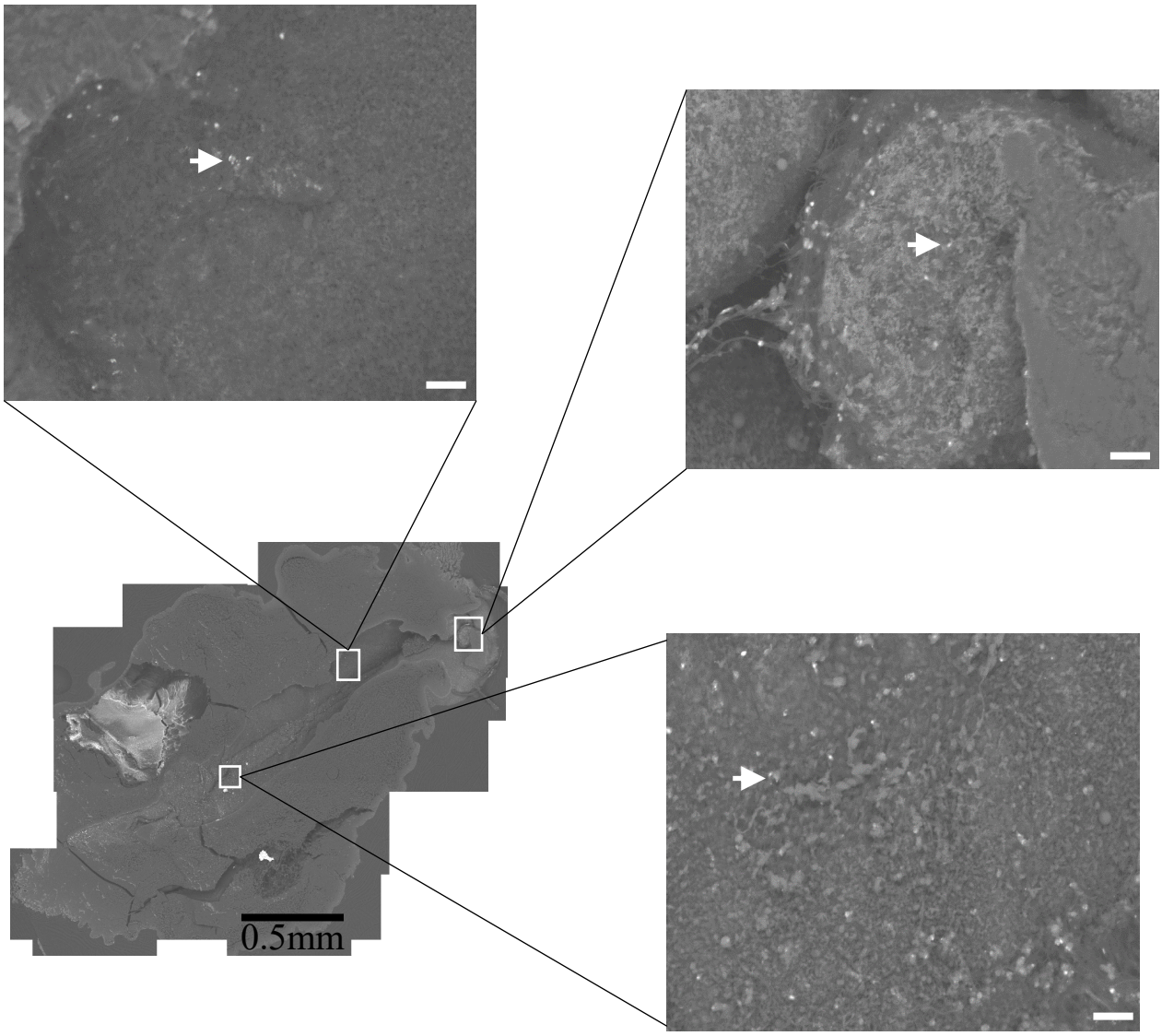

Figure 22. Montage of medial platelet clot section labeled with FGN-cAu-Fe_3O_4 nanoparticles. FGN-cAu-Fe_3O_4 nanoparticles appear as bright spots in the SEM images. FGN-cAu-Fe_3O_4 nanoparticles were found not only at the periphery but also inside platelet clots. Clusters of nanoparticles were scattered throughout the platelet clot. White boxes indicate areas shown at higher magnification. White arrows indicated representative FGN-cAu-Fe_3O_4 nanoparticles. White size bars equal 10μm.

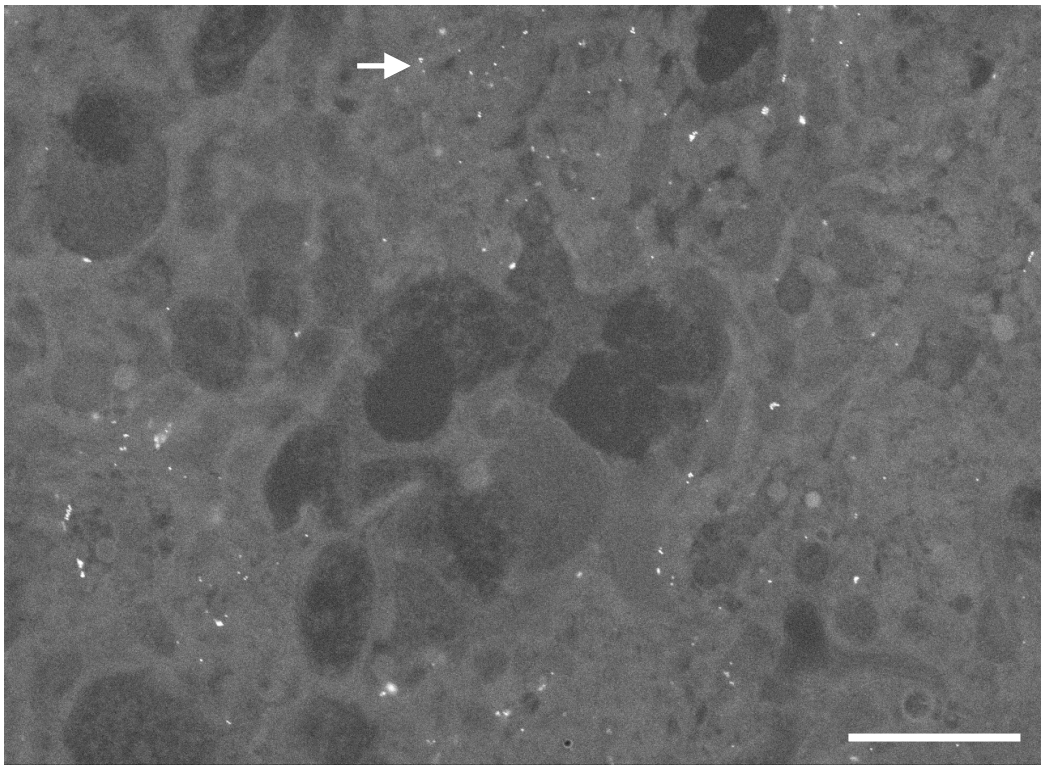

Figure 23. Cross-section of GFP clot labeled with FGN-cAu_{18} nanoparticles. FGN-cAu_{18} nanoparticles were found inside the GFP clot. FGN-cAu_{18} nanoparticles were scattered throughout the cross-section, primarily associated with fibrin strands. White arrow indicates FGN-cAu_{18} nanoparticles. Scale bar equals 1μm.

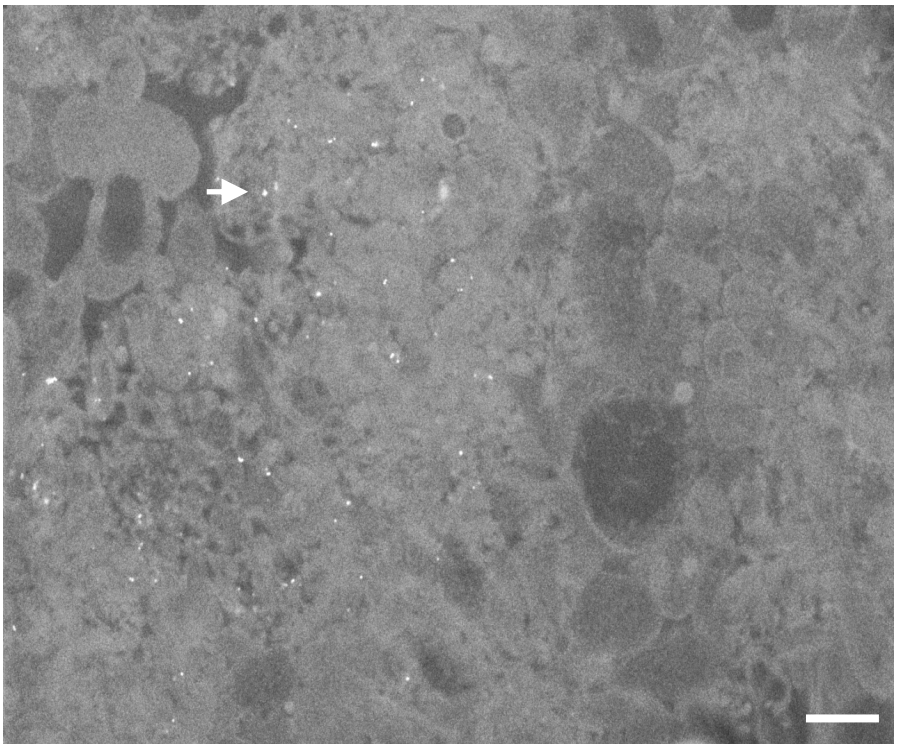

Figure 24. Cross-section of a GFP clot labeled with FGN-cAu-Fe_3O_4 nanoparticles. FGN-cAu-Fe_3O_4 nanoparticles were found inside the GFP clot. FGN-cAu-Fe_3O_4 nanoparticles were scattered throughout the cross-section, primarily associated with fibrin strands. White arrow indicates the FGN-cAu-Fe_3O_4 nanoparticles. Scale bar equals 1μm.

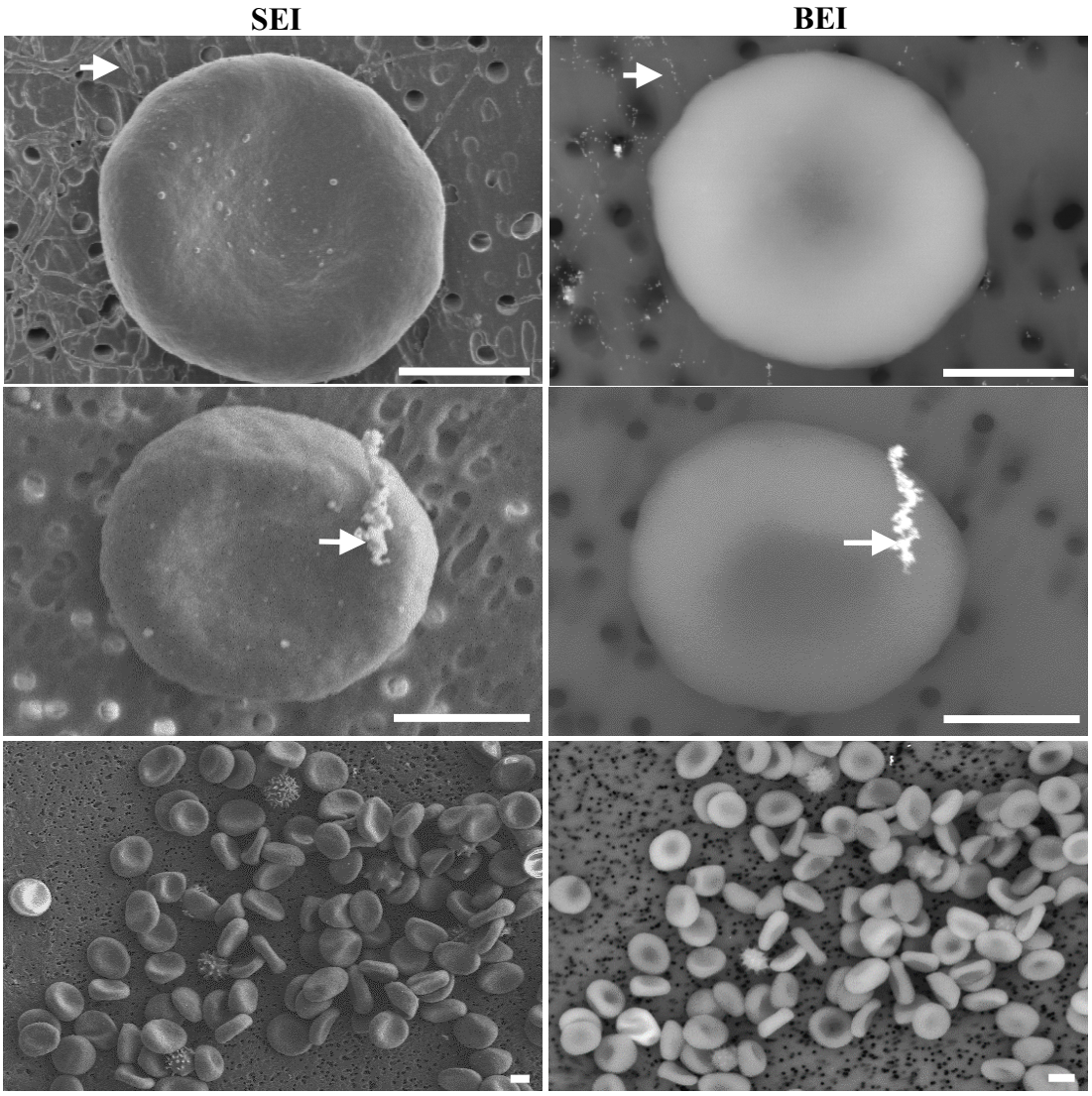

Figure 25. SEM micrographs of supernatant remaining over RBC clot labeled with FGN-cAu$_{18}$ nanoparticles. There was no noticeable interaction between RBCs and FGN-cAu$_{18}$ observed. A few nanoparticles were found on the surface of the RBCs; however, they appeared randomly and rarely. Additionally, most nanoparticles found in the sample were associated with fibrin strands. Secondary electron images (SEI) are on the left and backscattered electron images (BEI) taken of the same area are on the right. White arrows indicate the presence of FGN-cAu$_{18}$. Size bars equals 2μm.

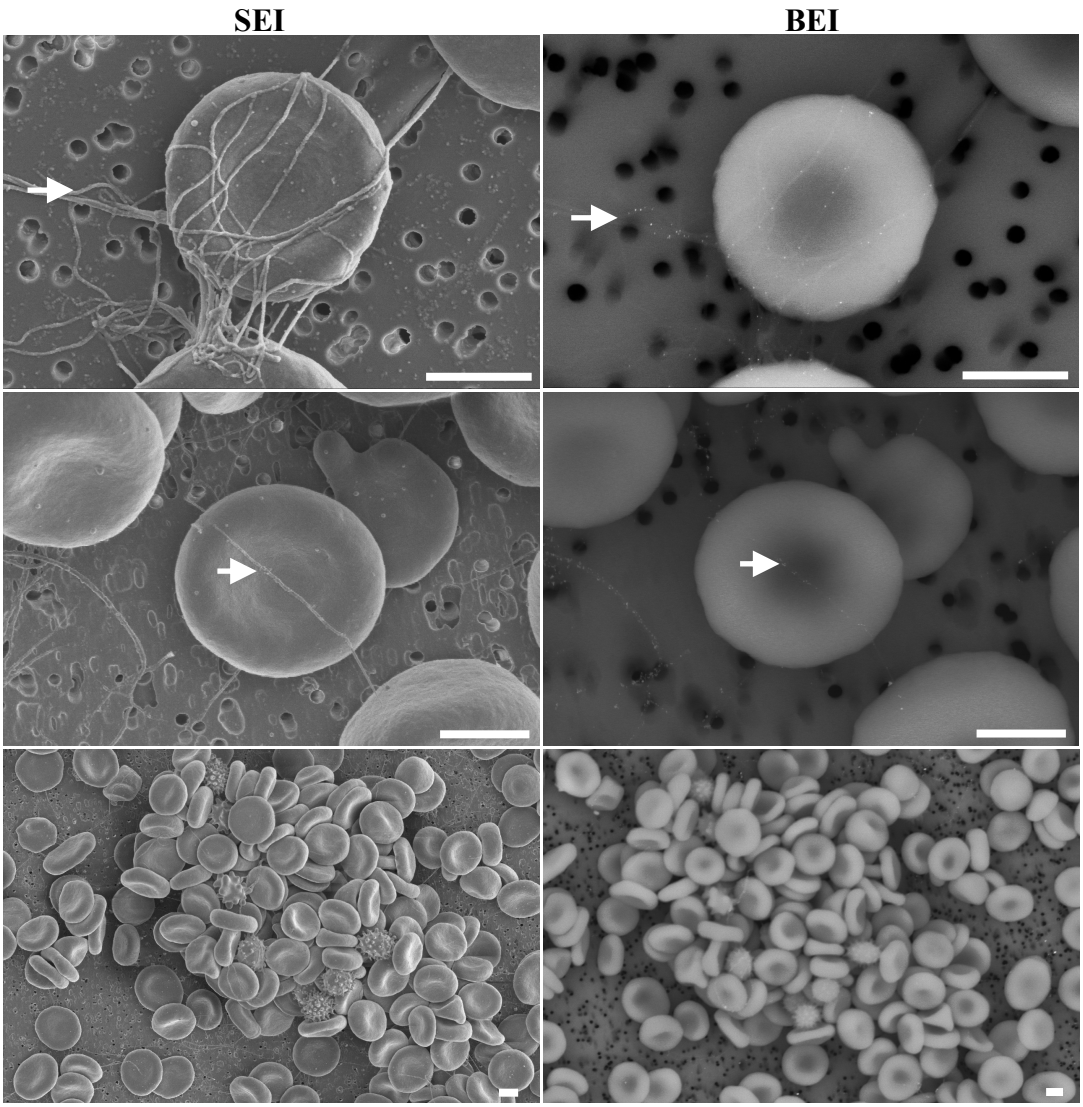

Figure 26. SEM micrographs of the supernatant remaining over RBC clot labeled with FGN-cAu-Fe_3O_4 nanoparticles. There was no specific interaction between RBCs and FGN-cAu-Fe_3O_4 observed. Few nanoparticles were found at the surface of the RBCs. Nanoparticle presence was random and rare. Additionally, most nanoparticles found in the sample were associated with fibrin strands. Secondary electron images (SEI) are on left and backscattered electron images (BEI) of the same area are on the right. White arrows indicate the presence of FGN-cAu-Fe_3O_4. Size bars equal 2μm.

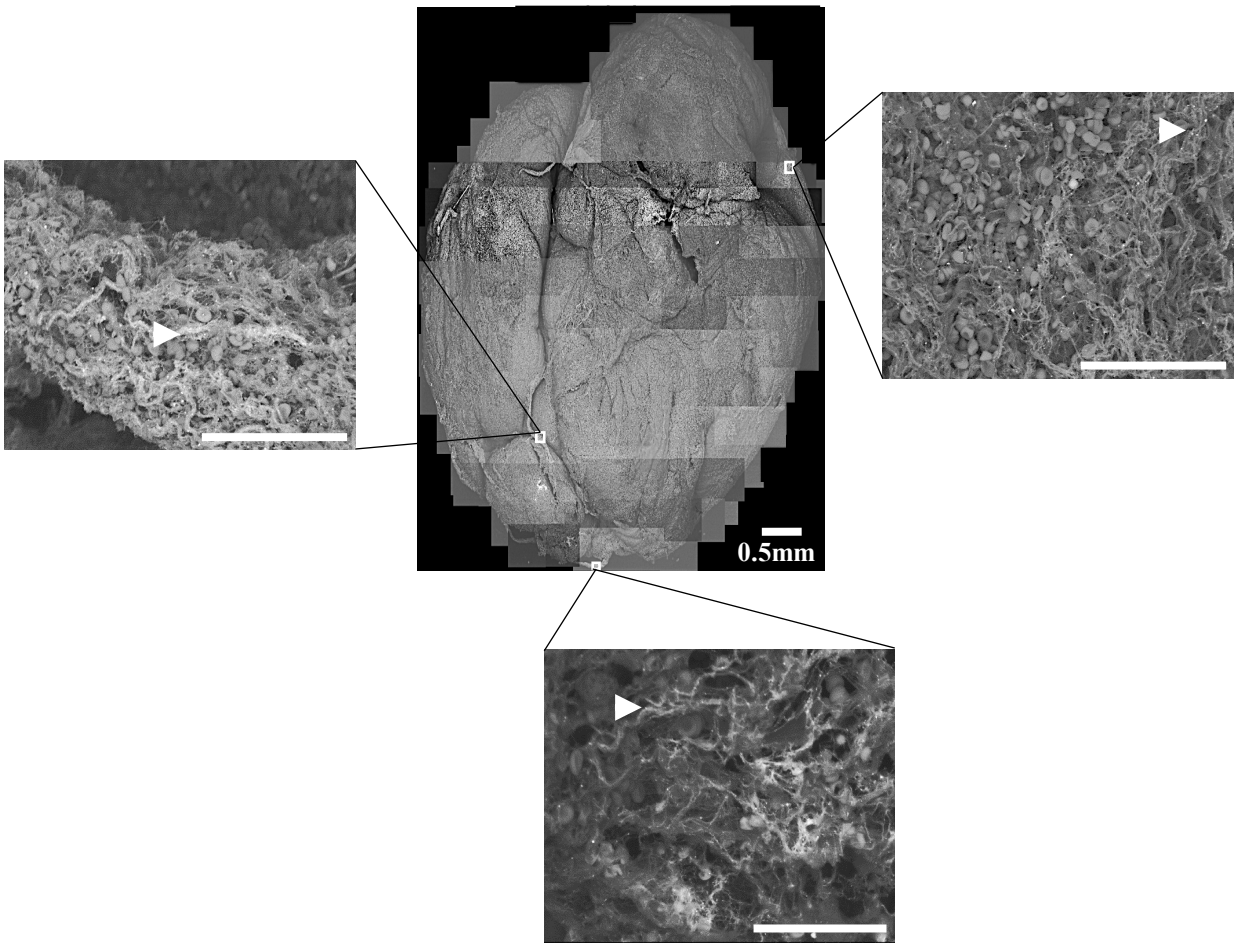

Figure 27. Montage of medial RBC clot section labeled with FGN-cAu_{18} nanoparticles. RBC clots appeared larger in size and more tightly packed with many RBCs wrapped by fibrin strands. Nanoparticles were found most at the periphery and associated with fibrin strands rather than RBCs. Also, moving from outside to inside of the RBC clot, the nanoparticle concentration decreased significantly, with no nanoparticles being found in the center of the RBC clot. White boxes indicate the areas shown at higher magnification. White arrows indicate representative FGN-cAu_{18} nanoparticles. White size bars equal 50μm unless indicated otherwise.

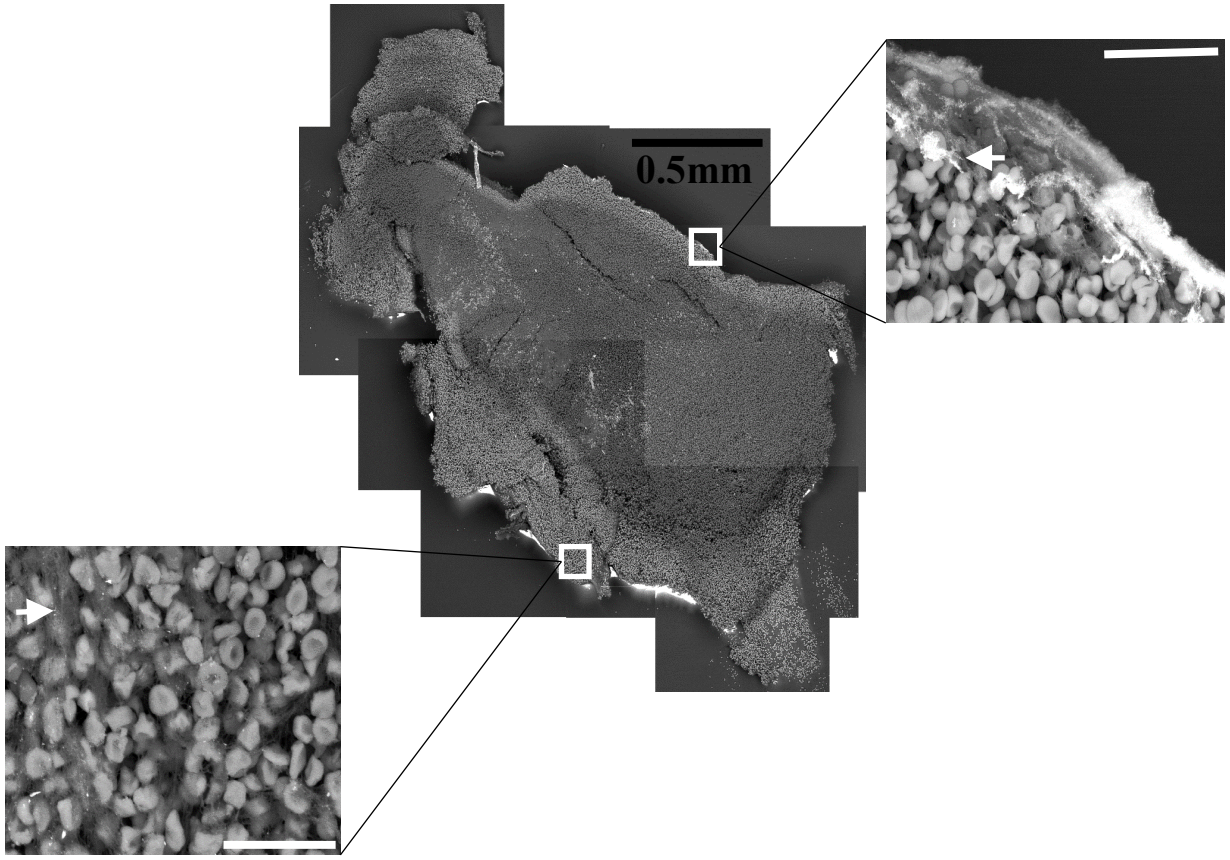

Figure 28. Montage of medial RBC clot section labeled with FGN-cAu-Fe_3O_4 nanoparticles. RBC clots were larger in size and tightly packed with many RBCs were wrapped by fibrin strands. Most labeling was found at the periphery, with no labels being found at the center of the RBC clot. Nanoparticles strongly interacted with fibrin, not RBCs. No labeling was observed on the RBCs. White boxes indicate areas shown at higher magnification. White arrows indicate representative FGN-cAu-Fe_3O_4 nanoparticles. White size bars equal 50μm.

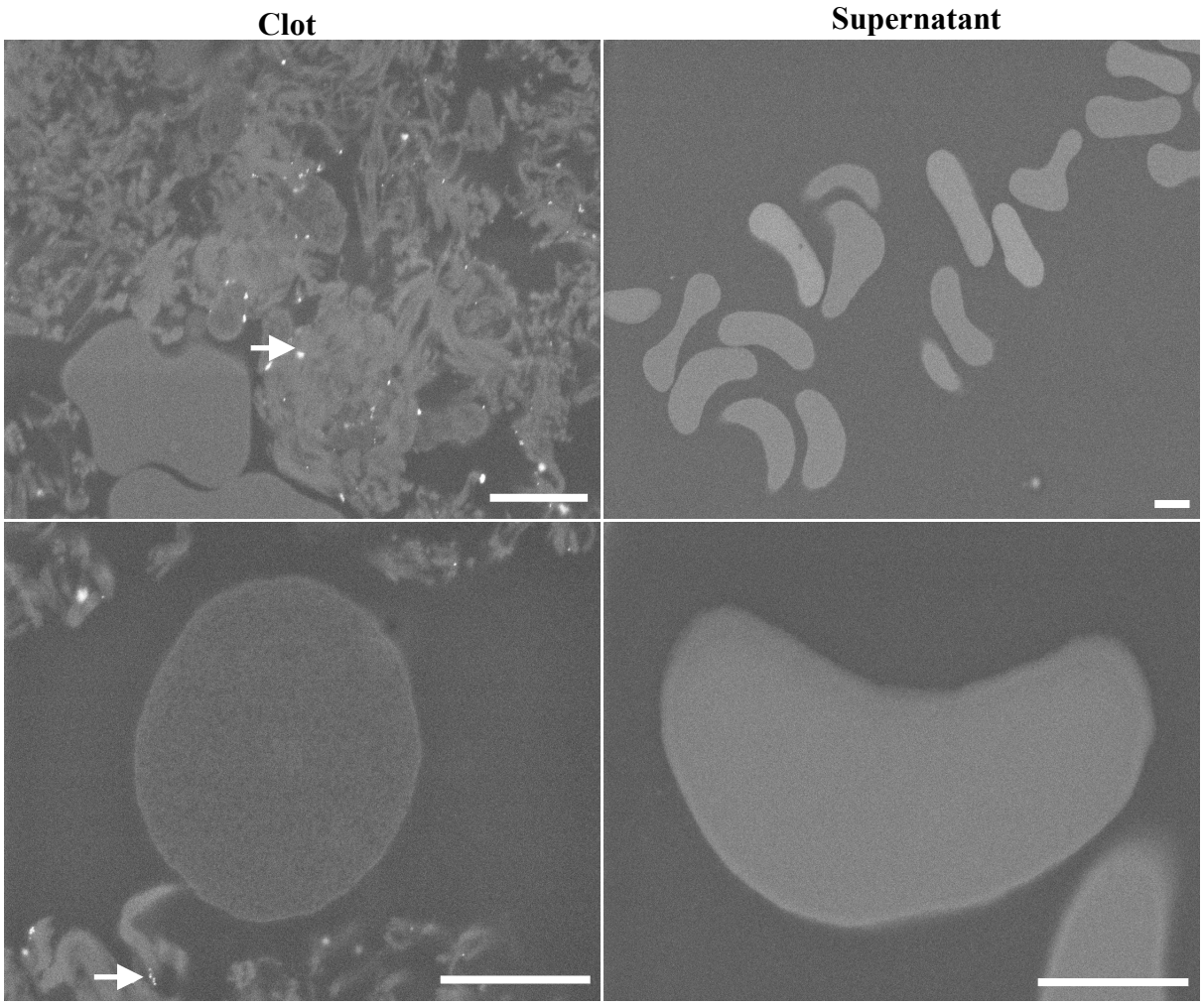

Figure 29. Cross-section of a RBC clot and the supernatant remaining over a RBC clot labeled with FGN-cAu_{18} nanoparticles. FGN-cAu_{18} nanoparticles were able to penetrate into the RBC clot. The bound nanoparticles associated mainly with fibrin but not RBCs. There were no nanoparticle interactions with RBCs in either clots or supernatant. White arrows indicate the FGN-cAu_{18} nanoparticles. Scale bars equal 2μm.

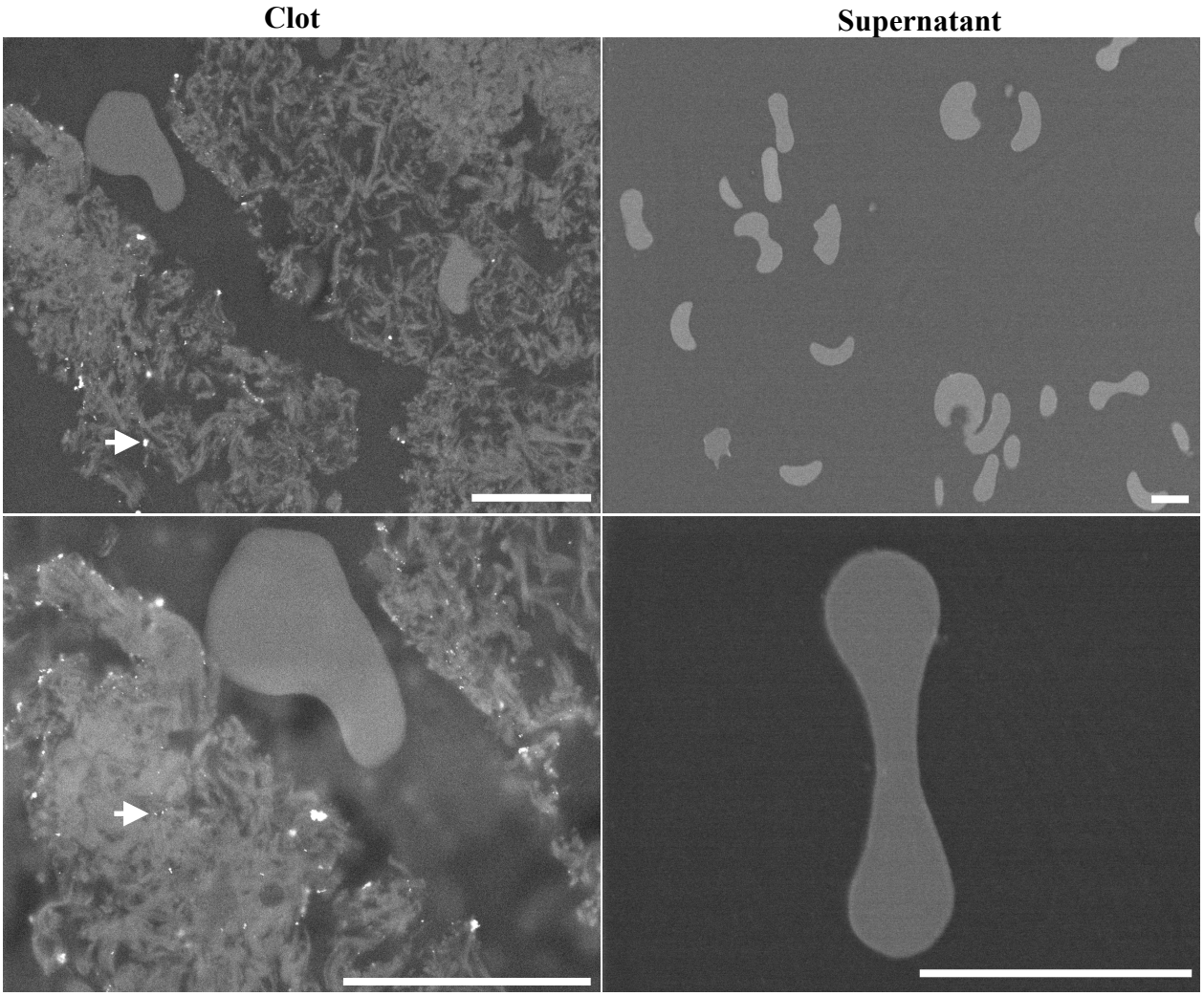

Figure 30. Cross-section of a RBC clot and the supernatant remaining over a RBC clot labeled with FGN-cAu-Fe_3O_4 nanoparticles. The bound nanoparticles associated only with fibrin strands and not RBCs. There were no nanoparticles found associated with the RBCs in either clots or supernatant. White arrows indicate the FGN-cAu-Fe_3O_4 nanoparticles. Scale bars equal 5μm.

References:

1. Krystofiak, E. S. 2013. Fibrinogen-Conjugated Gold-Coated Magnetite Nanoparticles for Antiplatelet Therapy. Doctoral Dissertation, University of Wisconsin- Milwaukee.

2. Koupenova, M., B. E. Kehrel, H. A. Corkrey, J. E. Freedman. 2017. Thrombosis and Platelets: An Update. European Heart Journal. 38: 785-791

3. Lippi, G., M. Franchini, G. Targher. 2011. Arterial Thrombus Formation in Cardiovascular Disease. Nature Review Cardiology. 8: 502-512. https://doi.org/10.1038/nrcardio.2011.91

4. Kim, S. K., W. Yoon, T. S. Kim, H. S. Kim, T. W. Heo, M. S. Park. 2015. Histologic Analysis of Retrieved Clots in Acute Ischemic Stroke: Correlation with Stroke Etiology and Gradient-Echo MRI. American Journal of Neuroradiology. 36(9):1756-1762

5. Sato, Y., H. Ishibashi-Ueda, T. Iwakiri, T. Matsuyama, K. Hatakeyama, Y. Asada. 2012. Thrombus Components in Cardioembolic and Atherothrombotic Strokes. Thrombosis Research. 130(2): 278-280

6. Sato, Y., K. Hatakeyaha, A. Yamashita, K. Marutsuka, A. Sumiyoshi, Y. Asada. 2005. Proportion of Fibrin and Platelets Differs in Thrombi on Ruptured and Eroded Coronary Atherosclerotic Plaques in Humans. Heart. 91: 526-530

7. Chernysh, I. N., C. Nagaswami, S. Kosolapova, A. D. Peshkova, A. Cuker, D. B. Cines, C. L. Cambor, R. I. Litvinov, J. W. Weisel. 2020. The Distinctive Structure and Composition of Arterial and Venous Thrombi and Pulmonary Emboli. Nature Research. 10: 5112. https://doi.org/10.1038/s41598-020-59526-x

8. Bennett, J. S. 2005. Structure and Function of the Platelet Integrin $\alpha_{IIb}\beta_3$. The Journal of Clinical Investigation. 115(2): 3363-3369

9. Ma, Y. Q., J. Qin, E. F. Plow. 2007. Platelet Integrin $\alpha_{IIb}\beta_3$: Activation Mechanisms. Journal of Thrombosis and Haemostasis. 5: 1345-1352

10. Bennett, J. S. 2001. The Platelet-Fibrinogen Interactions. Annals of The New York Academy of Science. 936: 340-354. https://doi.org/10.1111/j.1749-6632.2001.tb03521.x

11. Mosesson, M. W. 2005. Fibrinogen and Fibrin Structure and Functions. Journal of Thrombosis and Haemostasis. 3: 1894-1904

12. Wencel-Drake, J. D., C. Boudignon-Proudhon, M. G. Dieter, A. B. Criss., L. V. Parise. 1996. Internalization of Bound Fibrinogen Modulates Platelet Aggregation. Blood. 87(2): 602-612

13. Fox, J. E. B. 1985. The Organizations of Platelet Contractile Protein, Chapt. 13 in: Platelet Membrane Glycoproteins. J. N. Geogre, A. T. Nurden and D. R. Phillips (Eds.) Plenum Press, New York, pp. 273-298

14. Kunicki, T. J. 1985. Organization of Glycoproteins with the Platelet Plasma Membrane, Chapt. 4 in: Platelet Membrane Glycoproteins. J. N. Geogre, A. T. Nurden and D. R. Phillips (Eds.) Plenum Press, New York, pp. 87-104

15. Oliver, J. A., R. M. Albrecht. 1987. Colloid Gold Labeling of Fibrinogen Receptor in Epinephrine- and ADP-Activated Platelet Suspensions. Scanning Microscopy. 1(2): 745-756

16. Tucker, K. L., T. Sage, J. M. Gibbins. 2012. Clot Retraction. Methods in Molecular Biology. 788: 101-107. https://dx.doi.org/10.1007%2F978-1-61779-307-3_8

17. Tutwiler, V., H. Wang, R. I. Litvinov, J. W. Weisel, V. B. Sheynoy. 2017. Elasticity of Fibrin/Erythrocytes in Blood Clot Retraction. Biophysical Journal. 112(4): 714-723

18. Loftus, J. C., J. Choate, R. M. Albrecht. 1984. Platelet Activation and Cytoskeletal Reorganization: High Voltage Electron Microscopic Examination of Intact and Triton-Extracted Whole Mounts. Journal of Cell Biology. 98: 2019-2025

19. Albrecht, R. M., J. A. Oliver, and J. C. Loftus. 1986. Observation of Colloidal Gold Labelled Platelet Surface Receptors and the Underlying Cytoskeleton Using High Voltage Electron Microscopy and Scanning Electron Microscopy. The Science of Biological Specimen Preparation. 185-193

20. Loftus, J. C., and R. M. Albrecht. 1984. Redistribution of the Fibrinogen Receptor of Human Platelets after Surface Activation. Journal of Cell Biology. 99: 822-829

21. Simmons, S. R., P. A. Sims, R. M. Albrecht. 1997. Alpha IIb beta 3 Redistribution Triggered by Receptor Cross-linking. Arteriosclerosis, Thrombosis, and Vascular Biology. 17: 3311-3320

22. Olorundare, O. E., S. R. Simmons, R. M. Albrecht. 1992. Cytochalasin D and E: Effects on Fibrinogen Receptor Movement and Cytoskeletal Reorganization in Fully Spread, Surface-Activated Platelets: A Correlative Light and Electron Microscopic Investigation. Blood. 79: 99-109

23. Belitser, N., M. Anischuk, Y. Veklich, T. Pozdnjakova, O. Gorkun. 1993. Fibrinogen Internalization by ADP-Stimulated Blood Platelet. Ultrastructural Studies with Fibrinogen-Colloidal Gold Probes. Thrombosis Research. 69: 413-424

24. Escolar, G., E. Leistikow, J. G. White. 1989. The Fate of the Open Canalicular System in Surface and Suspension-Activated Platelets. Blood. 74: 1983-1988

25. White, J., G. Escolar. 1991. The Blood Platelet Open Canalicular System: A Two-way Street. European Journal of Cell Biology. 56: 233-242

26. Weisel, J. W. 2005. Fibrinogen and Fibrin. Advances in Protein Chemistry. 70: 247-299. https://doi.org/10.1016/S0065-3233(05)70008-5

27. Kattula, A., J. R. Byrnes, A. S. Wolberg. 2017. Fibrinogen and Fibrin in Hemostasis and Thrombosis. Arteriosclerosis, Thrombosis, and Vascular Biology. 37(3): e13-e21. doi:10.1161/ATVBAHA.117.308564

28. Weisel, J. W., R. I. Litvinov. 2017. Fibrin Formation, Structure and Properties. Subcellular Biochemistry. 82: 405-456

29. Mosesson, M, W., K. R. Siebenlist, D. A. Meh. 2006. The Structure and Biological Features of Fibrinogen and Fibrin. Annals of the New York Academy of Science. 936: 11-30. https://doi.org/10.1111/j.1749-6632.2001.tb03491.x

30. Carvalho, F. A., S. Connell, G. Miltenberger-Miltenyi, S. V. Pereira, A. Tavares, R. A. S. Ariens, N. C. Santos. 2010. Atomic Force Microscopy-Based Molecular Recognition of a Fibrinogen Receptor on Human Erythrocytes. ACS Nano. 4(8): 4609-4620

31. Lominadze, D., W. L. Dean. 2002. Involvement of Fibrinogen Specific Binding in Erythrocyte Aggregation. FEBS Letters. 517 (2002): 41-44

32. Maeda, N., M. Seike, S. Kume, T. Takaku, T. Shiga. 1987. Fibrinogen-Induced Erythrocyte Aggregation: Erythrocyte Binding Site in the Fibrinogen Molecule. Biochimica Et Biophysica Acta. 904: 81-91

33. Delamaire, M., F. Durand. 1990. Erythrocyte Aggregation and Vascular Pathology. Journal Des Maladives Vasculaires. 15: 344-346

34. Yin, W., Z. Xu, J. Sheng, X. Xie, C. Zhang. 2017. Erythrocyte Sedimentation Rate and Fibrinogen Concentration of Whole Blood Influences the Cellular Composition of Platelet-rich Plasma Obtained from Centrifugation Methods. Experimental and Therapeutic Medicine. 14: 1909-1918. DOI: 10.3892/etm.2017.4724

35. Walton, B. L., J. R. Byrnes, A. S. Wolberg. 2015. Fibrin, Red Blood Cells, and Factor XIII in Venous Thrombosis. Journal of Thrombosis and Haemostasis. 13(Suppl 1): S208–S215. doi:10.1111/jth.12918

36. Brust, M., O. Aouane, M. Thiebaud, D. Flormann, C. Verdier, L. Kaestner, M. W. Laschke, H. Selmi, A. Benyoussef, T. Podgorski, G. Coupier, C. Misbah, C. Wagner. 2014. The Plasma Protein Fibrinogen Stabilizes Clusters of Red Blood Cells in Microcapillary Flows. Scientific Report. 4: 4348. DOI: 10.1038/srep04348

37. Brynes, J. R., A. S. Wolberg. 2017. Red Blood Cells in Thrombosis. Blood. 130(16): 1795-1799

38. Oliveira, S. D., V. V. Almeida, A. Calado, H. S. Rosario, C. Saldanha. 2012. Integrin-Associated Protein (CD47) is a Putative Mediator for Soluble Fibrinogen Interaction with Human Red Blood Cells Membrane. Biochimica Et Biophysica Acta. 1818: 481-490

39. Carvalho, F. A., S. Oliveira, T. Freitas, S. Goncalves, N. C. Santos. 2011. Variations on Fibrinogen-Erythrocyte Interactions During Cell Aging. PLoS ONE 6(3): e18167. https://doi.org/10.1371/journal.pone.0018167

40. Lominadze, D., W. L. Dean. 2002. Involvement of Fibrinogen Specific Binding in Erythrocyte Aggregation. FEBS Letters. 517 (2002): 41-44

41. Weisel, J. W., R. I. Litvinov. 2017. Fibrin Formation, Structure and Properties. Subcellular Biochemistry. 82: 405-456

42. Schmid-Schoenbein, H., R. Wells, R. Schildkraut. 1969. Microscopy and Viscometry of Blood Flowing Under Uniform Shear Rate. Journal of Applied Physiology. 5: 674-678

43. Dimitrova, M. N., H. Matsumura, A. Dimitrova, V. Z. Neitchev. 2000. Interaction of Albumins from Different Species with Phospholipid Liposomes. Multiple Binding Sites System. International Journal of Biological Macromolecules. 27: 187-194

44. Wallach, D. F., S. P. Verma, E. Weidekamn, V. Bieri. 1974. Hydrophobic Binding Sites in Bovine Serum Albumin and Erythrocyte Ghost Proteins. Study by Spin-labeling, Paramagnetic Fluorescence Quenching and Chemical Modification. Biochimica Et Biophysica Acta. 356: 68-81

45. Freitas, L. F., G. H. C. Varca, J. G. S. Batista, A. B. Lugao. 2018. An Overview of the Synthesis of Gold Nanoparticles Using Radiation Technologies. Nanomaterials. 8(11): 939. doi:10.3390/nano8110939

46. Souza, C. D. D., B. R. Nogueira, M. E. C. M. Rostelato. 2019. Review of the Methodologies Used in the Synthesis Gold Nanoparticles by Chemical Reduction. Journal of Alloys and Compounds. 798: 714-740

47. Jazayeri, M. H., H. Amani, A. A. Pourfatollah, H. Pazoki-Toroudi, B. Sedighimoghaddam. 2016. Various Methods of Gold Nanoparticles (GNPs) Conjugation to Antibodies. Sensing and Bio-Sensing Research. 9: 17-22

48. Goodman, S. L., G. M. Hodges, D. C. Livingston. 1980. A Review of the Colloidal Gold Marker System. Scanning Electron Microscopy. Pt 2: 133-146

49. Gole, A., C. Dash, V. Ramakrishman, S. R. Sainkar, A. B. Mandale, M. Rao, M. Sastry. 2001. Pepsin-gold Colloid Conjugates: Preparation, Characterization and Enzymatic Activity. Langmuir. 17: 1671-1679

50. Krystofiak, E. S., V. Z. Matson, D. A. Steeber, J. A. Oliver. 2012. Elimination of Tumor Cells Using Folate Receptor Targeting by Antibody-Conjugated, Gold Coated Magnetite Nanoparticles in a Murine Breast Cancer Model. Journal of Nanomaterials. https://doi.org/10.1155/2012/431012

51. Krystofiak, S. E., C. Mattson, P. M. Voyles, C. J. Hirschmugl, R. M. Albrecht, M. Gajdardziska-Josifovska, J.A. Oliver. 2013. Multiple Morphologies of Gold-Magnetite Heterostructure Nanoparticles Are Effectively Functionalized with Protein for Cell Targeting. Microscopy and Microanalysis. 19(4): 821-834

52. Albrecht, R. M., O. E. Olorundare, S. R. Simmons, J. C. Loftus, D. F. Mosher, J. H. Jacek. 1992. Use of Correlative Microscopy with Colloidal Gold Labeling to Demonstrate Platelet Receptor Distribution and Movement. Methods in Enzymology. 215: 456-479

53. Grouse, L. H., J. G. White. 1989. Gold-labeled Bovine Fibrinogen for Study of Human Platelets. Thrombosis and Haemostasis. 62: 1112-1115

54. Frens, G. 1973. Controlled Nucleation for the Regulation of the Particles Size in Monodisperse Gold Suspension. Nature Physical Science. 241: 20-22

55. Massart, R. 1981. Preparation of Aqueous Magnetic Liquids in Alkaline and Acidic Media. Institute of Electrical Electronics Engineers Transactions on Magnetics. 17: 1247-1248

56. Lyon, J., D. A. Fleming, M. B. Stone, P. Schiffer, and M. E. Williams. 2004. Synthesis of Fe Oxide Core/Au Shell Nanoparticles by Iterative Hydroxylamine Seeding. Nano Letters. 4: 719-723

57. Holdorf, M. M., H. A. Owen, S. R. Lieber, L. Yuan, N. Adams, C. Dabney-Smith, C. A. Makaroff. 2012. Arabidopsis ETHE1 Encodes a Sulfur Dioxygenase That Is Essential for Embryo and Endosperm Development. Plant Physiology. 160: 226-236

58. Shattil, S. J., H. Kashwagi, N. Pampori. 1998. Integrin Signaling: The Platelet Paradigm. Blood. 91(8): 2645-2657

59. Leung, L., R. Nachman. 1986. Molecular Mechanisms of Platelet Aggregation. Annual Review of Medicine. 37: 179-186

60. Chernysh, I. N., C. Nagaswami, P. K. Purohit, J. W. Weisel. 2012. Fibrin Clots Are Equilibrium Polymers That Can Be Remodeled Without Proteolytic Digestion. Scientific Reports. 2: 879 (2012). https://doi.org/10.1038/srep00879

61. Vilar, R., R. J. Fish, A. Casini, M. Neerman-Arbez. 2020. Fibrin(ogen) in Human Disease: Both Friend and Foe. Haematologica. 105(2): 284-296

62. Sporns, P. B., U. Hanning, W. Schwindt, A. Velasco, J. Minnerup, T. Zoubi, W. Heindel, A. Jeibmann, and T. U. Niederstadt. 2017. Ischemic Stroke: What Does the Histological Composition Tell Us About the Origin of the Thrombus? Stroke. 48: 2206-2210

63. Marder, V. J., D.J. Chute, S. Starkman, A. M. Abolian, C. Kidwell, D. Liebeskind, B. Ovbiagele, F. Vinuela, G. Duckwiler, R. Jahan, P. M. Vespa, S. Selco, V. Rajajee, D. Kim, N. Sanossian, J. L. Saver. 2006. Analysis of Thrombin Retrieved from Cerebral Arteries of Patients with Acute Ischemic Stroke. Stroke. 37(8): 2086-2093

Chapter 3- Describing Clot Structure and Nanoparticle Penetration at a Physiologic Range of Thrombin Doses

Abstract:

We are investigating an alternative therapy for ischemic stroke that targets activated platelets rather than fibrin in occlusive clots using fibrinogen-conjugated magnetic nanoparticles and exposure to an oscillating magnetic field (OMF). This requires specific nanoparticle-receptor interactions on activated platelets in the clot. Previous studies have demonstrated the specific targeting of fibrinogen-conjugated, gold-coated magnetite nanoparticles (FGN-cAu-Fe_3O_4) to activated platelets in a purified platelet system. When followed by exposure to an oscillating magnetic field, the activated platelets in aggregates were disrupted. Platelet-rich plasma (PRP) and whole blood (WB) systems are more complex in terms of both the protein and cell components, but are also more representative of the physiological system. Developing FGN-cAu-Fe_3O_4 into an effective therapy will depend on how efficiently the nanoparticles penetrate into clots and their resulting final concentration inside clots. We have used the robust model of fibrinogen-conjugated gold nanoparticles (FGN-cAu_{18}) to examine the effect the 3-dimensional network of fibrin and blood cell components found in PRP and WB clots has on nanoparticle penetration. **We hypothesized that different fibrin architecture resulting from clotting at different physiological thrombin concentrations determines the extent of nanoparticle penetration into clots.** PRP and WB were clotted *in vitro* using low and high doses of thrombin, followed by soaking in FGN-cAu_{18}. Sections and medial cross-sections were analyzed by scanning electron microscopy to observe both the topography and interior of the clots. Frozen cross-sections were treated with silver enhancement and analyzed by light microscopy to quantify the depth of nanoparticle penetration observed in different donors.

From our experiments, we have found the following: First, the arrangement of cells through the clots differed between the systems. In PRP, fibrin and platelets were distributed

throughout the clot. In WB clots, a meshwork of fibrin and platelet aggregates was observed on the clot surface, and the interior consisted of closely packed, compressed polyhedral erythrocytes with very little fibrin present. Second, the dose of thrombin available during clotting significantly influenced the density of clot structure. High thrombin doses produced a dense network of small diameter fibrin filaments, and low doses produced a more open network of large diameter fibers. Third, the extent of nanoparticle penetration was inversely related to the density of the fibrin network and the number of activated platelets and erythrocytes. Fourth, while variation between donors was observed, its effect on nanoparticle penetration was largely overcome at high thrombin concentrations where there was a dense clot structure and an overall lower degree of nanoparticle penetration. These results provide important insight into the development of a nanoparticle-based therapeutic agent for treating ischemic stroke.

Introduction:

Previous studies have demonstrated the successful development and use of fibrinogen-conjugated, gold-coated magnetite nanoparticles to target activated platelets in a purified platelet system and the use of an OMF as a means to disrupt the activated platelet aggregates (1). However, an *in vivo* blood clot will also have a fibrin network, red blood cells (RBCs), and white blood cells (WBCs). Previous chapters discussed the interaction of nanoparticles with blood clot components including fibrin, activated platelets, and RBCs. We demonstrated that conjugated nanoparticles have the ability to bind to fibrin strands and activated platelets, but not RBCs. To build on these studies and support our overall hypothesis, this chapter will demonstrate proof of principle that labels can be incorporated into thrombi in the presence of plasma fibrin(ogen) and RBCs. It will allow us to observe the location and quantify the degree of penetration of the labels

into PRP and WB clots. We used both PRP and WB systems to address this instead of using only the WB system. We will start with the less complex PRP model, which will educate us about what problems we may encounter in the WB system and help us solve them efficiently. Additionally, efficient nanoparticle penetration into the clot interior depends on how the fibrin and blood cell components interact to form a 3-dimensional clot structure. This structure is dependent on the thrombin doses used. Therefore, determining the range of responses observed in our donor pool allows us to design *in vitro* experiments that have physiologic relevance to *in vivo* systems.

Upon vascular damage, tissue factor (TF) expressed on the subendothelial cells is exposed to blood. TF binds and serves as a cofactor for circulating factor VIIa (FVIIa), a serine protease, thereby significantly increasing its enzymatic activity. The TF and FVIIa complex catalyzes the conversion of the zymogen factors VII, IX, and X into activate serine proteases FVIIa, FIXa and FXa. TF-mediated generation of FXa is referred to as the extrinsic pathway of coagulation (2-4). FXa can also be generated via the intrinsic pathway. The intrinsic pathway begins with the formation of the primary complex on collagen by high molecular weight kininogen, prekallikrein, and factor XII. This causes the conversion of prekallikrein and factor XII into kallikrein and FXIIa, respectively. The activated FXIIa then turns factor XI into FXIa. Factor XIa activates factor IX, which with its co-factor FVIIIa, forms the tenase complex. This activates factor X into FXa (2,5,6). Like FVIIa and FIXa, FXa associates with a cofactor, FVa, thus forming the prothrombinase complex. The prothrombinase complex catalyzes conversion of the zymogen prothrombin (factor II) into thrombin (FIIa) (the common pathway) (2,3,7,8). Then, thrombin acts as a procoagulant by stimulating platelet activation via their protease activated receptors (PARs). It also catalyzes the cleavage of fibrinogen to insoluble fibrin monomers

which spontaneously polymerize to form fibrin strands that will attach to activated platelets and trap RBCs to form clots. Thrombin further supports coagulation by activating factor XIII to the transglutaminases FXIIIa that crosslink fibrin strands at lysine residues to strengthen and stabilize the blood clot and stop bleeding (9,10).

The formation of the clot depends on the availability of thrombin. In normal circulation, the range of thrombin in plasma is approximately 5.5 mIU/mL (0.055nM) or less. When coagulation is activated, the local thrombin concentration in plasma is likely to be between 6.6 mIU/mL to 10 IU/mL (0.066nM-100nM). Anything above 10 IU/ml, or 100nM, is considered an unrealistically high concentration of thrombin (11-14). The capacity of thrombin generation from circulating prothrombin is considered to represent an individual's ability to respond to tissue injury and prevent bleeding. However, directly and accurately measuring the *in vivo* thrombin concentration in plasma is very difficult for several reasons. First, thrombin has a very short half-life in plasma due to high concentration of its naturally occurring direct inhibitors such as antithrombin and other circulating protease inhibitors (14,15). Second, measuring thrombin concentration in the presence of plasma fibrinogen is challenging because thrombin rapidly interacts with fibrinogen to form insoluble fibrin strands, which in turn binds to and entraps active thrombin locally at the site of the clot (16). Third, thrombin generated in plasma following *in vitro* stimulation will vary between donors. Therefore, we will use the knowledge of physiologically relevant thrombin doses to investigate the impact of its concentration on clot structure and the penetration of nanoparticles. We examined the impact of thrombin doses between 0nM and 10nM.

The thrombin concentration present at the time of clotting dictates the fibrin clot structure. Low concentration (<1nM, <0.1 U/mL) of thrombin generates turbid, permeable, and

unstable fibrin clots that are composed of thick, loosely-woven fibrin strands. Higher thrombin concentration produces non-turbid, less permeable, and comparatively stable fibrin clots composed of thin, tightly-packed fibrin strands (17-22). In fact, many studies have shown that more dense and stable clots are associated with thrombosis; whereas, loosely-woven, unstable clots are related to bleeding disorders (23-30). Most previous studies have examined thrombin effects on fibrin structure in purified systems that consisted of only thrombin and purified fibrinogen. *In vivo*, many components beside fibrin participate in thrombus formation, including activated platelets, WBCs, and RBCs. In fact, fibrin can interact with and wrap around platelet aggregates to create a net that traps more platelets and other blood cells. Therefore, clot formation *in vivo* will be more complex. To more completely understand the role of thrombin in clot formation, PRP and WB systems should be taken into consideration. Therefore, to build our understanding of the role of blood clot architecture in thrombosis and how it might impact the development of a nanoparticle-based therapeutic agent for treating ischemic stroke, we used fibrin morphology to describe PRP and WB clot architecture produced over a range of physiologically relevant thrombin doses. We expected that at low thrombin concentrations, both PRP and WB clots would be loosely packed into less dense and more porous networks; whereas, higher thrombin doses would cause PRP and WB clots to be tightly pack into denser and less porous networks.

The differentiation of fibrin clot structures also contributes to the varying degrees of clot stability, including resistance to fibrinolysis and anticoagulants. In fact, using increasing thrombin concentrations produced fibrin clots composed of thinner, highly branched fibers that were less porous, less permeable, and more rigid; thereby, these clots were less susceptible to dissolution by fibrinolytic proteins. When fibrinogen was clotted with low thrombin

concentrations, a thicker fiber matrix was associated with a more permeable, more porous, and less rigid clot structure. Thus, these clots were less resistant to fibrinolysis (31,32).

The differences in architecture of PRP and WB clots that might occur at various thrombin concentrations might influence the degree of penetration of nanoparticles as well. The porous network of clots formed at low thrombin concentrations might be more susceptible to fibrinogen conjugated-nanoparticle penetration; whereas, tightly packed clot networks that resulted from higher thrombin doses might limit the access of nanoparticles into the interior of clots. Moreover, in the absence of RBCs, the PRP clot offers much better ability to investigate the fibrin architecture. However, including the RBCs is critical to evaluating the *in vivo* environment. Thus, using both PRP and WB clots to examine the efficiency of nanoparticle penetration will address whether our nanoparticle-based targeting of arterial clots in ischemic strokes is viable for clinical trials.

Investigating the nanoparticle penetration in both PRP and WB clots from different donors is also necessary. These experiments will allow us to evaluate the variation of nanoparticle penetration not only between PRP and WB systems, but also between donors. To some extent, different donors might respond differently to the same thrombin doses. It is also possible that donor clot structures might be distinct from one another, and the degree of nanoparticle penetration into clots might vary accordingly. Hence, we examined this potential phenomenon with the expectation that at the certain range of thrombin concentrations where clotting occurs, most donor responses will behave similarly in regard to nanoparticle penetration into clots.

As we discussed in previous chapters, fibrinogen-conjugated gold nanoparticles (FGN-cAu_{18}) and fibrinogen-conjugated gold-coated magnetite (FGN-cAu-Fe_3O_4) share a common

characteristic and functionalization in targeting of clots. In addition, FGN-cAu_{18} synthesis is a more robust procedure compared to FGN-Au-Fe_3O_4 synthesis. Therefore, FGN-cAu_{18} will be solely used for investigating nanoparticle penetration in this chapter.

The overall hypothesis of this chapter is that the different fibrin structures resulting from clotting at different thrombin doses will determine the penetration depth of fibrinogen-conjugated nanoparticles into the clots. Testing this hypothesis will provide us vitally important answers for the following questions: First, does thrombin concentration influence PRP and WB clot formation *in vitro*? Second, can nanoparticles be incorporated into thrombi in the presence of plasma fibrin(ogen)? Third, what efficiency of nanoparticle penetration into blood clots can we expect? Lastly, does variation of nanoparticle penetration exist between donors?

Materials and Methods:

PRP and WB sample preparation:

Fresh blood samples were collected from normal adult donors and processed to produce PRP and WB as described in Chapter 2.

Determine the range of responses to physiologically relevant thrombin doses in PRP:

PRP was adjusted to 150,000 cells per μL by diluting in PPP. The experiments were performed in a round bottom, 96-well microtiter plate (Thermo Scientific ™, Nunc™). First, 30μL of 5X $CaCl_2$ and thrombin (Haematologic Technologies), prepared in Tyrode's buffer (15mM HEPES, pH 7.4, 3.3mM Na_2HPO_4, 138mM NaCl, 2.7mM KCl, 5.5mM glucose, 1mM $MgCl_2$, 0.1% BSA) with 0.1% bovine serum albumin (BSA), was mixed to produce solutions with a final concentration of 5mM $CaCl_2$ and concentrations of 0nM, 0.5nM, 1nM, 5nM, and

10nM of thrombin in a final volume of 100µL. Solutions were added into wells on one row of the plate and incubated at 37°C for 3 minutes. Next, 80µL of PRP at 150,000 cells per µL was pipetted into a different row of the 96-well plate and incubated at 37°C for 1 minute. Clotting was initiated by using a multi-channel micropipettor to deliver and mix 20µL of the 5X $CaCl_2$ and thrombin solution with the 80µL PRP. The clotting reactions were allowed to run for 12-15 minutes at 37°C, with shaking every 5 seconds on a microtiter plate reader (Versa Max, Molecular Devices). Readings at 405nm were recorded as kinetic plots and analyzed using SoftMax Pro software. Clotting time was determined as the time to maximum velocity (V_{max}) of the change in turbidity, using 5 data points and approximating the midpoint of the curve to calculate V_{max} (33). The extent of clotting was measured as the volume of supernatant (in µL) remaining over the solid clot.

Determine the range of responses to physiologically relevant thrombin doses in WB:

A fibrometer (BBL®, FibroSystem®) was used to determine clotting time of WB at the various doses of thrombin. The fibrometer system employed is the same as is often used for routine coagulation tests. To measure clotting times, a series of 3X $CaCl_2$ and thrombin mixtures were prepared in Tyrode's buffer with 0.1%BSA to deliver a final concentration of 5mM $CaCl_2$, with concentrations of 0nM, 0.5nM, 1nM, 5nM, 10nM thrombin. These solutions were incubated with 200µL of WB on a fibrometer at 37°C. First, the 3X $CaCl_2$ and thrombin solutions were warmed to 37°C for 3 minutes. In a polypropylene cup beneath the fibrometer probes, 200 µL of WB was incubated at 37°C for 1 minute. Then, 100µL 3X $CaCl_2$ and thrombin were added to WB and the timer bar was simultaneously pressed, dropping the probe into the cup and starting the timer. When a strand of fibrin was picked up by the probe, the circuit was closed,

and the timer was stopped. The total time elapsed from delivery of the thrombin to the first fibrin formation was reported as the clotting time (in seconds).

Examine the architecture of clot structure at different thrombin concentrations:

PRP and WB were allowed to form clots in 96 well plates at various (0nM, 1nM, 0.5nM, 5nM and 10nM) thrombin concentrations as described above and followed by SEM and TEM preparation. SEM and TEM preparation to analyze both surface and interior structures of PRP and WB clots were performed as described in Chapter 2.

Analysis of porosity of PRP and WB clots using colloidal carbon, light microscopy and ImageJ:

PRP and WB clots were allowed to form in the microtiter plate reader at different thrombin concentrations (1nM and 10nM). The clots were then fixed in 1% glutaraldehyde in 0.1 HEPES, pH 7.4 for 30 minutes at RT. The clots were placed in Higgins India black ink that had been diluted 1:5 and soaked overnight at RT. After removal from ink, the clots were washed 3X with 0.1M HEPES. Each clot was then embedded in OCT compound (Triangle Biomedical Science, Inc) and frozen on dry ice. The sections were cut between 7µm and 10µm thick and taken from the center of the clot. They were collected onto with poly-L-lysine coated slides. Each clot was examined and then imaged under a Nikon Eclipse 50i and using PixelLink Megapixel Firewire camera. All photos of each clot were used to reconstruct an image of the entire clot in Adobe® Photoshop® CC. Once the reconstructed images were aligned, they were analyzed in ImageJ. In ImageJ, clot section images were converted to 32-bit grayscale for thresholding. The threshold of the grayscale image was adjusted until only the areas where the

ink had penetrated could be read. The program then calculated the proportion of black area to white area, and was reported as the percent area of the blood clot that was penetrated by ink.

Evaluate the degree of nanoparticle penetration into PRP and WB clots using SEM technique:

FGN-cAu$_{18}$ was prepared as described in Chapter 2. PRP and WB clots were allowed to form in the microtiter plate reader at different thrombin concentrations (1nM and 10nM). Then, they were incubated with FGN-cAu$_{18}$ for 15-20 minutes at 37°C and underwent SEM preparation through mounting onto stubs. The clots were fractured and coated with carbon. The backscattered images were taken at 15kV or 30kV accelerating voltage at low magnification (200X magnification) or high magnification (1000X-2000X magnification). Entire two-dimensional pictures of clot cross sections were reconstructed and assembled with Adobe® Photoshop® CC version 14.1.2 x 32 using images taken at 200X magnification.

Quantifying the penetration of nanoparticles into PRP and WB clots by using silver enhancement (SE) and light microscopy:

The clotting was performed in the microtiter plate reader as described above. Briefly, PRP and WB were clotted with 0nM, 1nM, 5nM and 10nM thrombin solutions before being labeled with FGN-cAu$_{18}$ for 15 minutes followed by fixation in 1% glutaraldehyde in 0.1M HEPES pH 7.4 for 30 minutes at RT. Then, the clots were washed with 0.1M HEPES pH before being embedded in OCT compound and frozen with dry ice. Frozen clots were sectioned on a cryostat (Leica CM 1900) between -18˚C and 20˚C, and the thickness of each section was about 7μm to 10μm thick. They were then picked up on poly-L-lysine coated slides and fixed with 1% glutaraldehyde for 5-10 minutes at RT. Sections were washed and rehydrated with Millipore

double deionized water (MDDW) before being treated with silver enhancement (SE) solution (Sigma-Aldrich). SE solution was prepared freshly by mixing solution A (silver salt) and solution B (initiator) in a 1:1 ratio according to the manufacture's direction. The SE solution was immediately applied to the slides that contained clots labeled with fibrinogen conjugated-gold nanoparticles and allowed to incubate in the dark for 3 to 5 minutes. During this period, the SE solution enlarged the gold colloid label by precipitation of metallic silver to give a high contrast signal visible under light microscopy. After 3-5 minutes, the sections were washed thoroughly with MDDW, fixed with 2.5% of sodium thiosulfate for 2-3 minutes, and then rinsed thoroughly with MDDW. Cover glasses were mounted using VectaMount® permanent media (Vector Laboratory) before being analyzed on a Nikon® TE2000U light microscope under the 4x, 10x, and 20x Plan Apo objectives. Images were captured on PixeLink Megapixel Firewire camera. An entire two-dimensional picture of a clot cross-section was reconstructed using Adobe® Photoshop® CC version 14.1.2 x 32 to assemble images that were taken with either 4x or 10x objectives. To measure the degree of nanoparticle penetration, diameters were measured at the widest dimension of the clot. Penetration of FGN-cAu_{18} was measured as the distance of the deepest silver deposition (determined at 20x) from the nearest edge of the clot. Percent penetration was calculated as the penetration distance divided by the diameter.

Results:

Previous studies have demonstrated the successful development of fibrinogen-conjugated, gold-coated magnetite nanoparticles as a means to target and disrupt activated platelet aggregates in a purified platelet system by exposure to an OMF. However, in a blood clot system, there will be a fibrin network, RBCs, and WBCs in addition to platelets. Hence, building

upon the isolated platelet system, we examined the architecture of PRP and WB clots over a range of physiologically relevant thrombin doses and characterized the range of responses in a normal donor pool. The penetration of nanoparticles into PRP and WB clots will be analyzed through these results, thus confirming whether the nanoparticles can incorporate into thrombi.

Determine the range of normal donor responses to physiologically relevant thrombin doses in PRP:

There were differences between donors that were observed from the PRP clotting curves (Figure 31). For example, the qualities unique to the individuals included baseline OD (due to the lipids in plasma), maximum OD (clot structure), the time to V_{max}, and rate of responses. Even though different donors have different clotting profiles, they still shared common clotting characteristics. First, recalcified PRP did not clot in the absence of thrombin in the microtiter plate assay. Second, PRP clotted between a 0.5nM and 10nM range for all donors. Third, increasing thrombin concentration decreased clotting time. It was observed that clotting time distinguished between low and high doses (Table 1 and Figure 32). Clotting time variation was reduced significantly at higher doses of thrombin (5nM-10nM) (Figure 32). Fourth, the size of the clot increased as the thrombin concentration increased, which was indicated as less supernatant remaining after clotting (Table 2 and Figure 33).

Determine the range of normal donor responses to physiologically relevant thrombin doses in WB:

The microtiter plate reader was also used to study WB clot formation at various thrombin concentrations in parallel with PRP. From our experiment, we observed that even in the absence

of thrombin, recalcified WB clotted. Overall, data from Table 3 and Figure 34 showed that WB clots were larger than PRP clots. Interestingly, various thrombin doses did not strongly influence the size of WB clots. In other words, once WB samples were sufficiently stimulated to clot, the size of WB clots stayed relatively constant between different thrombin concentrations. Minor donor to donor variation was observed in the size of the WB clot among thrombin doses.
The fibrometer method is more often used to study WB clotting rather than the microtiter plate assay. In the presence of a normal RBC count, measurements of visible light transmitted through wells of a microtiter plate cannot be made. The fibrometer measures clot formation by mechanical detection of the clot using a moving probe. Platelet-poor plasma (PPP) was used as a standard control for the fibrometer technique. Clotting time curves from PPP, PRP and WB all showed greater variation between donors at low thrombin doses (0.5nM, 1nM) than at higher doses (5nM, 10nM), where it was essentially eliminated. As the clotting system became more complex, the clotting times decreased (Table 4, Table 5, and Figure 35).

Examine the architecture of PRP clots at different thrombin concentrations:

The above data demonstrate that the normal range of thrombin responses show very similar results at 0.5nM and 1nM. Another cluster of similar results is found at 5nM and 10nM. We therefore defined thrombin doses as “low” at 1nM, and “high” at 10nM, and used these doses in our studies of clot ultrastructure.

When PRP clots were formed at low thrombin concentration, many spaces and pores were observed from the surface of the clots. Also, fibrin strands were loosely packed with low numbers of activated platelets. Observations of the interior of PRP clots were consistent with surface views. Clots contained many spaces, with few activated platelets associated with thick,

long, woven fibrin strands. Thus, low thrombin concentration PRP clots were very porous and might be permeable (Figure 36).

In contrast, PRP clots formed in high thrombin concentrations had surfaces that were tightly packed with many activated platelets and fibrin. No pores or spaces were found on the surface of the clots. The interior of PRP clots at high thrombin concentrations appeared with a lot of thin, chunky fibrin that interacted with many activated platelets to form highly dense networks with small spaces and pores. PRP clots at high thrombin concentrations were less porous and permeable (Figure 37).

Even though there were some slight differences in the number of activated platelets, fibrin diameter, and the number of pores found in the images from different donors, the overall results stayed consistent. Low thrombin concentration PRP clots appeared extremely porous, whereas high thrombin concentration PRP clots were less porous.

Examine the architecture of WB clots at different thrombin concentrations:

At low thrombin concentration, the surfaces of WB clots consisted of biconcave RBCs that were wrapped loosely with fibrin strands. Also, very few activated platelets were found at the exterior of WB clots. Since fibrin wrapped around the RBCs very loosely, there were many open pores that could be seen from the surface views. Inside the clot, biconcave RBCs and fibrin were present throughout. There were still spaces or pores inside WB clots (Figure 38).

At high thrombin concentration, the surface of WB clots contained many RBCs, activated platelets, and fibrin fibers. These components of the WB clot interacted with each other forming a very tight and significantly dense network. There, no such pores or holes could be seen from the surface. Interestingly, from the interior view provided by cross-sectioning, biconcave RBCs

changed their shape into polyhedrons. They seemed to be contracted and squeezed into the core of the clots and arranged side by side next to each other in a way that allowed no space between them. Fibrin and activated platelets were found inside the WB clot; however, the majority of these were accumulated at the clot periphery. High thrombin concentrations formed clots that tended to be impermeable and nonporous (Figure 39).

Three different donors shared very similar results of WB clot structures that formed at different thrombin concentrations. Low thrombin concentration produced open network clots containing biconcave RBCs, fibrin strands, and few activated platelets. In contrast, high thrombin concentration generated WB clots with high numbers of activated platelets, dense fibrin networks at the surface, and polyhedral RBCs in the clot core.

Analysis of the porosity of clots at different thrombin concentrations:

Since low thrombin concentration tended to form PRP clots with porous networks, we expected that these same clots would allow colloidal materials to migrate easily into the clot interior and appear throughout the clot network. Our results testing PRP clots formed at low thrombin concentrations with colloidal carbon met our expectation. The low thrombin concentration PRP clots appeared very dark due to the abundant presence of colloidal carbon. The black color present throughout the frozen cross-sections of the clots indicated that colloidal carbon was able to penetrate from the periphery inwards to the clot interior (Figure 40B). Without colloidal carbon, our control PRP clot looked white or transparent (Figure 40A and C).

With high thrombin concentration formed PRP clots, the colloidal carbon accumulated predominantly at the clot periphery. Few dark spots could be observed inside the clot. However,

the entirety of the clot did not look much different as compared to the control, with the exception of the periphery where the colloidal carbon accumulated (Figure 40D).

The WB clots looked red or pink in color. When a WB clot was stimulated with 1nM thrombin and soaked overnight with colloidal carbon, the carbon dye was able to penetrate into the clot through the pores and open spaces. We observed that most of the dye was present outside of the frozen cross-sections. Moving toward the center of the frozen cross-sections, dye concentration was significantly decreased, as was indicated by the lessening appearance of black color inside the clot. In addition, there was no colloidal carbon found at the center of the clot (Figure 41B). The size of WB clots formed at higher thrombin concentrations was larger in comparison to the size of clots formed at low thrombin concentrations. Also, the frozen cross-sections revealed a highly dense network. This was indicated by the intact samples and less tearing apart when sectioning. Moreover, the colloidal carbon was limited in its distance of migration into WB clots formed at high thrombin concentration. Colloidal carbon resided only at the periphery of the WB clot and none of it was able to move into the interior of the WB clot (Figure 41D). In the WB clot control samples, no colloidal carbon was observed, and the samples looked pink and red in color (Figure 41A and C).

Quantitative data of the percent area of the PRP clots penetrated by colloidal carbon was measured by the threshold function of ImageJ. Results from three different donors showed that low thrombin concentration formed clots had a higher percentage of area positive for colloidal carbon compared to high thrombin concentration formed clots, which had a lower percent of area containing colloidal carbon. For PRP clots, the average was 12% colloidal carbon for 1nM thrombin and 8.78% colloidal carbon for 10nM thrombin. For WB clots, there was an average of 3.57% and 1.55% of colloidal carbon areas for 1nM and 10nM thrombin, respectively. Also, as

the systems became more complex, the percent of area containing colloidal carbon decreased. Here, we observed that the percent of colloidal carbon positive areas in PRP clots was higher when compared with WB clots. Additionally, more donor to donor variation in the percent of area containing colloidal carbon areas in PRP clots was observed than in WB clots (Table 6, Figure 42).

Describe the penetration of nanoparticles into clots at different thrombin concentrations:

Since the three donors shared very similar characteristics in the penetration of colloidal materials into clots at different thrombin concentrations, Donor 1 samples were chosen as representative of the general observations relating to the degree of nanoparticle penetration.

When low thrombin concentration PRP clots were labeled with FGN-cAu_{18}, the labeling was found throughout PRP clots. It was easy to find and observe the nanoparticles using SEM analysis. High nanoparticle concentration was found at the outside edge of the clot. Moving into the middle of the sample, the nanoparticle concentration slightly decreased. Nanoparticles were able to migrate all through the clot to a final localization at the center (Figure 43). In high thrombin concentration PRP clots, nanoparticles were again found both at the clot periphery and interior. However, it was harder to recognize nanoparticles in the interior of the clot using the SEM since they occurred in low concentrations (Figure 44).

In WB clots formed at low and high thrombin concentration, the majority of nanoparticles were localized to the peripheral area of the clots. In low thrombin concentration WB clots, few nanoparticles were able to migrate into the clot interior, resulting in a limited depth of penetration and internal concentration of FGN-cAu_{18} (Figure 45). In terms of high

thrombin concentration WB clots, it was extremely rare to find any nanoparticles at the center of the clots, thus nanoparticle penetration was restricted to the clot periphery (Figure 46).

There were several general observations from data that were collected from three different donors. First, nanoparticle concentration was always higher at the periphery for both PRP and WB clots. Second, the number of nanoparticles was reduced as we looked further into the interior of the clot. Third, more nanoparticles were able to penetrate into PRP clots and less nanoparticles were able to penetrate into WB clots. The SEM results from three donors were consistent in terms of overall depth of nanoparticle penetration and concentration (Figure 47-50).

Quantify nanoparticle penetration into PRP and WB clots using silver enhancement:

Since we only roughly estimated the nanoparticle penetration by using SEM, here we sought to quantify the degree of nanoparticle penetration from various donors using silver enhancement (SE) and light microscopy.

1. SE and light microscopy as a quick screening method for nanoparticle penetration:

In FGN-cAu_{18} labeled PRP clot cross-sections, without the treatment of SE the periphery of the clot looked pink and the interior of the clot looked white or transparent. With the use of SE, the borders of the clots appeared to be darker or black instead of pink, and some dark spots were scattered throughout the clot. The black areas indicated the presence of metallic silver deposited at the site of the FGN-cAu_{18} labeling. In the control samples, which lacked the labeling of FGN-cAu_{18}, with SE treatment, a few minor artifacts were observed; however, in comparison with the absence of SE treatment, there were no significant differences between these samples (Figure 51). In regard to the WB clot samples, SE improved the contrast between the red color of the WB

and the pink color of gold nanoparticles; thus, SE provided a better visualization of the difference between WB and gold nanoparticles within the sample. In the presence of SE, gold nanoparticles appeared black in color instead of the pink that was commonly observed in the samples without the treatment of SE. Again, in the control without gold and with or without SE, the sample was pink in color (Figure 51). Using the SE and light microscopy method usually allowed us to obtain data within the same day of the experiment. As a result, data analysis could be done the day following the experiment.

2. SE and light microscopy in studying clot network structure and nanoparticle penetration:

PRP and WB clots were formed at different thrombin concentrations (0.5nM, 1nM, 5nM, and 10nM) to observe the fibrin network density. Also, these PRP and WB clots were labeled with FGN-cAu_{18} to quantify the degree of nanoparticle penetration into clots at different thrombin concentrations.

In PRP, low thrombin concentration (0.5nM and 1nM) clots had smaller diameters, more pores, and open spaces inside; whereas, high thrombin concentration (5nM and 10nM) clots had larger diameters and contained less internal spaces, fewer pores, and a denser fibrin network within the clots. Also, it was observed that nanoparticles were found both outside and inside of clots formed at low thrombin concentrations; in contrast, the nanoparticles were limited to the edge of clots formed with high thrombin concentrations. These were reflected by the calculations of percent nanoparticle penetration into clots. By using the deepest distance of the nanoparticle penetration divided for the largest diameter of the clot, we calculated the percent of nanoparticle penetration into 0.5nM, 1nM, 5nM, and 10nM PRP clots of example donor 5 were 35%, 23%, 8.3% and 4% respectively (Figure 52).

In WB, both low and high thrombin concentration clots were tightly packed with RBCs in addition to the fibrin network. Not many spaces nor pores were found within the WB clots. The nanoparticle penetration was mostly limited to the periphery of the WB clot. It was slightly deeper when the WB clot was formed with low thrombin concentration. Using Donor 5 as an example, there were about 22% and 18% of nanoparticle penetration for 0.5nM and 1nM thrombin clots, respectively. The nanoparticle penetration was reduced to 14% and 11% for 5nM and 10nM thrombin clots (Figure 53).

3. Quantify the nanoparticle penetration using silver enhancement and light microscopy:

The diameter of the clots increased as the thrombin concentration increased for all six donors in both PRP and WB clots. Also, WB clots appeared bigger in size compared to PRP clots. For PRP, the average of diameter of clots from six donors was 1.68mm, 1.86mm, 2.1mm, and 2.45mm for concentrations of 0.5nM, 1nM, 5nM and 10nM thrombin, respectively. In WB clots, average diameters were 2.39mm, 3.09mm, 3.03mm, and 3.56mm for concentrations of 0.5nM, 1nM, 5nM, and 10nM thrombin, respectively. We also observed that both the distance of maximum nanoparticle penetration and percent of nanoparticle penetration were inversely related to thrombin doses. In other words, as thrombin concentration increased, there was a decrease in the depth of nanoparticle penetration. The average of distance of migration from the six donors' PRP clots at different thrombin concentrations were 0.45mm, 0.39mm, 0.27mm, and 0.22mm for 0.5nM, 1nM, 5nM, and 10nM of thrombin, respectively. For WB clots, the average distance of nanoparticle migration was 0.43mm, 0.49mm, 0.297mm, and 0.3mm formed using 0.5nM, 1nM, 5nM and 10nM of thrombin, respectively. For the percent of nanoparticle penetration, the averages were 18.1%, 15.8%, 9.58%, and 8.11% for 0.5nM, 1nM, 5nM, and 10nM thrombin

formed PRP clots; whereas, the averages were 26.17%, 19.61%, 12.58%, and 9.57% for the percent of nanoparticle penetration in WB clots formed at 0.5nM, 1nM, 5nM, and 10nM, respectively (Tables 7 and 8).

The graph of thrombin concentration versus percent of nanoparticle penetration was created based on the data from Tables 7 and 8. In PRP clots, there was a higher degree of donor to donor variation in percent of nanoparticle penetration. The variation in percent of nanoparticle penetration was reduced at higher thrombin concentration. In WB clots, donor to donor variation in percent of nanoparticle penetration decreased. Also, the percent of nanoparticle penetration between low and high thrombin concentration-formed clots was only slightly different. In addition, WB clots showed lower percent of nanoparticle penetration than PRP clots (Figure 54).

Discussion:

The use of fibrinogen-conjugated gold nanoparticles to target PRP and WB clots *in vitro* was evaluated with an emphasis on describing the architecture of PRP and WB clots over a range of physiologically relevant thrombin doses including characterization of the range of responses in different donors and investigation of the penetration of nanoparticles into the clots. First, the normal range of normal donor responses to physiologically relevant thrombin doses was determined between 0nM and 10nM thrombin for our blood clotting system. We also further categorized them into two distinct groups. Low doses of thrombin were indicated at 1nM or below and high doses of thrombin were between 5nM and 10nM. Low doses of thrombin were similar in their characteristics of longer clotting time, lower maximum OD, and variation in clotting between donors. High doses of thrombin showed extremely shorter clotting time, higher maximum OD, and greater consistency in clotting between donors. With these results, we

learned to expect that low thrombin concentrations would enhance differences between donors and high thrombin concentrations would reduce such variations. Second, the availability of thrombin at the time of clotting strongly influences the architecture of PRP and WB clots. High thrombin concentration produced less porous, highly compact and stable clots; whereas, low thrombin concentration generated loose, more porous, and unstable clots. The stability of a clot affects how easily the clot can be dissolved or disrupted *in vivo.* Hence, high thrombin concentration clots will be well protected from fibrinolysis and nanoparticle penetration. In contrast, clots formed at low thrombin concentrations will be permeable and highly susceptible to fibrinolysis and nanoparticle penetration. Third, nanoparticle penetration was highly impacted by the density and organization of blood clot components. The depth of nanoparticle penetration was limited to the periphery of the clot when it contained a denser fibrin network and more activated platelets and RBCs. *In vivo*, thrombi are expected to be even more complex and closely packed with proteins and blood cell components. Thus, it is reasonable to expect that *in vivo* (1) no, or only a few, nanoparticles could migrate into the interior of the clots and (2) the depth of nanoparticle penetration could be limited to the clot edge. These observations proved that nanoparticles can be incorporated into preexisting clots such as those that form occlusions. However, in order to improve the efficiency of nanoparticle penetration and concentration, we may need to optimize the labeling procedures. Also, multiple applications of nanoparticles may provide better outcomes. Fourth, there was variation in the percent of nanoparticle penetration between different donors. However, we observed that at higher thrombin concentrations in the WB clot system, the variation between donors was almost eliminated. At a high thrombin dose (10nM), variation between different donors was minimal. This means that the potential

therapeutic effect of nanoparticles used to target an occlusive clot *in vivo* could be consistent between patients.

Determine the range of normal donor responses to physiologically relevant thrombin doses:

Different labs prefer different doses of thrombin as the routine stimulus of *in vitro* clot formation. Thus, depending on the purposes of a given experiment, particular thrombin concentrations can be used. Thrombin is a potent coagulant produced by the cleavage of prothrombin by factor Xa. Thrombin is then actively involved in clot formation and is not directly measurable as a circulating protein. Rather, prothrombin time assays are used to measure the time it takes for a clot to form. Therefore, determining the exact thrombin concentration is still very challenging. Many studies use large ranges of thrombin concentrations to observe its impact on fibrin clot structures *in vitro*, some between 0.0055nM and hundreds of nM. Some fibrinogen assays even used thrombin concentrations above hundreds of nM that cannot be found in normal plasma (34-38). Our experiments are interested in looking at donor responses to physiologically relevant thrombin doses. Hence, concentrations between 0nM and 10nM thrombin were investigated.

In PRP, clotting curve profiles from different donors were unique. Clotting curves may vary by day, or even hour, with the same donor. This could be due to many factors such as diet, time of blood draw, daily stress, and amount of available proteins, lipids, and other blood components in circulation. The microtiter plate reader experiments were able to demonstrate that 0.5nM and 1nM of thrombin doses shared similar clotting characteristics including longer clotting time and lower maximum OD_{405}. Also, 0.5nM and 1nM thrombin clots appeared smaller in size. In comparison, clots formed with 5nM and 10nM thrombin had shorter clotting times and

were larger. Subsequent analysis showed that clots that produced higher maximum OD_{405} values has dense fibrin networks. At 5nM and 10nM thrombin, the clotting times and maximum OD_{405} values were consistent, with minimal variation between donors.

Our study using the fibrometer method resulted in similar findings. More variation in clotting time versus log thrombin concentration at 0.5nM and 1nM was observed, compared to the variation in clotting time versus log thrombin concentration at 5nM and 10nM. As the system became more complex, the clotting time was reduced significantly. WB had the shortest clotting time compared to PPP and PRP.

Together, we concluded that 0.5nM and 1nM could be grouped and considered as low thrombin doses, while 5nM and 10nM could be considered as high thrombin doses. Since 0.5nM appeared more inconsistent in clot formation, 1nM thrombin was preferred as an experimental low dose. Thus, 1nM and 10nM were chosen to represent low and high thrombin doses in the study of clot structure and its effects on nanoparticles throughout this chapter. Moreover, concentrations above 100nM thrombin were not considered for our study because they are not representative physiologically and might not occur *in vivo*. It is possible that different clotting characteristics between donors such as clot density, and clotting times might be completely overcome at overdoses of thrombin. Therefore, we might not be able to investigate the effects of thrombin doses in clot formation.

Examine the architecture of clots at different thrombin concentrations:

Most previous studies have examined fibrin clot formation in the absence of cells or else in purified platelet systems (1,17,36,39). Here, our study reveals additional information on how

fibrin, activated platelets and RBCs associate with each other to form clots under physiologic thrombin concentrations.

In PRP, low thrombin concentration resulted in fibrin and a few platelets loosely packed into a porous network. High thrombin concentration allowed clots to form with fibrin and many activated platelets tightly packed together into a dense network. At low thrombin concentration, WB clots consisted mostly of fibrin loosely wrapped around biconcave RBCs, with a few activated platelets throughout the clot. At high thrombin concentration, WB clots consisted of highly branched fibrin with many activated platelets at the surface, while polyhedral RBCs resided compactly at the core. Due to the differences in blood components between PRP and WB, the clots' structure and organization of blood components were different. In PRP, fibrin and activated platelets interacted with each other and appeared throughout clot. Since PRP is a less complex system, the clot tended to be smaller in size with more open spaces. In WB, especially at high thrombin concentration, fibrin and activated platelets organized at the periphery of the clots and RBCs were squeezed into the interior. In general, WB formed larger clots that were highly compacted and less porous. These experiments used blood obtained from three different donors. The results obtained were consistent between donors.

These results suggested that clots formed at low thrombin concentrations might be more permeable and less protected from fibrinolysis compared to clots formed at high thrombin concentrations. Also, WB clots would be more of a challenge for both fibrinolysis and penetration by nanoparticles compared to PRP clots. We expect thrombi found *in vivo* would have similar characteristics to the experimental clot formed with the combination of high thrombin concentration and WB complexity.

Analysis of clot porosity at different thrombin concentrations:

A perfusion chamber is commonly used to determine the porosity of the clot *in vitro* (40-42). The flow, shear, and pressure can be adjusted to mimic physiologic conditions found *in vivo*. Then, the volume can be collected to report the porosity, permeability, and diffusivity of the clots. Setting up the flow through to be like *in vivo* conditions requires the assembling of a perfusion apparatus, and optimizing and motoring the rate of flow, shear and pressure. Here, our experiments utilized a rough measurement of clot porosity with a simple system. We soaked the clots in colloidal carbon, visualized the porosity of clots with light microscopy, and quantified the porosity of clots with ImageJ. Although our model is static, our goal was to evaluate the different porosity of clots formed at different thrombin concentrations, so we did not expect that introducing flow and shear would be necessary to address the question. Also, the presence of shear and flow could have made the system more complicated and difficult to evaluate.

Observations of the architecture of clots formed at different thrombin concentrations were made. Clots formed at low thrombin concentrations appeared porous and hollow inside; whereas, clots were less porous and not hollow when formed at high thrombin concentrations. In addition, the more complex in components the clots were, represented by WB clots in our experiments, the less pores and internal spaces were found inside of the clots. Our results regarding the porosity of clots at different thrombin concentrations supported these observations. The PRP clots formed at low thrombin concentrations had more pores, and thus colloidal carbon was able to occupy a greater percentage of the clot area. WB clots formed at high thrombin concentrations had results at the opposite end of the spectrum compared to the PRP clots formed at low thrombin concentrations. We found less area occupied by colloidal carbon inside of these clots. That means WB clots formed with high thrombin concentrations had less porosity. The

porosity of the clots can be used to predict the stability of clots in fibrinolysis (31, 32) and we expect it will also predict the efficiency of using nanoparticles to label the clots. With more open network and pores, these clots allow for proteins, or our labels, to be able to penetrate and interact with their targets inside of blood clots. The access of the labels or proteins could have limited entry to the clot interior if the clots were solid and less hollow and porous.

In vivo, we expect that the thrombi would result from local thrombin concentration in the range of our high dose or even above (17, 43) and would be likely to resist fibrinolysis and nanoparticle penetration. These clots would appear less porous and hollow in the interior of the clots. Thus, these results imply that using nanoparticles to target the activated platelets in the clots would mainly occur at the clot surface.

Describe the penetration of nanoparticles into clots at different thrombin concentrations:

The degree of nanoparticle penetration into clots depended on both the thrombin concentration available at the time of clotting and the complexity of blood clot components. Different fibrin organizations resulted from clotting with different thrombin doses, which in turn determined penetration depth of fibrinogen-conjugated nanoparticles into the clots. The penetration of nanoparticles was inversely related to thrombin concentration. High thrombin doses produced a dense network of small diameter fibrin filaments. This phenomenon prevented nanoparticle penetration. Low doses produced a more open network of large diameter fibers; thereby, allowing nanoparticles to migrate deep into the interior of the clots. The extent of nanoparticle penetration was also inversely related to the density of the fibrin network and the number of activated platelets and erythrocytes. Nanoparticle penetration was found at both the

periphery and interior of PRP clots; whereas, nanoparticle migration was limited to the outer edge of WB clots.

WB clots at high thrombin concentration were impermeable; thereby, they resisted nanoparticle penetration. Previously, we demonstrated that high thrombin concentration WB clots contain many activated platelets at the periphery, and fewer in the interior of the clots. We propose using fibrinogen-conjugated nanoparticles to target only the activated platelets in the occlusive clots. Hence, FGN-cAu$_{18}$ still interacted with many activated platelets on the clots' surface even though the clots might have been tightly packed without spaces and pores internally. Also, it is possible that there was an extremely low number of nanoparticles that were able to penetrate deep into the clots due to fewer activated platelets and high resistance to penetration. The success of our magnetic nanoparticle-induced hyperthermia to disrupt occlusive clots requires both depth of nanoparticle penetration and concentration. Therefore, in order to bring nanoparticles into the interior of clots, we might need multiple rounds of labeling and subsequent exposure to the OMF. This would, step by step, slowly destroy activated platelets from the clot periphery to the interior. Eventually, clots would become small in size and no longer able to block blood flow. In terms of polyhedral RBCs at the clot center, we anticipate that they will bounce back into biconcave-shaped individuals and flow away in circulation.

The shear stress observed within the circulatory system is an important factor in the complex and dynamic human *in vivo* environment that might strongly impact the effectiveness of nanoparticle penetration and delivery. First, shear stress can change the interaction between cells and nanoparticles (44, 45). Thus, it is possible that a reduction in the binding strength between nanoparticles and activated platelets could occur if there are increasing shear forces experienced by the nanoparticles. Second, the flow can influence the distribution of nanoparticles in the

plasma by preventing gravitational settling (45, 46). Third, shear stresses found *in vivo* could induce changes in the morphology of clots including the thickness of fibrin, the tightness of clot structures, and the presence of additional blood components (47- 49). These changes could decrease the efficiency of nanoparticle penetration into clots.

Human bodies are a highly complex system and possess a dynamic environment that will represent a challenge for nanoparticle delivery and penetration. By evaluating nanoparticle penetration in classic stasis *in vitro*, these conditions might be oversimplified and lead to an overall low predictability towards their behavior clinically. If possible, shear stress should be taken into account in the continued study of nanoparticle penetration into occlusive clots. These findings will have important implications in the development of nanoparticle delivery strategies for disrupting clot formation and enhancing clot dissolution.

Quantify nanoparticle penetration into clots using silver enhancement:

The screening method utilizing silver enhancement and light microscopy was used to quantify the nanoparticle penetration into clots from donors in our pool. Silver enhancement with light microscopy has advantages over SEM. It is less time consuming in sample preparation; thereby, shortening the time of analysis. Also, silver enhancement is considered less expensive in terms of reagents and equipment. Moreover, SEM requires extensive training. However, there are some limitations in using silver enhancement to observe nanoparticles in clots. First, unspecific binding of metallic silver onto samples can cause artifacts if the samples were exposed too long with silver enhancement or the samples were not washed thoroughly before the application of silver enhancement reagents. Second, since nanoparticles are below the resolution limit of compound light microscopy, single nanoparticles might be undetectable. However, silver

enhancement is very good for detecting small clusters of nanoparticles, and our method of disrupting clots depends on high nanoparticle concentration residing inside of the clots. It is still valid to utilize silver enhancement to assist our analysis.

In both PRP and WB systems, different donors showed different percentages of nanoparticle penetration. The differences appeared more varied at lower thrombin doses (0.5nM and 1nM). As thrombin concentration increased, a reduction in nanoparticle penetration was observed. At high thrombin concentrations (10nM), the differences in nanoparticle penetration between donors was significantly diminished. In addition, WB clots had lower percent nanoparticle penetration and less donor variation compared to PRP clots. Taken together, this data suggests that at thrombin concentrations similar to those in thrombi formation, nanoparticle penetration might occur to the same degree in different individuals, and the potential therapeutic effect could be consistent between patients.

Expected *in vivo* application:

These results provided several important insights into how the architecture of PRP and WB clots over a range of physiologically relevant thrombin doses influences nanoparticle penetration. The complex structure of PRP and WB clots is challenging for nanoparticle penetration due to the presence of fibrin and RBCs. However, our results suggested that fibrinogen-conjugated nanoparticles are able to penetrate into clots even in the more challenging WB clot system. Since the WB clot is the best representation of the physiologic clot found *in vivo*, it can serve as a platform to predict the efficiency of nanoparticle penetration into occlusive clots *in vivo*. In addition, in terms of the pathological conditions of ischemic stroke, we expect that local thrombin concentration will be at the high end of the physiological range, or elevated

above it. As a result, occlusive clots will contain a high-density fibrin network associated with many activated platelets on the exterior, wrapped around a core of RBCs. These factors can cause clots to become protected from fibrinolysis and penetration of externally applied nanoparticles. In order to overcome the limits of nanoparticle penetration into WB clots, we might need to optimize the labeling concentration, time of incubation, or even use multiple nanoparticle applications to improve both nanoparticle concentration and penetration inside of clots *in vivo*.

Furthermore, we experienced that at high thrombin concentrations in a WB system, variation of nanoparticle penetration was significantly reduced between donors. This means that at thrombin concentrations like those that may be found at the thrombus causing an ischemic stroke, variability could be minimized. So *in vivo* or even clinically, we expect that the potential therapeutic effect would be consistent between individuals.

In vivo, the presence of shear stress in blood flow is another aspect that should be taken into account since we did not address this in our static *in vitro* experiments. The contribution of flow and shear would potentially add layers of complexity and dynamics to our system, but it would provide a better model of *in vivo* conditions. It is possible that flow and shear could influence clot structure and the efficacy of nanoparticle penetration. This could produce considerable challenges and lead us to modify our conclusions of how efficient a nanoparticle-based therapeutic for treating ischemic stroke can be.

Figures and Figure Legends:

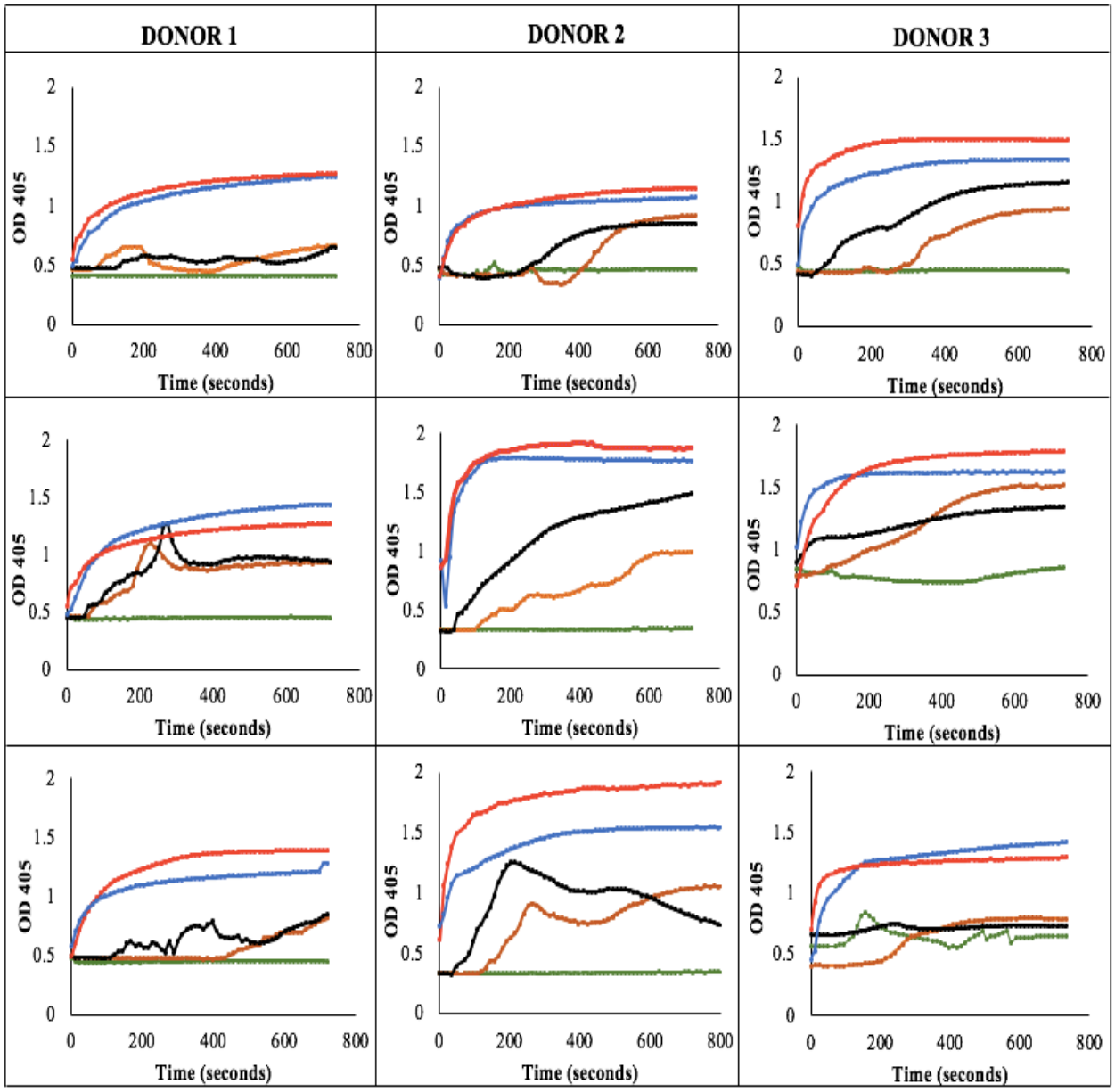

Figure 31

Figure 31. PRP clotting curves from different donors using various thrombin concentrations. These experiments were done using three different normal donors, each tested on three different days. Green, orange, black, blue and red lines represent 0nM, 0.5nM, 1nM, 5nM and 10nM respectively. In the absence of thrombin, no significant clotting is observed in any donors. 0.5nM to 10nM thrombin concentration can be considered as a physiologically relevant clotting range *in vitro*. In general, little difference is observed between 0.5nM and 1nM, but the responses are qualitatively different from those seen with 5nM and 10nM. Similarly, little difference is seen between 5nM and 10nM. Therefore, 0.5nM and 1nM can be considered to represent a "low" thrombin dose, and 5nM and 10nM can be considered to represent a "high" thrombin dose. For low thrombin concentration clotting curves, the overall maximum OD_{405} value was lower than the overall maximum OD_{405} value of high thrombin concentration clotting curves. Also, the rate of response with high thrombin doses was faster, indicated by shorter lag times and steeper slopes.

Donor 1 - Time to Vmax (seconds)			
[Thrombin]	**Exp #1**	**Exp #2**	**Exp #3**
0.5nM	1025	212	900
1nM	1183	245	849
5nM	58	53	33
10nM	48	56	37
Donor 2 - Time to Vmax (seconds)			
[Thrombin]	**Exp #1**	**Exp #2**	**Exp #3**
0.5nM	911	405	295
1nM	521	214	157
5nM	40	46	27
10nM	42	27	22
Donor 3 - Time to Vmax (seconds)			
[Thrombin]	**Exp #1**	**Exp #2**	**Exp #3**
0.5nM	560	289	449
1nM	166	208	291
5nM	32	20	48
10nM	23	26	26

Table 1. Clotting time data obtained from PRP clotting curves measured in microtiter plate reader experiments. Clotting times vary at lower thrombin concentrations (0.5nM-1nM). Higher thrombin doses reduce variation in clotting times.

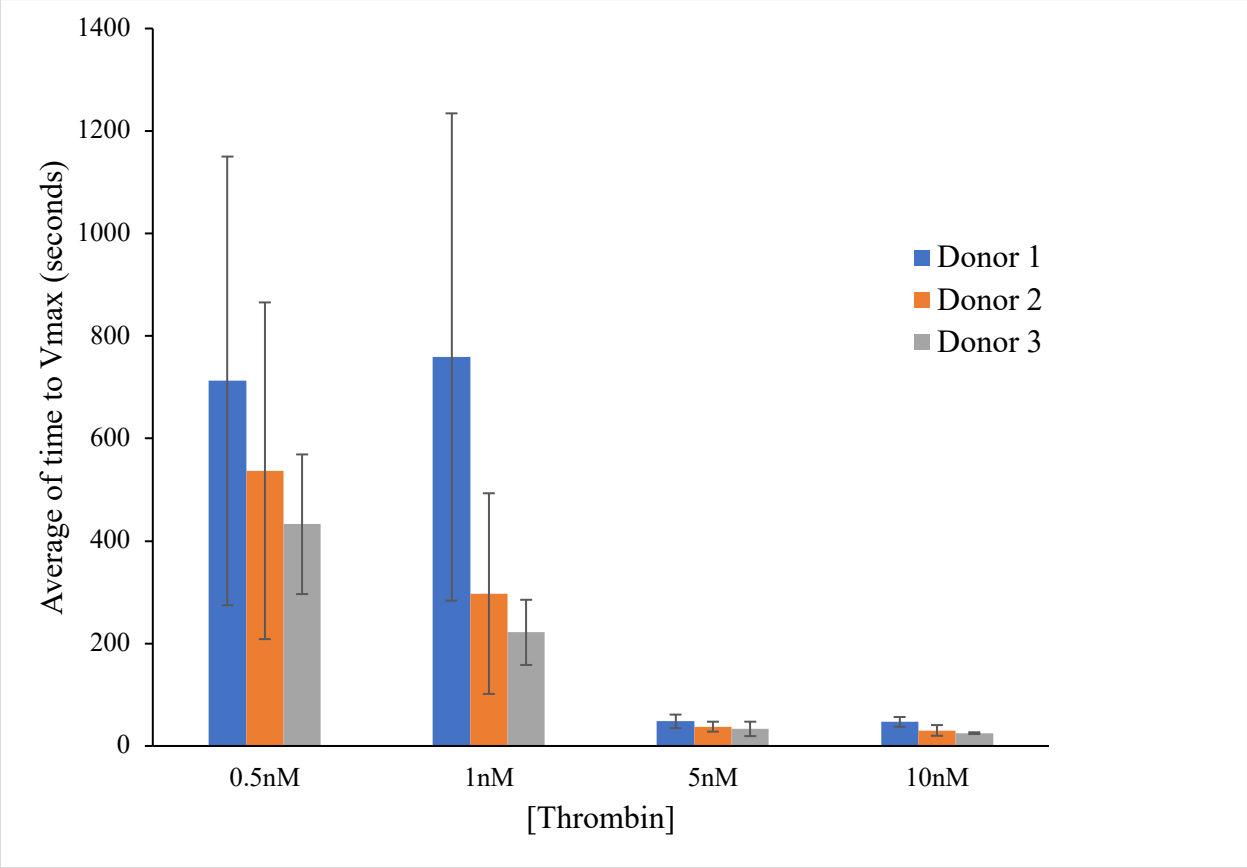

Figure 32. Time to V_{max} in response to different doses of thrombin. Increasing thrombin concentration decreased clotting time. Day to day variation for a single donor was as great as donor to donor variation at low doses of thrombin. Clotting time variation was eliminated at higher doses of thrombin. The graph was created from the data shown in Table 1. The time to V_{max} was averaged for each donor at each concentration. Error bars represent standard deviation.

Donor 1- PRP Supernatant (µL)			
[Thrombin]	**Exp #1**	**Exp #2**	**Exp #3**
0nM	99	100	91
0.5nM	75	84	79
1nM	70	74	75
5nM	65	70	75
10nM	58	69	40
Donor 2- PRP Supernatant (µL)			
[Thrombin]	**Exp #1**	**Exp #2**	**Exp #3**
0nM	90	100	94
0.5nM	80	84	71
1nM	68	74	67
5nM	54	69	62
10nM	51	67	58
Donor 3- PRP Supernatant (µL)			
[Thrombin]	**Exp #1**	**Exp #2**	**Exp #3**
0nM	100	99	80
0.5nM	75	81	71
1nM	75	74	51
5nM	76	70	37
10nM	76	67	31

Table 2. Volume of supernatant remaining after PRP clot formation. Data correspond to the experiments report in Table 1 and Figure 32. Increasing the thrombin concentration reduced the volume of plasma remaining after clotting, indicating a greater percentage of clotting occurred. That is, a lower volume of residual plasma indicated larger clot sizes. Total starting volume used was 100µL.

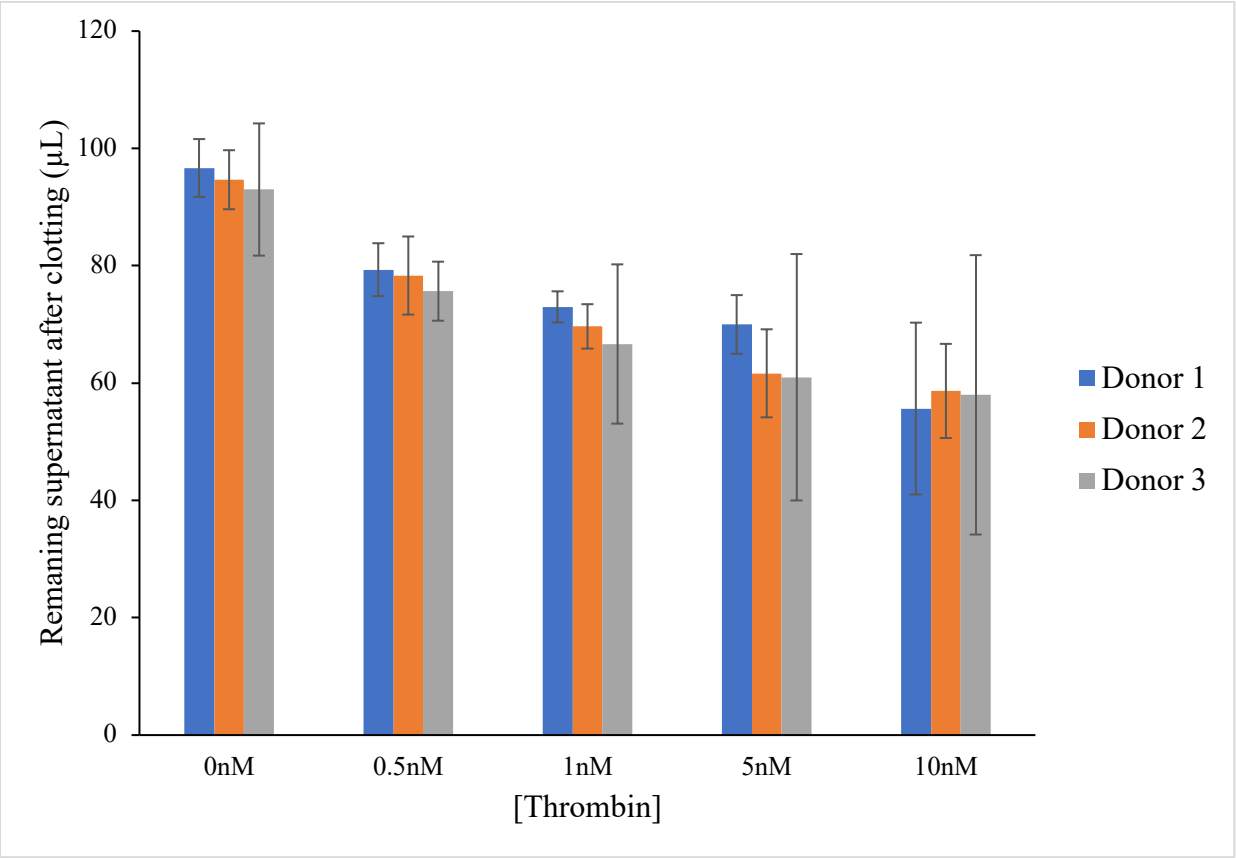

Figure 33. The volume of supernatant remaining after PRP clots formed at different thrombin concentrations. This graph was generated from data shown in Table 2. Increasing thrombin concentration generally decreased the residual plasma after PRP clotting, indicating larger clots. Error bars represent standard deviation.

Donor 1- WB Supernatant (µL)			
[Thrombin]	**Exp #1**	**Exp #2**	**Exp #3**
0nM	46	45	46
0.5nM	40	38	36
1nM	45	41	42
5nM	46	42	37
10nM	44	38	38
Donor 2- WB Supernatant (µL)			
[Thrombin]	**Exp #1**	**Exp #2**	**Exp #3**
0nM	45	53	63
0.5nM	46	59	47
1nM	45	54	51
5nM	46	54	50
10nM	40	53	49
Donor 3- WB Supernatant (µL)			
[Thrombin]	**Exp #1**	**Exp #2**	**Exp #3**
0nM	54	52	48
0.5nM	56	60	59
1nM	54	61	54
5nM	54	52	51
10nM	44	50	54

Table 3. Volume of supernatant remaining after WB clots formed, obtained from samples clotted in the microtiter plate reader in parallel with PRP samples. Data are from the same three normal donors tested on the same three days. As thrombin concentration increased, the amount of residual supernatant changed only slightly, but much less than was observed in the PRP system. Clot sizes among thrombin doses was relatively consistent, including in the absence of thrombin. Clots were larger than the corresponding PRP clots at every thrombin concentration. Total starting volume used in the experiment was 100µL.

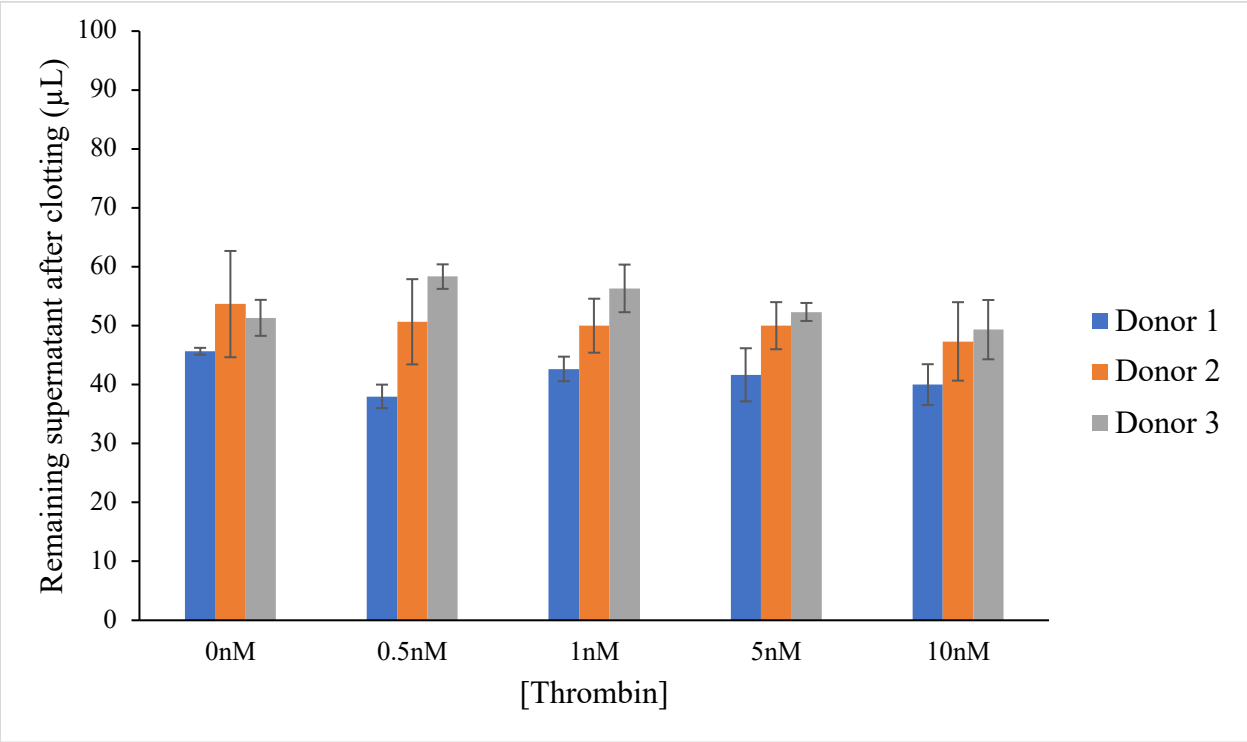

Figure 34. The volume of supernatant remaining after WB clots formed at different thrombin concentrations, obtained from the microtiter plate reader experiments. This graph was constructed from data in Table 3. When thrombin concentration increased, the amount of remaining supernatant left over slightly changed. The variation in clot size seemed consistent among thrombin doses. Less volume indicated bigger clot size. The total volume used in starting experiment was 100µL. Error bars represent standard deviation.

	Clotting Time (seconds)								
Donor 1	**Exp #1**			**Exp #2**			**Exp #3**		
[Thrombin]	**PPP**	**PRP**	**WB**	**PPP**	**PRP**	**WB**	**PPP**	**PRP**	**WB**
0nM	no clot	332.7	195.9	no clot	240	216.4	no clot	234	106.9
0.5nM	277.4	250.8	96.4	219	189.9	100.9	197.9	159	98.5
1nM	120.4	97.9	73.9	187.9	115	59.4	191.4	97	67.2
5nM	21.9	20.9	19.9	22	20.4	18.9	20.9	21	18.9
10nM	12.9	12.9	2.7	16	11.4	11.5	18.4	18	10.6
Donor 2	**Exp #1**			**Exp #2**			**Exp #3**		
[Thrombin]	**PPP**	**PRP**	**WB**	**PPP**	**PRP**	**WB**	**PPP**	**PRP**	**WB**
0nM	no clot	686.9	122.5	no clot	371.7	273.5	no clot	222.4	195.9
0.5nM	231.4	350.5	119.4	228	183.4	264.4	237.4	163.9	96.4
1nM	170.5	120.3	50	179	135.4	108.9	231.4	101.9	73.9
5nM	21	19.9	17	29.4	29	22	31.4	26.4	19.9
10nM	18.9	18.9	10	25.9	19.4	14.4	21	14.9	11.7
Donor 3	**Exp #1**			**Exp #2**			**Exp #3**		
[Thrombin]	**PPP**	**PRP**	**WB**	**PPP**	**PRP**	**WB**	**PPP**	**PRP**	**WB**
0nM	no clot	222.4	171.9	no clot	180.4	179.4	no clot	332.1	97.4
0.5nM	315.5	163.9	86.9	217.4	167.5	153.4	227.4	167.5	96
1nM	208.9	121.9	73.3	209.9	110.9	101.3	200.9	101.9	74.9
5nM	35.3	26.4	18.4	34.9	27.5	21.4	30.1	19.9	18.9
10nM	17.3	14.9	4.3	21.5	21	12.9	19.9	18.9	9.7

Table 4. The clotting time data obtained from the fibrometer experiments. The table shows the clotting time (in seconds) for platelet poor-plasma (PPP), platelet rich-plasma (PRP), and whole blood (WB) that were collected from three different donors tested on each of three different days. In general, PPP had the longest clotting time and WB had the shortest clotting time. In addition, thrombin concentration strongly influenced the clotting time. 0nM, 0.5nM, and 1nM thrombin had prolonged clotting time; whereas, 5nM and 10nM had significantly reduced clotting time.

PPP		Mean Clotting Time (seconds)		
[Thrombin]	**Log [Thrombin]**	**Donor 1**	**Donor 2**	**Donor 3**
0.5nM	-0.3	231.4	232.3	253.4
1nM	0.0	166.6	193.6	206.6
5nM	0.7	21.6	27.3	33.4
10nM	1.0	15.8	21.9	19.6
PRP		**Mean Clotting Time (seconds)**		
[Thrombin]	**Log [Thrombin]**	**Donor 1**	**Donor 2**	**Donor 3**
0.5nM	-0.3	199.9	232.6	166.3
1nM	0.0	103.3	119.2	111.6
5nM	0.7	20.8	25.1	24.6
10nM	1.0	14.1	17.7	18.3
WB		**Mean Clotting Time (seconds)**		
[Thrombin]	**Log [Thrombin]**	**Donor 1**	**Donor 2**	**Donor 3**
0.5nM	-0.3	98.6	160.1	112.1
1nM	0.0	66.8	77.6	83.2
5nM	0.7	19.2	19.6	19.6
10nM	1.0	8.3	12.0	9.0

Table 5. The average clotting time of PPP, PRP, and WB calculated from Table 4. These averaged data were used to graph the clotting time versus log thrombin concentration shown in Figure 35.

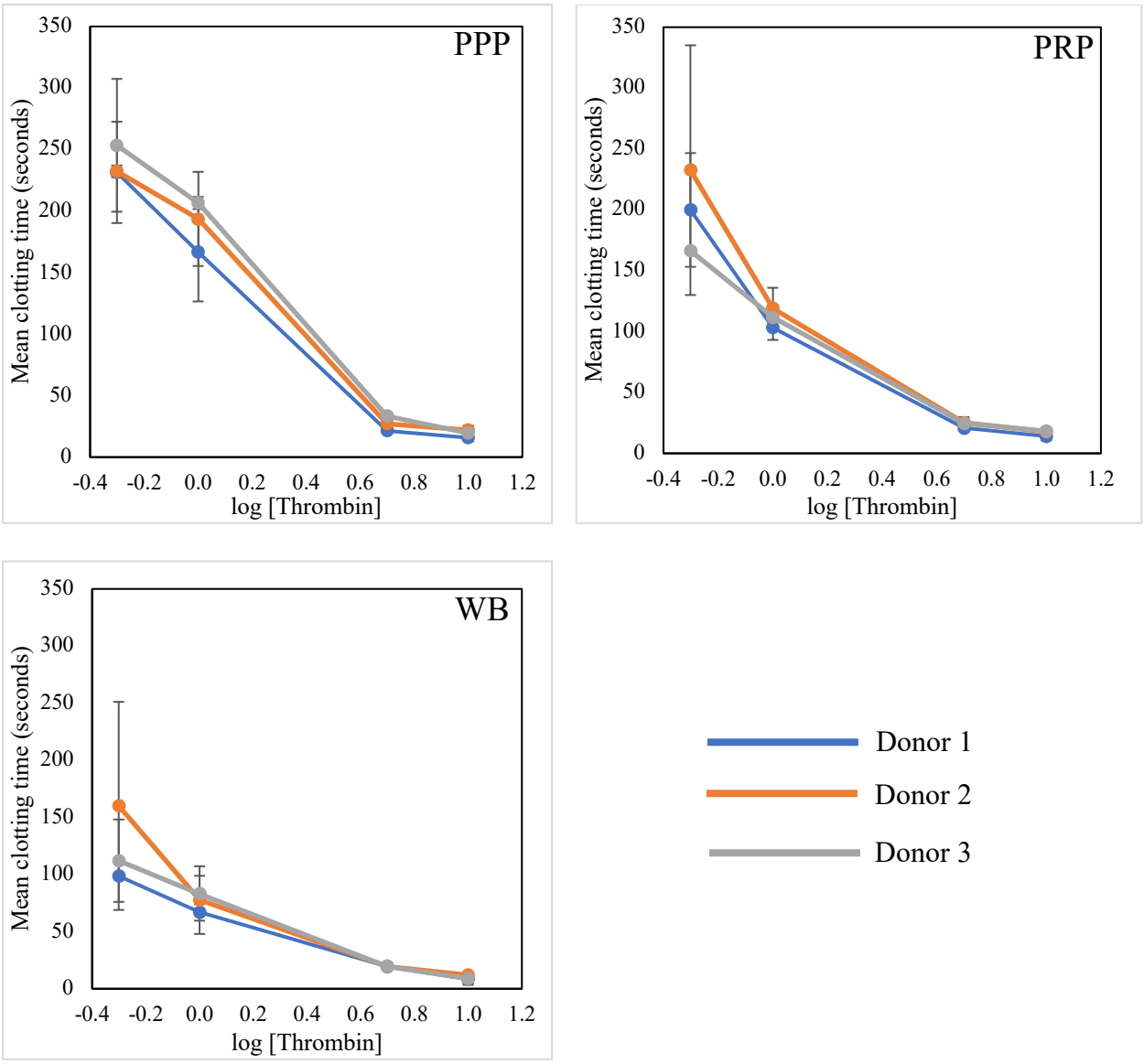

Figure 35. Platelet poor-plasma (PPP), platelet rich-plasma (PRP), and whole blood (WB) clotting time versus log thrombin concentration obtained from a fibrometer. Each curve represents the average of three different experiments from Table 4. Clotting time curves show that when thrombin concentration increased, clotting time decreased. As thrombin doses increased (5nM-10nM), clotting time variation was eliminated. Error bars represent standard deviation.

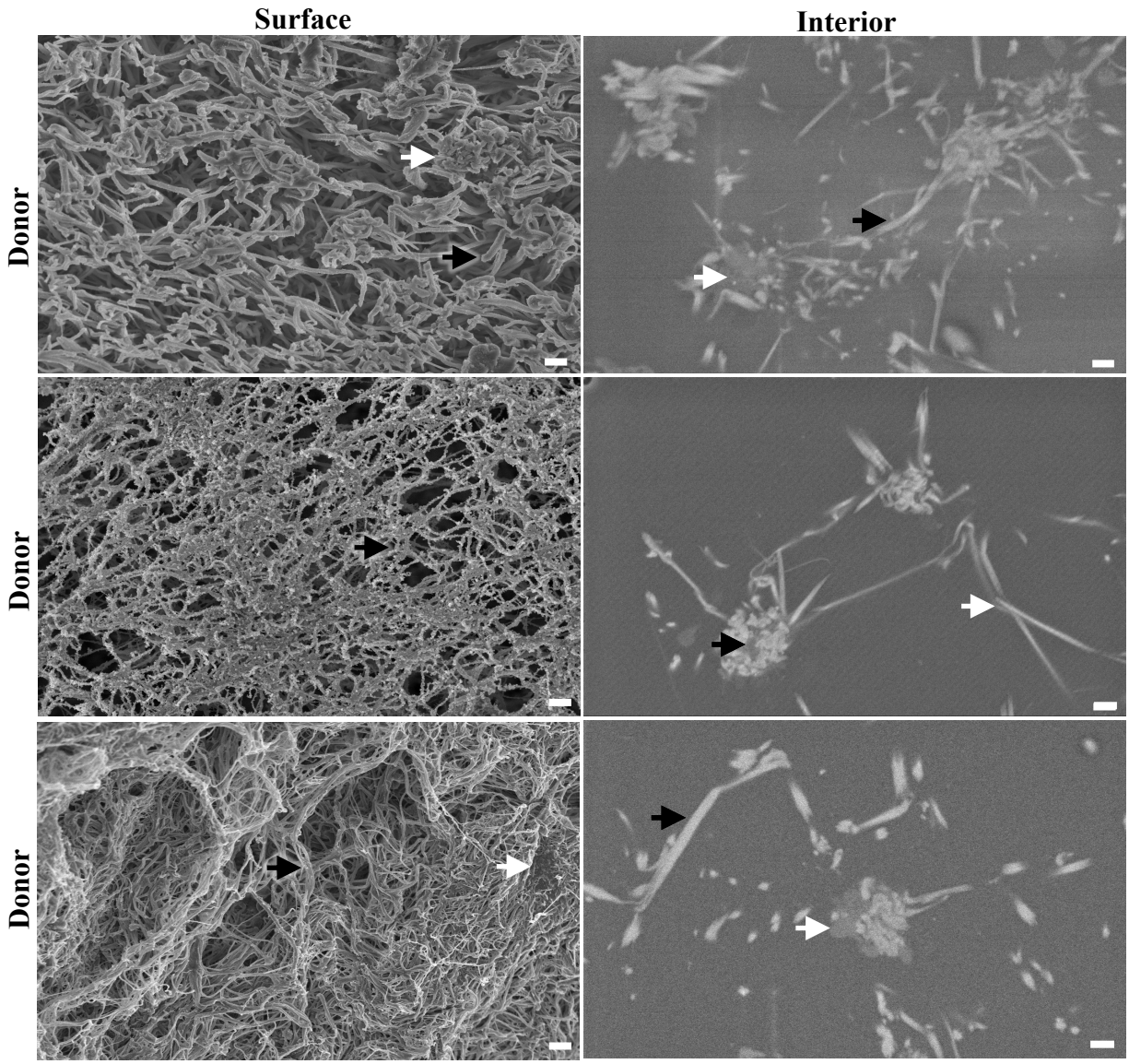

Figure 36. PRP clot structures formed at low thrombin doses from three different donors. Overall, PRP clot surfaces from three different donors share similar characteristics. At low doses of thrombin (1nM), thick, long, woven fibrin strands were loosely associated with some activated platelets. The surfaces of clots were open with many pores. Within the clots, there were empty spaces. These clots appear more permeable. Surface images are secondary electron images and interior images are backscattered images. White and black arrows indicate activated platelets and fibrin, respectively. Size bars equal 1μm.

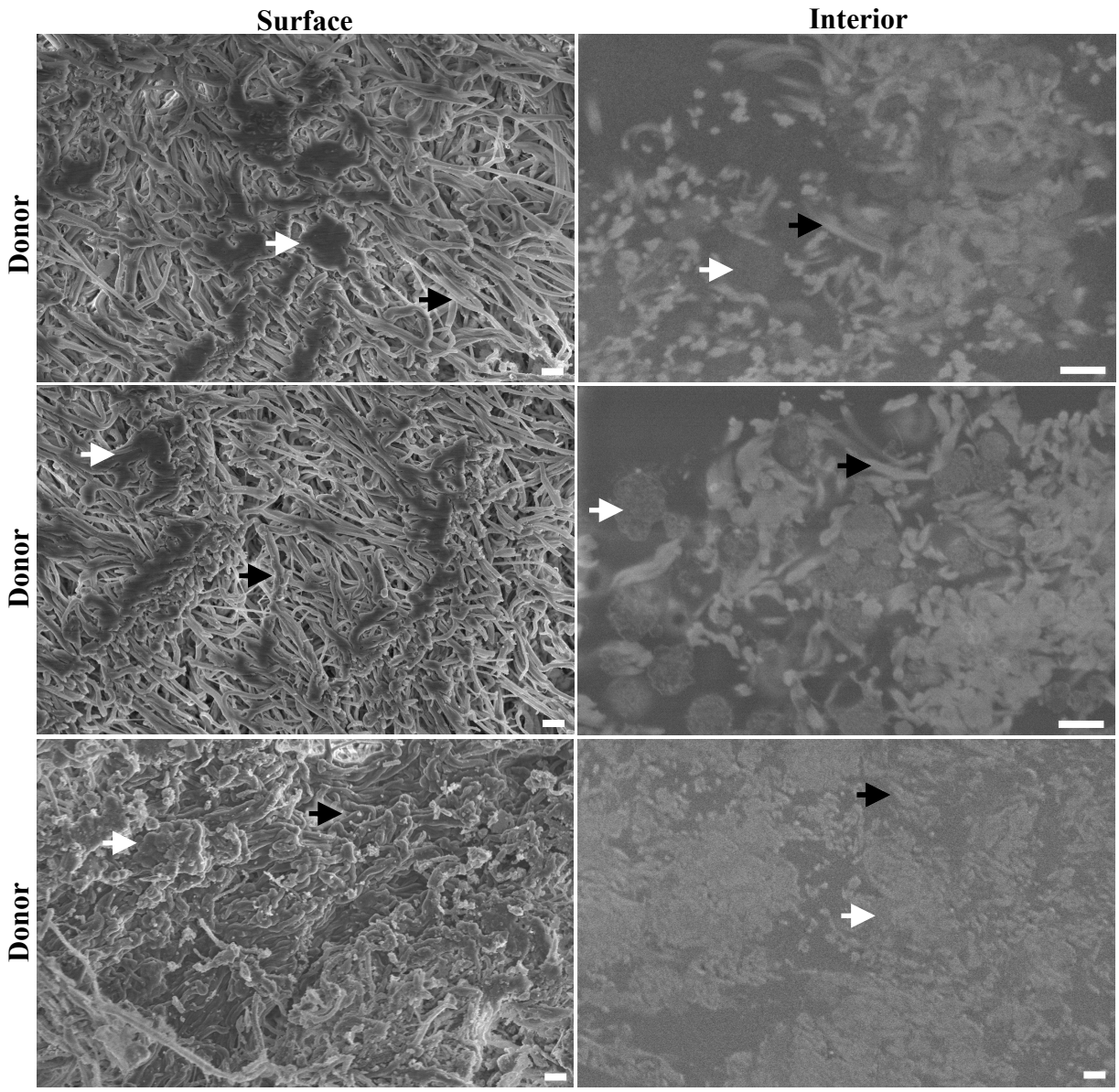

Figure 37. PRP clot structures formed at high thrombin doses from three different donors. At high doses of thrombin (10nM), externally many activated platelets bind to fibrin strands forming a tightly dense network without many pores. Thinner and shorter fibrin strands cooperated with activated platelets creating the compact architecture inside of the clot. The clots appear less permeable. Surface images are secondary electron images and interior images are backscattered images. White and black arrows indicate activated platelets and fibrin, respectively. Size bars equal 1μm.

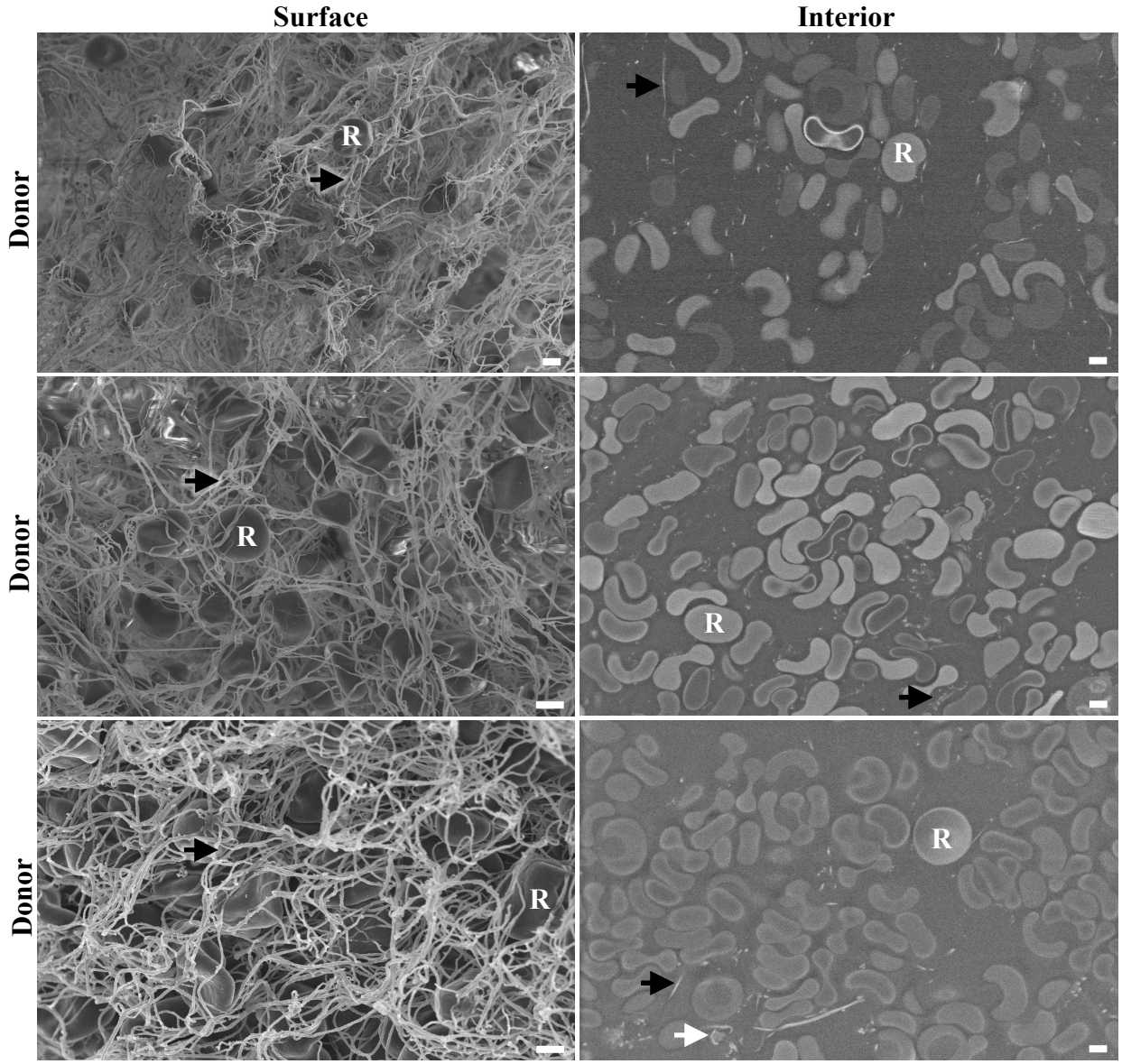

Figure 38. WB clot structures formed at low thrombin doses from three different donors. At low thrombin concentration, the surface of the WB clot consisted of loose fibrin strands that wrapped around biconcave RBCs, with a very limited number of activated platelets found. Inside the clots, biconcave RBCs associated with fibrin strands and the clots contained many spaces. Surface images are secondary electron images and interior images are backscattered images. White arrows and black arrows indicate activated platelet and fibrin, respectively, and R indicates RBCs. Size bars equal 2μm.

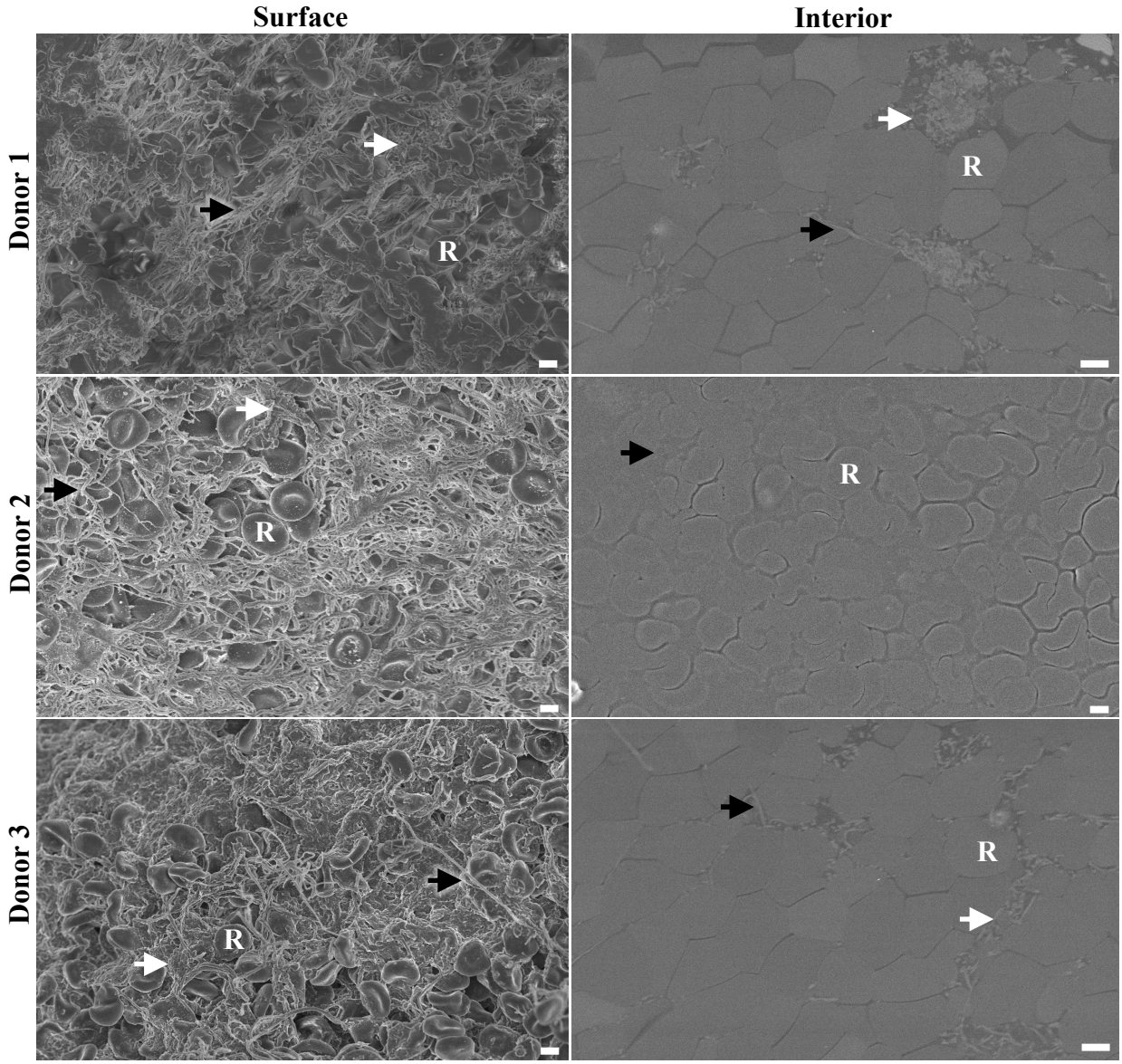

Figure 39. WB clot structures formed at high thrombin doses from three different donors. At high thrombin concentration, fibrin strands, activated platelets, and RBCs formed a dense network. No pores were found at the surface of the clot. Inside the clot, the RBCs changed their shape from regular biconcave to polyhedral shape and orientated into the core of the clot as activated platelets and fibrin were arranged at the periphery. Surface images are secondary electron images and interior images are backscattered images. White arrows and black arrows indicate activated platelets and fibrin, respectively. R indicates RBCs. Size bars equal 2μm.

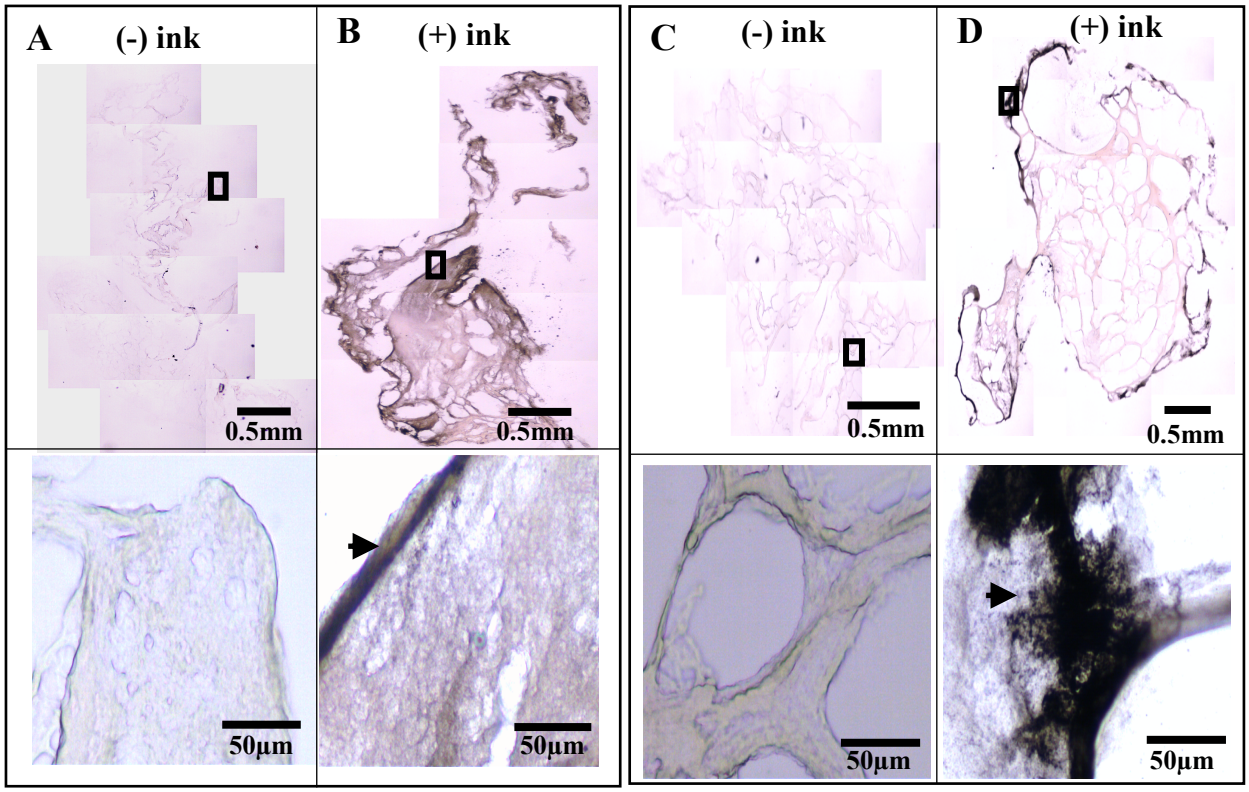

Figure 40. Visualization of colloidal carbon penetration into PRP clots formed at low (A, B) and high (C, D) thrombin concentrations. Boxed areas in the upper images are shown below at higher magnification. At low thrombin concentration, ink migrated throughout the clot and the clot looked darker compared to the control without ink. At high thrombin concentrations, the ink appeared only at the border of the clot. This indicated that high thrombin concentration clots had a less porous network compared to low thrombin concentration clots. Black arrows indicate colloidal carbon.

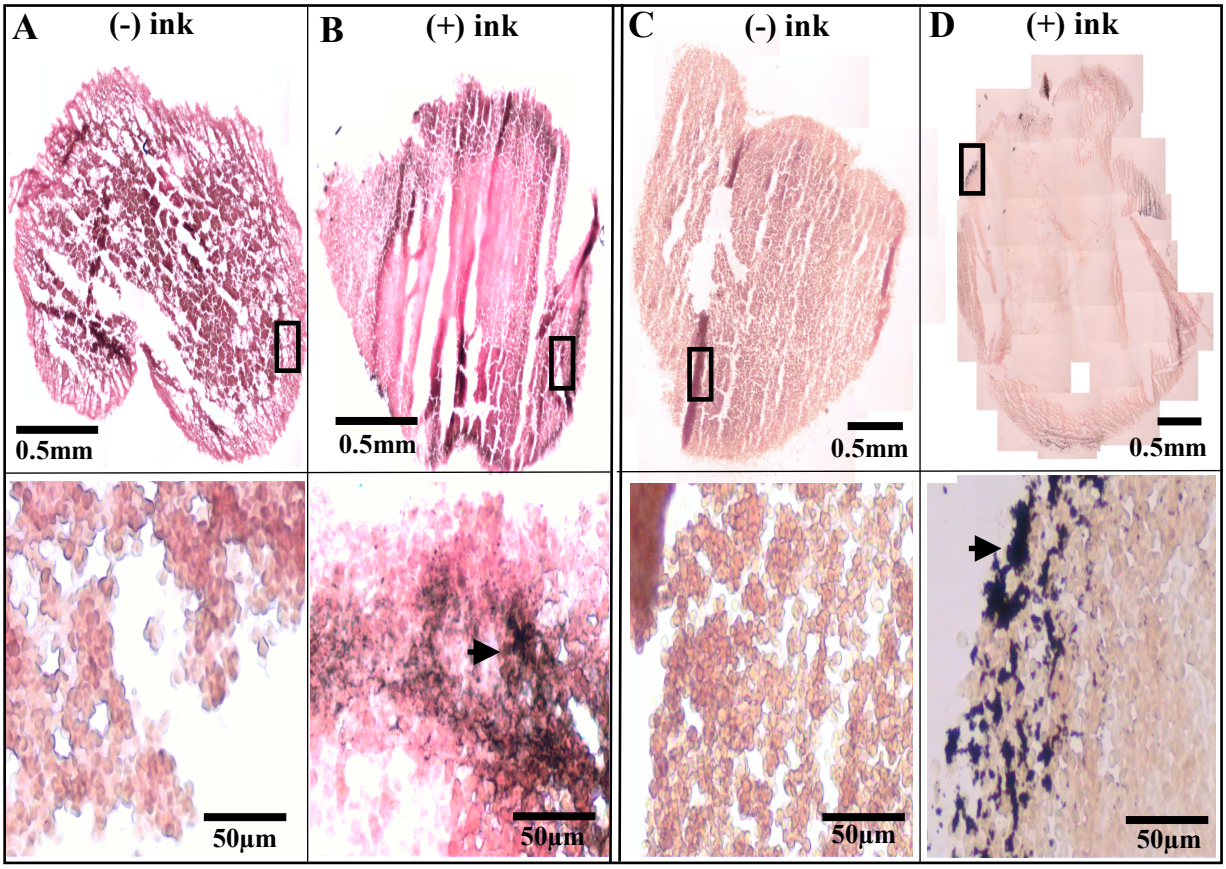

Figure 41. Visualization of colloidal carbon penetration into WB clots formed at low (A, B) and high (C, D) thrombin concentrations. Boxed areas in the upper images are shown below at higher magnification. Ink was able to permeate into the low thrombin clot but was mostly limited to the periphery. Ink was restricted to the rim of the clot at high thrombin concentrations. These results suggested that low thrombin concentration WB clots might contain more pores while high thrombin concentration WB clots might have less pores. Black arrows indicate colloidal carbon accumulation.

	The percent of area of the blood clot that was penetrated by ink			
	PRP		**WB**	
[Thrombin]	1nM	10nM	1nM	10nM
Donor 1	12.60%	10.60%	3.80%	2%
Donor 2	10.21%	7.04%	3.77%	1.60%
Donor 3	13.20%	8.70%	3.14%	1.06%

Table 6. The percent area of the PRP and WB clots penetrated by colloidal carbon measured by the threshold function of the ImageJ program. In general, PRP clots had a higher percentage of area permeated by ink in comparison with WB clots. Low thrombin concentration clots had a higher percent of area permeated by ink. There were slight differences in percent ink areas between donors in WB clots; whereas, more variation occurred among donors in PRP clots. These results suggested that PRP clots formed with low thrombin concentration might be more porous than WB clots formed at high thrombin concentration.

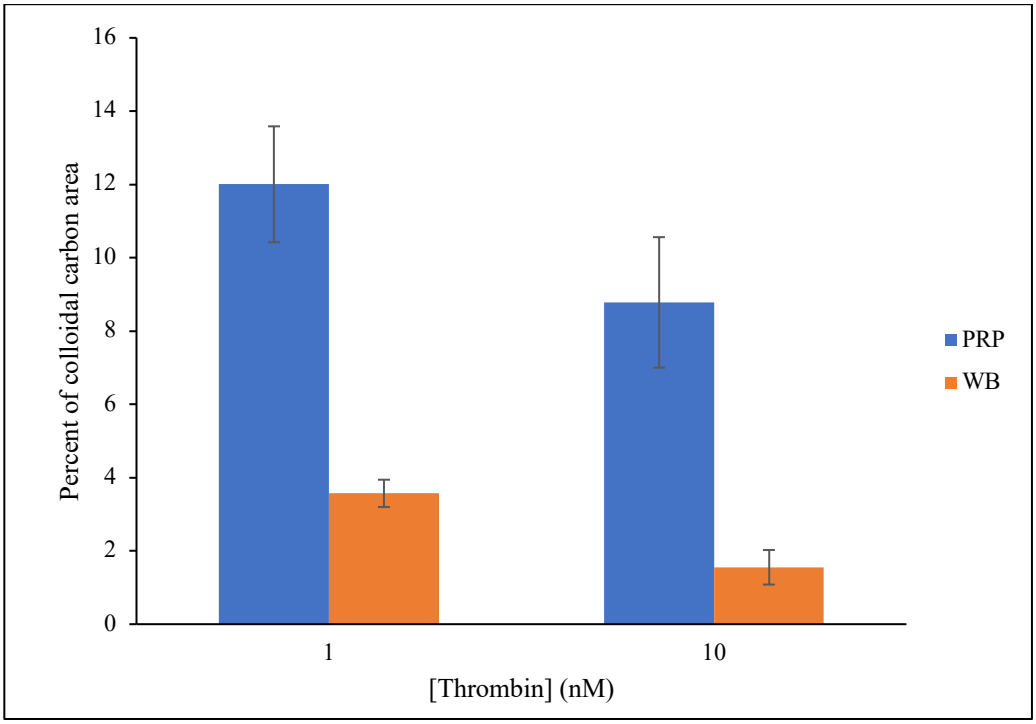

Figure 42. Comparison of area penetrated by colloidal carbon ink in clots formed from platelet-rich plasma (PRP) and whole blood (WB). Both PRP and WB clots were created with 1nM or 10nM of thrombin followed by soaking overnight in ink. The graph was generated by the average from three donors of the percent of area of the PRP and WB clots penetrated by colloidal carbon measured by the threshold function of the ImageJ program (Table 6). Error bars represent standard deviation.

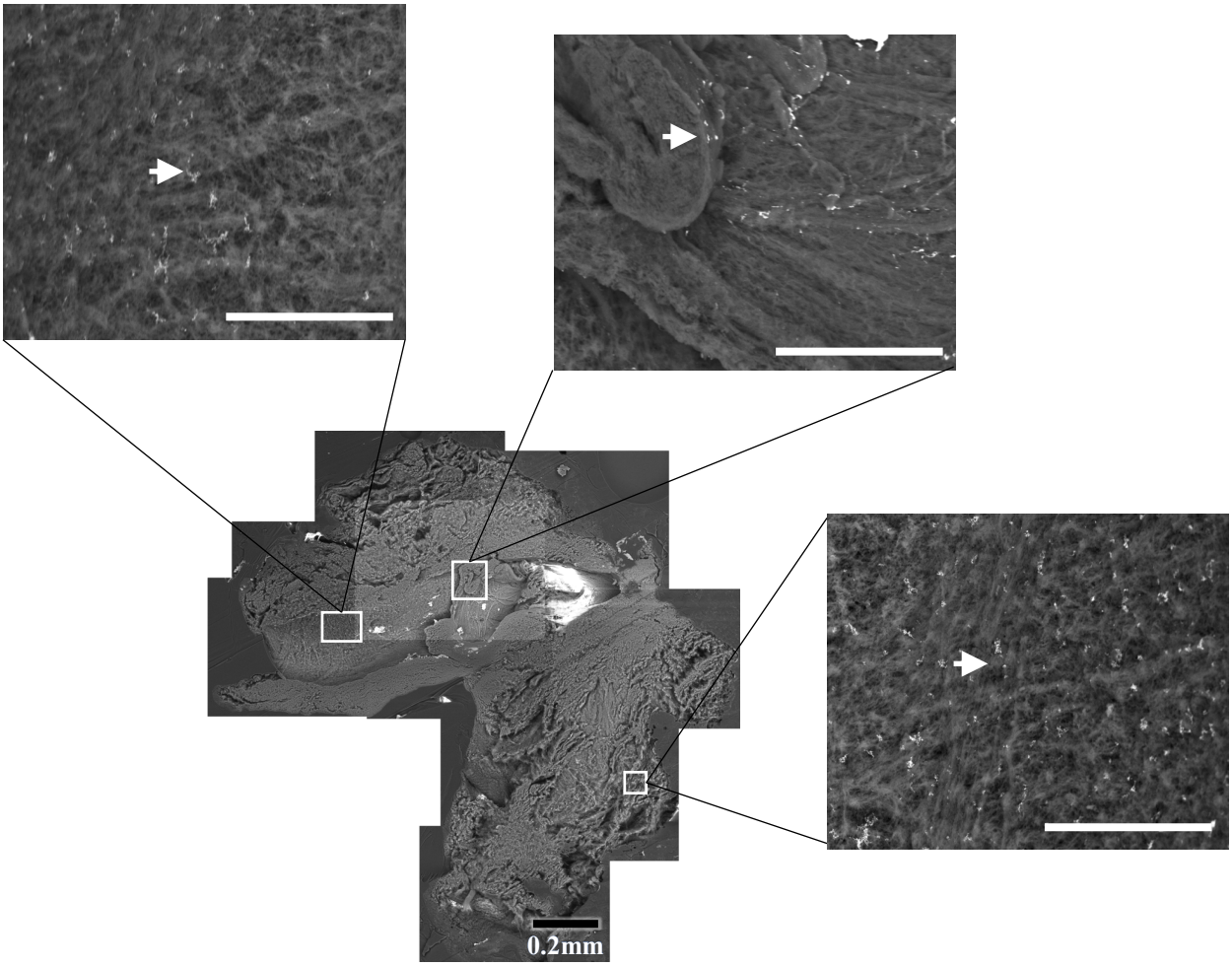

Figure 43. SEM montage of a medial cross-section of a PRP clot from Donor 1 formed at low thrombin concentration (1nM). Examples of sites where FGN-cAu_{18} were found inside clots are indicated by boxes, with high magnification micrographs of those areas shown. Nanoparticles appeared throughout PRP clots formed at low thrombin concentration. Higher nanoparticle concentration was found at the periphery, with decreasing nanoparticle concentration found as observations moved toward the interior of the clot. The percent of nanoparticle penetration was about 40%. White arrows indicate FGN-cAu_{18}. White size bars equal 50μm.

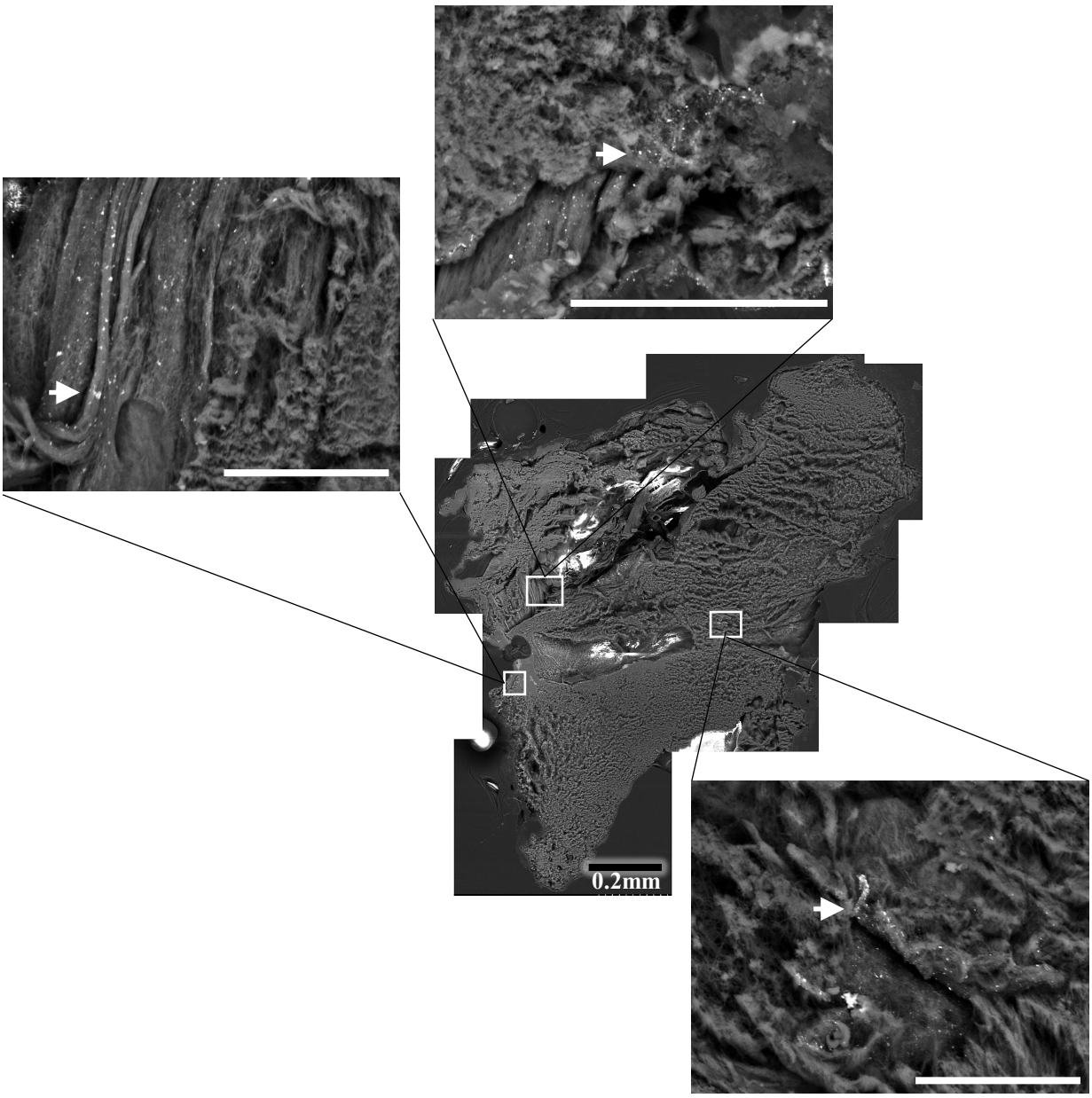

Figure 44. SEM montage of a medial cross-section of a PRP clot from Donor 1 formed at high thrombin concentration (10nM). Examples of sites where FGN-cAu_{18} were found inside clots are indicated by boxes, with high magnification micrographs of those areas shown. Nanoparticles were found both at the periphery and interior of clot, with slightly less concentration at the interior. The percent of nanoparticle penetration was 17%. White arrows indicate FGN-cAu_{18}. White size bars equal 50μm.

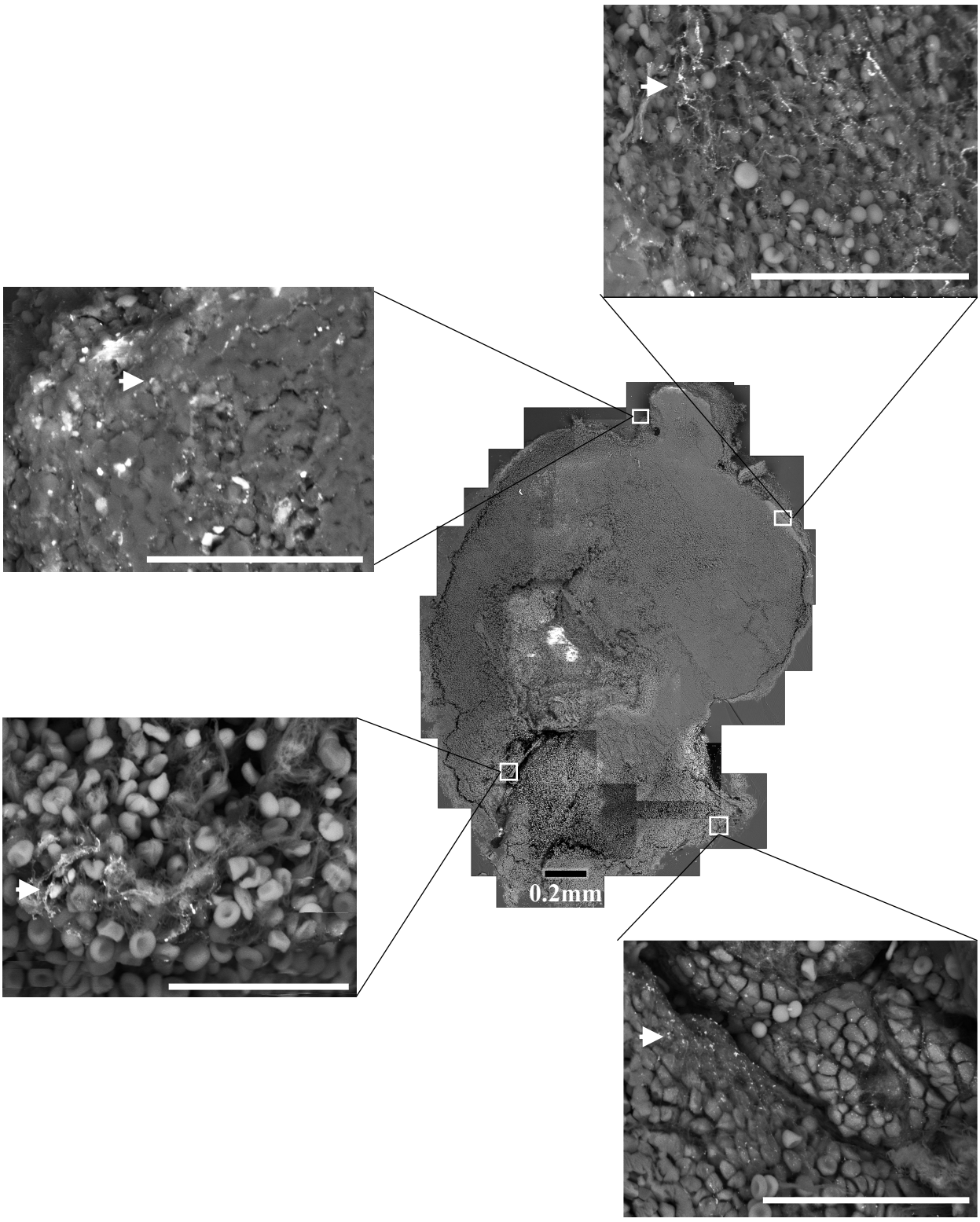

Figure 45

Figure 45. SEM montage of a medial cross-section of a WB clot from Donor 1 formed at low thrombin concentration (1nM). Examples of sites where FGN-cAu_{18} were found inside clots are indicated by boxes, with high magnification micrographs of those areas shown. Nanoparticles were mostly found on the outside, and few nanoparticles were able to migrate into the interior, limiting both concentration and depth of penetration of FGN-cAu_{18}. The percent of nanoparticle penetration was 18%. White arrows indicate FGN-cAu_{18}. White size bars equal 30μm.

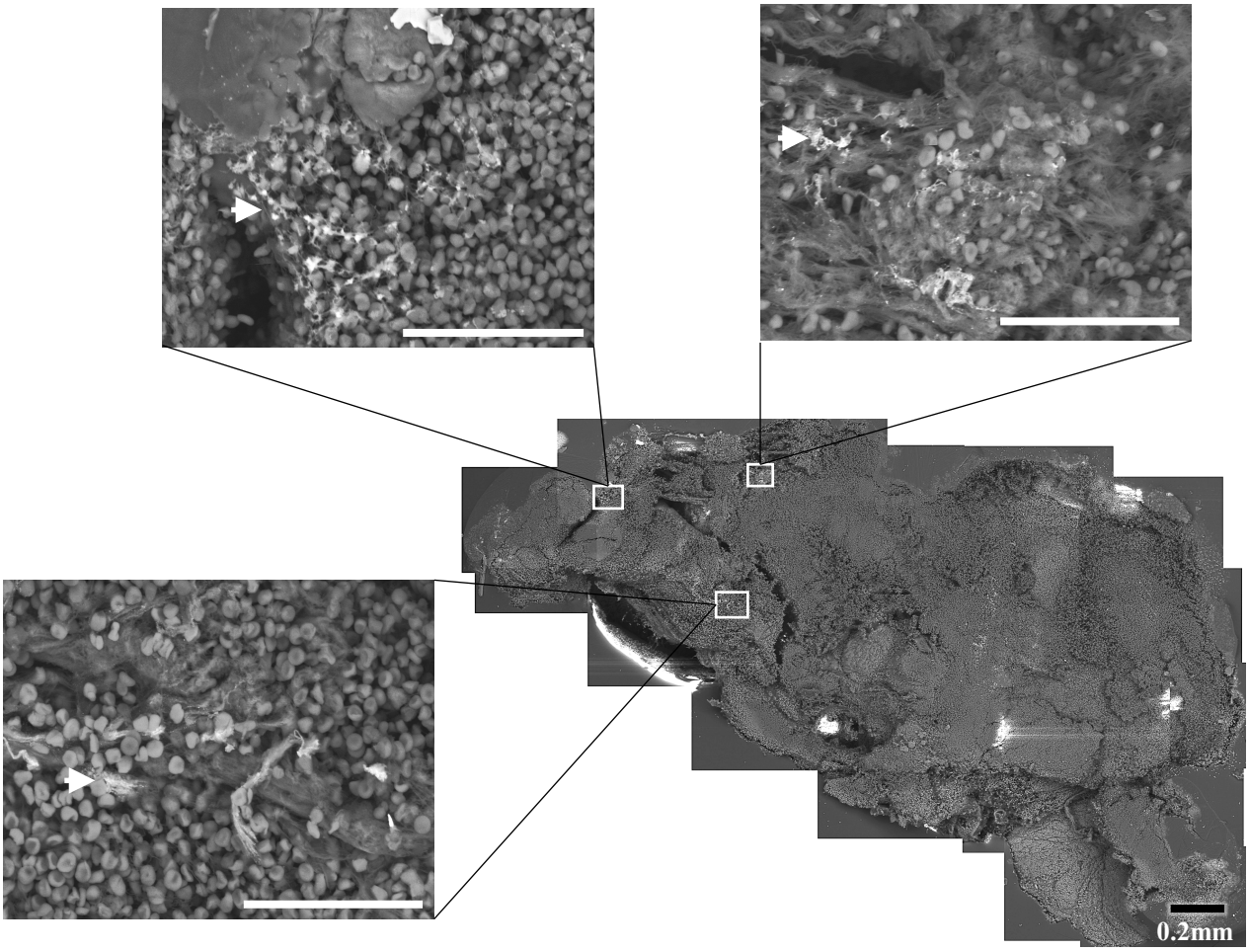

Figure 46. SEM montage of a medial cross-section of a WB clot from Donor 1 formed at high thrombin concentration (10nM). Examples of sites where FGN-cAu_{18} were found inside clots are indicated by boxes, with high magnification micrographs of those areas shown. At high thrombin doses, nanoparticles were found only at the edge of the clot. No nanoparticles appeared in the center of the clot. The percent of nanoparticle penetration was 14%. White arrows indicate FGN-cAu_{18}. White size bars equal 30μm.

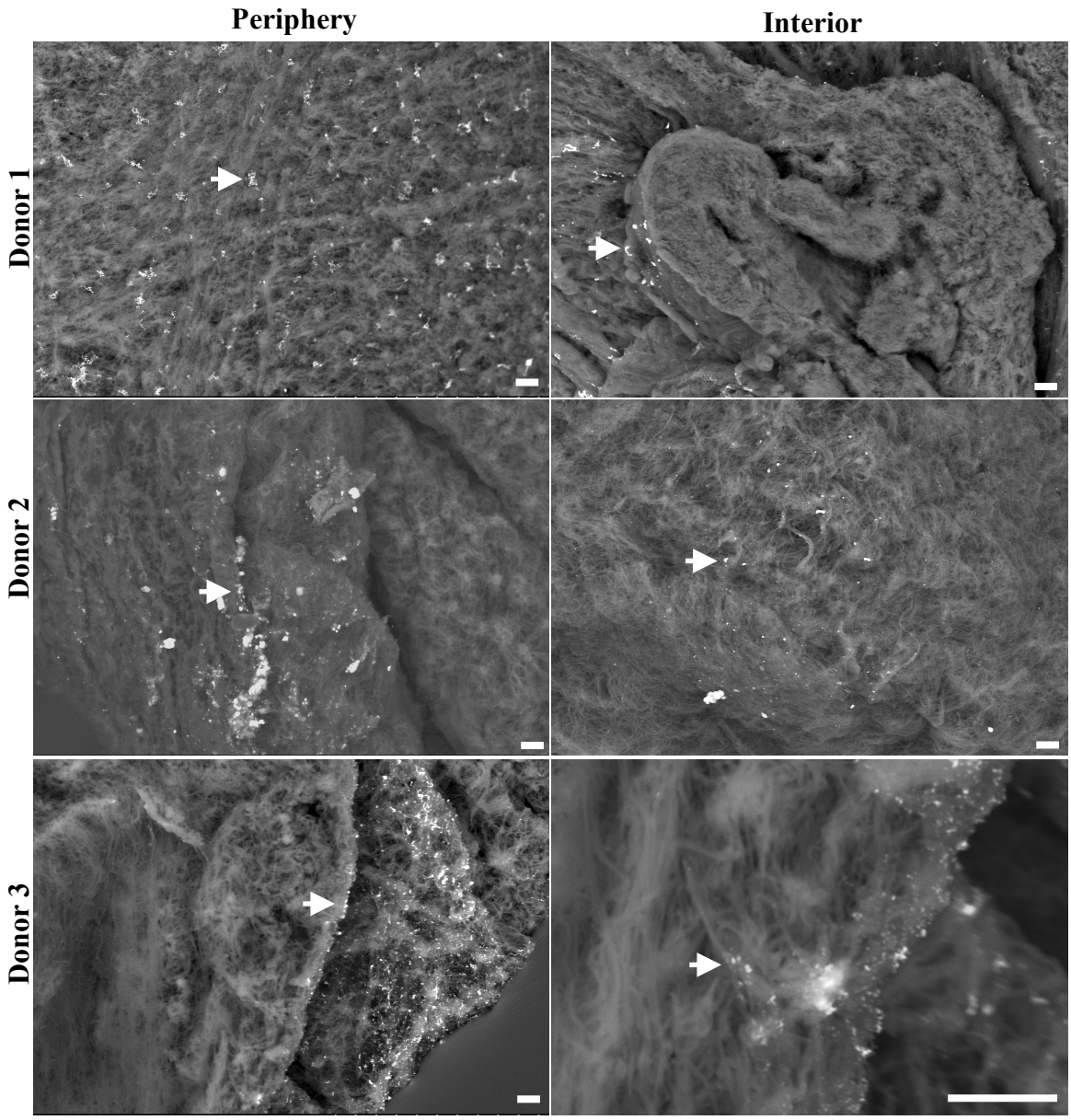

Figure 47. Representative images showing the penetration of FGN-cAu$_{18}$ into PRP clots from three different donors formed at low thrombin concentration (1nM). Medial cross-sections were examined; images from the edge and the area where the deepest nanoparticle penetration was detected are shown. Labeling was found throughout the clot. Near the periphery, a higher concentration of the nanoparticles was observed while lower concentrations of nanoparticles were found near the center of the clot. White arrows indicate FGN-cAu$_{18}$. Size bars equal 5μm.

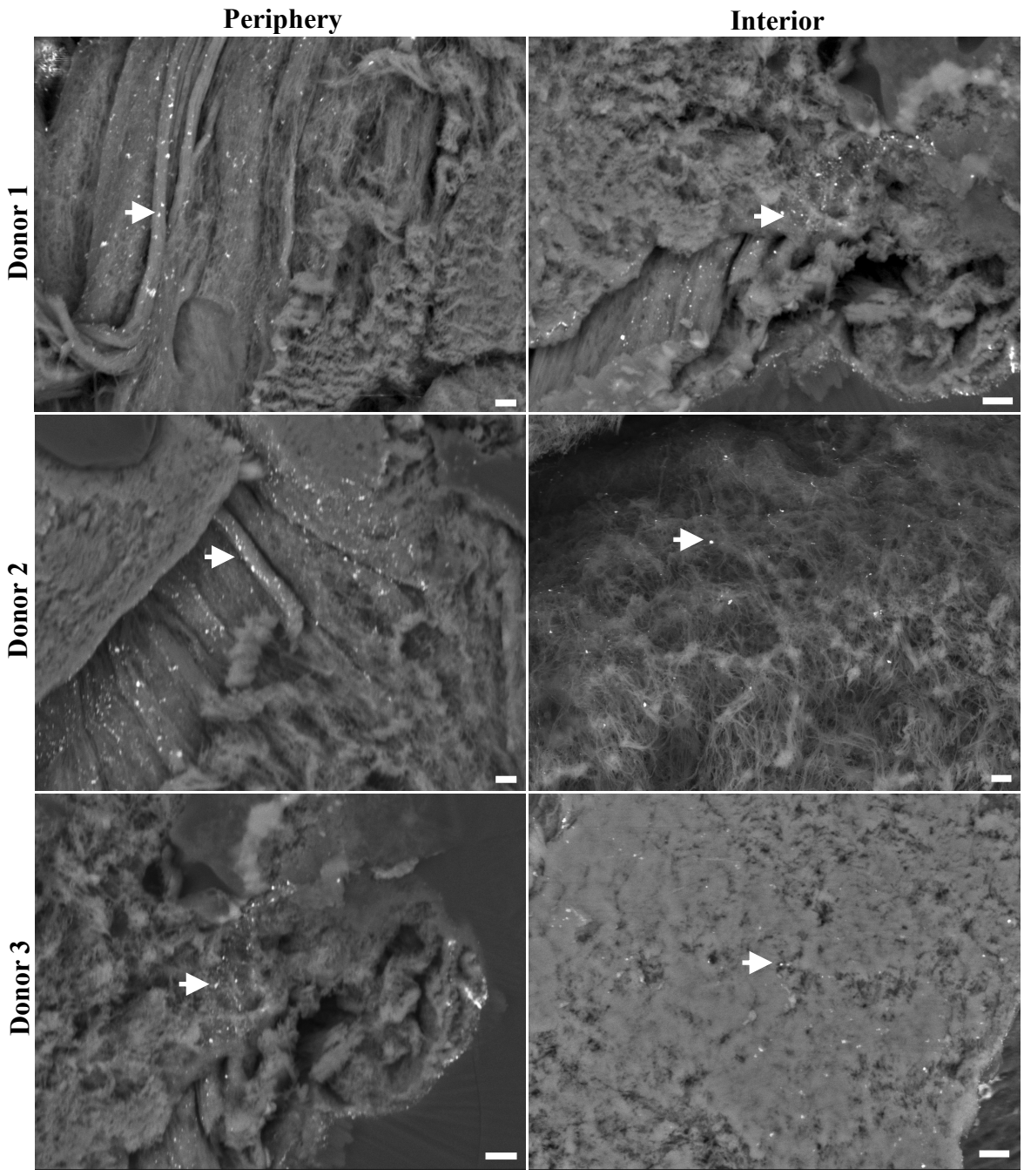

Figure 48

Figure 48. Representative images showing the penetration of FGN-cAu$_{18}$ into PRP clots from three different donors at high thrombin concentration (10nM). Medial cross-sections were examined; images from the edge and the area where the deepest nanoparticle penetration was detected are shown. The labeling was found both at the periphery and interior of the clot. Near the periphery, a higher concentration of nanoparticles was observed and a lower concentration of nanoparticles was found near the center of the clot. Compared with the low thrombin concentration of thrombin formed PRP clot, the accumulation of nanoparticles was reduced both inside and outside due to the tightly dense structures of associated fibrin and activated platelets. White arrows indicate FGN-cAu$_{18}$. Size bars equal 5μm.

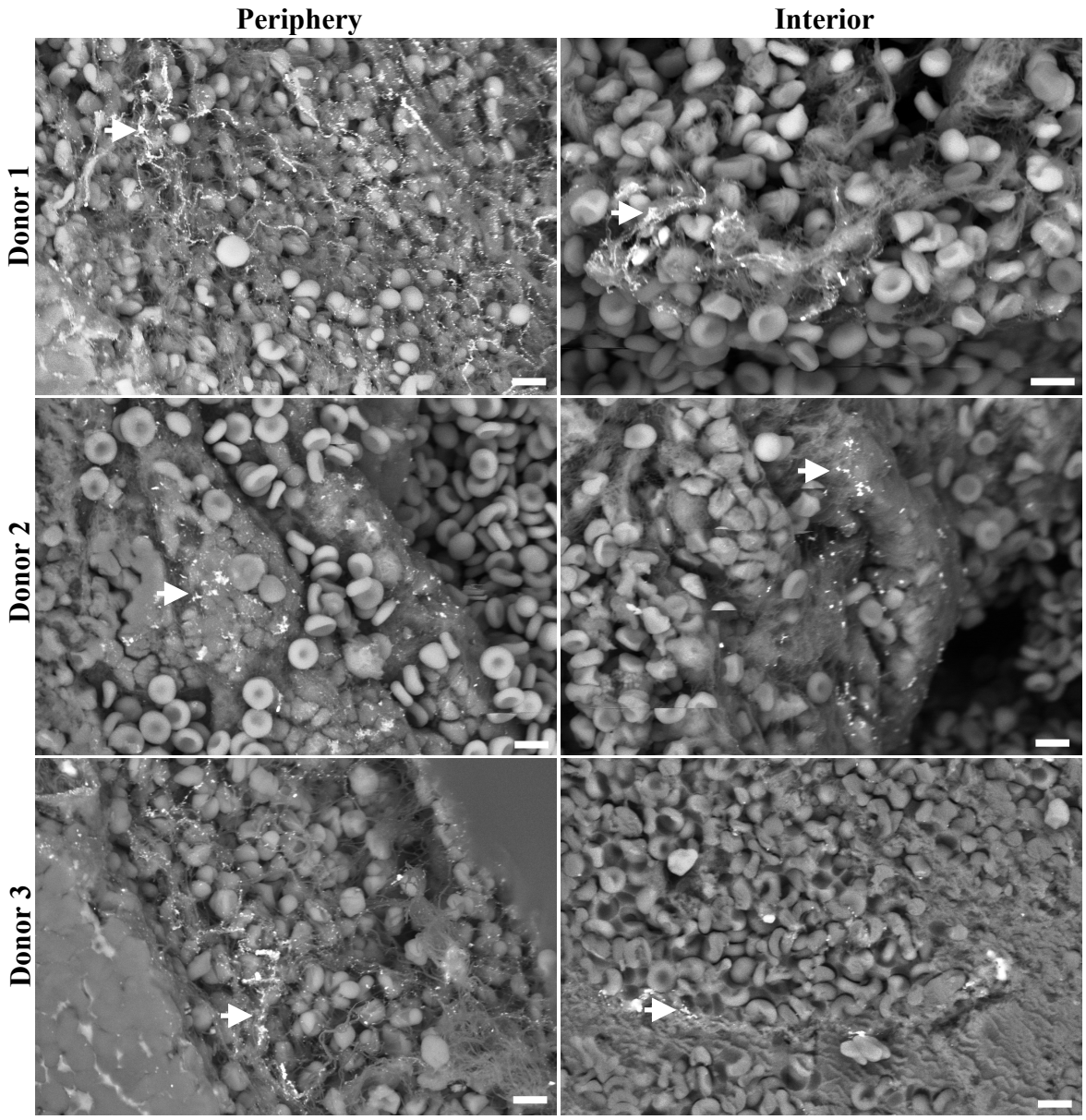

Figure 49. Representative images showing the penetration of nanoparticles into WB clots from three different donors formed at low thrombin concentration (1nM). Medial cross-sections were examined; images from the edge and the area where the deepest nanoparticle penetration was detected are shown. Most of the label was detected near the periphery. Some label migrated to the interior, but this was very limited in both concentration and depth. The FGN-cAu_{18} nanoparticles are indicated by white arrows. Size bars equal 5μm.

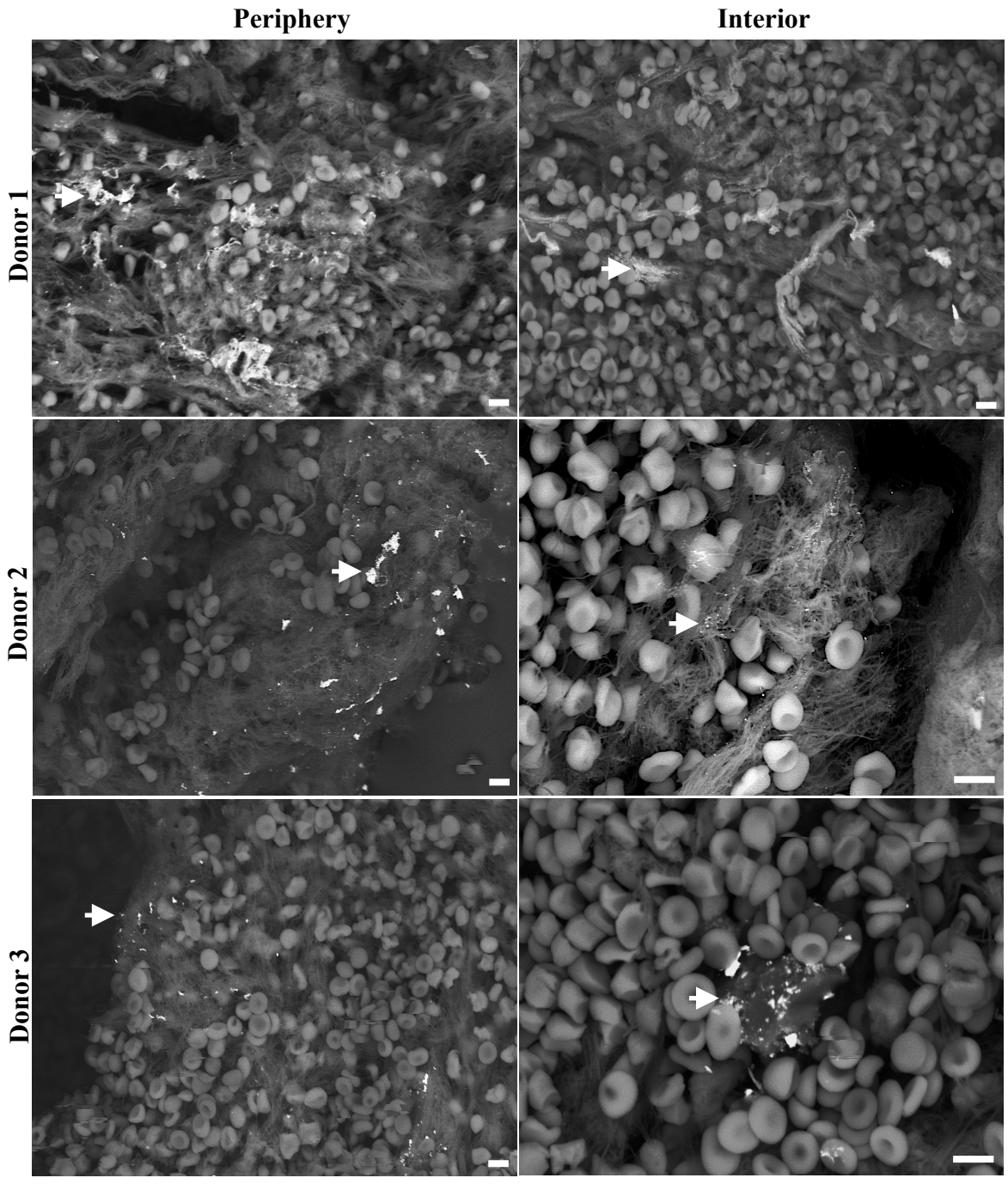

Figure 50

Figure 50. Representative images showing the penetration of nanoparticles into WB clots from three different donors formed at high thrombin concentration (10nM). Medial cross-sections were examined; images from the edge and the area where the deepest nanoparticle penetration was detected are shown. The labelling was mostly found at the periphery and at very low concentrations. There was little chance in finding nanoparticles residing in the center of the clots. Due to the high dose of thrombin, resulting in the organization of RBCs coordinated with fibrin and activated platelets into dense networks, limited penetration of nanoparticles occurred. FGN-cAu_{18} nanoparticles indicated in white arrows. Size bars equal 5μm.

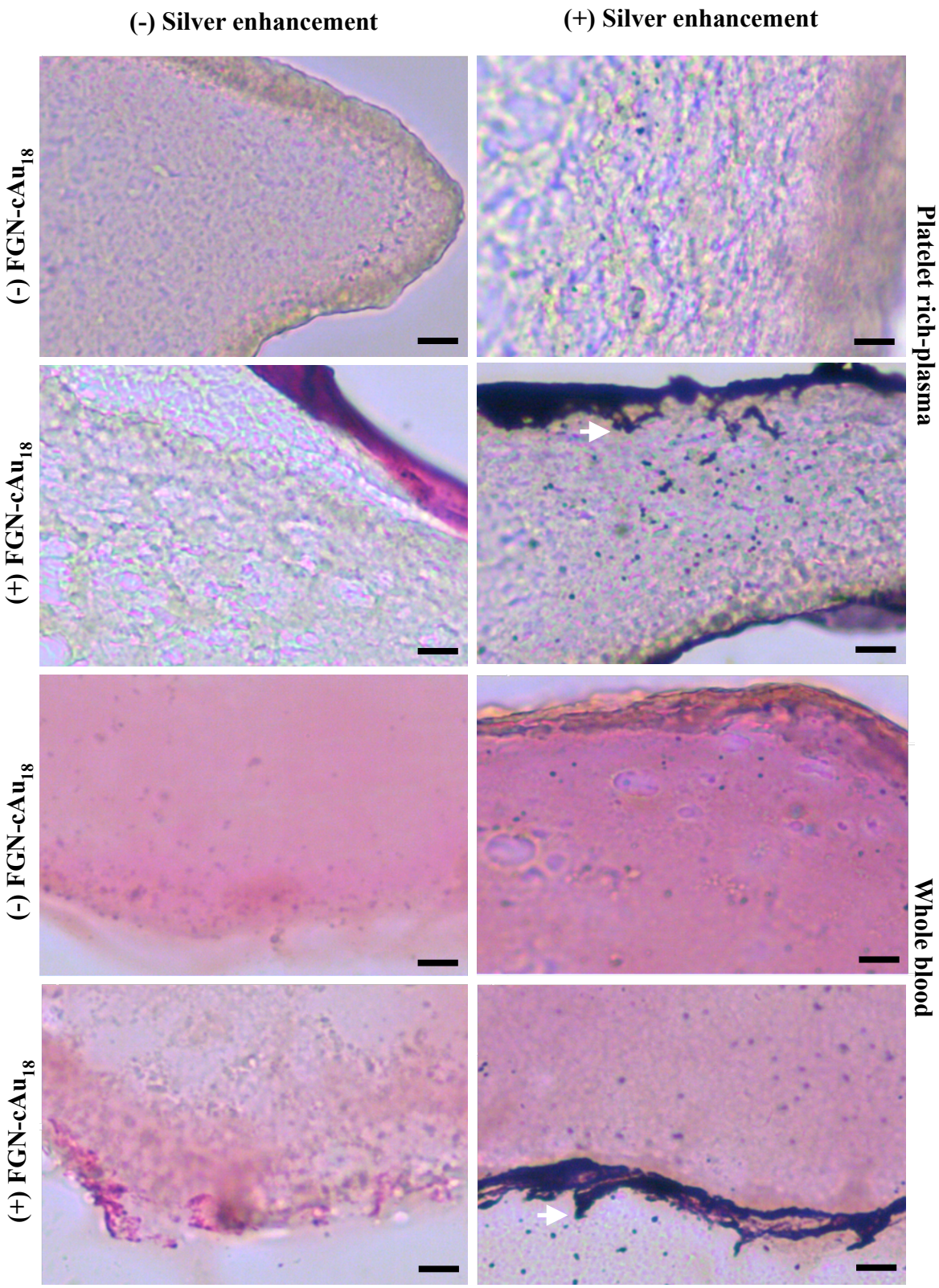
(-) Silver enhancement
(+) Silver enhancement
(-) FGN-cAu18
(+) FGN-cAu18
(-) FGN-cAu18
(+) FGN-cAu18
Platelet rich-plasma
Whole blood

Figure 51

Figure 51. Light microscopy images with and without silver enhancement (SE) of FGN-cAu_{18} in labeled PRP and WB clots. In the presence of SE, FGN-cAu_{18} appeared darker in both PRP and WB clot sections. There were a few artifacts of SE deposition in the sections. However, clusters of FGN-cAu_{18} always looked significantly darker. Thus, for the purposes of quick screening, SE can still be utilized to study nanoparticle penetration into clots. White arrows indicate FGN-cAu_{18}. Size bars equal 10μm.

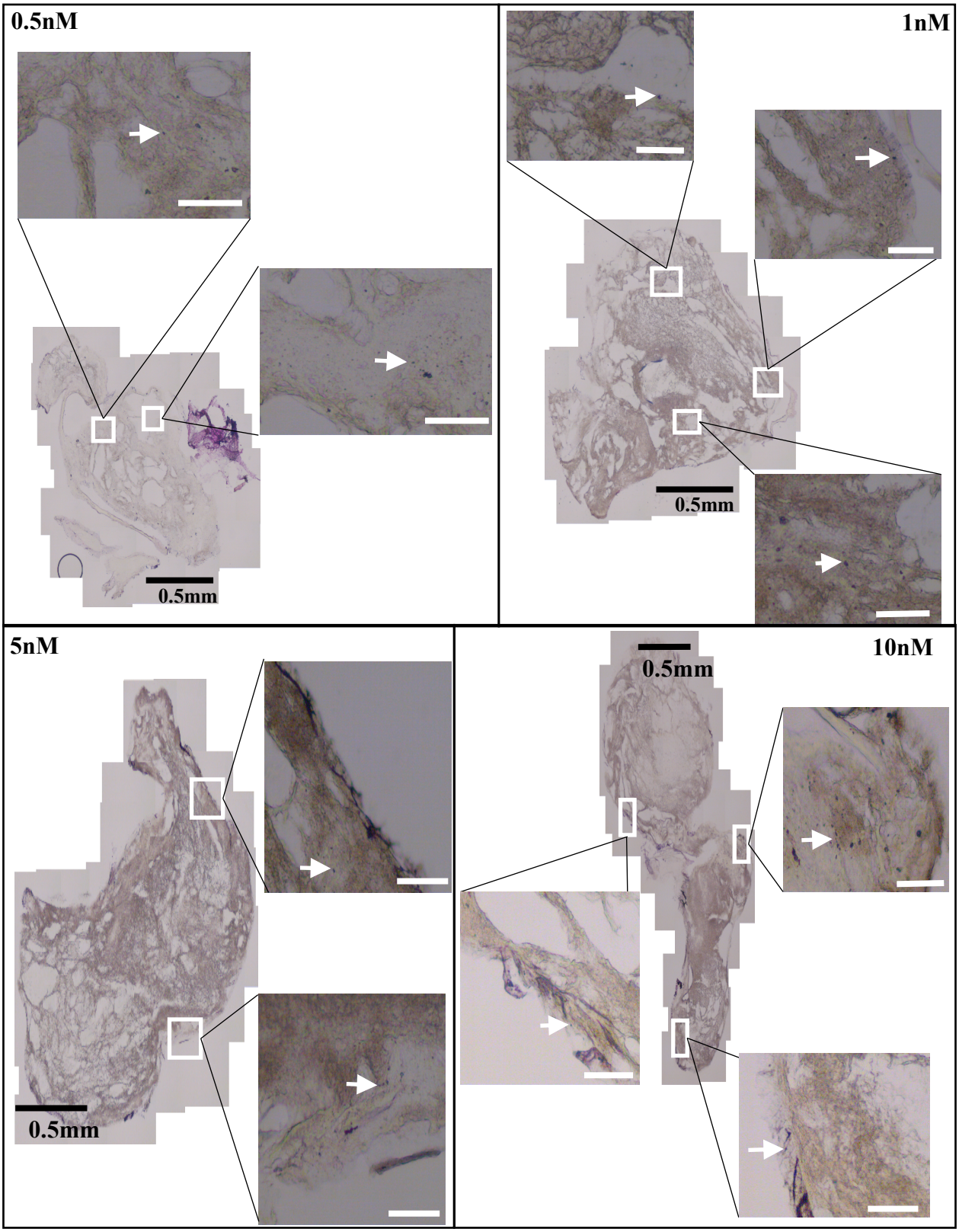

Figure 52

Figure 52. Reconstruction of the frozen sections of PRP clots formed at different thrombin concentrations (0.5nM, 1nM, 5nM and 10nM) labeled with FGN-cAu_{18} and treated with SE. High magnification images as examples of areas containing nanoparticles are from regions indicated by boxes. Low thrombin concentration clot sections (0.5nM and 1nM) were smaller in size with a less dense fibrin network. As a result, nanoparticle penetration was deeper. High thrombin concentration clot sections were larger with a high-density fibrin network; therefore, nanoparticles accumulated primarily at the edge of the clots. The percentage of penetration was calculated using the deepest distance of nanoparticle migration into the clot divided by the diameter of the clot. Percentage of nanoparticle penetration into these PRP clots was approximately 35%, 23%, 8.3%, and 4% for 0.5nM, 1nM, 5nM, and 10nM thrombin concentrations, respectively. White arrows indicate FGN-cAu_{18}. White size bars equal 50μm.

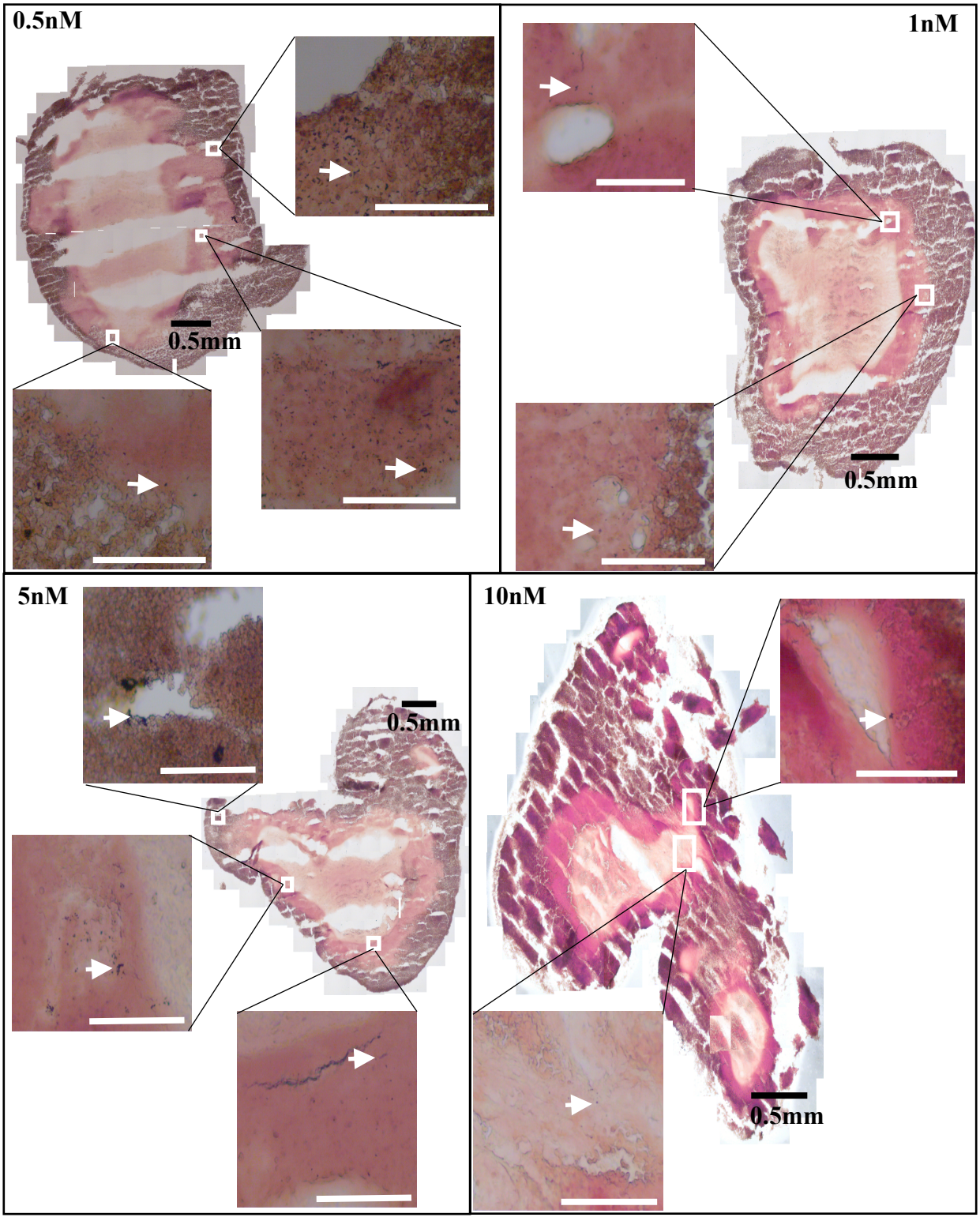

Figure 53

Figure 53. Reconstruction of frozen cross-sections of WB clots formed at different thrombin concentrations (0.5nM, 1nM, 5nM and 10nM) and treated with SE. High magnification images as examples of areas containing nanoparticles are from regions indicated by boxes. When WB clots were formed at 0.5 and 1nM thrombin concentrations, nanoparticles were found at both the periphery and interior of WB clots, with the latter having a low number of nanoparticles. Nanoparticles were limited in both distance of migration and concentration when WB clots were formed at 5nm and 10nM thrombin. The percentage of nanoparticle penetration was 22%, 18%, 14%, and 11% for 0.5nM, 1nM, 5nM, and 10nM thrombin concentrations, respectively. White arrows indicate FGN-cAu_{18}. White size bars equal 50μm.

	[Thrombin] (nM)	Diameter (mm)	Distance migration (mm)	% Penetration
Donor 1	0.5	1	0.2	20
	1	1	0.2	20
	5	2	0.18	9
	10	2	0.14	7
Donor 2	0.5	2	0.34	17
	1	2	0.26	13
	5	1.5	0.14	9.3
	10	2	0.16	8
Donor3	0.5	2	0.4	20
	1	2	0.3	15
	5	2.2	0.24	10.9
	10	2.5	0.16	6.4
Donor 4	0.5	1	0.26	26
	1	1.5	0.16	10.7
	5	1.5	0.18	12
	10	2	0.2	10
Donor 5	0.5	1.8	0.63	35
	1	1.9	0.44	23
	5	3	0.25	8.3
	10	4	0.16	4
Donor 6	0.5	2.25	0.88	39
	1	2.78	1	36
	5	2.38	0.63	26
	10	2.2	0.5	22

Table 7. Measurements of clot diameters, deepest distance of nanoparticle penetration, and percentages of nanoparticle penetration of PRP clots formed at various thrombin concentrations from 6 donors using the quick screening method (silver enhancement incorporated with light microscopy). Even though there were donor-donor variations, all donors shared a similar trend. As the thrombin dose stimulating clot formation was increased, clot diameter increased, and nanoparticle penetration decreased. Thus, the percentage of penetration was reduced with increasing thrombin concentration.

	[Thrombin] (nM)	Diameter (mm)	Distance migration (mm)	% Penetration
Donor 1	0.5	2	0.34	17
	1	2	0.44	22
	5	3	0.26	8.7
	10	3	0.2	6.7
Donor 2	0.5	1.38	0.28	20
	1	4.5	0.62	13.8
	5	3	0.23	7.7
	10	3	0.22	7.3
Donor3	0.5	3	0.56	18.7
	1	3	0.48	16
	5	3	0.2	6.7
	10	3.5	0.14	4
Donor 4	0.5	3	0.34	11.3
	1	3	0.32	10.7
	5	2.5	0.18	7.2
	10	3	0.26	8.7
Donor 5	0.5	3.57	0.78	22
	1	3.67	0.67	18
	5	4.17	0.58	14
	10	4.9	0.56	11
Donor 6	0.5	1.36	0.28	19.8
	1	2.38	0.34	14.3
	5	2.5	0.33	13.2
	10	3.96	0.45	11

Table 8. Measurements of clot diameters, deepest distance of nanoparticle migration, and percentages of nanoparticles penetration of WB clots formed at various thrombin doses from 6 different donors using the SE screening method. Clot size increased as thrombin concentration increased. The nanoparticle penetration and percentage of nanoparticle penetration were inversely related to thrombin concentration.

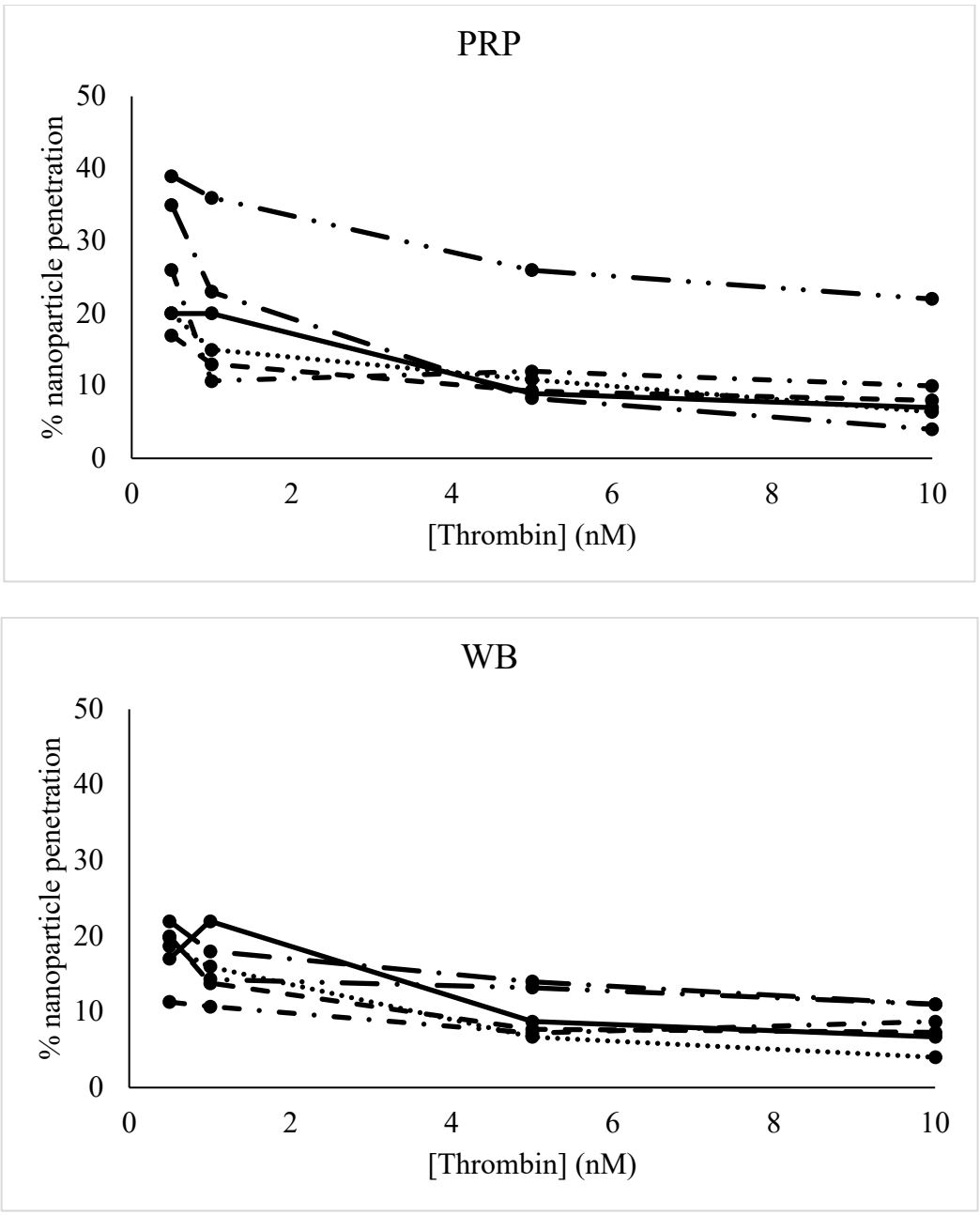
PRP
% nanoparticle penetration
50
40
30
20
10
0
0
2
4
6
8
10
[Thrombin] (nM)
WB
% nanoparticle penetration
50
40
30
20
10
0
0
2
4
6
8
10
[Thrombin] (nM)
Donor 1
Donor 2
Donor 3
Donor 4
Donor 5
Donor 6

Figure 54

Figure 54. Quantification of nanoparticle penetration in platelet rich-plasma (PRP) and whole blood (WB) clots using silver enhancement. Donor to donor variation was seen in percentage of nanoparticle penetration in both PRP and WB systems. Between the two systems, PRP had higher variation and WB had lower nanoparticle penetration. The variation in nanoparticle penetration between donors was largely overcome at high thrombin concentrations. Each line represents data from one donor. The graphs were generated by using data shown in Table 8.

Reference:

1. Krystofiak, E. S. 2013. Fibrinogen-Conjugated Gold-Coated Magnetite Nanoparticles for Antiplatelet Therapy. Doctoral Dissertation, University of Wisconsin- Milwaukee.

2. Palta, S., R. Saroa, A. Palta. 2014. Overview of The Coagulation System. Indian Journal of Anesthesia. 58(5): 515-513

3. Smith, S. A., R. J. Travers, J. H. Morrissey. 2015. How It All Starts: Initiation of The Clotting Cascade. Critical Reviews in Biochemistry and Molecular Biology. 50 (4): 326-336

4. Mackman, N., R. E. Tilley, N. S. Key. 2007. Role of The Extrinsic Pathway of Blood Coagulation in Hemostasis and Thrombosis. Arteriosclerosis, Thrombosis and Vascular Biology. 27: 1687-1693

5. Grover, S. P., N. Mackman. 2019. Intrinsic Pathway of Coagulation and Thrombosis Insights from Animal Models. Arteriolosclerosis, Thrombosis, and Vascular Biology. 39: 331-338

6. Gailani, D., T. Renne. 2007. The Intrinsic Pathway of Coagulation: A Target for Treating Thromboembolic Disease? Journal of Thrombosis and Haemostasis. 5: 1106-1112

7. Krishnaswamy, S. 2014. The Transition of Prothrombin to Thrombin. Journal of Thrombosis and Haemostasis. 11(1): 265-276

8. Lundblad, R. L., R. A. Bradshaw, D. Gabriel, T. L. Ortel, J. Lawson, K. G. Mann. 2004. A Review of The Therapeutic Uses of Thrombin. Journal of Thrombosis and Haemostasis. 91(5): 851-860

9. Crawley, J. T. B., S. Zanardelli, C. K. N. K. Chion, D. A. Lane. 2007. The Central Role of Thrombin in Hemostasis. Journal of Thrombosis and Haemostasis. 5(Suppl.1): 95-101

10. Lane, D. A., H. Philippou, J. A. Huntington. 2005. Directing Thrombin. Blood. 106(8): 2605-2612

11. Stief, T. W. 2008. Innovative Tests of Plasmatic Hemostasis. Labmedicine. 39(4): 225-230

12. Bastiaans, J., J. C. V. Meurs, V. C. Mulder, N. A. Nagtzaam, M. S. Nijenhuis, D. C. M. D. Goorbergh, P. M. V. Hagen, H. Hooijkaas, W. A. Dik. 2014. The Role of Thrombin in Proliferative Vitreoretinopathy. Investigative Ophthalmology & Visual Science. DOI:10.1167/iovs.14-14818

13. Kumar, V., J, R, Chapman. 2007. Whole Blood Thrombin: Development of a Process for Intra-Operative Production of Human Thrombin. The Journal of The American Society of Extra-Corporeal Technology. 39:18-23

14. Konugsbrugge, O, S. Koder, J. Riedl, S. Panzer, I. Pabinger, C. Ay. 2017. A New Measure for In Vivo Thrombin Activity in Comparison with In Vitro Thrombin Generation Potential in Patients with Hyper- and Hypocoagulability. Clinical and Experimental Medicine. 17(2): 251-256

15. Tanka-Azevedo, A. M., K. Morais-Zani, R. J. S. Torquato, A. S. Tanaka. 2010. Thrombin Inhibitors from Different Animals. Journal of Biomedicine and Biotechnology. 2010: 641025. https://dx.doi.org/10.1155%2F2010%2F641025

16. DeAnglis, A. P., I. Nur, A. J. Gorman, R. Meidler. 2017. A Method to Measure Thrombin Activity in A Mixture of Fibrinogen and Thrombin Powders. Blood Coagulation and Fibrinolysis. 28(2): 134-138

17. Wolberg, A. S., R. A. Campbell. 2008. Thrombin Generation, Fibrin Clot Formation and Hemostasis. Transfusion and Apheresis Science. 38: 15-23

18. Wolberg, A. S. 2010. Plasma and Cellular Contributions to Fibrin Network Formation, Structure and Stability. Haemophilia. 16(3): 7-12

19. Weisel, J. W., C. Nagaswami. 1992. Computer Modeling of Fibrin Polymerization Kinetics Correlated with Electron Microscope and Turbidity Observations: Clot Structure and Assembly Are Kinetically Controlled. Biophysical Journal. 63(1): 111–128

20. Ryan, E. A., L. F. Mockros, J. W. Weisel, L. Lorand. 1999. Structural Origins of Fibrin Clot Rheology. Biophysical Journal. 77:2813–2826

21. Blomback B. D. Banerjee, K. Carlsson, A. Hamsten, B. Hessel, R. Procyk, A. Silveria, L. Zacharski. 1990. Native Fibrin Gel Networks and Factors Influencing Their Formation in Health and Disease. Advances in Experimental Medicine and Biology. 281:1–23

22. Shah, G. A., C. H. Nai, D. P. Dhall. 1985. Physiological Studies on Fibrin Network Structure. Thrombosis Research. 40:181–188

23. Collet, J. P., D. Park, C. Lesty, J. Soria, G. Montalescot, J. W. Weisel. 2000. Influence of Fibrin Network Conformation and Fibrin Fiber Diameter on Fibrinolysis Speed: Dynamic and Structural Approaches by Confocal Microscopy. Arteriosclerosis, Thrombosis, and Vascular Biology. 20:1354–1361

24. Marchi, R., U. Lundberg, J. Grimbergen, J. Koopman, A. Torres, N. B. DeBosch, F. Haverkate, C. L. Arocha Pinango. 2000. Fibrinogen Caracas V, An Abnormal Fibrinogen with An Alpha 532 Ser-->Cys Substitution Associated with Thrombosis. Thrombosis and Haemostasis. 84:263–270

25. Collet, J-P., J. Soria, M. Mirshahi, M. Hirsch, F. B. Dagonnet, J. Caen, C. Soria. 1993. Dusart Syndrome: A New Concept of The Relationship Between Fibrin Clot Architecture

and Fibrin Clot Degradability: Hypofibrinolysis Related to An Abnormal Clot Structure. Blood. 82(8):2462–2469

26. Collet, J-P., J. L. Woodhead, J. Soria, C. Soria, M. Mirshahi, J. P. Caen, J. W. Weisel. 1996. Fibrinogen Dusart: Electron Microscopy of Molecules, Fibers and Clots, and Viscoelastic Properties of Clots. Biophysical Journal. 70(1): 500–510

27. Gabriel, D. A., K. Muga, E. M. Boothroyd. 1992. The Effect of Fibrin Structure on Fibrinolysis. Journal of Biological Chemistry. 267(34): 24259–24263

28. Carr, M. E., R. M. Jr, Dent, S. L. Carr. 1996. Abnormal Fibrin Structure and Inhibition of Fibrinolysis in Patients with Multiple Myeloma. Journal of Laboratory and Clinical Medicine. 128: 83–88

29. Dunn, E. J., R. A. Ariens, P. J. Grant. 2005. The Influence of Type 2 Diabetes on Fibrin Structure and Function. Diabetologia. 48(6):1198–1206

30. Sugo, T., C. Nakamikawa, N. Yoshida, K. Niwa, M. Sameshima, J. Mimuro, J. W. Weisel, A. Nagita, M. Matsuda. 2000. End-linked Homodimers in Fibrinogen Osaka VI with a B Beta-Chain Extension Lead to Fragile Clot Structure. Blood. 96:3779–3785

31. Bagoly, Z., R. A. Ariens, D. C. Rijken, M. Pieters, A. S. Wolberg. 2017. Clot Structure and Fibrinolysis in Thrombosis and Hemostasis. BioMed Research International. https://doi.org/10.1155/2017/4645137

32. Farkas, A. Z., V. J. Farkas, L. Szabo, A. Wacha, A. Bota, L. Csehi, K. Kolev, C. Thelwell. 2019. Structure, Mechanical, and Lytic Stability of Fibrin and Plasma Coagulum Generated by Staphylocoagulase From *Staphylococcus aurerus*. Frontiers in Immunology. 10:2967. https://doi.org/10.3389/fimmu.2019.02967

33. Pratt, C. W., D. M. Monroe. 1992. Microplate Coagulation Assays. Biotechniques. 13(3): 430-433

34. Mann, K. G., K. Brummel, S. Butenas. 2003. What Is All That Thrombin For? Journal of Thrombosis and Haemostasis. 1(7): 1504-1514

35. Greene, R. W., J. McConaughy. 1955. Effects of Thrombin and Platelet Concentrations and of Clot Retraction on Fibrin Strand Widths. Journal of Clinical Investigation. 34(3): 417-427

36. Domingues, A. M., F. L. Macrae, C. Duval, H. R. McPherson, K. I. Bridge, R. A. Ajjan, V. C. Ridger, S. D. Connel, H. Philippou, R. A. S. Ariens. 2016. Thrombin and Fibrinogen γ' Impact Clot Structure by Marked Effects on Intrafibrillar Structure and Protofibril Packing. Thrombosis and Hemostasis. 127(4): 487-495

37. Liu, C. Y., H. L. Nossel, K. L. Kaplan. 1979. The Binding of Thrombin by Fibrin. The Journal of Biological Chemistry. 254(20): 10421-10425

38. Mann, K. G., S. Butenas, K. Brummel. 2003. The Dynamics of Thrombin Formation. Arterioscelerosis, Thrombosis, and Vascular Biology. 23(1): 17-25

39. Wolberg, A. S. 2007. Thrombin Generation and Fibrin Clot Structure. Blood. 21(3): 131-142

40. Schoeman, R. M., M. Lehmann, K. B. Neeves. 2017. Flow Chamber and Microfluidic Approaches for Measuring Thrombus Formation in Genetic Bleeding Disorders. Platelets. 28(5): 463-471

41. Gersh, K. C., C. Nagaswami, J. W. Weisel. 2009. Fibrin Network Structure and Clot Mechanical Properties are Alternated by Incorporation of Erythrocytes. Journal of Thrombosis and Haemostasis. 102(6): 1169-1175

42. Gorog, D. A., Z. A. Fayad, V. Furster. 2017. Arterial Thrombus Stability. Does It Matter and Can We Detect It? Journal of the American College of Cardiology. 70(16): 2036-2047

43. Xi, G., G. Reiser, R. F. Keep. 2002. The Role of Thrombin and Thrombin Receptors in Ischemic, Hemorrhagic and Traumatic Brain Injury: Deleterious or Protective? Journal of Neurochemistry. 84(1): 3-9

44. Shurbaji, S., G. G. Anlar, E. A. Hussein, A. Elzatahry, H. C. Yalcin. 2020. Effect of Flow-Induced Shear Stress in Nanomaterial Uptake by Cells: Focus on Targeted Anti-Cancer Therapy. Cancers. 12(7). 1916. https://doi.org/10.3390/cancers12071916

45. Godoy-Gallardo, M., P. K. Ek, M. M. T. Jansman, B. M. Wohl, L. Hosta-Rigau. 2015. Interaction Between Drug Delivery Vehicles and Cells Under the Effect of Shear Stress. Biomicrofluidics. 9(5): 052605. https://dx.doi.org/10.1063%2F1.4923324

46. Mahto, S. K., T. H. Yoon, S. W. Rhee. 2010. A New Perspective on *In Vitro* Assessment Method for Evaluating Quantum Dot Toxicity by Using Microfluidics Technology. Biomicrofluidics. 4(3): 034111. https://dx.doi.org/10.1063%2F1.3486610

47. Badiei, N., A. M. Sowedan, D. J. Curtis, M. R. Brown, M. J. Lawrence, A. I. Campell, A. Sabra, P. A. Evans, J. W. Weisel, I. N. Chernysh, C. Nagaswami, P. R. Williams, K. Hawkins. 2015. Effect of Unidirectional Flow Shear Stresses on The Formation, Fractal Microstructure and Rigidity of Incipient Whole Blood Clots and Fibrin Gels. Clinical Hemorheology and Microcirculation. 60(4): 451-464

48. Onasoga-Jarvis, A. A., T. J. Puls, S. K. O'Brien, L. Kuang, H. J. Liang, K. B. Neeves. 2013. Thrombin Generation and Fibrin Formation under Flow on Biomimetic Tissue Factor-Rich Surfaces. Journal of Thrombosis and Haemostasis. 12(3): 373-382

49. Girdhar, G., D. Bluestein. 2008. Biological Effects of Dynamic Shear Stress in Cardiovascular Pathologies and Devices. Expert Review of Medical Devices. 5(2): 167-181

Chapter 4 - Optimizing the Penetration of Nanoparticles and Disrupting Labeled Clots

Abstract:

Ischemic stroke patients have limited treatment options available. The only FDA-approved drug comes with a significant risk of bleeding. We are investigating an alternative treatment that targets activated platelets in occlusive clots using fibrinogen-conjugated gold-coated magnetite nanoparticles (FGN-cAu-Fe_3O_4) for hyperthermia. The success of disrupting clots requires both a significant number of nanoparticles localized deep inside occlusive clots and the efficacy of magnetite nanoparticles. We have found that the penetration and concentration of the nanoparticles were limited to the outside of clots that formed at high thrombin concentration, especially in whole blood (WB) clots. Moreover, magnetite nanoparticle synthesis is not a robust procedure. Heating and killing quality of magnetite nanoparticles is inconsistent between batches. Hence, we proposed using a phagocytic cell model to test the magnetite nanoparticle heating and killing efficacy. **We hypothesize that increasing label concentration and incubation time could increase the depth of penetration and concentration of nanoparticles into clots. Also, using a phagocytic cell model combined with light microscopy would allow rapid observation of both cell morphology and viability; therefore, allowing us to predict the efficacy of magnetite nanoparticles.** We examined the impact of label concentration and incubation time on nanoparticle penetration and concentration by using an *in vitro* model in which platelet-rich plasma (PRP) and WB were clotted using different thrombin concentrations followed by labeling with the robust fibrinogen-conjugated gold nanoparticles (FGN-cAu_{18}) at different concentrations for 15 or 60 minutes. Frozen cross-sections were treated with silver enhancement (SE) and analyzed by light microscopy. As expected, short incubation time and low concentration of FGN-cAu_{18} result in low label concentration and penetration inside clots. By increasing FGN-cAu_{18} concentration and

incubation time, penetration and concentration of nanoparticles improves significantly in PRP clots, but only slightly in WB clots. These results suggest that multiple applications of nanoparticles may be necessary for the success of a targeted nanoparticle therapy for ischemic stroke. To test the efficacy of magnetite nanoparticles, the RAW 264.7 murine macrophage cell line was used. The cells were allowed to ingest magnetite nanoparticles before exposure to an oscillating magnetic field, followed by analysis using light microscopy and scanning electron microscopy (SEM). We observed that magnetite nanoparticles had ability to destroy RAW 264.7 cells and would also kill the activated platelets. Therefore, the RAW 264.7 model allowed for a reasonable prediction of the efficacy of magnetite nanoparticles. Together, these results provided important information in the development of a nanoparticle-based therapeutic agent for treatment of ischemic stroke.

Introduction:

Many studies have shown that increasing temperature can disrupt and destroy cells. Hyperthermia therapy is a type of medical treatment in which body tissue is exposed to temperature above the physiologic optimum, around 40°C and above (1-4). Most hyperthermia treatments are primarily focused on attacking tumors. As anti-cancer therapy, hyperthermia treatment delivers heat directly to the cancer cells to either destroy them or make them more sensitive to the effects of more conventional treatments, such as enhancing chemotherapy or radiation. Hyperthermia affects cells and tissues on multiple levels. For example, hyperthermia results in a profound increase in blood flow, causing vascular occlusion or hemorrhage in tumors (1). Another pronounced physiological change in tumors is a decrease in tumor pH upon heating. Cancer cell proliferation is a more vulnerable target under acidic conditions (2-5). Raising

temperatures cause the cell to release heat shock proteins; thereby, inducing the immune system to target the cancer cells (6-8). Also, hyperthermia can directly induce DNA damage including DNA breaks and chromosomal aberrations. Moreover, hyperthermia can disturb multiple DNA repair pathways via disabling or inhibiting intracellular DNA repair enzymes. Thus, hyperthermia sensitizes cells to a broad range of DNA-damaging agents, helping it take a more central role in clinical cancer treatment (9-11). In addition to the above effects, raising the cells' temperature can cause protein and membrane damage (9,12,13), interfere with the cell cycle (14,15), impact lipid membrane dynamics and stability (16,17), and cause metabolic imbalance (18,19).

Hyperthermia can be administered by a variety of methods from relatively simple bulk heating to quite complex targeted methods including whole-body, regional, and local hyperthermia. In whole-body hyperthermia, either radiative heat or extracorporeal technologies are used to raise the temperature of the entire body to at least 41°C. Radiative heating can be produced by thermal chambers, inductive loops, and hot water blankets to heat up the entire body superficially. Extracorporeal whole-body hyperthermia works by circulation of extracorporeally heated blood. The extracted blood is heated by crossing it through a water bath or hot air and then infused into the main vein. Whole-body hyperthermia is useful in treating metastatic cancer that has spread widely through the body (20-22). Regional hyperthermia commonly distributes heat to large areas and is used to treat advanced tumors. In one approach, applicators are positioned around the surface of an organ or body cavity, and then high energy waves are produced and directed at the area. These devices release microwave or radiofrequency energy with a frequency of 350 kHz to 700 kHz to heat the area being treated. Another approach to regional hyperthermia is perfusion. As with extracorporeal heating, the patient's blood is isolated

from the circulation, heated by heating devices, and then pumped back into the desired area. Typically, anticancer drugs can be pumped in at the same time (20,23-26). Local hyperthermia is used to treat relatively small tumors. Different types of energy including microwave, radiofrequency and ultrasound are used to deliver heat. Depending on the tumor location, local hyperthermia can be performed by different approaches. In external approaches, high energy waves are aimed at a tumor located near the body's surface using outside applicators. Alternatively, a probe can be inserted directly into the tumor. The tip of the probe then releases the energy to heat the surrounding cancerous tissue (20,24,26-28).

Hyperthermia treatment technology has been approved by the FDA to treat malignant tumors on either superficial or interstitial parts of the body. However, conventional hyperthermia methods have several disadvantages. First, hyperthermia treatments require invasive procedures, special equipment, and skilled treatment teams. Because of that, not all cancer treatment centers have available hyperthermia treatments. Second, despite the ability of hyperthermia to synergistically enhance the efficacy of radiotherapy and chemotherapy treatments, the heating methods are rather crude and do not distinguish between heating of malignant and healthy tissues. Since the target and the surrounding normal tissues might respond similarly to hyperthermia, this non-selective tissue heating can cause serious toxic side effects. Hence, the conventional hyperthermia methods have barriers to their clinical application. Therefore, it is desirable to improve hyperthermia to target a specific tissue. To do this, most applications require a method to produced highly localized heating with minimally invasive procedures.

The development of nanomaterials and nanotechnology provide a novel and original solution to the aforementioned disadvantages. Nanoparticle-based heating methods that use specific binding of molecules to target a tissue or cell type have been developed (29-35). These

treatments concentrate on utilizing nanoparticles to convert energy from extrinsic sources into localized heat, causing hyperthermia solely at the area containing nanoparticles. The most common external energy sources used for generating heat using nanoparticles are light and an alternating (or oscillating) magnetic field (36-41).

Photothermal hyperthermia occurs upon generation of surface plasmon resonance in gold nanoparticles when they absorb light near the infrared range. Then, the surface electrons become excited and intensively resonant, quickly converting light to heat (34). In order to absorb near infrared light efficiently, gold nanoparticles can be synthesized into different shapes such as rod shape (37), hollow spheres (42) and silica-gold core-shell like structures (43). Another way to enhance the effectiveness of gold nanoparticles in near infrared light absorption is to promote their agglomeration at the site of interest so that the energy absorption per unit area is increased (38). Nanoparticles can be functionalized and delivered specifically to the target cells by different methods including conjugation with proteins or physiologic transportation. Several studies have shown that photothermal therapies work successfully *in vitro*, but often have limitations *in vivo* due to the attenuation of near infrared light through scattering and absorption within the tissues, limiting penetration and heating (44-46). Thus, despite promising results *in vitro*, there are challenges that must be addressed before this technique can progress to the clinic.

Magnetic hyperthermia utilizes magnetic nanoparticles to transform electromagnetic energy from an external high frequency field to heat. Magnetite (Fe_3O_4) and maghemite (γ-Fe_2O_3) nanoparticles are the most commonly used materials for magnetic hyperthermia and they are usually referred to as magnetic iron oxide nanoparticles. When exposed to an alternating magnetic field, these nanoparticles produce heat via two main mechanisms, which are hysteresis loss and relaxational losses. Hysteresis loss happens when large magnetic iron oxide

nanoparticles are subjected to the magnetic field; whereas, below 100nm magnetic iron oxide nanoparticles become superparamagnetic in the presence of the magnetic field and heat is mainly generated by Néel relaxation and Brownian relaxation (47-50).

There are many advantages of using magnetic iron oxide nanoparticles. First, iron is a biologically essential component of the human body. The average human adult naturally carries approximately 3.5-4 grams of iron. These 3-4 grams are distributed throughout the body in hemoglobin, tissues, muscles, bone marrow, blood proteins, enzymes, ferritin, hemosiderin and circulating in plasma bound to transferrin (51). Consequently, magnetic iron oxide nanoparticles have been systemically administrated safely in large quantities in clinical settings unlike other inorganic nanoparticles (52). In fact, the FDA already approved the application of magnetic iron oxide nanoparticles as a contrast agent in computed tomography (CT) at high concentration and magnetic resonance imaging (MRI) at low concentration. This is useful since the magnetic iron oxide nanoparticle concentration within the tumors can be measured by CT, aiding the estimation of hyperthermia dosimetry (47,52,53). Moreover, magnetic iron oxide nanoparticles can undergo surface modification and functionalization. For specific cellular targeting, magnetic iron oxide nanoparticles can be functionalized with organic molecules or proteins. Iron oxide nanoparticles can also be coated first with gold and then conjugated with protein (54-60). Not surprisingly, magnetic iron oxide nanoparticles for magnetic hyperthermia has gained a significant interest as a potential therapy for cancer treatment among other applications.

Our particular interest is utilizing magnetite nanoparticles to target fibrinogen receptors on platelets for magnetically-induced hyperthermia to disrupt an occlusive clot causing ischemic stroke. In the purified platelet system, gel-filtered platelet (GFP) aggregates labeled with fibrinogen conjugated, gold-coated magnetite nanoparticles (FGN-cAu-Fe_3O_4) that were exposed

to a 500 kHz OMF at 8mT for 30 minutes were successfully disrupted and sustained significant damage (60). High concentrations of labels were found throughout the aggregates in that system. In previous chapters we have demonstrated that fibrinogen-conjugated nanoparticles are able to incorporate into the clots of PRP and WB systems. However, we also noted that the complex components of PRP and WB challenge the effectiveness of nanoparticle penetration. The depth of nanoparticle penetration and the total concentration inside of the clot contribute significantly to the success of clot disruption. Hence, we will evaluate the penetration of label in more complex PRP and WB clots, as seen previously in GFP aggregates. This will be done under conditions that approximate *in vivo* physiology as closely as possible to lay the groundwork for future animal experiments. The conditions to be investigated include physiologically achievable label concentration and incubation time. We hypothesize that under optimized conditions the FGN-conjugated nanoparticles can access the interior of both PRP and WB clots. In these experiments, FGN-cAu_{18} will be used to label clots, because penetration of gold nanoparticles is a more robust, and reproducible procedure than preparation of gold-coated magnetite nanoparticles. SEM and light microscopy techniques will be used to analyze the data.

Besides the efficiency of nanoparticle penetration into the clot, the efficacy of magnetite nanoparticles plays an important role in clot disruption. We are using coprecipitation methods to synthesize the magnetite nanoparticles. The coprecipitation method possesses advantages. It is simple, ecofriendly, non-toxic in physiological conditions, and the solvent-free process gives water-soluble and biocompatible superparamagnetic magnetite nanoparticles. The dilemma here pertains to the quality of the colloids produced from the coprecipitation reaction. Coprecipitation produce nanoparticles with a broad size distribution (Figure 55). This leads to non-ideal magnetic behavior compared to the uniform size nanoparticles obtained from other methods of

synthesis such as the thermal decomposition and electrochemical method (61-63). In fact, within the same batch of magnetite nanoparticles produced by coprecipitation, several monodisperse populations of particles coexist and become magnetically inequivalent, leading to a difference in heat generation when exposed to the OMF. Thus, batch-to-batch variability in the heating capacity of nanoparticles is a continuing issue. Here, we have used the RAW 264.7 murine macrophage cell line with light microscopy as a phagocytic cell model to test the heating and killing properties of Fe_3O_4 nanoparticles before coating them for targeting experiments. Relatively rapid scanning with the light microscope allowed us to observe the cells' morphology and viability. Here, we hypothesized that using a phagocytic cell model combined with light microscopy will allow us to predict the efficacy of magnetite nanoparticles in destroying activated platelets in clots.

The results of these studies will provide insight for the development of nanoparticle-based targeting *in vivo*.

Materials and Methods:

PRP, WB and gel-filter platelet (GFP) preparation:

GFP, PRP and WB were prepared as described in Chapter 2.

Fibrinogen-conjugated gold-coated magnetite synthesis:

Magnetite nanoparticle synthesis (cFe_3O_4), gold-coated magnetite nanoparticles, conjugation of fibrinogen to gold-coated magnetite nanoparticles (FGN-cAu-Fe_3O_4), gold nanoparticle synthesis (cAu_{18}), and conjugation of fibrinogen to gold nanoparticles (FGN-cAu_{18}) were described in Chapter 2.

Effect of nanoparticle concentration and labeling time on penetration of FGN-cAu$_{18}$ into clots:

PRP and WB were allowed to form clots at low (1nM) and high (10nM) thrombin concentrations for 10-15 minutes at 37°C on the microtiter plate reader as described in Chapter 3. After clots were formed, they were transferred into fresh microcentrifuge tubes that contained FGN-cAu$_{18}$ with the concentration adjusted to give OD_{522}= 0.2 or OD_{522}=1.0. FGN-cAu$_{18}$ were supplemented with $CaCl_2$ to a final concentration of 2mM. Clots were incubated in FGN-cAu$_{18}$ for 15 or 60 minutes at 37°C. Then, the clots were washed thoroughly in Tyrode's buffer with 0.1% BSA three times before fixing in 1% glutaraldehyde in 0.1M HEPES, pH 7.4, for 30 minutes at room temperature (RT).

For visualization of nanoparticles inside of clots, the samples were processed through standard SEM preparation procedures including post-fixation in 0.05% OsO4, dehydration in a graded ethanol series, critical point drying, and carbon coating. Samples were analyzed by using a Hitachi S-4800 FE-SEM operating at 15KV for backscattered electron imaging.

For measuring nanoparticle penetration, after primary fixation with 1% glutaraldehyde, samples were washed three times with 0.1M HEPES before embedding in OCT. The samples were frozen on dry ice. The frozen clots were sectioned on a cryostat and the sections were picked up on poly-L-lysine coated slides. Then, the sections were fixed with 1% glutaraldehyde for 5 minutes. They were rinsed excessively with Millipore double deionized water (MDDW) and then treated with a Sigma-Aldrich silver enhancing kit according to the manufacturer's directions. The treated sections were then fixed with 2.5% sodium thiosulfate, and then washed three times with MDDW and air dried overnight. Cover slips were mounted using VectaMount

medium and analyzed by light microscopy to measure the nanoparticle penetration. Both SEM preparation and silver enhancement were described in detail in Chapters 2 and 3, respectively.

Oscillating magnetic field device:

A custom made OMF device was constructed in-house and used to heat magnetite particles. The OMF device was built using a resonant circuit. The system consisted of a hand-wound inductor coil with water cooling (described below) connected as an autotransformer, which was paired with a set of suitable fixed capacitors in series and a parallel variable air dielectric capacitor. The OMF system was powered by an AG Series 1024 RF amplifier with internal signal generator (T&C Power Conversion, Rochester, NY). The signal generator was used to produce a 500kHz waveform by using internal power output control to reach the desired field amplitude.

The air core solenoid or the inductor is the source of an OMF. It was built by wrapping 3.175mm diameter copper tubing (Phillips and Johnston, Glen Ellyn, IL) around a 5cm diameter glass cylinder for a total of 50 turns. Flowing water ran through the hollow copper tubing, pulling heat as it wound around the inductor during operation, to prevent overheating during operation. To provide electrical insulation to prevent short circuiting, the coils were wrapped in vinyl tape.

In order to tune the OMF circuit, a BK Precision 4017B signal generator was used to generate a 5volt sinusoidal waveform at 500kHz. The waveform bias was adjusted with the DC offset voltage. The output power is limited by an internal source resistance of 50Ω. The frequency and the amplitude range could be selected with pushbuttons on the signal generator. Since the various combinations of fixed capacitors with a variable capacitor functioned as

resistors affecting the voltage that could be delivered to the solenoid to which they were attached, the voltage could be measured and applied to calculate the magnetic flux in the solenoid using Coulomb's Law. The strength of magnetic field produced by the OMF was determined by using a 15-gauge cooper wire that was shaped into a square loop with an area of $1cm^2$, placed in the middle of the solenoid. The potential across the wire was measured with a BK Precision 2125A analog oscilloscope. The magnetic field, in tesla (T), can be calculated by Coulomb's equation:

$$B=E/ (2 * \pi * F * A)$$

Where B is magnetic field produced in tesla, E is the potential across the copper loop in volts, F is the frequency of the OMF in hertz and A is the area of the copper loop in square meters.

Tuning was further refined by adjusting the variable capacitor when the system was powered by the RF amplifier at 10Watts forward power. Optimal tuning was achieved when the reflected power was detected at less than 10% of forward power (60,64).

Testing the efficacy of cFe_3O_4 batches:

The heating capacity of cFe_3O_4 nanoparticles varies from batch to batch. Therefore, their capacity to heat and kill cells was tested in a phagocytosis model using the *Mus musculus* macrophage cell line RAW 264.7 as previous described (64), with minor modifications. 70,000 cells were allowed to adhere onto 13mm Thermanox® plastic coverslips (NUNC™, NY, USA) and grown in high glucose Dulbecco's modified eagle medium (DMEM) (Fisher Scientific, Gibco™) supplemented with 10% fetal bovine serum (FBS) overnight at 37°C in a 5% CO_2 atmosphere. 50µL undiluted cFe_3O_4 nanoparticles were added to 450µL media and incubated

with the cells for 30 minutes at RT. As controls, media alone and 18nm gold nanoparticles were added and incubated in the same manner. Cells were washed twice in Dulbecco's phosphate buffered saline (PBS) to remove free nanoparticles, then exposed to the OMF at 500kHz, 8mT for 1minute. Cell viability was measured by exclusion of 0.04% trypan blue in PBS. Light micrographs were collected with a Nikon TE2000U inverted light microscope with a CoolSNAP ES camera (Photometrics) using Metaview software (Molecular Devices).

In some instances, SEM standard preparation was used to further analyze the damage of the cells. For this, cells were washed with PBS, followed by fixing in 1% glutaraldehyde in 0.1M HEPES, pH 7.4 for 30 minutes at RT. Then, samples were washed and post-fixed with 0.05% OsO_4 for 15 minutes. Samples were dehydrated using a graded series of ethanol and dried by the critical point drying procedure. The dried samples were mounted onto SEM stubs with carbon tape and coated with carbon using a carbon evaporator. Samples were analyzed using a Hitachi S-4800 FE-SEM operating at 1kV for secondary electron imaging and 15-30kV for backscattered electron imaging. Batches of cFe_3O_4 that killed at least 70% of the cells were coated with gold to be conjugated with fibrinogen and used in hyperthermia experiments.

Hyperthermia of surface activated platelets:

Gel-filtered platelets were supplemented with 2mM $CaCl_2$ and allowed to spread on Thermanox® coverslips between 10-15 minutes. The spread adhered platelets were then incubated with FGN-cAu-Fe_3O_4, or FGN-cAu_{18}, or left unlabeled in Tyrode's buffer with 0.1%BSA for 15 minutes. Unbound labels were washed off by dunking the coverslips in excess buffer. Then, the coverslips were washed three times by incubating a drop of buffer on the cover slips for 5 minutes. The coverslips were covered in buffer and transferred to a 35mm Petri dish,

then exposed to the OMF at 500kHz, 8mT for 5 x 2.5 minutes bursts with a one-minute cool down between bursts. Negative controls received no magnetic field exposure and were kept away from the OMF apparatus. The samples were then washed and processed by SEM standard preparation methods to observe the morphology of the cells. SEM preparation and analysis were similar to that described above for testing the efficacy of Fe_3O_4 in the RAW 264.7 cell line.

Results:

The success of disrupting clots depends on several factors, including the efficiency of magnetite nanoparticles, having a sufficient amount of nanoparticles accumulated in the interior of the clot, and the depth of nanoparticle penetration into the interior of the clot. In Chapter 2, it was demonstrated that increasing the complexity of the clot components challenged the extent to which nanoparticles could penetrate and concentrate deep inside of the clot. In the most challenging condition, WB clots formed at high dose of thrombin, the penetration and concentration of the nanoparticles were limited to the outside of the clot due to the high density of the fibrin network. Thus, evaluating the effect of varying nanoparticle concentration and labeling time on nanoparticle penetration into PRP and WB clots formed at different thrombin concentrations will inform us about the potential of nanoparticle-based targeting performed *in vivo*. Additionally, cFe_3O_4 synthesis remains a challenge because of batch-to-batch variability in heating capacity of nanoparticles produced. Hence, a faster light microscopy method will be utilized to confirm the efficacy of cFe_3O_4 nanoparticles before coating them for targeting experiments.

Effect of nanoparticle concentration and labeling time on penetration of FGN-cAu$_{18}$ into PRP clots:

When PRP clots formed at low thrombin concentration were incubated a short time (15 minutes) with FGN-cAu$_{18}$ at low concentration (OD_{522nm}= 0.2), nanoparticles were mainly found at the periphery of the clot. Some were able to migrate into the interior, but to a limited extent. The percent nanoparticle penetration was 29% and 15% for Donors 1 and 2, respectively.

When the time of incubation increased to 60 minutes, slightly more FGN-cAu$_{18}$ nanoparticles were incorporated (Figure 56), and they penetrated deeper into the clots. Nanoparticle penetration was 30% clots from in both donors. Increasing the FGN-cAu$_{18}$ concentration (OD_{522nm}= 1.0) led to a slight increase in concentration of FGN-cAu$_{18}$ at the periphery of the PRP clot, but did not significantly improve the concentration of FGN-cAu$_{18}$ in the interior of the clot at 15 minutes incubation (Figure 56). Nanoparticle penetration was 20%-23% in this set of experiments. When both nanoparticle concentration and time of incubation were increased (OD_{522nm}=1.0 and 60 minutes incubation), both degree of penetration and concentration of FGN-cAu$_{18}$ were markedly increased throughout the PRP clots, including at the deep interior (Figure 56). The percent nanoparticle penetration was calculated at 45% and 41% for Donor 1 and Donor 2, respectively (Table 9).

For the PRP clots formed at 10nM thrombin, either low nanoparticle concentration and short time of labeling (OD_{522nm}= 0.2 and 15 minutes) or high nanoparticle concentration and short time of labeling (OD522nm= 1 and 15 minutes), led to shallow nanoparticle penetration into the clot. Most of the labeling was accumulated at the edge rather than deep inside the clots (Figure 57). The short time incubation time combined with either a low or high labeling concentration showed only 15% and 24% of nanoparticle penetration for Donor 1, and only 25%

and 10% for Donor 2 (Table 10). Increasing incubation time but not label concentration (OD_{522nm}= 0.2, and 60 minutes incubation), improved penetration. There were a few more labels to be found near the center of the clot (Figure 57), but the total amount of label still was still quite low. Depth of nanoparticle penetration under this condition was 36%-37% for both donors. When both nanoparticle concentration and incubation time were increased (OD_{522nm}= 1, and 60 minutes incubation), the improvement in nanoparticle concentration was apparent (Figure 57). The depth of nanoparticle penetration was 28% in Donor 1, and improved to 41% for Donor 2 (Table 10).

Effect of nanoparticle concentration and labeling time on penetration of FGN-cAu$_{18}$ into WB clots:

WB clots formed with 1nM thrombin and labeled with a low concentration of nanoparticles for short time had only a few nanoparticles detected in the interior of the clot (Figure 58). Most of them were found near the outside of the WB clot. This is reflected by only 14% nanoparticle penetration under these condition for both donors (Table 11). As the time of labeling increased, nanoparticles moved slightly inwards from the edge toward the interior of the clot; however, the majority were still accumulated at the periphery. The total number of nanoparticles appeared to increase, but still was low (Figure 58). Nanoparticle penetration improved to 21% and 25% for Donors 1 and 2, respectively (Table 11). When the nanoparticle concentration was increased (OD_{522nm}= 1.0) but the time of incubation remained short (15 minutes), a higher concentration of nanoparticles was found at the periphery of the clot and nanoparticle penetration was limited to the periphery of the clot (Figure 58). The degree of nanoparticle penetration remained low and comparable to results using low concentration and

short time incubation, at 11% and 17% for Donors 1 and Donor 2, respectively (Table 11). When both concentration and time of incubation were increased (OD_{522nm}= 1.0, and 60 minutes incubation), the penetration of nanoparticles was nearly to the center of the clot for Donor 1 with 34% nanoparticle penetration; whereas, the nanoparticle migration was more peripheral for Donor 2 at 21%. The nanoparticle concentration inside of the clots appeared to slightly increase in both donors, but still remained relatively low (Figure 58).

In the interior of WB clots formed with 10nM thrombin, nanoparticle concentration was limited and generally difficult to detect (Figure 59). With high FGN-cAu_{18} concentration and long incubation time (OD_{522nm}=1, and 60 minutes incubation), a few more nanoparticles were detected in the interior of the clots (Figure 59). However, the nanoparticle concentration was still lower than what was observed in 1nM WB clots, and much lower than what was observed in PRP clots. The percent of nanoparticle penetration increased slightly as the time of incubation increased to 60 minutes. Between 22% and 26% nanoparticle penetration were obtained for both donors. Increasing the FGN-cAu_{18} concentration did not improve the depth of nanoparticle penetration at the short incubation time. Less than 20% nanoparticle penetration occurred in Donor 1 and Donor 2 with 15 minutes of labeling (Table 12).

Testing the efficacy of cFe_3O_4 in heating and killing cells in a phagocytosis model:

The quality of the cFe_3O_4 nanoparticles plays a critical role in disrupting the clots. Batch-to-batch variability in heating capacity is a continuing issue. Thus, a faster light microscopy model was utilized to test the heating and killing properties of Fe_3O_4 nanoparticles before coating them for targeting experiments. Relatively rapid scanning with the light microscope allowed us to observe the cells' morphology and viability. When RAW 264.7 cells had no nanoparticles or

were incubated with the cAu_{18} nanoparticles, regardless of whether or not they were exposed to the OMF, the cell density was very high. The cells looked healthy, and firmly adhered. On the other hand, when RAW 264.7 cells were incubated with cFe_3O_4 nanoparticles and treated with the OMF, the majority of the cells had lifted from the coverslip, resulting in a very low density. More than half of the remaining adherent cells were stained with trypan blue, compared to an insignificant number of the control cells (all incubation conditions without OMF treatment, and incubation without nanoparticles or incubation with cAu_{18} treated with the OMF) (Figure 60). In backscattered electron images, cells that were incubated with gold nanoparticles appeared very bright. A less bright but distinct signal came from inside the cells, which indicated cells had ingested magnetite nanoparticles. The control cells without nanoparticles had a very dim signal corresponding to granules in the interior of the cell (Figure 61). The backscattered electron signal is most likely due to OsO_4 staining of the granule membranes, with some contribution from the granule contents. Additionally, secondary electron analysis showed that all samples without OMF exposure were healthy, well spread, and had no membrane damage. The cells incubated with cAu_{18} and no nanoparticles, as expected, show no damage even when they were treated with the OMF. Cells exposed to both cFe_3O_4 and the OMF showed extensive cell damage. Frequently, traces of cells observed as membrane debris were found (Figure 62).

Hyperthermia treatment of surface-activated platelets:

After using the RAW 264.7 cells to test the killing capacity of the cFe_3O_4 (the magnetite nanoparticles), cFe_3O_4 were then coated with gold and conjugated to fibrinogen. After, FGN-cAu-Fe_3O_4 were used to target the surface-activated platelets. First, we observed that the labeling pattern of FGN-cAu-Fe_3O_4 was similar to that of FGN-cAu_{18} on well-spread platelets. The labels

were found near the granulomere in very high numbers. FGN-cAu_{18} has higher electron density under backscatter mode compared to fibrinogen conjugated-gold coated-magnetite nanoparticles, and thus appeared brighter (Figure 63). Second, we wanted to examine the killing ability of FGN-cAu-Fe_3O_4 nanoparticles on the surface-activated platelets under exposure to the OMF. There was no damage observed on either unlabeled or FGN-cAu_{18} labeled cells. But there was membrane damage, and amorphous cell structure was observed in FGN-cAu-Fe_3O_4 labeled platelets (Figure 64). All the batches of cFe_3O_4 nanoparticles tested that showed heating and killing ability in RAW 264.7 cells also showed killing capacity with surface-activated platelets after they were coated and conjugated to make FGN-cAu-Fe_3O_4.

Discussion:

Optimizing the penetration and concentration of nanoparticles in clots and testing the heating and killing efficacy of magnetite nanoparticles were evaluated in this chapter in order to improve the chances of successfully disrupting labeled clots when they are exposed to the OMF. In the PRP clot system, improvement of both nanoparticle penetration and concentration in the interior of clots occurred as the label concentration and time of incubation were increased. The WB clots exhibited the same phenomenon. However, the amount of increase in nanoparticle penetration was minimal, and nanoparticle accessibility was still limited to just the periphery of the clots, especially in WB clots formed with 10nM thrombin. We also demonstrated the feasibility of using a faster light microscopy method with RAW 264.7 cells, that allowed us to predict the heating and killing efficacy of batches of cFe_3O_4 before coating them with gold and employing them to target activated platelets in experiments that require lengthy analysis.

Effect of nanoparticle concentration and labeling time on nanoparticle penetration into clots:

We hypothesized that optimizing the nanoparticle concentration and labeling time would improve nanoparticle penetration into clots. It was determined that longer labeling time with high concentration of FGN-cAu_{18} gave noticeably better outcomes. We were able to observe higher nanoparticle deposition closer to the center of clots.

We expected that clots formed with high thrombin concentration (10nM) would challenge nanoparticle penetration more than clots formed with low thrombin concentration (1nM) in all conditions that we tested. This is, in fact, what we observed. The overall amount of nanoparticles that penetrated and their concentration inside the 10nM thrombin clots were less than with 1nM thrombin clots. The thrombin concentration present at the time of clot formation affects the fibrin structure formed; thereby influencing the permeability of the clot. When a high thrombin concentration was available during clot formation, more and thinner individual fibers for a given amount of fibrinogen were generated; while a low thrombin concentration produced thicker and fewer individual fibers per fibrinogen content (65-67). As a result, the low thrombin dose allowed formation of a porous and permeable clot; therefore, it was more susceptible to penetration of FGN-cAu_{18} into the interior compared to the high thrombin clot that has a dense, tightly packed network. The data suggested that while FGN-cAu_{18} nanoparticles were incorporated into the clot, their migration through the three-dimension fibrin network might be a rate-limiting determinant for nanoparticle penetration. That means it might be more difficult to disrupt the high thrombin concentration clot than the low thrombin concentration clot. By elevating both nanoparticle concentration and time of labeling, low nanoparticle penetration and concentration issues could be overcome, and we may be able to successfully disrupt even those clots with a dense fibrin network.

Differences in clot components could also impact the effect of nanoparticle penetration into clots. The more complex system (WB clot) remarkably limits nanoparticle penetration, whereas the less complex system (PRP clot) gives only slight resistance to nanoparticle penetration. It is likely that the addition of RBCs to fibrin and activated platelets contributed significantly to the solid matrix, bulk and occlusive nature of whole blood clots, thereby, enhancing stability. The WB clot was well protected from external permeation, such as the labeling with FGN-cAu_{18} nanoparticles or fibrinolysis (68-70). Moreover, due to steric hindrance, the presence of RBCs could cover or block the access of FGN-cAu_{18} to interact with the integrin receptors on the activated platelet surface (70). Additionally, the activated contractile platelets pulling on fibrin cause the contraction of the blood clot. This results in the compaction of the RBCs to the core of the clots and redistribution of activated platelets and fibrin toward the outside of the clot. Consequently, RBCs that gather together in the center of the contracting clot undergo a shape transformation from their native biconcave shape to polyhedral shape (71,72). This remarkable event reduces clot permeability because the polyhedral shape is able to minimize the space between the cells, which help to create an impermeable seal at the site of vessel injury to prevent bleeding (72,73). However, this biologically important event could reduce the effectiveness of nanoparticle penetration into WB clots. In the WB clots, especially those formed at 10nM thrombin concentration, despite the increase of both nanoparticle concentration and incubation time, the increase of nanoparticle penetration was still minimal, and the label was only able to migrate and accumulate primarily at the periphery rather than at the core of the clot. It is likely that WB clots labeled with FGN-cAu-Fe_3O_4 would be more challenging to disrupt than labeled PRP clots when they are exposed to the OMF.

Overall, the effect of nanoparticle penetration could be improved by increasing both labeling time and concentration in PRP clots, but the effect with WB clots are less promising especially in clots formed with high thrombin concentration. *In vivo*, the high thrombin WB clot would be the most likely type to occur at the site of stroke. Therefore, in order to further increase the ability of nanoparticle penetration to enhance the chance of successful clot disruption in a WB system, several approaches are advisable. First, instead of only one application of nanoparticles, clots could be exposed to nanoparticles multiple times. If the degree of nanoparticle penetration remains unchanged or only slightly changes, an additional OMF exposure might be applied between each labeling step. Multiple OMF exposures would disrupt clots layer by layer, each time exposing a new surface of the clot for repeated labeling. As a result, we could bring the label to the center of the clot after several rounds of labeling and OMF treatments. The implication for *in vivo* applications is that eventually the clot would be small enough that is would no longer block the vessels, thereby, restoring blood flow. Administration of tissue plasminogen activator (tPA) synergistically with nanoparticle labeling and OMF treatment could be another potential approach. With this approach, tPA dissolves fibrin, and nanoparticle-induced hyperthermia destroys activated platelets of the clots, providing a two-pronged strategy for clot disruption.

Testing the efficacy of Fe_3O_4 in heating and killing cells in a phagocytosis model:

The RAW 264.7 model allows for predicting the heating and killing efficacy of cFe_3O_4 magnetite nanoparticles. In this study, this cultured macrophage cell line was incubated with cFe_3O_4. The macrophages were then exposed to the OMF, and cells that ingested cFe_3O_4 nanoparticles were damaged as a result of nanoparticle heating. Our experiment demonstrated

that all of the magnetite nanoparticle batches that killed macrophage cells also damaged surface-activated platelets after coating with gold and conjugating with fibrinogen. In the past, SEM analysis was the only way to confirm the damage done to activated platelets by magnetite nanoparticles. However, SEM is time consuming, complex procedurally, and labor intensive. A technique using phagocytic cell cultures and light microscopy could determine the efficacy of magnetite nanoparticle in a significantly shorter amount of time. Therefore, we could avoid spending too much time and resources on using an unsuccessful batch of magnetite nanoparticles in targeting experiments. RAW 264.7 cells served as a good phagocytic model in our hands, providing a method with intermediate difficulty that can be used to test the efficacy of magnetite nanoparticles before targeting clots, both *in vitro* and *in vivo*.

Figures and Figure Legends:

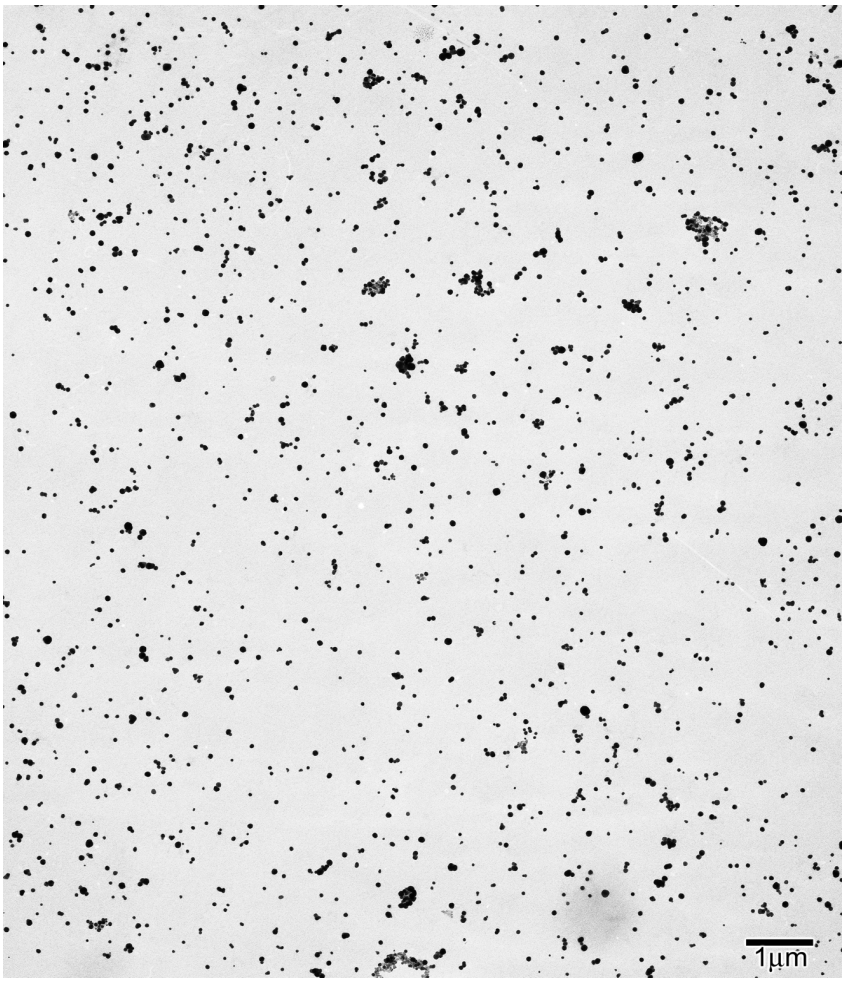

Figure 55. TEM micrograph of magnetite nanoparticles produced by coprecipitation method after 3 days aging under argon. The magnetite nanoparticles were dried onto a formvar-coated nickel grid before imaging by TEM. Coprecipitation produced nanoparticles with a broad size distribution. ImageJ software was used to measure the size of random 100 random magnetite nanoparticles. The size of nanoparticles ranged between 3nm and 100nm in diameter. The population was very heterogeneous, with a coefficient of variation of approximately 32%. The most common size found in this batch was between 9nm and 13nm in diameter.

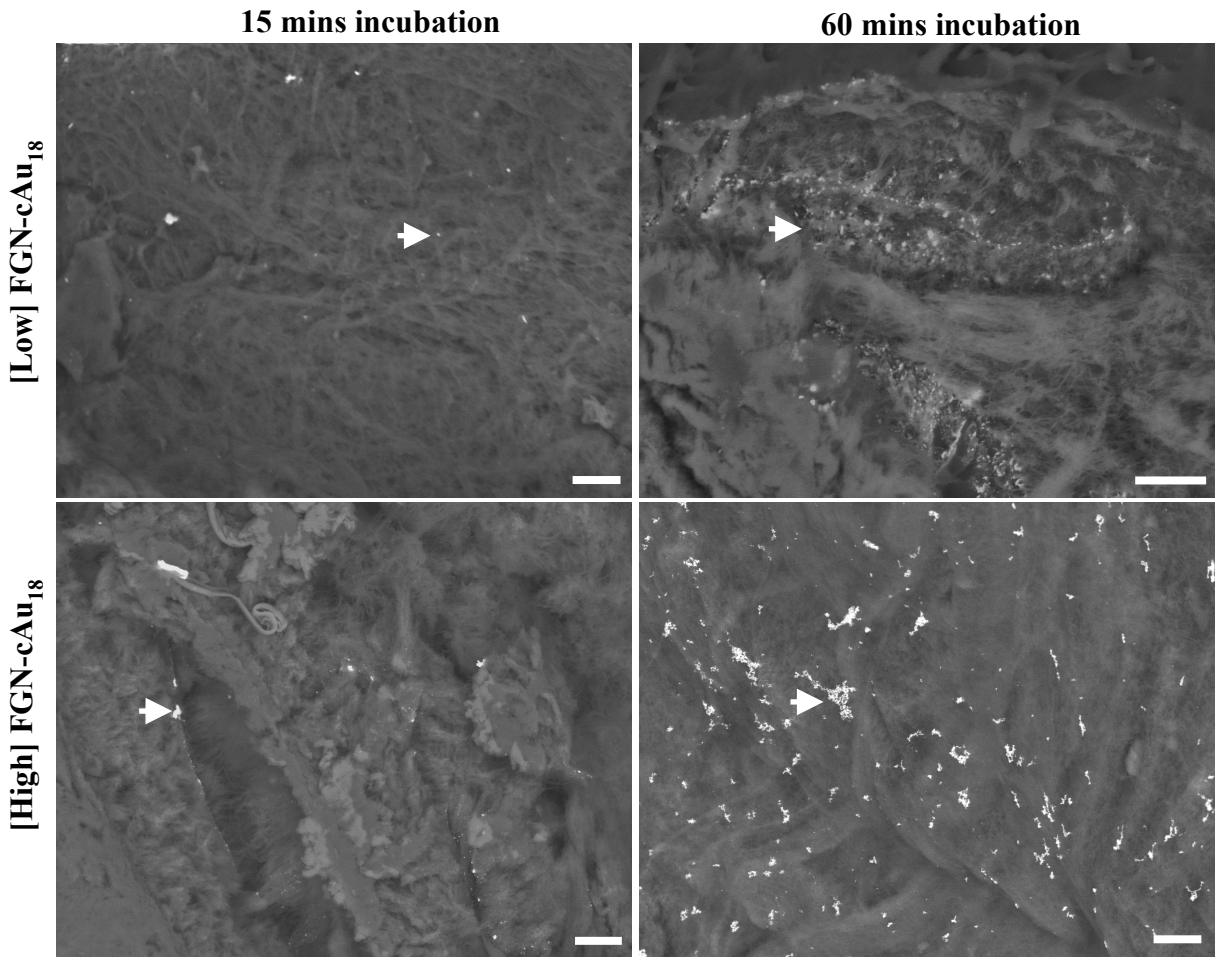

Figure 56. Effect of nanoparticle concentration and labeling time on nanoparticle penetration into PRP clots formed with 1nM thrombin. The images were taken at the interior of the clot where nanoparticles had penetrated deepest. At low concentration of FGN-cAu$_{18}$ and short time of incubation, few nanoparticles were found inside of the clot. When label concentration or time incubation were increased, more nanoparticles were presented in the interior of the PRP clot. With both high concentration of FGN-cAu$_{18}$ and long incubation, the effectiveness of nanoparticle penetration was improved significantly, indicated by the huge number of nanoparticles found in the PRP clot. Micrographs were taken under backscattered mode. White arrows indicated FGN-cAu$_{18}$. Scale bars equal 10μm.

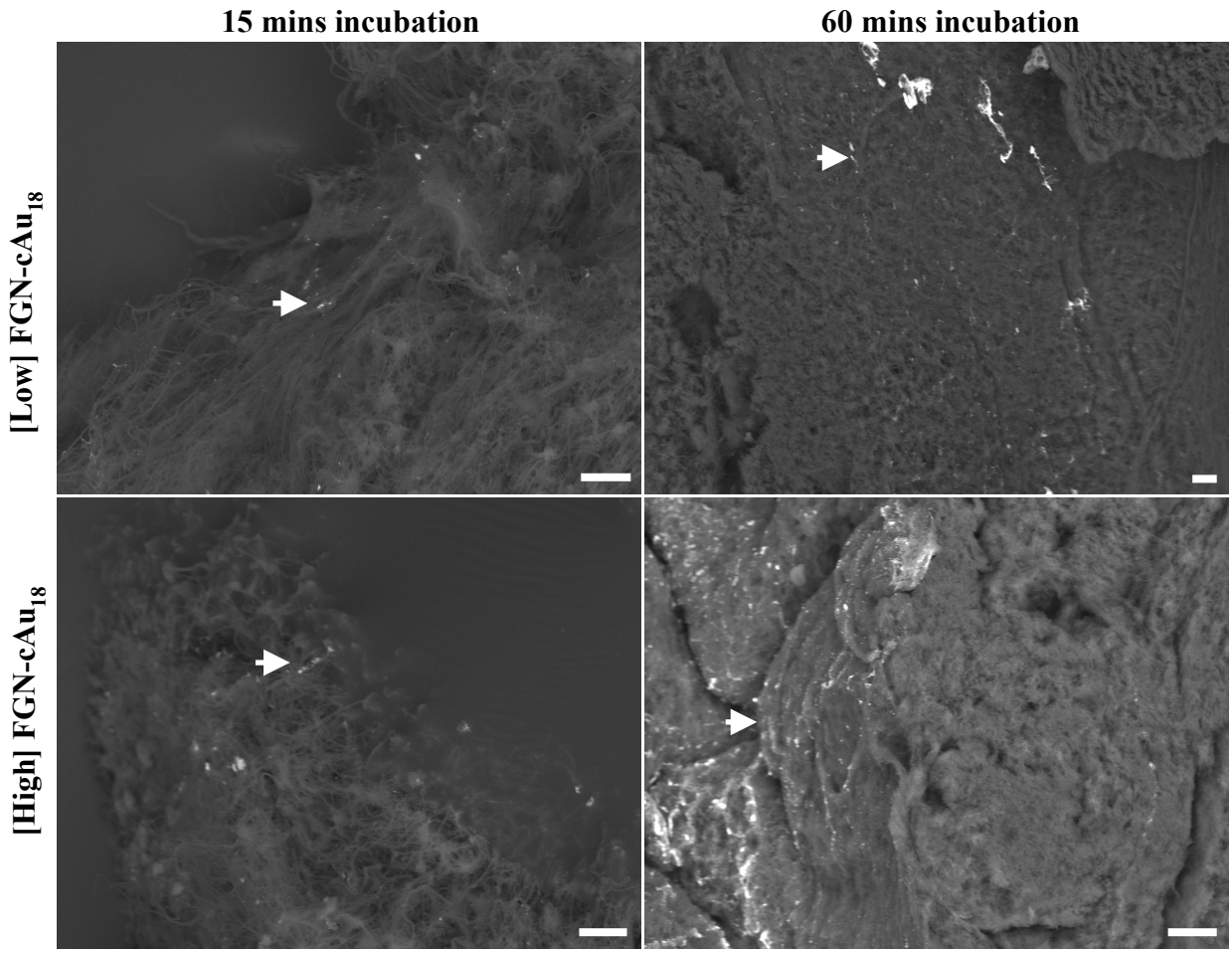

Figure 57. Effect of nanoparticle concentration and labeling time on nanoparticle penetration into PRP clots formed at 10nM thrombin. Despite higher labeling concentrations, few nanoparticles were found, and were found only near the edge of the clots, when they were labeled for 15 minutes. It was very difficult to find nanoparticles at the center of the clots. Increasing the labeling time appeared to improve nanoparticle concentration in the clot. When the PRP clot was labeled at high FGN-cAu$_{18}$ concentration with a long incubation time, the nanoparticle penetration and concentration inside of the clot were improved significantly. Micrographs were taken under backscattered mode. White arrows indicate FGN-cAu$_{18}$. Scale bars equal 10μm.

PRP clots formed at 1nM thrombin					
Donor	**OD_{522}, [label]**	**Labeling time (mins)**	**Clot diameter (mm)**	**Distance migration (mm)**	**Percent penetration (%)**
#1	0.2	15	1.9	0.56	29
#1	0.2	60	2	0.6	30
#1	1	15	2.4	0.56	23
#1	1	60	1.5	0.68	45
#2	0.2	15	1.7	0.25	15
#2	0.2	60	2.2	0.67	30
#2	1	15	1.5	0.3	20
#2	1	60	2.7	1.1	41

Table 9. Quantification of nanoparticle penetration in PRP clotted with 1nM thrombin, labeled with low or high concentration of FGN-cAu_{18} and incubated for either 15 or 60 minutes. At short incubation time and low label concentration, the percent nanoparticle penetration was relatively low. As the incubation time and nanoparticle concentration increased, the percent nanoparticle penetration increased substantially. Percent penetration was calculated by distance of migration divided by clot diameter. The data were obtained from light microscopy and silver enhancement methods.

PRP clots formed at 10nM thrombin					
Donor	**OD_{522}, [label]**	**Labeling time (mins)**	**Clot diameter (mm)**	**Distance migration (mm)**	**Percent penetration (%)**
#1	0.2	15	1.5	0.22	15
#1	0.2	60	1.49	0.53	36
#1	1	15	1	0.24	24
#1	1	60	2.5	0.7	28
#2	0.2	15	1.2	0.3	25
#2	0.2	60	1.88	0.69	37
#2	1	15	1.97	0.2	10
#2	1	60	0.75	0.32	43

Table 10. Quantification of nanoparticle penetration in PRP clotted with 10nM thrombin, labeled with low or high concentration of FGN-cAu_{18} and incubated for either 15 or 60 minutes. Despite the higher density clot formed at high thrombin concentration, the percent penetration of nanoparticles was still increased when the clots were treated with higher nanoparticle concentration and longer incubation time. Percent penetration was calculated by distance of migration divided by clot diameter. The data were obtained from light microscopy and silver enhancement methods.

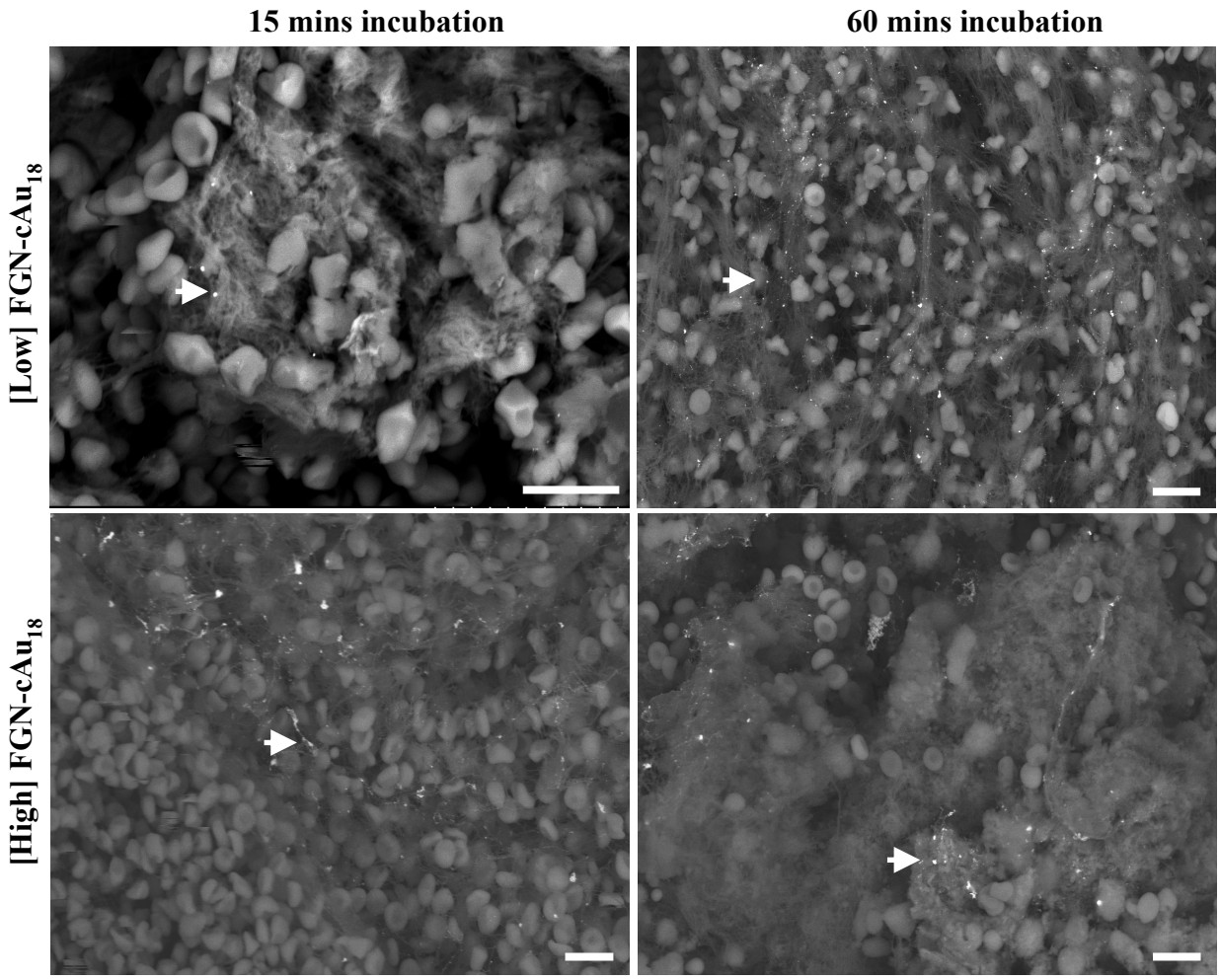

Figure 58. Effect of nanoparticle concentration and labeling time on nanoparticle penetration into WB clots formed with 1nM thrombin. Nanoparticles appeared at very low concentration in the interior of WB clots that were labeled at low FGN-cAu$_{18}$ concentration and short time of incubation. When the FGN-cAu$_{18}$ concentration and incubation time were increased, the effect of nanoparticle penetration improved slightly. Under these conditions, nanoparticles were still more likely to be found at the periphery of the clot rather than at the center. Micrographs were taken under backscattered mode. White arrows indicate FGN-cAu$_{18}$. Scale bars equal 10μm.

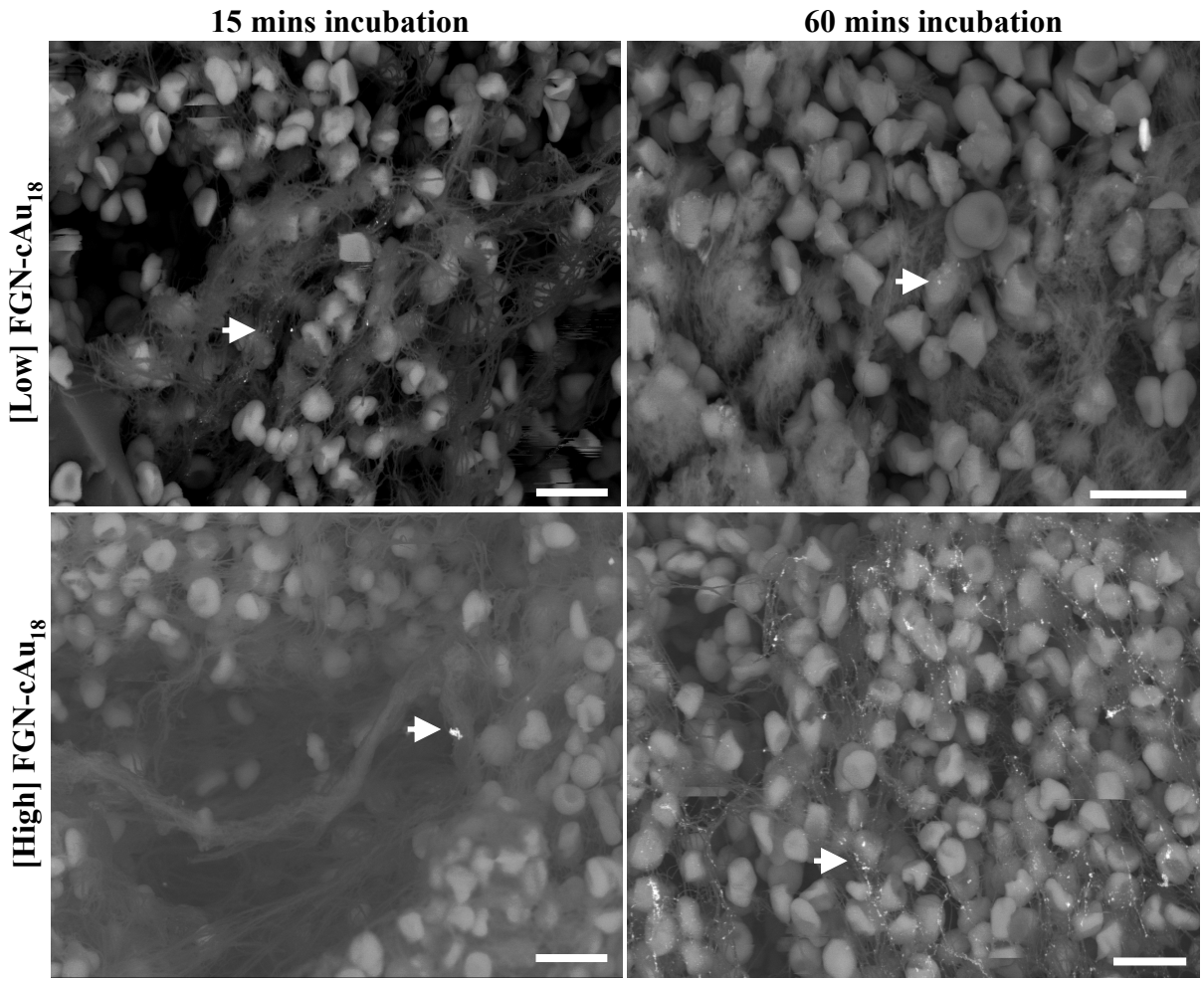

Figure 59. Effect of nanoparticle concentration and labeling time on nanoparticle penetration into WB clots formed with 10nM thrombin. Under these conditions, finding nanoparticles in the interior of the clots was rare. Very few nanoparticles were found near the center of the clots that were labeled at low FGN-cAu_{18} concentration at the short incubation time. There was a slight increase of nanoparticle concentration when clots were labeled at high FGN-cAu_{18} concentration and long incubation time. However, nanoparticles appeared to be abundant only at the periphery of the clots. Micrographs were taken under backscattered mode. White arrows indicate FGN-cAu_{18}. Scale bars equal 10μm.

WB clots formed at 1nM thrombin					
Donor	**OD_{522}, [label]**	**Labeling time (mins)**	**Clot diameter (mm)**	**Distance migration (mm)**	**Percent penetration (%)**
#1	0.2	15	3.5	0.5	14
#1	0.2	60	2.7	0.58	21
#1	1	15	2.8	0.3	11
#1	1	60	3.27	1.1	34
#2	0.2	15	2.8	0.4	14
#2	0.2	60	3.33	0.83	25
#2	1	15	2.4	0.4	17
#2	1	60	3.6	0.75	21

Table 11. Quantification of nanoparticle penetration in WB clotted with 1nM thrombin, labeled with low or high concentration of FGN-cAu_{18} and incubated for either 15 or 60 minutes. The percent of nanoparticle penetration into WB clots was low at the low concentration with short time of labeling. Increasing the time of incubation improved nanoparticle penetration, while the effect of increasing nanoparticle concentration was less clear. As expected, nanoparticle penetration was improved most when both incubation time and label concentration were increased. Percent penetration was calculated by distance of migration divided by clot diameter. The data were obtained from light microscopy and silver enhancement methods.

WB clots formed at 10nM thrombin					
Donor	**OD_{522}, [label]**	**Labeling time (mins)**	**Clot diameter (mm)**	**Distance migration (mm)**	**Percent penetration (%)**
#1	0.2	15	3.9	0.45	12
#1	0.2	60	2	0.5	25
#1	1	15	2.79	0.36	13
#1	1	60	2.2	0.48	22
#2	0.2	15	1.66	0.34	20
#2	0.2	60	1.68	0.43	26
#2	1	15	1.94	0.26	13
#2	1	60	2.48	0.62	25

Table 12. Quantification of nanoparticle penetration in WB clotted with 10nM thrombin, labeled with low or high concentration of FGN-cAu_{18} and incubated for either 15 or 60 minutes. WB clots formed at high thrombin concentration posed a significant challenge to nanoparticle penetration. Thus, even when both label concentration and incubation time were increased, nanoparticle penetration improved only slightly. Percent penetration was calculated by distance of penetration divided by clot diameter. The data were obtained from light microscopy and silver enhancement methods.

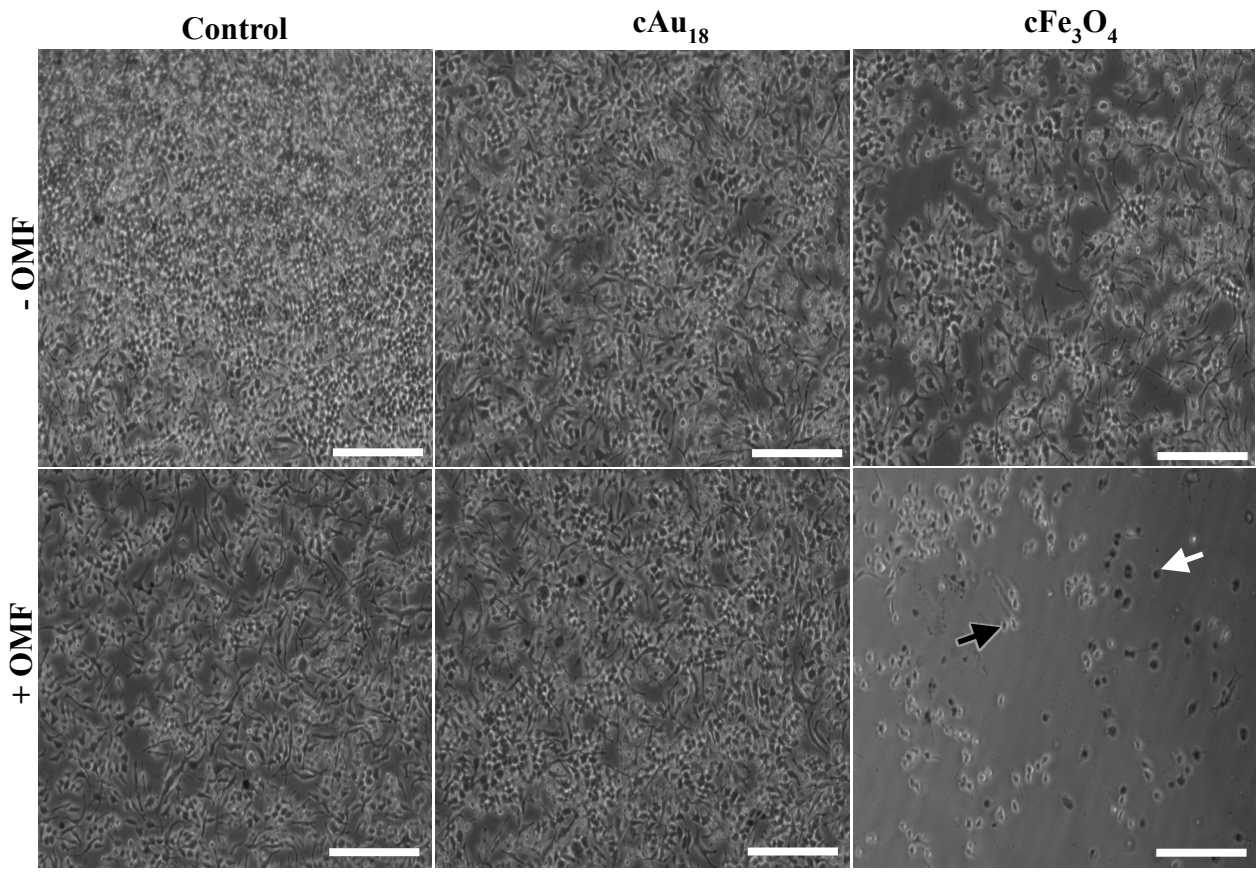

Figure 60. Light microscopy analysis of magnetite nanoparticles and oscillating magnetic field (OMF) treatment in RAW 264.7. In the control and colloidal gold (cAu_{18}) samples, with or without OMF treatment, cells were viable (indicated by exclusion of trypan blue), adhered, well spread and present at high density on the surface of the coverslip. However, when the cells were incubated with colloidal iron oxide (cFe_3O_4) and exposed to the OMF, the density of adherent cells was significantly reduced, and many remaining cells had a rounded morphology. Also, many cells were stained with trypan blue. White and black arrows indicate examples of trypan blue positive and rounded cells, respectively. Scale bars equal 100μm.

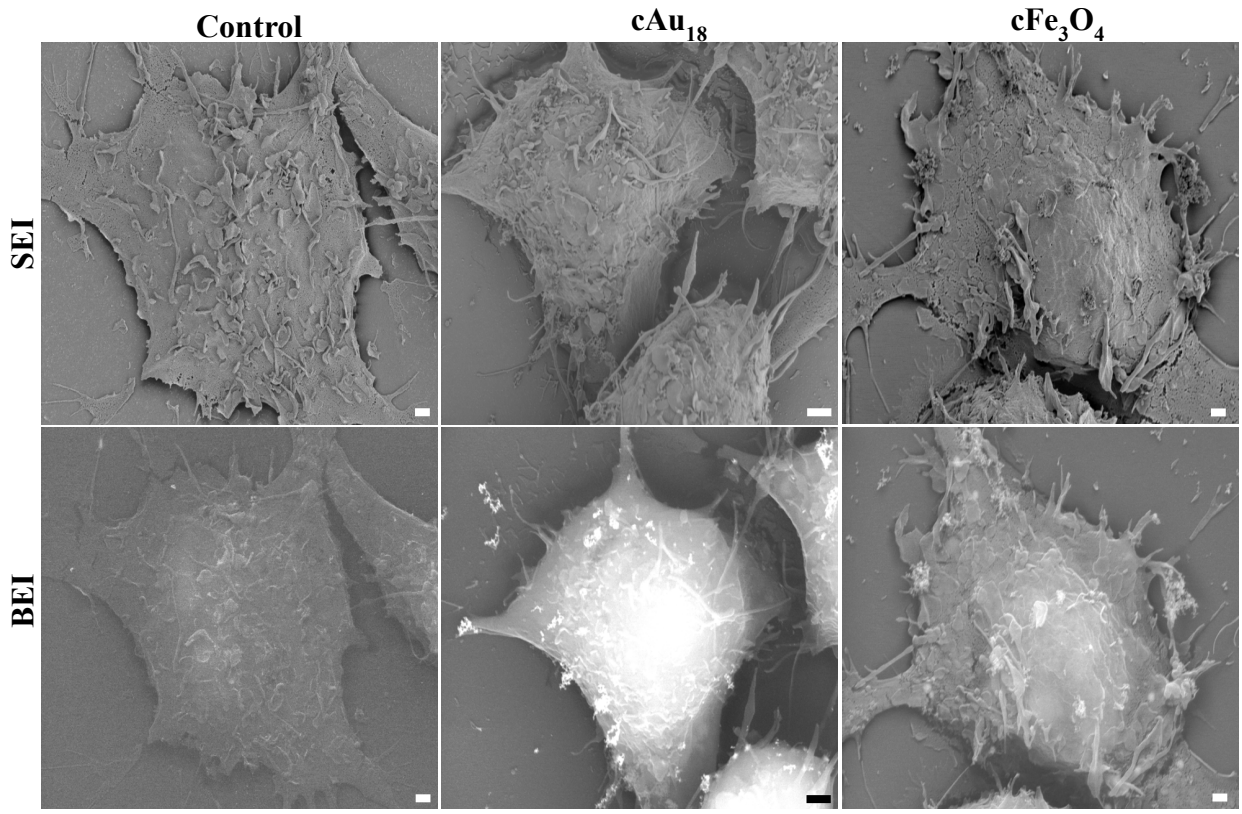

Figure 61. SEM micrographs showing the uptake of magnetite nanoparticles by RAW 264.7. In the secondary electron images (SEI), the RAW 264.7 cells appeared well spread, healthy and adhered to the cover slip for all samples. In the backscattered images (BEI), cells that ingested colloidal gold (cAu_{18}) looked brighter than cells that ingested colloidal magnetite (cFe_3O_4). Control cells without any nanoparticles show only minor internal signal from the OsO_4 fixative. Scale bars equal 1μm.

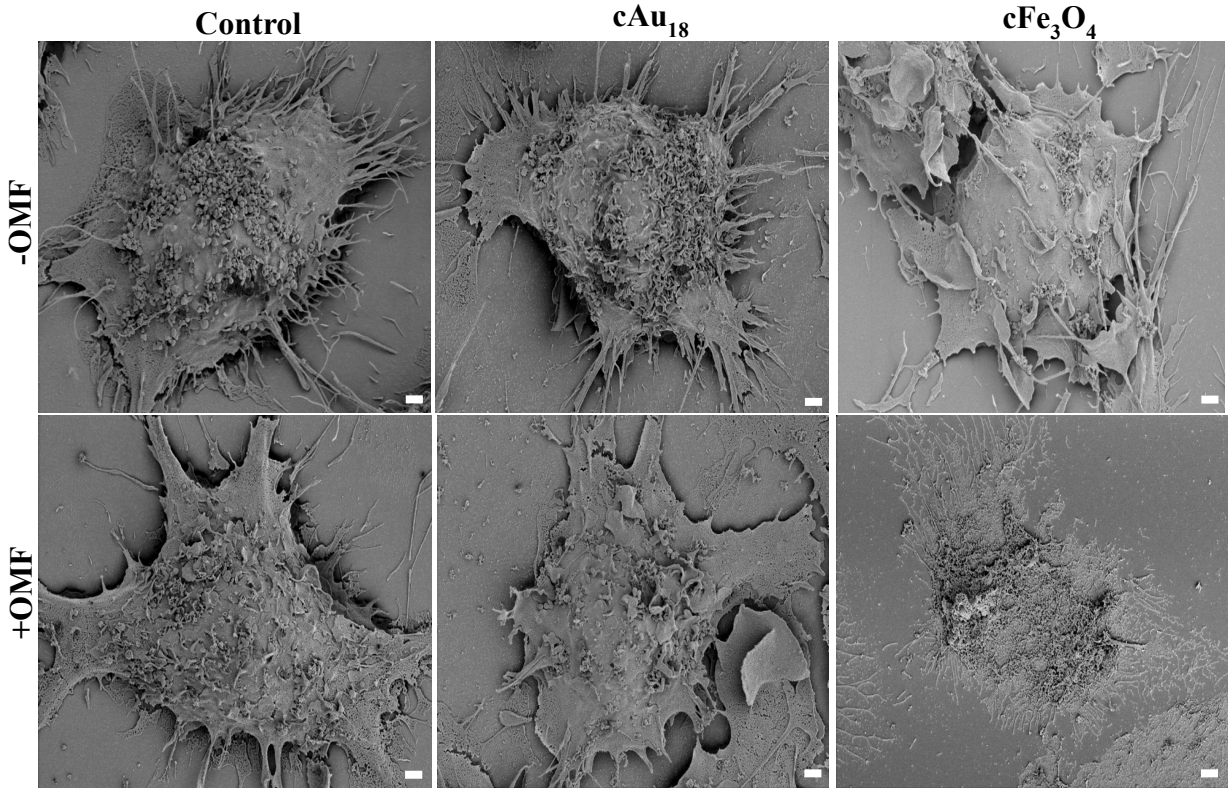

Figure 62. SEM micrographs of the RAW 264.7 cells labeled with cAu_{18} (gold) or cFe_3O_4 (magnetite) nanoparticles and exposed under the oscillating magnetic field (OMF). Cell morphology was undamaged in control and cAu_{18} samples, with or without OMF treatment. When the cells ingested cFe_3O_4 nanoparticles and were exposed to the OMF, the cells were destroyed, and there were bits of membrane and debris left behind. Thus, damage of the cells depended on both the uptake of cFe_3O_4 nanoparticles and OMF treatment. Scale bars equals 1μm.

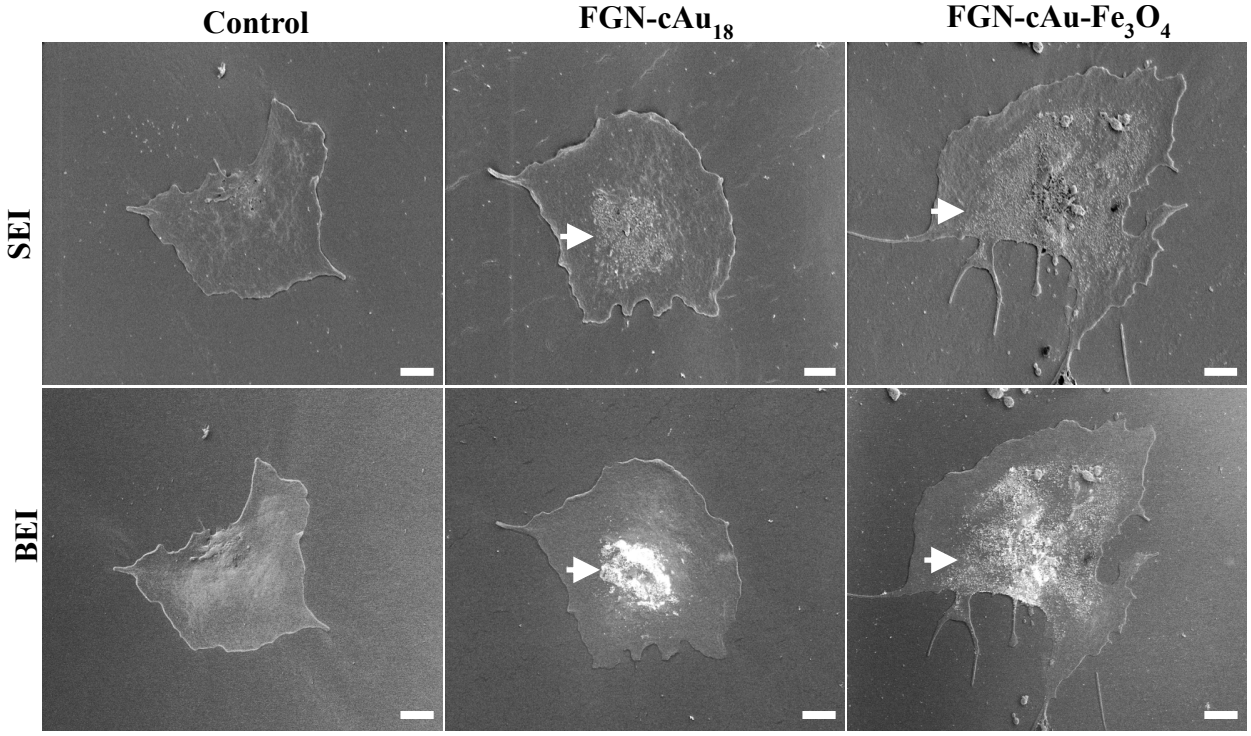

Figure 63. SEM micrographs of surfaced-activated platelets labeled with fibrinogen-conjugated gold nanoparticles (FGN-cAu$_{18}$) and fibrinogen-conjugated gold-coated magnetite nanoparticles (FGN-cAu-Fe_3O_4). All samples are in the absence of OMF exposure. High numbers of both FGN-cAu$_{18}$ and FGN-cAu-Fe_3O_4 are found around the granulomere of the platelets in secondary electron images (SEI) and backscattered electron images (BEI). The arrows indicate the localization of the nanoparticles. Scale bars equal 1μm.

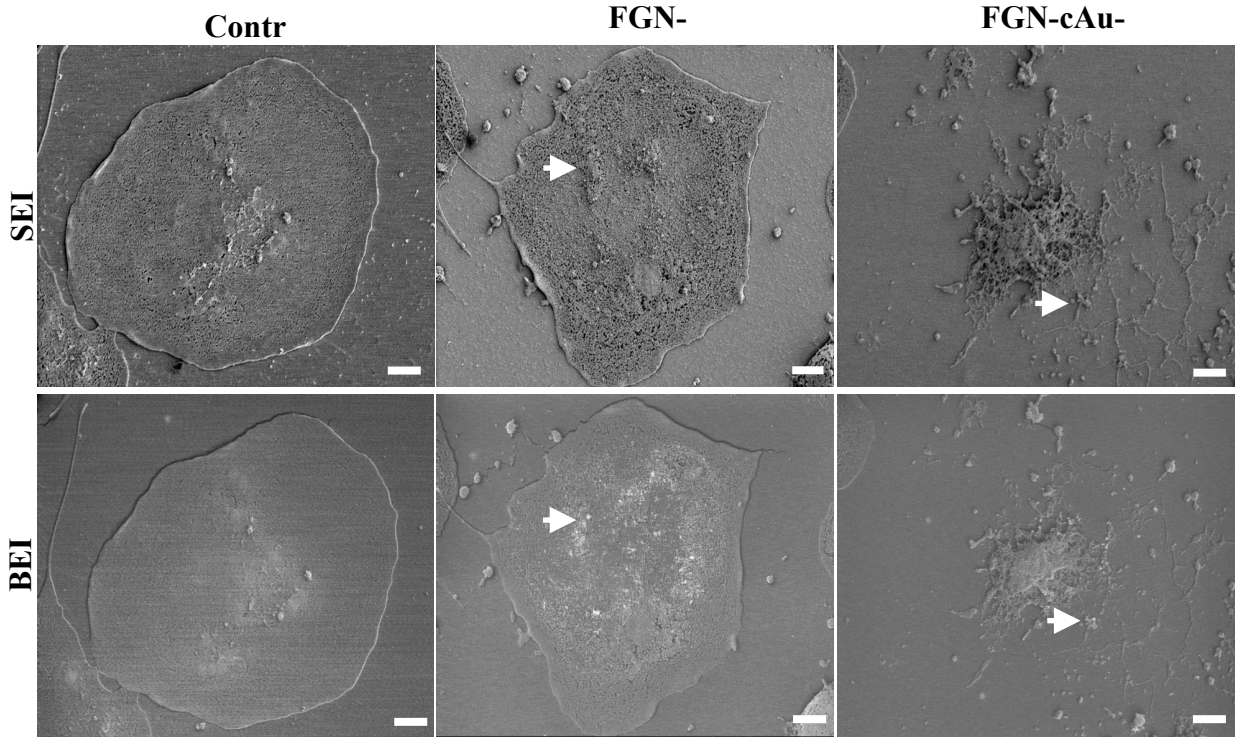

Figure 64. SEM micrographs of targeted gold and magnetite nanoparticles and OMF killing surfaced-activated platelets. All samples were exposed to the OMF. In secondary electron images (SEI), the samples with no label (control) and labeled with fibrinogen-conjugated gold nanoparticles (FGN-cAu$_{18}$), showed platelets that were well spread and adherent. No damage was observed with either the control or FGN-cAu$_{18}$ treatment. In contrast, the cells died and were fragmented in the fibrinogen-conjugated gold-coated magnetite nanoparticles (FGN-cAu-Fe_3O_4) sample as a result of OMF treatment. The arrows indicate the localization of nanoparticles. Scale bars equal 1μm.

References:

1. Emami, B., C. W. Song. 1984. Physiological Mechanism in Hyperthermia: A Review. International Journal of Radiation Oncology, Biology, Physics. 10(2): 289-295

2. Hiraoka, M., G. M. Hahn. 1989. Comparison Between Tumor pH and Cell Sensitivity to Heat in RIF-1 Tumors. Cancer Research. 49: 3734-3736

3. Song, C. W., M. S. Kang, J. G. Rhee, S. H. Levitt. 1980. The Effect of Hyperthermia on Vascular Function, pH, and Cell Survival. Radiology. 137(3): 795-803

4. Hasegawa, T., Y. H. Gu, T. Takahashi, T. Hasegawa, Y. Tanaka. 2001. Effects of Hyperthermia-Induced Changes in pH Value on Tumor Response and Thermotolerance. Thermotherapy for Neoplasia, Inflammation, and Pain. 433-438

5. Lan, A., D. Lagadic-Gossmann, C. Lemaire, C. Brenner, G. Jan. 2007. Acidic Extracellular pH Shifts Colorectal Cancer Cells Death from Apoptosis to Necrosis Upon Exposure to Propionate and Acetate, Major End-Products of The Human Probiotic Propionibacteria. Apoptosis. 12(3): 573-591

6. Calderwood, S. K., J. R. Theriault, J. Gong. 2005. How Is The Immune Response Affected by Hyperthermia and Heat Shock Proteins? International Journal of Hyperthermia. 21(8): 713-716

7. Tsan, M. F., B. C. Gao. 2009. Heat Shock Proteins and Immune System. Journal of Leukocyte Biology. 85: 905-910

8. Chatterjee, S., T. Burns. 2017. Targeting Heat Shock Proteins in Cancer: A Promising Therapeutic Approach. International Journal of Molecular Sciences. 18(9): 1978. doi:10.3390/ijms18091978

9. Oei, A. L., L. E. M. Vriend, J. Crezee, N. A. P. Franken, P. M. Krawczyk. 2015. Effects of Hyperthermia on DNA Repair Pathways: One Treatment to Inhibit Them All. Radiation Oncology. 10: doi:10.1186/s13014-015-0462-0

10. Fu, Q., J. Wang, T. Huang. 2018. The Effect of Hyperthermia on The DNA Damage Response Induced by γ-Rays, As Determined Through *In Situ* Cell Tracking. Journal of Radiation Research. 59(5): 577-582

11. Mantso, T., G. Goussetis, R. Franco, S. Botaitis, A. Pappa, M. Panayiotidis. 2016. Effects of Hyperthermia as a Mitigation Strategy in DNA Damage-Based Cancer Therapies. Seminar in Cancer Biology. 37(38): 96-105

12. Zhang, Y., S. K. Calderwood. 2011. Autophagy, Protein Aggregation and Hyperthermia: A Mini-Review. International Journal of Hyperthermia. 27(5): 409-414

13. Calatayud, M. P., E. Soler, T. E. Torres, E. Campos-Gonzalez, C. Junquera, M. R. Ibarra, G. F. Goya. 2017. Cell Damage Produced by Magnetic Fluid Hyperthermia on Microglial BV2 Cells. Scientific Reports. 7: 8627. doi.org/10.1038/s41598-017-09059-7

14. Furusawa, Y. 2016. Cell Cycle Responses to Hyperthermia. Hyperthermic Oncology from Bench to Bedside. 61-75. doi.org/10.1007/978-981-10-0719-4_6

15. Roti, J. L. 2009. Cellular Responses to Hyperthermia (40-46°C): Cell Killing and Molecular Events. International Journal of Hyperthermia. 24(1): 3-15

16. Csoboz, B., G. E. Balogh, E. Kusz, I. Gombos, M. Peter, T. Crul, B. Gungor, L. Haracska, G. Bogdanovics, Z. Torok, I. Horvath, L. Vigh. 2013. Membrane Fluidity Matters: Hyperthermia from the Aspects of Lipids and Membranes. International Journal of Hyperthermia. 29(5): 491-499

17. Konings, A. W. T. 1988. Membranes as Targets for Hyperthermic Cell Killing. Preclinical Hyperthermia. W. Hinkelbein, G. Bruggmoser, R. Englhardt, and M. Wannenmacher, eds. Springer, Berlin. 9-21

18. Vidair, C. A., W. C. Dewey. 1988. Two Distinct Modes of Hyperthermic Cell Death. Radiation Research. 116: 157-171

19. Vaupel, P.W., D. K. Kelleher. 2010. Pathophysiological and Vascular Characteristics of Tumors and Their Importance for Hyperthermia: Heterogeneity is The Key Issue. International Journal of Hyperthermia. 26: 211-223

20. Behrouzki, Z., Z. Joveini, B. Keshavarzi, N. Eyvazzadeh, R. Z. Aghdam. 2016. Hyperthermia: How Can It Be Used? Oman Medical Journal. 31(2): 89-97

21. Milligan, A. J. 1984. Whole-body Hyperthermia Induction Techniques. Cancer Research. 44: 4869s-4872s

22. Kerner, T., M. Deja, O. Ahlers, J. Loffel, B. Hildebrandt, P. Wust, H. Gerlach, H. Riess. 1999. Whole Body Hyperthermia: A Secure Procedure for Patients with Various Malignancies? Intensive Care Medicine. 25: 959-965

23. Bagge, R. O., J. Mattsson, L. Hafstrom. 2014. Regional Hyperthermic Perfusion with Mephalan After Surgery for Recurrent Malignant Melanoma of the Extremities-Long-Term Follow-Up of a Randomized Trial. International Journal of Hyperthermia. 30(5): 295-298

24. Jha, S., P. K. Sharma, R. Malviya. 2016. Hyperthermia: Role and Risk Factor for Cancer Treatment. Achievements in the Life Sciences. 10(2): 161-167

25. Baker, H. W., P. A. Snedecor, J. C. Goss, W. P. Galen, J. J. Gallucci, I. J. Horowitz, K. Dugan. 1982. Regional Hyperthermia for Cancer. The American Journal of Surgery. 143(5): 586-590

26. Zee, J. V. D. 2002. Heating the Patient: A Promising Approach? Annals of Oncology. 13(8): 1173-1184

27. Gao, S., M. Zheng, X. Ren, Y. Tang, X. Liang. 2016. Local Hyperthermia in Head and Neck Cancer: Mechanism, Application and Advance. Oncotarget. 7(35): 57367-57378

28. Brezovich. I. A., W. J. Atkinson, M. B. Lilly. 1984. Local Hyperthermia with Interstitial Techniques. Cancer Research. 44: 4752s-4756s

29. Kolosnjaj-Tabi, J., I. Marangon, A. Nicolas-Boluda, A. K. A. Silva, F. Gazeau. 2017. Nanoparticle-Based Hyperthermia, A Local Treatment Modulating the Tumor Extracellular Matrix. Pharmacological Research. 126: 123-137

30. Sharma, S. K., N. Shrivastava, F. Rossi, D. T. Le, T. K. R. Nguyen. 2019. Nanoparticles-Based Magnetic and Photo Induced Hyperthermia for Cancer Treatment. Nanotoday. 29: 100795. https://doi.org/10.1016/j.nantod.2019.100795

31. Gupta, A. K., M. Gupta. 2005. Synthesis and Surface Engineering of Iron Oxide Nanoparticles for Biomedical Applications. Biomaterials. 26: 3995-4021

32. Lin, F. C., C. H. Hsu, Y. Y. Lin. 2018. Nano-Therapeutic Cancer Immunotherapy Using Hyperthermia-Induced Heat Shock Proteins: Insights from Mathematical Modeling. International Journal of Nanomedicine. 13: 3529-3539

33. Manuchehrabadi, N., L. Zhu. 2017. Gold Nanoparticle-Based Laser Photothermal Therapy. In: Kulacki F. (eds). Handbook of Thermal Science and Engineering. Springer. 1-33

34. Yao, C., L. Zhang, J. Wang, Y. He, J. Xin, S. Wang, H. Xu, Z. Zhang. 2016. Gold Nanoparticle Mediated Phototherapy for Cancer. Journal of Nanomaterials. 5497136. https://doi.org/10.1155/2016/5497136

35. Bonvin, D., J. A. M. Bastiaansen, M. Stuber, H. Hofmann, M. M. Ebersold. 2017. Folic Acid on Iron Oxide Nanoparticles: Platform with High Potential for Simultaneous Targeting, MRI Detection and Hyperthermia Treatment of Lymph Node Metastases of Prostate Cancer. Dalton Transactions. 46(37): 12692-12704

36. Kaur, P., M. L. Aliru, A. S. Chadha, A. Asea, S. Krishnan. 2017. Hyperthermia Using Nanoparticles-Promises and Pitfalls. International Journal of Hyperthermia. 32(1): 76-88

37. Goodrich, G. P., L. Bao, K. Gill-Sharp, K. L. Sang, J. Wang, J. D. Payne. 2010. Photothermal Therapy in a Murine Colon Cancer Model Using Near-Infrared Absorbing Gold Nanorods. Journal of Biomedical Optics. 15: 018001-018001

38. Zharov, V. P., E. N. Galitovskaya, C. Jothson, T. Kelly. 2005. Synergistic Enhancement of Selective Nanophotothermolysis with Gold Nanoclusters: Potential for Cancer Therapy. Lasers in Surgery and Medicine. 37: 219-226

39. Moran, C. H., S. M. Wainerdi, T. K. Cherukuri, C. Kittrell, B. J. Wiley, N. W. Nicholas, S. A. Curley, J. S. Kanzius, P. Cherukuri. 2009. Size-Dependent Joule Heating of Gold Nanoparticles Using Capacity Coupled Radiofrequency Fields. Nano Research. 2: 400-405

40. Rudolf, H., D. Silvio, M. Robert, Z. Matthias. 2006. Magnetic Nanoparticle Hyperthermia: Nanoparticle Magnetism and Materials Development for Cancer Therapy. Journal of Physics: Condensed Matter. 18: S2919

41. Laurent, S., S. Dutz, U. O. Hafeli, M. Mahmoudi. 2011. Magnetic Fluid Hyperthermia: Focus on Superparamagnetic Iron Oxide Nanoparticles. Advances in Colloid and Interface Science. 166: 8-23

42. Prevo, B. G., S. A. Esakoff, A. Mikhailovsky, J. A. Zasadzinski. 2008. Scalable Routes to Gold Nanoshells with Tunable Sizes and Responses to Near-Infrared Pulsed-Laser Irradiation. Small. 4: 1183-1195

43. Cole, J. R., N. A. Mirin, M. W. Knight, G. P. Goodrich, N. J. Halas. 2009. Photothermal Efficiencies of Nanoshells and Nanorods for Clinical Therapeutic Applications. Journal of Physical Chemistry C. 113: 12090-12094

44. Kim, H. S., D. Y. Lee. 2018. Near-Infrared-Responsive Cancer Photothermal and Photodynamic Therapy Using Gold Nanoparticles. Polymers. 10(9): 96. https://dx.doi.org/10.3390%2Fpolym10090961

45. Riley, R. S., E. S. Day. 2017. Gold Nanoparticle-Mediated Photothermal Therapy: Applications and Opportunities for Multimodal Cancer Treatment. Wiley Interdisciplinary Reviews Nanomedicine and Nanobiotechnology. 9(4). https://dx.doi.org/10.1002%2Fwnan.1449

46. Popp, M. K., I. Oubou, C. Shepherd, Z. Nager, C. Anderson, L. Pagliaro. 2014. Photothermal Therapy Using Gold Nanorods and Near-Infrared Light in Murine Melanoma Model Increases Survival and Decreases Tumor. Journal of Nanomaterials. https://doi.org/10.1155/2014/450670

47. Chang, D., M. Lim, J. A. C. M. Goos, R. Qiao, Y. Y. Ng, F. M. Mansfeld, M. Jackson, T. P. Davis, M. Kavallaris. 2018. Biologically Targeted Magnetic Hyperthermia: Potential and Limitations. Frontiers in Pharmacology. https://doi.org/10.3389/fphar.2018.00831

48. Cazares-Cortes, E., S. Cabana, C. Boitard, E. Nehlig, N. Griffete, J. Fresnais, C. Wilhelm, A. Abou-Hassan, C. Menager. 2019. Recent Insights in Magnetic Hyperthermia: From the "Hot-Spot" Effect for Local Delivery to Combined Magneto-Photo-Thermia Using Magneto-Plasmonic Hybrids. Advanced Drug Delivery Reviews. 138(1): 233-246

49. Giustini, A. J., A. A. Petrk, S. M. Cassim, J. A. Tate, I. Baker, P. J. Hoopes. 2010. Magnetic Nanoparticle Hyperthermia in Cancer Treatment. Nano Life. https://dx.doi.org/10.1142%2FS1793984410000067

50. Liu, X., Y. Zhang, Y. Wang, W. Zhu, G. Li, X. Ma, Y. Zhang, S. Chen, S. Tiwari, K. Shi, S. Zhang, H. M. Fan, Y. X. Zhao, X. Liang. 2020. Comprehensive Understanding of Magnetic Hyperthermia for Improving Antitumor Therapeutic Efficacy. Theranostics. 10(8): 3793-3815

51. Abbaspour, N., R. Hurrell, R. Kelishadi. 2014. Review on Iron and Its Importance for Human Health. Journal of Research in Medical Sciences. 19(2): 164-174

52. Anselmo, A. C., S. Mitragotri. 2015. A Review of Clinical Translation of Inorganic Nanoparticles. The American Association of Pharmaceutical Scientists. 17(5): 1041-1054

53. Johannsen, A., U. Gneveckow, B. Thiesen, K. Taymoorian, C. H. Cho, N. Waldofner, R. Scholz, A. Jordan, S. A. Loening, P. Wust. 2007. Thermotherapy of Prostate Cancer Using Magnetic Nanoparticles: Feasibility, Imaging, and Three-Dimensional Temperature Distribution. European Urology. 52(6): 1653-1661

54. Sonvico, F., S. Mornet, S. Vasseur, C. Dubernet, D. Jaillard, J. Degrouard, J. Hoebeke, E. Duguet, P. Colombo, P. Couvreur. 2005. Folate-Conjugated Iron Oxide Nanoparticles for Solid Tumor Targeting as Potential Specific Magnetic Hyperthermia Mediators: Synthesis, Physicochemical Characterization, and *In Vitro* Experiments. Bioconjugate Chemistry. 16: 1181-1188

55. Lattuada, M., T. A. Hatton. 2006. Functionalization of Monodisperse Magnetic Nanoparticles. Langmuir. 23: 2158-2168

56. Mornet, S., J. Portier, E. Duguet. 2005. A Method for Synthesis and Functionalization of Ultrasmall Superparamagnetic Covalent Carrier Based on Maghemite and Dextran. Journal of Magnetism and Magnetic Materials. 293: 127-134

57. Hu, F. Q., L. Wei, Z. Zhou, Y. L. Ran, Z. Li, M. Y. Gao. 2006. Preparation of Biocompatible Magnetite Nanocrystals for *In Vivo* Magnetic Resonance Detection of Cancer. Advances in Materials. 18: 2553-2556

58. Krystofiak, E. S., V. Z. Matson, D. A. Steeber, J. A. Oliver. 2012. Elimination of Tumor Cells Using Folate Receptor Targeting by Antibody-Conjugated, Gold-Coated Magnetite Nanoparticles in a Murine Breast Cancer Model. Journal of Nanomaterials. Article ID 431012

59. Krystofiak, E. S., E. C. Mattson, P. M. Voyles, C. J. Hirschmug, R. M. Albrecht, M. Gajdardziska-Josifovska, J. A. Oliver. 2013. Multiple Morphologies of Gold-Magnetite

Heterostructure Nanoparticles are Effectively Functionalized with Protein for Cell Targeting. Microscopy and Microanalysis. 19: 821-834

60. Krystofiak, E. S. 2013. Fibrinogen-Conjugated Gold-Coated Magnetite Nanoparticles for Antiplatelet Therapy. Doctoral Dissertation, University of Wisconsin- Milwaukee

61. Wallyn, J., N. Anton, T. F. Vandamme. 2019. Synthesis, Principles, and Properties of Magnetite Nanoparticles for *In Vivo* Imaging Application- A Review. Pharmaceutics. 11(11): 601. https://dx.doi.org/10.3390%2Fpharmaceutics11110601

62. Ali, A., H. Zafar, M. Zia, I. U. Haq, A. R. Phull, J. S. Ali, A. Hussain. 2016. Synthesis, Characterization, Applications, and Challenges of Iron Oxide Nanoparticles. Nanotechnology Science and Applications. 9: 49-67

63. Macias-Martinez, B. I., D. A. Cortes-Hernandez, A. Zugasti-Cruz, B. R. Cruz-Ortiz, E. M. Muzquiz-Ramos. 2016. Heating Ability and Hemolysis Test of Magnetite Nanoparticles Obtained by a Simple Co-precipitation Method. Journal of Applied Research and Technology. 14(4): 239-244

64. Kandela, I. 2006. Colloid Magnetite Nanoparticles for Targeted Cytotoxicity. Master Thesis, University of Wisconsin-Madison.

65. Wolberg, A. S. 2007. Thrombin Generation and Fibrin Clot Structure. Blood Reviews. 21(3): 131-142

66. Carr, M. E., B. M. Alving. 1995. Effect of Fibrin Structure on Plasmin-Mediated Dissolution of Plasma Clots. Blood Coagulation and Fibrinolysis. 6(6): 567-573

67. Collet, J. P., D. Park, C. Lesty, J. Soria, C. Soria, G. Montalescot, J. W. Weisel. 2000. Influence of Fibrin Network Conformation and Fibrin Fiber Diameter on Fibrinolysis Speed. Arteriosclerosis, Thrombosis and Vascular Biology. 20(5): 1354-1361

68. Varin, R., S. Mirshahi, P. Mirshahi, C. Klein, J. Jamshedov, J. Chidiac, E. Perzborn, M. Mirshahi, C. Soria, J. Soria. 2013. Whole Blood Clots Are More Resistant to Lysis than Plasma Clots—Greater Efficacy of Rivaroxaban. Thrombosis Research. 131(3):e100-109. https://doi.org/10.1016/j.thromres.2012.11.029

69. Gersh, K. C., C. Nagaswami, J. W. Weisel. 2009. Fibrin Network Structure and Clot Mechanical Properties Are Altered by Incorporation of Erythrocyte. Thrombosis and Haemostasis. 102(6): 1169-1175

70. Wohner, N., P. Sotonyi, R. Machovich, L. Szabo, K. Tenekedjiev, M. M. C. G. Silva, C. Longstaff, K. Kolev. 2012. Lytic Resistance of Fibrin Containing Red Blood Cells. Arteriosclerosis, Thrombosis and Vascular Biology. 31(10): 2306-2313

71. Tutwiler, V., A. R. Mukhitov, A. D. Peshkova, G. L. Minh, R. R. Khismatullin, J. Vicksman, C. Nagaswami, R. I. Litvinov, J. W. Weisel. 2018. Shape Changes of Erythrocytes During Blood Clot Contraction and the Structure of Polyhedrocytes. Scientific Reports. 8, 17907. https://doi.org/10.1038/s41598-018-35849-8

72. Cines, D. B., T. Lebedeva, C. Nagaswami, V. Hayes, W. Massefski, R. I. Litvinov, L. Rauova, T. J. Lowery, J. W. Weisel. 2014. Clot Contraction: Compression of Erythrocytes into Tightly Packed Polyhedra and Redistribution of Platelets and Fibrin. Thrombosis and Hemostasis. 123(10): 1596-1603

73. Leong, L., I. N. Chernysh, Y. Xu, D. Sim, C. Nagaswami, Z. D. Lange, S. Kosolapova, A. Cuker, K. Kauser, J. W. Weisel. 2017. Clot Stability as a Determinant of Effective Factor VIII Replacement in Hemophilia A. Research and Practice in Thrombosis and Haemostasis. 1(2): 231-241

Chapter 5- Conclusions

The holy grail of ischemic stroke treatment is to develop an agent that is highly effective at reopening the occluded vessel without causing bleeding. To this end, it is important to remember that hemostasis is a protective, physiologic process of clot formation that prevents blood loss at the site of injury; whereas, thrombosis is considered to be a pathological condition due to hemostasis in an exaggerated form. That means thrombosis and hemostasis share a common mechanism, and appropriate, tight regulation of hemostasis is required to maintain the delicate balance of normal processes between hemorrhage and thrombosis. Consequently, the potency of any current antiplatelet strategy inevitably carries a risk of bleeding complications (1). In this regard, we eagerly seek to develop the potential magic bullet of antiplatelet therapies, one that is highly effective in treating thrombosis and yields little to no bleeding risk.

Integrin $\alpha_{IIb}\beta_3$ receptors are highly expressed on platelets and are capable of binding ligand with high affinity, regulated through distinct conformational changes in the integrin. Normally, about 80,000 $\alpha_{IIb}\beta_3$ receptors are expressed on the platelet surface, and further numbers can mobilize from intracellular stores during platelet activation (2). Upon activation, $\alpha_{IIb}\beta_3$ receptors become competent to bind to their ligand fibrinogen. The receptors crosslinked by the ligand then move through the platelet membrane, internalizing through the open canalicular system, and concentrating at the center of the platelet (3,4). The binding of fibrinogen to platelet integrin $\alpha_{IIb}\beta_3$ receptors has been recognized as a powerful target for antiplatelet therapy (5). For example, the antibody treatment abciximab can inhibit platelet function through blockage of fibrinogen binding to platelet integrin $\alpha_{IIb}\beta_3$ receptors, thereby blocking platelet aggregation. This has shown effectiveness in reducing platelet aggregation and preventing re-occlusion in a clinical setting. However, abciximab does not distinguish between integrin $\alpha_{IIb}\beta_3$

receptors on activated and quiescent platelets (1,6). As a result, it has been considered to be associated with higher bleeding rates in patients with acute ischemic stroke.

We expect our fibrinogen-based targeting to be able to select for activated platelets involved in thrombi formation while leaving circulating platelets unaffected. Hence, we proposed that using fibrinogen-conjugated nanoparticle targeting followed by magnetically induced hyperthermia could be a better option than current antibody treatments in terms of increasing therapeutic effects through highly localized hyperthermia, and concomitantly reducing bleeding complications. Building upon our previous work (7), we have demonstrated here that fibrinogen-conjugated nanoparticles are able to specifically associate with activated platelets in the presence of plasma fibrinogen and red blood cells (RBCs). However, this method has a few challenges that might prevent the fibrinogen-conjugated nanoparticles from effectively interacting with activated platelets in clots that must be considered.

First, plasma fibrinogen can interact with unoccupied $\alpha_{IIb}\beta_3$ receptors of activated platelets. At the same time, plasma fibrinogen can strongly associate with our nanoparticle labels. Thus, we observed that fibrinogen-conjugated nanoparticles heavily bind to fibrin in preformed platelet-rich plasma (PRP) and whole blood (WB) clots. In fact, the presence of plasma fibrin(ogen) is unavoidable at the site of an occlusive clot *in vivo*; thereby, its binding is likely to inhibit and compete with fibrinogen-conjugated nanoparticles in binding to $\alpha_{IIb}\beta_3$ receptors of activated platelets. Moreover, the presence and generation of thrombin during clot formation could be a factor causing a reduction in penetration of fibrinogen-conjugated nanoparticles into clots. Due to the ability to cleave fibrinogen into fibrin, thrombin possibly can convert both plasma fibrinogen and conjugated fibrinogen to fibrin. The combination of the polymerized product of thrombin-cleaved fibrinogen, fibrin within the preformed clot, and

plasma fibrinogen is likely to have caused steric hindrance and competition that further prevents the association of fibrinogen-conjugated nanoparticles to their target deep in the interior of the clot.

To deal with plasma fibrinogen competition in binding to $\alpha_{IIb}\beta_3$ receptors on activated platelets and the steric hindrance of fibrin due to thrombin activity, an effective ischemic stroke treatment could include a co-administration of tissue plasminogen activator (tPA) along with fibrinogen-conjugated nanoparticles. The tPA will activate the fibrinolysis pathway by lysing fibrin within the blood clot to promote a reduction in the structural integrity of the blood clot, as well as reducing the amount of fibrin network surrounding the clot. Consequently, the fibrinogen-conjugated nanoparticles will have better access to their targets and better opportunity to produce their desired effects. In addition, fibrinogen-conjugated nanoparticles can integrate strongly with the fibrin network within a blood clot and may be able to promote clot release by causing hyperthermia to the fibrin network directly. Even without tPA co-administration, fibrinogen-conjugated nanoparticle administration may be still able to dissolve the blood clot and can be considered as a second method to dissolve the blood clot. On the other hand, due to an ability to associate significantly with fibrinogen-conjugated nanoparticles, fibrin(ogen) can be considered as another potential site-specific target to treat ischemic stroke. Arterial clots consist mainly of fibrin and activated platelets (8,9). Thus, if fibrinogen-conjugated nanoparticles can bind specifically to both protein and cellular components, it might strengthen our targeting strategy.

We demonstrated that fibrinogen-conjugated nanoparticles do not interact with RBCs. This implies that our targeting strategy could be specific and safe when administrating *in vivo* to treat ischemic stroke. However, the contribution of RBCs to the bulk of occlusive and arterial

clots at high thrombin concentration is problematic in preventing the binding of the nanoparticle label to its target $\alpha_{IIb}\beta_3$ receptors on activated platelets within clots. In WB clots formed at high thrombin concentration, a meshwork of fibrin and platelet aggregates was observed mostly on the clot surface, and the interior consisted of closely packed, compressed polyhedral erythrocytes with very little fibrin and activated platelets present. Despite increasing both nanoparticle concentration and labeling time, the access of nanoparticle labels was limited to the periphery of the clot. As a result, under the oscillating magnetic field (OMF), we might expect the disruption to occur mainly at the periphery of the clot where fibrin and activated platelets were located. Also, the disruption might not be sufficient to dissolve the clot and restore blood flow as our method has proposed.

There are a few ways that we can overcome this problem. First, we could label the clot multiple times with fibrinogen-conjugated nanoparticles. Also, OMF exposure could be applied after each labeling, if multiple labeling does not improve nanoparticle penetration and concentration within the clot alone. By doing that, we could slowly shave off clot layers and eventually, the clot would become small enough that it would no longer obstruct blood flow. As mentioned above, tPA co-administration could be utilized to further speed up and improve the labeling process by lysing fibrin within the clot and allowing fibrinogen-conjugated nanoparticles to interact more easily with their intended platelet targets.

The co-precipitation method is the simplest and easiest way to synthesize magnetite nanoparticles. However, the synthesis procedure is not robust and commonly produces nanomaterials with a large size distribution leading to a non-ideal magnetic behavior (10). This could influence the clot heating and killing ability of magnetite nanoparticles. Using the phagocytic cell model combined with light microscopy to test the efficacy of magnetite

nanoparticles is relatively quick. It also provides a reliable way to determine whether or not the magnetite nanoparticles will be successful in disrupting activated platelets after being coated with gold and conjugated to fibrinogen. However, improving and refining magnetite nanoparticle synthesis procedures will need to be a priority because a more robust synthesis would increase chances of successful clot disruption. To achieve a reproducible magnetite synthesis procedure, several parameters have to be carefully mastered to keep control over the range of sizes, colloidal stability, and oxidation surfaces of the magnetite nanoparticles. These include the reaction temperature (10,11), oxygen presence (12), pH (13,14), ionic force (13,14) and the addition of stabilizers (15). Another possible contributor affecting hyperthermia damage efficacy of magnetite nanoparticles is the different morphologies of gold-coated magnetite nanoparticles. In fact, it is somewhat difficult to control the particle aggregation, uniformity, and thickness of the gold deposition (16,17). In the future, it may be worth examining whether one particular nanoparticle morphology preferentially binds to platelets and is responsible for the majority of localized hyperthermia. Also, examining and characterizing whether different morphologies of gold-coated magnetite nanoparticles are more easily conjugated to fibrinogen would provide additional knowledge into designing and synthesizing high-quality magnetite nanoparticles for use as an agent in treating ischemic stroke.

Future directions:

Our current work demonstrated that it is possible to specifically target activated platelets in clots by using fibrinogen-conjugated nanoparticles. The next logical step would be using nanoparticle-induced hyperthermia to disrupt PRP and WB clots *in vitro*. We anticipate that PRP clots will be dissolved more readily than WB clots. WB clots may require multiple labeling in

combination with multiple OMF exposures to acquire sufficient clot disruption. Additionally, we might encounter that hyperthermia does not generate enough damage to the clot. This could be due to the superparamagnetic nanoparticles not heating up efficiently at the applied frequency of 500kHz. Further improvements to platelet hyperthermia may come from the optimization of the frequency of the OMF. Many studies about superparamagnetic nanoparticle heating showed that frequencies below 500kHz cause better heat generation (18-21). Thus, it is possible that our fibrinogen-conjugated gold-coated magnetite nanoparticles would heat more efficiently at lower frequencies.

The essential role of shear stress, produced by the blood flow on arterial thrombus formation in native human blood, is another aspect that we could explore in future experiments. In fact, the changing flow and shear rate could facilitate certain organizations and amounts of blood clot components within clots. The actual efficacy of many antithrombotic agents is flow and shear dependent (22,23). Since we demonstrated that nanoparticle penetration significantly relies on clot structure and organization of its components, it is apparent that the efficacy of magnetite nanoparticle penetration could be flow and shear dependent as well. Moreover, the current experiments occurred in the absence of flow; therefore, this gives an incomplete understanding about nanoparticle dosage, and the interaction strength of nanoparticles with the clot.

It would be interesting to observe fibrinogen-conjugated, gold-coated magnetite nanoparticles in use as a platelet targeted ischemic stroke treatment *in vivo* using a murine model of carotid artery thrombosis. To do that, we would use the ferric chloride-induced injury model to generate platelet-rich thrombi in murine carotid arteries because the occlusive clots formed with this method are relatively similar to those seen in human ischemic stroke patients (24-26).

Then, fibrinogen-conjugated nanoparticles could be injected through the tail vein, with normal blood circulation distributing the nanoparticles to the activated platelets at the occlusive site. Alternatively, nanoparticles can be directly administered to the site of an occlusive clot by catheter. After nanoparticle administration, the mouse would be exposed to the OMF. The treatment would be monitored by measuring the blood flow through the artery using an ultrasonic probe. The success of the treatment will be examined and evaluated by electron microscopy. However, these *in vivo* experiments have significant technical challenges. First, microsurgery is not a simple technique. Indeed, when microsurgery is performed on an anesthetized mouse to expose the carotid artery, any additional damage to the vessel and surrounding tissue must be avoided. Also, due to the small size of the murine vasculatures, catheterizing an artery can cause thrombotic events by itself. Therefore, it may not be feasible to effectively delivery a dose of nanoparticles to the blood clot that will be sufficient to result in disruption.

There will be many challenges that need to be overcome before our novel treatment for ischemic stroke, which is specific cell targeting with nanoparticles for hyperthermia, can be introduced to *in vivo* applications. However, the meaningful results of our characterization of the targeting of fibrinogen-conjugated nanoparticles in both PRP and WB clot systems provided important insights in how to further develop this ischemic stroke treatment. Additionally, through the development of this novel anti-platelet therapy for ischemic stroke, determining and optimizing the treatment conditions will be useful not only for targeting platelets, but also other pathologic cell types such as cancer.

References:

1. Schafer, A. I. 1997. Antiplatelet Therapy with Glycoprotein IIb/IIIa Receptor Inhibitors and Other Novel Agents. Antiplatelet Therapy. 24(2): 90-96

2. Durrant, T. N., M. T. Bosch, I. Hers. 2017. Integrin $\alpha_{IIb}\beta_3$ Outside-In Signaling. Blood. 130(14): 1607-1619

3. Escolar, G., E. Leistikow, J. G. White. 1989. The Fate of The Open Canalicular System in Surface and Suspension-Activated Platelets. Blood. 74(6): 1983-1988

4. Loftus, J. C., R. M. Albrecht. 1984. Redistribution of The Fibrinogen Receptor of Human Platelets After Surface Activation. Journal of Cell Biology. 99: 822-829

5. Coller, B. S., S. J. Shattil. 2008. The GPIIb/IIIa (Integrin $\alpha_{IIb}\beta_3$) Odyssey: A Technology-Driven Saga of a Receptor with Twists, Turns, and Even a Bend. Blood. 112: 3011-3025

6. Adam, H. P., Jr., M. B. Effron, J. Torner, A. Davalos, J. Frayne, P. Teal, J. Leclerc, B. Oemar, L. Padgett, E. S. Barnathan, W. Hacke. 2008. Emergency Administration of Abciximab for Treatment of Patients with Acute Ischemic Stroke: Results of an International Phase III Trial: Abciximab in Emergency Treatment of Stroke Trial (AbESTT-II). Stroke. 39: 87-99

7. Krystofiak, E. S. 2013. Fibrinogen-Conjugated Gold-Coated Magnetite Nanoparticles for Antiplatelet Therapy. Doctoral Dissertation, University of Wisconsin- Milwaukee

8. Chernysh, I. N., C. Nagaswami, S. Kosolapova, A. D. Peshkova, A. Cuker, D. B. Cines, C. L. Cambor, R. I. Litvinov, J. W. Weisel. 2020. The Distinctive Structure and Composition of Arterial and Venous Thrombi and Pulmonary Emboli. Scientific Reports. 10(1):5112. https://dx.doi.org/10.1038%2Fs41598-020-59526-x

9. Koupenova, M., B. E. Kehrel, H. A. Corkrey, J. E. Freedman. 2017. Thrombosis and Platelets: An Update. European Heart Journal. 38(11): 785-791

10. Wallyn, J., N. Anton, T. F. Vandamme. 2019. Synthesis, Principles, and Properties of Magnetite Nanoparticles for In Vivo Imaging Applications - A Review. Pharmaceutics. 11(11): 601. https://dx.doi.org/10.3390%2Fpharmaceutics11110601

11. Lu, A. H., E. L. Salabas, F. Schuth. 2007. Magnetite Nanoparticles: Synthesis, Protection, Functionalization, and Application. A Journal of the German Chemical Society. 46(8): 1222-1244

12. Cotica, L. F., V. F. Freitas, G. S. Dias, I. A. Santos, S. C. Vendrame, N. M. Khalil, R. M. Mainardes, M. Staruch, M. Jain. 2012. Simple and Facile Approach to Synthesize Magnetite Nanoparticles and Assessment of Their Effects on Blood Cells. Journal of Magnetism and Magnetic Materials. 324(4): 559-563

13. Mascolo, M. C., Y. Pei, T. A. Ring. 2013. Room Temperature Co-precipitation Synthesis of Magnetite Nanoparticles in a Large pH Window with Different Bases. Materials. 6: 5549-5567

14. Baumgartner, J., L. Bertinetti, M. Widdrat, A. M. Hirt, D. Faivre. 2013. Formation of Magnetite Nanoparticles at Low Temperature: From Superparamagnetic to Stable Single Domain Particles. PLOS One. 8(3): e57070. https://doi.org/10.1371/journal.pone.0057070

15. Zarnegar, Z., J. Safari. 2017. Modified Chemical Coprecipitation of Magnetic Magnetite Nanoparticles Using Linear-Dendritic Copolymers. Green Chemistry Letters and Reviews. 10(4): 235-240

16. Felix, L. L., B. Sanz, V. Sebastian, T. E. Torres, M. H. Sousa, J. A. H. Coaquira, M. R. Ibarra, G. F. Goya. 2019. Gold-Decorated Magnetic Nanoparticles Design for Hyperthermia Applications and as A Potential Platform for Their Surface-Functionalization. Scientific Reports. 9. 4185. https://doi.org/10.1038/s41598-019-40769-2

17. Silva, S. M., R. Tavallaie, L. Sandiford, R. D. Tilley, J. J. Gooding. 2016. Gold Coated Magnetic Nanoparticles: From Preparation to Surface Modification for Analytical and Biomedical Applications. Chemical Communications. 52:7528-7540

18. Shah, R. R., T. P. Davis, A. L. Glover, D. E. Nikles, C. S. Brazel. 2015. Impact of Magnetic Field Parameters and Iron Oxide Nanoparticle Properties on Heat generation for Use in Magnetic Hyperthermia. Journal of Magnetism and Magnetic Materials. 387: 96-106

19. Martinez, B. I., D. A. Cortes-Hernandez, A. Zugasti-Cruz, B. R. Cruz-Ortiz, E. M. Muzquiz-Ramos. 2016. Heating Ability and Hemolysis Test of Magnetite Nanoparticles Obtained by a Simple Co-Precipitation Method. Journal of Applied Research and Technology. 14: 239-244

20. Li, Z., M. Kawashita, N. Araki, M. Mitsumori, M. Hiraoka, M. Doi. 2010. Magnetite Nanoparticles with High Heating Efficiencies for Application in the Hyperthermia of Cancer. Journal of Materials Science and Engineering. 30(7): 990-996

21. Chen, L., C. Chen, P. Wang, T. Song. 2017. Mechanism of Cellular Effects Directly induced by Magnetic Nanoparticles Under Magnetic Fields. Journal of Nanomaterials. 1564634. https://doi.org/10.1155/2017/1564634

22. Sakariassen, K. S., L. Orning, V. T. Turitto. 2015. The Impact of Blood Shear Rate on Arterial Thrombus Formation. Future Science OA. 1(4): FSO30. https://dx.doi.org/10.4155%2Ffso.15.28

23. Godoy-Gallardo, M., P. K. Ek, M. M. T. Jansman, B. M. Wohl, L. Hosta-Rigau. 2015. Interaction Between Drug Delivery Vehicles and Cells Under the Effect of Shear Stress. Biomicrofluidics. 9(5): 052605. https://dx.doi.org/10.1063%2F1.4923324

24. Bonnard, T., C. E. Hagemeyer. 2015. Ferric Chloride-Induced Thrombosis Mouse Model on Carotid Artery and Mesentery Vessel. Journal of Visualized Experiments. 100: e82838. https://dx.doi.org/10.3791%2F52838

25. Li, W., M. Nieman, A. S. Gupta. 2016. Ferric Chloride-Induced Murine Thrombosis Models. Journal of Visualized Experiments. 115: e54479. doi:10.3791/54479

26. Huttinger, A. L., D. G. Wheeler, S. Gnyawali, D. Dornbos, J. M. Layzer, N. Venetos, N, S. Talentino, N. J. Musgrave, C. Jones, C. Bratton, M. E. Joseph, C. Sen, B. A. Sullenger, S. M. Nimjee. 2018. Ferric Chloride-Induced Canine Carotid Artery Thrombosis: A Large Animal Model of Vascular Injury. Journal of Visualized Experiments. 139: https://doi.org/10.3791/57981

CURRICULUM VITAE

Cammy N. Truong

Education
University of Wisconsin – Milwaukee, Milwaukee, WI
Ph.D Biological Sciences 2014-2020
Thesis Advisor: Dr. Julie A. Oliver
Thesis Title: Fibrinogen-conjugated gold-coated magnetite nanoparticles targeting activated platelets in a whole blood system

University of Wisconsin – Milwaukee, Milwaukee, WI
B.S. Biochemistry 2009-2014

Awards
Microscopy & Microanalysis Student Scholar Award 2020
Microscopy & Microanalysis virtual PMCx60 Poster Award 2020
Ruth Walker Grant-in-Aid 2016, 2019
Joseph B. Baier Award 2017, 2018

Teaching
Instructor for laboratory in Genetics and Cell Biology 2020
Teaching Assistant for laboratory in Genetics and Cell Biology 2016-2020
Teaching Assistant for laboratory Introductory Anatomy and Physiology 2014-2017

Publication
Truong, C. N., C.N. Cazzola, S.A. Benzow, A.P. Norberg, A.R. Chramega, H.A. Owen and J.A. Oliver. 2020. Combining Scanning Electron Microscopy and Light Microscopy to Study How Blood Cell Directed-Architecture Influences Nanoparticle Penetration into Clots. Microscopy and Microanalysis. In press.

Presentations:
(Invited) Truong, C. N., C.N. Cazzola, S.A. Benzow, A.P. Norberg, A.R. Chramega, H.A. Owen and J.A. Oliver. 2020. Combining Scanning Electron Microscopy and Light Microscopy to Study How Blood Cell Directed-Architecture Influences Nanoparticle Penetration into Clots. Microscopy & Microanalysis 2020, August 03, 2020, Milwaukee, WI, Virtual.

Truong, C. N., C.N. Cazzola, S.A. Benzow, A.P. Norberg, A.R. Chramega, H.A. Owen and J.A. Oliver. 2020. Combining Scanning Electron Microscopy and Light Microscopy to Study How Blood Cell Directed-Architecture Influences Nanoparticle Penetration into Clots. Microscopy & Microanalysis 2020, August 06, 2020, Milwaukee, WI, Virtual (Virtual Poster presentation).

Truong, C. N., C. C. N. Cazzola, and S. A. Benzow. Quantifying the Penetration of Platelet-Targeted Nanoparticles in Platelet-Rich Plasma (PRP) and Whole Blood (WB) Clots by Utilizing Silver Enhancement and Light Microscopy. Biological Sciences Research Symposium 2019, April 19, 2019, University of Wisconsin-Milwaukee (Oral Presentation).

Truong, C. N., and J. A. Oliver. The Degree of Nanoparticle's Penetration into Clots Determined by Blood Cell Directed-Architecture. Biological Sciences Research Symposium 2018, April 13, 2018, University of Wisconsin-Milwaukee (Oral Presentation).

Truong, C. N., and J. A. Oliver. Penetration of Fibrinogen- Conjugated Gold Nanoparticles into Platelet-Rich-Plasma (PRP) and Whole Blood Clots. Biological Sciences Research Symposium 2017, April 21, 2017, University of Wisconsin-Milwaukee (Oral Presentation).

Truong, C. N., and J. A. Oliver. Direct Targeting of Murine Breast Cancer Tumor Cells Using Folic Acid-Bovine Serum Albumin (FA-BSA)-Conjugated Nanoparticles. University of Wisconsin-Milwaukee Graduate Student Research Symposium 2016, October 2016, University of Wisconsin-Milwaukee (Oral Presentation).

Truong, C. N., and J. A. Oliver. Targeting Fibrinogen-Conjugated Nanoparticles to Activated Platelets in the Presence of Fibrin. Biological Sciences Research Symposium 2015, April 2015, University of Wisconsin-Milwaukee (Poster Presentation).